Eesti Maaülikool
Estonian University of Life Sciences

POLYMER ENCAPSULATION OF ZINC OXIDE NANOSTRUCTURES FOR PHOTODIODE APPLICATIONS

TSINKOKSIIDI NANOSTRUKTUURIDE POLÜMEERKAPSELDAMINE FOTODIOODRAKENDUSTE JAOKS

KESHAV NAGPAL

A Thesis
for applying for the degree of Doctor of Philosophy
in Engineering Sciences

Väitekiri
filosoofiadoktori kraadi taotlemiseks
tehnikateaduse erialal

Tartu 2024

Eesti Maaülikooli doktoritööd

**Doctoral Theses of the
Estonian University of Life Sciences**

Eesti Maaülikool
Estonian University of Life Sciences

POLYMER ENCAPSULATION OF ZINC OXIDE NANOSTRUCTURES FOR PHOTODIODE APPLICATIONS

TSINKOKSIIDI NANOSTRUKTUURIDE POLÜMEERKAPSELDAMINE FOTODIOODRAKENDUSTE JAOKS

KESHAV NAGPAL

A Thesis
for applying for the degree of Doctor of Philosophy
in Engineering Sciences

Väitekiri
filosoofiadoktori kraadi taotlemiseks
tehnikateaduse erialal

Tartu 2024

Institute of Forestry and Engineering,
Estonian University of Life Sciences

According to verdict No. 6-14/5-6 of June 10, 2024, the Doctoral Committee of the Engineering Sciences of the Estonian University of Life Sciences has accepeted the thesis for the defence of the degree of Doctor of Philosophy in Engineering Sciences.

Opponents: **Professor Ola Nilsen, PhD**
Center for material science and nanotechnology
University of Oslo, Norway
Associate Professor Bertrand Vilquin, PhD
Université Claude Bernard Lyon1
Ecole Centrale de Lyon, France

Supervisors: **Professor Protima Rauwel, PhD**
Insititute of Forestry and Engineering
Estonian University of Life Sciences
Professor Erwan Yann Rauwel, PhD
Institute of Veterinary Medicine and Animal Sciences
Estonian University of Life Sciences

Defence of the thesis: Estonian university of Life Sciences, room A202, Kreutzwaldi 56, Tartu, on August 26, 2024, at 13:00.

The Estonian language in the current thesis was revised by Mrs. Ülle Sihver from Language Center.

European Union
European Regional
Development Fund

Investing
in your future

CONTENTS

LIST OF ORIGINAL PUBLICATIONS

I. **K. Nagpal**, L. Rapenne, D. S. Wragg, E. Rauwel, P. Rauwel, "The role of CNT in surface defect passivation and UV emission intensification of ZnO nanoparticles" Nanomaterials and Nanotechnology, **12**, 1–10 (2022) (1.1 ETIS classified with database on WEB of Science)

II. **K. Nagpal**, E. Rauwel, E. Estephan, M. R. Soares, P. Rauwel, "Significance of Hydroxyl Groups on the Optical Properties of ZnO Nanoparticles Combined with CNT and PEDOT:PSS" Nanomaterials **12**, 3546 (2022) (1.1 ETIS classified with database on WEB of Science)

III. **K. Nagpal**, E. Rauwel, F. Ducroquet, I. Gelard and P. Rauwel, "Relevance of alcoholic solvents in the growth of ZnO nanoparticles and ZnO hierarchical nanorod structures on their optical and opto-electrical properties" , Nanotechnology **34**, 485602 (2023) (1.1 ETIS classified with database on WEB of Science)

IV. **K. Nagpal**, E. Rauwel, F. Ducroquet, P. Rauwel "Assessment of the optical and electrical properties of light emitting diodes containing carbon-based nanostructures and plasmonic nanoparticles: a review", Beilstein J. Nanotechnol. **12**, 1078–1092 (2021) (1.1 ETIS classified with database on WEB of Science, Review article)

V. **K. Nagpal**, M. S. Rosario, K. Praakle, E. Rauwel, P. Rauwel, "Investigation of the optical and antibacterial properties of biosynthesized ZnO nanoparticles using Thuja tincture" Journal of Physics: Conference Series 2315, 012016 (2022) (3.1 ETIS classified with database on WEB of Science)

VI. **K. Nagpal**, E. Rauwel, F. Ducroquet, I. Gelard, P. Rauwel, "Fabrication and evaluation of figures of merit of ZnO-polymer based hybrid UV photodiodes" APL Materials **12**(6), (2024) (1.1 ETIS classified with database on WEB of Science)

The author's contribution to the articles:

Article	Study design	Data collection	Data Processing	Manuscript preparation
I	**KN**, ER, PR	**KN**, PR, LR, DW	**KN**, ER, PR	**KN,** PR, ER
II	**KN**, ER, PR	**KN**, MS, PR, EE	**KN**, PR, ER	**KN**, PR, ER
III	**KN**, PR, ER	**KN**, FD, IG, ER, PR	**KN**, PR, FD	**KN**
IV	**KN**, ER, PR	**KN**, PR, ER	**KN**	**KN**, ER, PR
V	**KN**, ER, PR	**KN**, ER, PR	**KN**	**KN**, ER, PR, KP
VI	**KN**, ER, PR	**KN**, FD, IG	**KN,** IG	**KN**

KN-Keshav Nagpal, LR-Laetitia Rapenne, DW-David S Wragg, EE-Elias Estephan, KP-Kristi Praakle, MS-Maria Rosario Soaeres, FD-Frederique Ducroquet, IG- Isabelle Gelard, ER- Erwan Rauwel, and PR-Protima Rauwel

ABBREVIATIONS AND SYMBOLS

Abbreviations

0D	Zero-dimensional
1D	One-dimensional
BBC	British Broadcasting Corporation
CNT	Carbon nanotubes
DI	De-ionized water
DFT	Density functional theory
DLE	Deep level emission
e-h	Electron-hole pair
EU	European Union
EQE	External quantum efficiency
FWHM	Full width half maximum
F8BT	Poly(9,9-dioctylfluorene-*alt*-benzothiadiazole)
FTIR	Fourier transform infrared spectroscopy
HCl	Hydrochloric acid
HOMO	Highest occupied molecular level
HMTA	Hexamethylenetetramine
IEA	International Energy Agency
ITO	Indium tin oxide
LDA	Local density approximation
LED	Light-emitting diodes
LUMO	Lowest unoccupied molecular level
MWCNT	Multi walled carbon nanotubes
NBE	Near band edge emission
NaOH	Sodium hydroxide
PL	Photoluminescence sepectroscopy
PPC	Persistent photoconductivity
PEDOT:PSS	Poly(3,4-ethylenedioxythiophene)-poly(styrenesulfonate)

pDOS	Partial density of states
rpm	Revolutions per minute
SEM	Scanning electron microscopy
SIC-PP	Self-interaction corrected pseudopotential
SWCNT	Single walled carbon nanotubes
TEM	Transmission electron microscopy
UV	Ultra-violet
XRD	X-Ray diffraction analysis
XPS	X-ray photoelectron spectroscopy
ZnO	Zinc oxide

Symbols and units

~	Approximately
η	Diode ideality factor
μm	Micrometer
Ω	Ohm
λ	Wavelength
A	Ampere
Å	Angstrom
A_{eff}	Effective area of the UV light
cm	Centimeter
^0C	Degree Celsius
E(x)	Electric field
E_F	Fermi energy level
eV	Electron volts
F	Farad
g	Grams
GPa	Gigapascal
h	Hours
I	Current
$I_{forwrad}$	Diode current under forward bias

$I_{reverse}$	Diode current under reverse bias
I_{dark}	Current under dark conditions
I_{UV}	Current under UV radiations
I-V	Current-Voltage
I-t	Current-time
M	Molarity of solution
ml	milliliter
mg	milligrams
mm	Milimeter
nm	Nanometer
$P_{incident}$	Incident power of the UV light source
ps	Pico-second
R	Responsivity
S	Sensitivity
s	Seconds
$S.cm^{-1}$	Siemens per centimeter
t	Time
T	Absolute temperature
T_{rise}	Time taken to rise current from 10% to 90% under the UV radiations
T_{decay}	Time taken to fall current from 90% to 10% when there is no supplied UV radiations
TWh	Terawatt-hour
V	Volts
V_{Bin}	Built in potential within depletion region
V_{ext}	External applied potential
V_b	Break down potential of a diode

INTRODUCTION

The energy sector is rapidly expanding in order to quickly adapt to the continuously evolving energy policies. In addition, the 2050 EU energy transition towards decarbonized energy production and use has pushed the energy sector to review the overall energy consumption of devices during their life cycle. Therefore, the present focus is on creating energy-efficient and cost-effective devices. According to the International Energy Agency (IEA), the total global electricity consumption is increasing by 1.7% per annum, and is at ~22.848 TWh today. In addition, energy prices are directly linked to the national economy. Therefore, today due to the energy crisis, devices must be energy-efficient. Additionally, the semiconductor technology used in these devices should be cost-effective. The present devices for energy applications such as light-emitting diodes, solar panels and photodetectors consisting of semiconductors of GaN, Si, GaAs or InGaN have shown advances in energy efficiency leading to energy saving [1-4]. Nevertheless, their production requires state-of-the-art and high-cost thin film growth technologies such as physical and chemical vapor depositions, making these devices expensive and niche. In that regard, for the development of optoelectronic devices, nanomaterials are seen as promising candidates [5,6]. In fact, the 21st century can be considered as the century of nanotechnology because of its omnipresence in research and everyday life [7,8]. According to a BBC report, the nanotechnology market is expected to grow from USD 5.2B in 2021 to USD 23.6B by 2026, implying the expansion of nanotechnologies to several sectors.

Today, nanomaterials including metals, metal oxides, semiconductors, perovskites, and carbon-based materials have become the backbone of various modern energy devices, such as batteries, fuel cells, solar cells, supercapacitors, gas sensors, photo-catalysis, light emitting diodes, and photodiodes [9-11]. Synthesizing nanomaterials with a high yield and low-cost is of importance for the aforementioned applications. Therefore, during the past two decades, a huge development in the field of nanomaterial synthesis has been achieved, using several top-down and bottom-up methodologies [12,13]. In the top-down approach, nanomaterials are prepared by breaking larger pieces of a material until nanostructuring is achieved. Whereas, in a bottom-up approach individual atoms and molecules interact to form the nanomaterials.

Between the two approaches, the bottom-up approach allows a better control of defect production, chemical compositions, morphologies and sizes of nanomaterials. In fact, at the nanoscale, materials demonstrate novel electrical, chemical, optical and magnetic properties compared to their bulk counterpart, owing to their high surface-to-volume ratio [14]. These properties are highly dependent on the shape and size of a nanomaterial, which in turn depend on their synthesis conditions, such as temperature, time, pH, precursor, chemical environment, surfactants and the presence of water or hydrates during the reaction process. Therefore, a nanomaterial, whose physical, chemical, and optical properties are customizable via its synthesis conditions, has an important position in the field of nanotechnology.

In that regard, the intrinsic n-type ZnO semiconductor has demonstrated an enormous technological development, with being one of the most popular inorganic semiconductor materials [15]. The prominence of ZnO is associated with its facile synthesis methods, Earth-abundance and non-toxicity, compared to other related inorganic semiconductors such as GaN, SiC, and GaAS [16]. In addition, ZnO is a versatile functional material that can be grown as nanoparticles and hierarchical nanostructures, including nanospheres, nanowires, nanobelts, nanocombs, nanotubes, nanorods, and tetrapods [17,18]. The zero-dimensional (0D) nanostructures of ZnO, for example nanospheres are mainly applied to commercial photocatalysis and for sunscreen applications. Whereas, for optoelectronic applications, the one-dimensional (1D) nanostructures of ZnO, including nanorods and nanowires, are mainly employed [19]. In particular, for UV sensors, light-emitting diodes and photodiode applications; 1D ZnO nanorods have become one of the major focal points, owing to their high aspect ratio, facile synthesis on various substrates, long-range order and excellent photoelectric properties [20]. Conversely, the lower amount of surface defects in 1D ZnO nanostructures engenders rapid excitonic recombination, which is a disadvantage for photodiode applications but an advantage in light-emitting diode (LED) applications [21]. To overcome these issues for photodiode applications, hybridization of ZnO nanostructures with polymers and carbon nanotubes (CNT) has shown promising results [21,22].

This dissertation presents the development of a hybrid diode for UV-photodiode application. In order to achieve the hybrid-diode device,

1D ZnO nanorods were synthesized and hybridized with p-type polymers of Poly(9,9-dioctylfluorene-*alt*-benzothiadiazole) (F8BT) and Poly(3,4-ethylenedioxythiophene)-poly(styrenesulfonate) (PEDOT:PSS). The ZnO nanorods were grown by a cost-effective hydrothermal method and by varying the seed layer solvents. The effect of seed-layer solvents on the growth, optical, electrical and photoresponse properties of ZnO nanorods was subsequently investigated. Four different solvents, including absolute methanol, absolute ethanol, absolute isopropanol and aqueous ethanol (70%) were used as seeding solvents for the preparation of seed layers for ZnO nanorod growth. These nanorods on their own were efficient UV sensors and present complementary properties for charge storage via the phenomenon of persistent photoconductivity. Since the nanorod growth depends on the ZnO seed or nucleation layer, a study of the role of the nuclei in inducing the formation of defects during the nanorod growth was carried out. To that end, the synthesis of ZnO nanoparticles using various seed-layer solutions via sol-gel routes was first studied. In addition, the crystalline, morphological, chemical and optical properties of the as-synthesized ZnO nanoparticles were fully investigated. The as-synthesized ZnO nanoparticles were then combined with CNT and PEDOT:PSS polymer. Therefore, in order to achieve an energy-efficient and cost-effective photodiode device, a primary study of ZnO nanostructures and their hybrids was conducted in order to optimize the synthesis conditions. These studies were instrumental in evaluating the figures of merit of the UV photodiodes.

The novelty of this thesis lies in the use of different alcoholic solvents to modify the physical, chemical, optical and electrical properties of ZnO nanostructures, which has not been previously carried out, to the best of our knowledge. The novelty aspects are enumerated below.

1. Synthesis of ZnO nanoparticles via non-aqueous routes using different alcoholic solvents.

2. Growth of ZnO nanorods using different alcoholic seeding solvents and their roles as UV sensors and in persistent photoconductivity (PPC) for charge storage.

3. Fabrication of a hybrid UV-photodiode with the following device configuration: ITO/n-type ZnO nanorods/ p-type F8BT polymer/ p-type PEDOT:PSS.

All these nanostructures were systematically characterized in order to evaluate their physical, chemical, morphological, optical and electrical properties.

This thesis is based on the results and work of six publications by the author in which, five are research articles and one is a review article. The articles are presented in the list of original publications and the author contributions are presented in the author contribution table. The results included in this theis are divided in to three sections; A: ZnO nanoparticles, B: ZnO nanorods and C: ZnO-nanorod-based photodiodes.

The results of this thesis have been presented at three international conferences as one oral presentation and three poster presentations. All of the publications by authors are available in Thomson Reuters WEB of Science database and Scopus. The author is the first author of all the six articles presented in this thesis.

1. REVIEW OF THE LITERATURE

1.1. Nucleation and growth of nanoparticles

There are mainly three stages involved in a typical nanoparticle growth process viz., nucleation, growth and isolation of nanoparticles. Figure 1.1 schematizes the typical steps involved during the growth of nanoparticles starting from a precursor in a solvent. According to the classical LaMer's theory, when a precursor is added to a solvent, the number of monomers increases with time in the solution until it attains a supersaturation state after which, the monomers undergo a burst-nucleation, as shown in figure 1.1(a-c). Following nucleation, the nuclei already present consume new nuclei generated from the continuous decomposition of the precursor, engendering the growth of particles through a condensation process. Two main types of growth processes are proposed following nucleation, as shown in figure 1.1(d). The first process called Ostwald ripening depends on the high solubility and high surface energy of smaller particles that anchor on larger particles through diffusion in the solvent, leading to the growth of larger particles through the coagulation process, and resulting in lower number of nanoparticles for a fixed volume of a solution. The second growth process is coalescence during which, two or more nuclei merge to form one bigger particle. Therefore, Ostwald ripening involves merging of nanoparticles, whereas coalescence involves merging of nuclei, with the former occurring exclusively in solutions. Irrespective of the process, several amorphous clusters of particles are usually obtained during the growth stage. Subsequently, these clusters combine to form the final precipitated nanoparticles, as shown in figure 1.1(e).
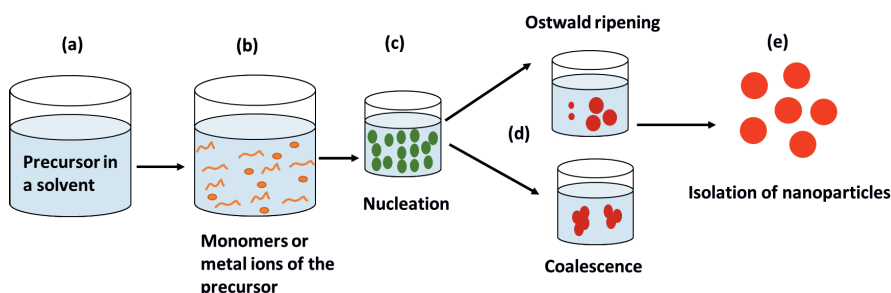

Figure 1.1. Schematic of the step-by-step nanoparticle percipitaion process, (a) dissolution of precursor in solvent, (b) monnomers formation, (c) nucleation, (d) growth of nanoparticles, and (e) isolation of nanoparticles.

1.2. ZnO compound

ZnO is a n-type semiconductor of II-VI group that has attracted interest for various applications, such as transparent electronics, photovoltaics, photocatalysis, photodetectors, LED, lasers and sensors [23-35]. Its most significant properties include a wide bandgap of 3.4 eV and a high excitation binding energy of 60 meV, due to which it is used in ultra-violet (UV) detection and laser applications [36-38]. ZnO is the second most abundant metal oxide after iron and is found in the Earth's crust as the zincite mineral [39]. Owing to its low-cost production and low toxicity, it is suitable for many industrial applications such as cosmetics, paints, antimicrobial agents and food additives [40-46]. In addition, ZnO also exhibits high chemical stability, excellent piezoelectricity and remarkable electronic and optical properties, which makes it a promising candidate for applications in optoelectronics, spintronic and piezoelectric sensors [46-48]. Today, the challenge is to obtain a stable p-type ZnO in order to fabricate p-n homojunction diodes [49,50]. There are accounts of ZnO p-n homojunction, but further optimization is still required [51,52]. Nevertheless, heterojunctions consisting of n-type ZnO with other p-type inorganic materials, such as GaN, GaAs, AlGaN, Si, CdTe, NiO, as well as organic materials such as PEDOT:PSS polymer, are more feasible to achieve. These heterojunctions are already incorporated into LED, photodiode and other optoelectronic applications [53,54].

In addition, ZnO is a very versatile material that can be grown as nanostructures of various morphologies, such as nanosheets, nanospheres, nanowires, nanorings, nanowalls, nanoflowers, and nanorods [55-57]. Various wet chemical synthesis methods, such as precipitation, hydrothermal, solvothermal, high energy ball mining, as well as physical deposition methods, such as chemical bath deposition, electrochemical deposition, pulsed laser deposition, and spray pyrolysis have been reported for the synthesis of ZnO nanostructures [16,58-61].

1.2.1. Crystal structure of ZnO

ZnO exists in three different crystal configurations viz., wurtzite (B4), zinc blende (B3), and rock salt (B1), where B4, B3, and B1 denote the Strukturbericht designation of three phases [62,63]. Figures 1.1(a-c) are the schematic representations of rock salt, zinc blende and wurtzite structure of ZnO, respectively. In terms of space groups, the wurtzite

structure of ZnO belongs to group *P63mc*, zinc blende to *F4̄3m* and rock salt to *Fm3m*. At ambient temperature and pressure, ZnO thermodynamically stabilizes in the wurtzite crystal structure, which has a hexagonal unit cell with lattice parameters 'a', and 'c' [64]. For the ideal wurtzite crystal structure, the ratio of the two lattice parameters or c/a = 1.633; however, the c/a ratio is reported to be ~1.60, with a = 3.2503 Å and c = 5.2031 Å [65,66]. In the Wurtzite ZnO structure, every zinc ion (Zn^{2+}) is surrounded by four oxygen ions (O^{2-}), or vice-versa, coordinated at the edges of a tetrahedron and stacked alternatively along the c-axis [67]. This tetrahedral coordination in the ZnO wurtzite structure results in a non-centro-symmetric structure that determines the crystal growth, defect formation and piezoelectric properties of ZnO [68]. Other crystal structures of ZnO i.e., zinc blende and rock salt stabilize only under specific conditions. For example, the metastable zinc blende structure can only be stabilized by heteroepitaxial growth on a cubic-phase substrate, such as ZnS, GaAS/ZnS, Pt/Ti/SiO$_2$/Si [18]. These substrates offer favorable topological compatibilities and provide the necessary substrate-induced strain for the stabilization of the zinc blend structure. On the other hand, the rocksalt structure of ZnO cannot be stabilized through epitaxial growth [69]. Nevertheless, a metastable rocksalt structure of ZnO can be obtained by applying a pressure greater than 10 GPa to the hexagonal wurtzite structure of ZnO. At such high pressures, the phase transition from hexagonal wurtzite to rocksalt structure is associated with a large decrease in volume of ~17% [70].

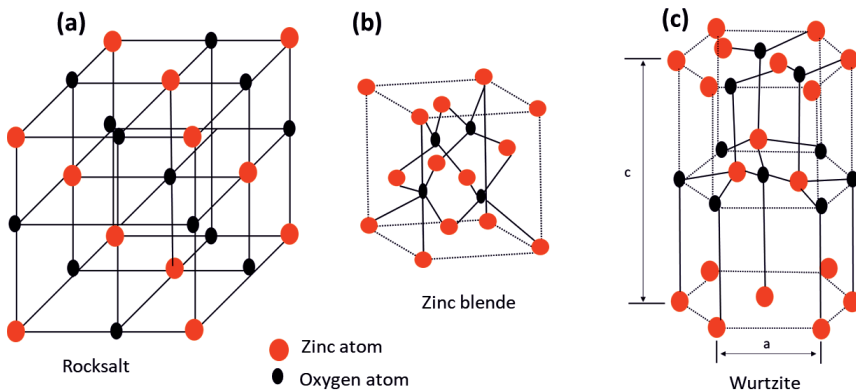**Figure 1.2**. Ball-stick representation of ZnO structures (a) Rocksalt, (b) Zinc blende and (c) Wurtzite.

1.2.2. Growth of ZnO nanorods

Another important characteristic of the ZnO wurtzite structure is its polar surfaces i.e., [0001] and [000$\bar{1}$] that are Zn and O terminated, respectively [71]. It also possesses six non-polar surfaces belonging to the family of planes [$\bar{1}$100], containing both Zn and O ions, whereupon contributing to their electrical neutrality [72]. However, polar surfaces have non-transferable ionic charges, making them highly reactive during the chemical synthesis of ZnO nanostructures [72,73]. Furthermore, the growth rate of individual crystallographic planes in ZnO depends on the principle of energy minimization [72]. Therefore, the growth of nanostructures requires the minimization of the electrostatic energy arising from the polar surfaces of ZnO [72]. This results in the growth of polar surface-dominated growth or along the [0001] crystallographic direction, allowing growth of ZnO in various hierarchical nanostructures, such as nanowires, nanocombs, nanobelts, nanorings, tetrapods, and nanorods [17,72,74-77].

1.2.3. Electronic structure and bandgap of ZnO

The electronic structure and band gap of ZnO have been studied by several theoretical first-principles methods, with the density functional theory (DFT) being the most popular. Various approximations, such as local density approximation (LDA), Hubbard U or LDA+U approximation and self-interaction corrected pseudopotential (SIC-PP) approximation have been employed within the DFT to study the electronic and band gap properties of ZnO. Compared to standard LDA approximation, the effect of Zn 3d electrons has been included in the SIC-PP approximation, which improved the band gap calculations of ZnO. Figure 1.3(a) shows the LDA band structure of ZnO calculated using SIC-PP approach [78,79]. In this figure, there are ten bands at around -9 eV below the valence band, which correspond to the Zn 3d electronic state. However, these bands are generally absent in the standard LDA approximation calculations because the effect of the Zn 3d electron is not considered [79]. The six bands between -5 to 0 eV represent the O 2p bonding states. By the SIC-PP approach, a band gap of 3.37 eV has been calculated, which is very close to the experimental band gap of 3.34 eV. On the other hand, the standard LDA approach shows a band gap of only 3.0 eV, due to the exclusion of Zn 3d electronic state. Similar to SIC-PP approximation, when both Hubbard terms, i.e., U_d to Zn d-orbitals

and U_p to O p-orbitals are included in the LDA+U approximation, then the calculated band gap of ZnO is close to the experimental value [80,81]. These electronic band modifications and electron-transition states in ZnO could be explained in depth through the partial density of states (pDOS). Figure 1.3(b) is the pDOS of ZnO using LDA+U approximation for U_d=5 and U_p=7 [81]. In this figure, the Fermi energy level is at 0 eV and is marked with a dotted line. The states below 0 eV represent the valance band and above 0 eV represent the conduction band. The closest state below 0 eV i.e., in valance band is dominated by O-2p states, followed by Zn-3d states, whereas Zn-4s states dominate the conduction band, followed by some overlapping between Zn-3d and O-2p states. This shows that the electronic transitions occurring in ZnO are mainly from O-2p states to Zn-4s states.

Apart from theoretical approaches, several experimental approaches, such as X-ray induced photo absorption, photoemission spectroscopy, and angle resolved photoelectron spectroscopy have been also used to calculate the band structure of the electronic states of ZnO [81-83]. Figure 1.3(c) is the band structure of Wurtzite ZnO at the Γ point of the Brillouin zone, obtained from the experimental approaches [83,84]. Due to the crystal-field splitting and spin-orbit interactions, the valance band of ZnO splits into three sub-bands A, B and C; whereas, there is no splitting of the conduction band. Splitting of energies between the sub-bands A, B and C are ΔE_{AB} = 4.9 meV and ΔE_{BC} = 43.7 meV. The conduction band, sub-band A and C possess the Γ_7 symmetry, while the sub-band B possesses the Γ_9 symmetry. At room temperature, ZnO has a wide band gap of ~3.44 eV, which is the energy difference between the minimum of the conduction band and the maximum of the valance band A [85,86]. The dependence of the band gap on temperature (upto 300K) is given by the following empirical relationship [87].

$$Eg = Eg(T = 0) - \frac{5.05 X 10^{-4} T^2}{900 - T}. \qquad (1.1)$$

In addition, ZnO is a direct band gap semiconductor because its conduction band minimum and valance band maximum are centered to Γ-point, k=0, of the Brillioun zone. A property of a direct band gap semiconductor is the favorable electron-hole pair generation in ZnO with no change in momentum or no k-shift. This makes ZnO a favorable material for optical emission applications, such as LED and UV lasers.
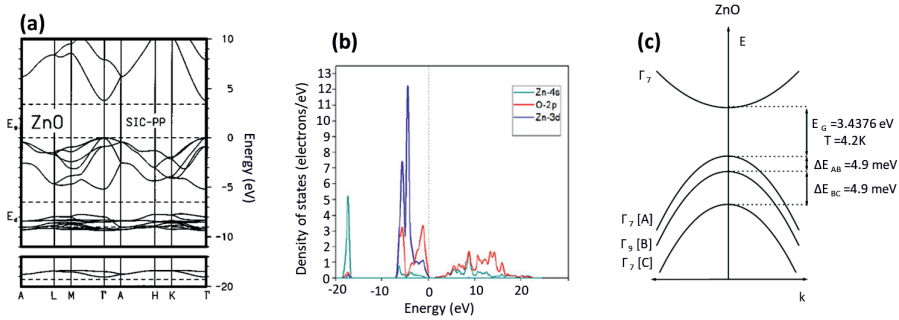
Figure 1.3. (a) LDA band structure of ZnO calculated using SIC pseudopotentials, reproduced with permission from [79], (b) pDOS of ZnO calculated using LDA+U approximation for $U_d=5$ and $U_p=7$, reproduced with permission from [81], and (c) Band structure splitting in ZnO due to crystal field and spin-orbit splitting, reproduced with permission from [84].

1.2.4. Doping, defect states, band bending and their effects on the optical properties of ZnO

ZnO is an intrinsically n-doped material with intrinsic defects, including zinc interstitials (Zn_i) and oxygen vacancies (V_O) acting as donors. In general, bulk ZnO shows a free electron density of $10^{16} cm^{-3}$ [88]. However, at the nanoscale the free electron density increases up to 10^{18} cm^{-3} [89]. The increase in electron density at the nanoscale is generally attributed to the intrinsic donor defects in ZnO arising from either Zn_i, V_O or their complexes. Similarly, modification of the optical, electrical and electronic properties of ZnO is generally obtained by doping. The most common dopants for ZnO are metal ions, including aluminum (Al), indium (In), manganese (Mn), lanthanum (La), and chromium (Cr), or non-metals like carbon (C) and nitrogen (N) atoms [90,91]. Depending on the oxidation states of the dopant, the generation of V_O or zinc vacancies (V_{Zn}) in the lattice of ZnO occurs [92,93]. In general, a zinc vacancy is found to be a powerful hole trap, which is reported to be stable in three charge states 0, -1 and -2. Therefore, zinc-vacancy-acceptor levels have been determined by DFT within LDA approximation and the 0/-1 and -2/-1 zinc vacancy are located at ~0.18 eV and ~0.87 eV, above the valance band maximum [94]. On the other hand, by using temperature dependent PL spectroscopy, oxygen vacancies with three charge states have been identified viz., the doubly ionized oxygen vacancy (V_O^{++}), the singly ionized oxygen vacancy (V_O^+) and neutral oxygen vacancy (V_O^x) [95]. In fact, V_O^x does not capture electrons, V_O^+ captures only one electron and V_O^{++} can capture two electrons to then turn neutral [96].

The position of the V_O^{++} state is ~2.2 eV, of V_O^+ is ~2.48 eV and of V_O^x is ~2.78 eV above the valance band, as shown in figure 1.4(a). In addition, the adsorption of oxygen radicals or hydroxyl groups on the surface of ZnO nanoparticles by chemisorption or physisorption processes, creates a surface-depletion region that leads to upward band bending in ZnO [97], as shown in figure 1.4(b). At this point V_O^+ converts to V_O^{++} by capturing holes from the surface-depletion region. Subsequently, a conduction band electron recombines with V_O^{++} to emit a photon of 2.2 eV [98]. Remarkably, the dominant emission in ZnO nanoparticles is the green emission related to the surface oxygen vacancies.

At room temperature, the PL spectrum of ZnO nanoparticles consists of two emission peaks that include near band edge emission (NBE) in the UV region and deep level emission (DLE) in the visible region [85,99]. The origin of NBE is attributed to the recombination of free excitons due to band-to-band transitions [100,101]. Whereas, the DLE originates from the combination of several intrinsic points and extended defects such as oxygen vacancies (V_O), zinc vacancies (V_{Zn}), oxygen interstitials (O_i), Zn_i, oxygen antisite (O_{Zn}) and zinc antisite (Zn_O) [102,103]. The transitions between various defects lead to many visible emissions including violet (~2.8 eV), blue (~2.7 eV), green (~2.5 eV and 2.3 eV), yellow (~2.2 eV), orange (~2.1 eV), and red (~1.9 eV), covering the entire visible spectrum [55,104], as shown in figure 1.4(a). Nevertheless, emission wavelengths are highly dependent on the shape, size and morphology of ZnO nanoparticles, which in turn depend on the synthesis conditions, such as reaction temperature, time, and precursor [105,106]. In general, small nanoparticles of less than 10 nm in size tend to promote the DLE at the detriment of the NBE, because of the higher amounts of surface defects, originating from the high surface-to-volume ratio.
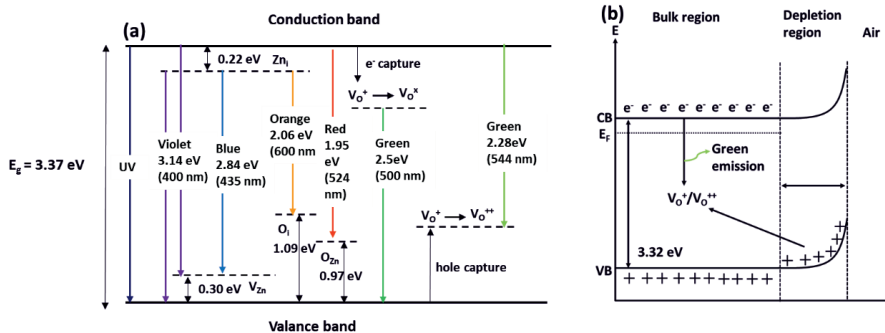
Figure 1.4. (a) Radiative and non-radiative electronic transitions between conduction band, defect levels and valence band in ZnO and (b) Upward band bending in ZnO due to surface-depletion region and the mechanism of green luminescence.

1.3. Carbon nanotubes (CNT)

Carbon nanotubes (CNT) belong to the fullerene family of carbon allotropes [107]. They are hollow cylindrical molecules consisting of a hexagonal arrangement of sp^2 hybridized carbon atoms with C-C bond distance of approximately 1.44 Å [108]. The sp^2 bonds between the individual carbon atoms in CNT are even stronger than sp^3 bonds in diamond [108]. In general, CNT have many useful characteristics like remarkable flexibility, high length to diameter ratio (aspect ratio), high surface area, high thermal conductivity, good stability under high currents, and good electrostatic properties [109-111]. CNT sheet electrode with a thickness of ~25 μm exhibits a high capacitance in the range of ~39 F.cm^{-3} to 90 F.cm^{-3} [112]. Therefore, due to their superior physical and electrical properties, CNT are extensively used for many applications, such as in nanoelectronics, sensors, catalysis, medicine, supercapacitors, nanocomposites, and for various other fields of nanotechnology [113-119].

Generally, CNT are classified into two categories i.e., single walled CNT (SWCNT) and multi-walled CNT (MWCNT) (IV). A SWCNT is made by rolling a single layer of graphene from edge-to-edge into a seamless cylinder. It has a diameter of 1-2 nm and length up to 1 mm [120]. On the other hand, a MWCNT has several concentric cylindrical tubes of graphene with varying diameters in the range of 7-100 nm and length up to 1 mm [119]. The electronic properties of these two types of CNT are highly dependent on their chirality, which is defined by two integers n and m [121]. Based on these two integers, various

configurations of CNT are available. For m=0 the configuration is a zigzag, for n=m the configuration is an armchair and for other values of n and m chiral configurations are formed. In addition, based on the chirality, a SWCNT can exhibit metallic or semiconducting properties. As a general rule, for a given (n,m) nanotube, if (2n+m) is a multiple of 3, then the nanotube is metallic, otherwise it is semiconducting. In metallic SWCNT the band gap between its valance and conduction band is zero, while semiconducting SWCNT generally exhibit a band gap of ~0.08 eV [122]. On the other hand, MWCNT contain multiple layers of graphene and each layer can have its own chirality, due to which it is more complicated to predict the electronic properties of MWCNT than SWCNT [123]. Nevertheless, MWCNT are in general metallic.

The synthesis of CNT is mainly carried out by three common routes; chemical vapor deposition, electric arc discharge, and laser ablation [124,125]. Other methods to produce CNT are thermal synthesis, gas-phase, flame, and plasma enhanced chemical vapor deposition methods [126,127]. Many of these synthesis methods lead to metallic or carbonaceous impurities in as-synthesized CNT. The typical metallic impurities are Fe, Ni, Co and Mo, which originate from the catalyst used during the synthesis. Whereas, carbonaceous impurities are mainly associated with amorphous and nano-graphitic carbon [128]. These impurities deteriorate the electrical, thermal and mechanical properties of CNT. The inertness of CNT is another issue, when considering nanocomposite synthesis, which hinders the dispersion and interfacial interaction of CNT with other materials and thus affects the performance of CNT-based devices. In addition, during the synthesis process, CNT tend to agglomerate into bundles, due to strong Van der Waals forces of attraction [129]. In order to overcome such issues, functionalization of CNT with reactive moieties is a necessity and is mainly performed by two methods, i.e., covalent and non-covalent functionalization methods. The most common covalent functionalization of CNT is carried out by highly reactive oxidants, which results in the formation of carbonyl (-CO), hydroxyl (-OH) or a combination of both to produce carboxyl functional groups (-COOH) [130]. In fact, during the oxidation process, defects are created at the open ends and on the sidewalls of CNT due to oxidation with strong acids, such as HNO_3, or H_2SO_4 H_2SO_4/HNO_3 or with strong oxidants, such as potassium permanganate ($KMnO_4$), ozone, and reactive plasma [130]. The defects formed after oxidizing can be stabilized by bonding with -COOH or -OH, carbonyl, amine

and ester functional groups. Therefore, covalent functionalization of CNT improves the dispersion, solubility, interfacial interactions and compatibility of CNT with other materials because the character of CNT is transformed from hydrophobic to hydrophilic due to the attachment of polar functional groups. On the other hand, non-covalent functionalization of CNT is mainly performed by physical adsorption of low molecular weight surfactants (anionic/cationic), polymers, liquid crystalline p-conjugated oligomers, and amphiphilic cationic polymer molecules. For example, the suspension of CNT in polymers, such as poly(p-phenylene vinylene) leads to the wrapping of the polymer around the CNT due to the Van der Waals interaction and π-π stacking between CNT and polymer chains containing aromatic rings [131]. In another work, during the sonication of CNT in polystyrene sulfonate (PSS), CNT underwent polymer wrapping by the polyanion PSS, resulting in the suspension of CNT in water without any covalent functionalization. The possible functional groups on CNT sidewalls are presented in figure 1.5.
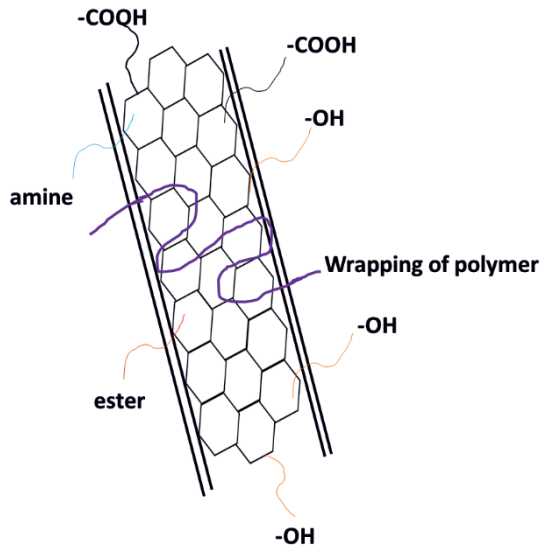

Figure 1.5. A schematic of functionalization of CNT on the sidewalls, defects and edges with different functional groups and wrapping of polymer on the surface of CNT.

1.4. Polymers

1.4.1. Poly(3,4-ethylenedioxythiophene):poly(styrenesulfonate) (PEDOT:PSS)

PEDOT:PSS is a conducting polymer composite consisting of the positive charge-conjugated PEDOT and the negative charge-saturated PSS [132], as shown in figure 1.6(a). It has a high work function of 4.8-5.2 eV with a highest occupied molecular level (HOMO) of -5.2 eV and a lowest unoccupied molecular level (LUMO) of -3.5 eV [133,134]. In figure 1.6(c), the HOMO and LUMO levels of PEDOT:PSS are schematically represented. PEDOT is generally insoluble in many solvents but combining PEDOT with PSS enables the dispersion and stabilization of PEDOT in water and in other solvents because PSS acts as a surfactant [135]. Presently, aqueous solution of PEDOT:PSS is one of the most feasible conducting polymers for practical applications, such as ink-jet printing, organic solar cells, organic LEDs, dye sensitized solar cells, conducting electrode, supercapacitors, energy storage, fuel cells, and flexible devices [132,136-142]. The wide areas of application of PEDOT:PSS is facilitated by its good transparency and film forming properties; high flexibility, high thermal stability, high conductivity and low cost of production [143]. The electrical conductivity of commercially available pure PEDOT:PSS is lower than other conductive polymers and metal oxides, which is less than 1 S.cm^{-1} [144]. However, it is possible to increase the conductivity of PEDOT:PSS by introducing some solvents such as ethylene glycol, dimethyl sulfoxide, or by treating PEDOT:PSS with acids such as sulfuric acid, and sulfonic acid [145,146]. These methods help to increase the electrical conductivity of PEDOT:PSS through structural changes [147]. In general, PEDOT:PSS exhibits a compressed coil form, which changes to an expanded coil or linear form via external treatments [148]. This leads to the transition of PEDOT:PSS from the less conductive benzenoid structure to the more conductive quinoid structure. As a result, the electrical conductivity of PEDOT:PSS can be tuned from 10^{-2} to 10^{3} S.cm^{-1} [149,150]. Therefore, the high conductivity and high stability of PEDOT:PSS in ambient conditions, makes it an interesting alternative for flexible electrodes with regards to ITO with electrical conductivity of ~10^{4} S.cm^{-1}, in photovoltaics, organic LEDs and display devices [151,152]. Furthermore, PEDOT:PSS exhibits high optical and electrical stability in ambient conditions and it can be easily coated on rigid or flexible substrates by various solution processing

techniques, such as spin coating, slot die coating, blade coating, spray deposition and screen printing [153-155]. However, PEDOT:PSS-based electrodes are still not up to the mark in order to replace ITO, mainly because of their one order lower electrical conductivity than ITO.

1.4.2. Poly(9,9-dioctylfluorene-alt-benzothiadiazole) (F8BT)

F8BT is a fluorene based conjugated copolymer with alternating 9,9-dioctylfluorene (F8) and benzothiadiazole (BT) units [156], as shown in figure 1.6(b). It is generally soluble in solvents like toluene, chlorobenzene, dichlorobenzene, and trichloromethane [157]. F8BT possesses luminescent properties with PL quantum yield up to 60%, a band gap of 2.6 eV with a HOMO level at -5.9 eV and a LUMO level at -3.3 eV (figure 1.6(c)), along with a high electron field-effect mobility of $10^{-3} cm^2 V^{-1} s^{-1}$ [158,159]. Owing to these properties, F8BT is widely used as an active component in polymer LED, photovoltaic cells, and field effect transistors [160-162]. The PL spectrum of F8BT reveals two main emission peaks at 2.3 eV and 2.2 eV. Therefore, F8BT is used as a yellow-green emitter in the organic LEDs and lasers [163]. For enhanced performances of organic LEDs, F8BT is generally blended with other fluorene copolymers such as poly(9,9'-di-*n*-octylfluorene-*alt*-*N*-(4-butylphenyl)diphenylamine) (TFB), poly(9,9'-di-*n*-octylfluorene-*alt*-bis-*N*-*N*'-(4-butylphenyl)bis-*N*,*N*'-phenyl-1,4-phenylenediamine) (PFB), Poly(9,9-di-n-octylfluorenyl-2,7-diyl) (F8), etc. [164,165]. In addition, F8BT possesses a high electron affinity of ~3.3 eV and a large ionization potential of ~5.9 eV, due to which, it is used as an electron acceptor material in all polymer bulk heterojunctions [166]. F8BT has also demonstrated to be an efficient optical gain medium in optically pumped lasers and waveguides [163,167]. Another advantage of F8BT is that it can be easily coated as a thin film on a substrate by spin- and slot-die- coating techniques [168,169]. However, depending on the molecular weight and for annealing temperatures above 150°C, the optoelectronic properties and charge transport in these thin films vary [156]. Moreover, the polymer's packing also varies with annealing as compared to the thin film of pristine polymer.
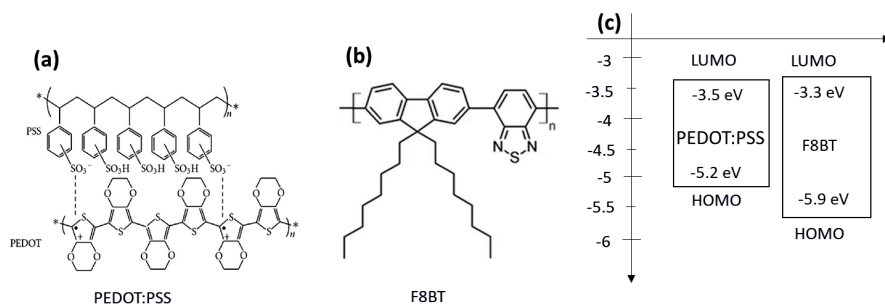
Figure 1.6. Chemical structure of (a) PEDOT:PSS, and (b) F8BT, reproduced with permissions from [170], and [171], respectively, and (c) Comparison of the HOMO and LUMO energy levels of PEDOT:PSS and F8BT.

1.5. p-n junction

A p-n junction is the interface formed between p-type and n-type semiconducting materials when in contact. Holes are the majority carriers in the p-type material, while electrons are the majority carriers in the n-type material, as shown in figure 1.7(a). On combining the two types of materials, the holes from the p-region diffuse towards the n-region, leaving behind negative immobile acceptor ions in the p-region. Similarly, electrons from the n-region diffuse to the p-region leaving behind immobile positively donor ions in the n-type region. The diffused charge carriers recombine with the free charge carriers in their respective region, resulting in the depletion area near the p-n interface, as shown in figure 1.7(b). The immobile ions induce an electric field ($E(x)$) towards the p-side originating from the n-side, which opposes the field, due to diffusion of charge carriers. The process of diffusion continues until a thermal equilibrium is reached between the induced electric field to the oppositely directed field of the diffusion. At this point, a depletion region is formed at the p-n interface that is devoid of free carriers.
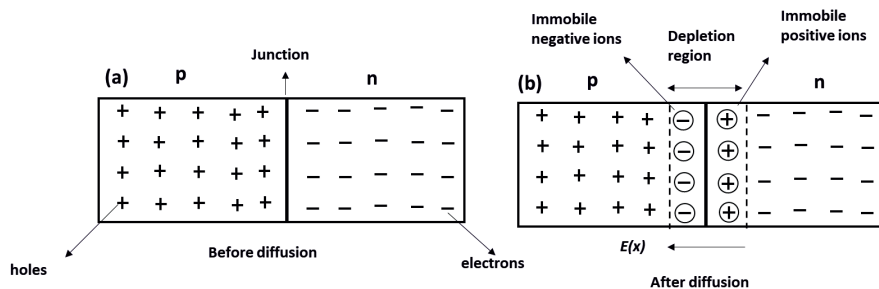

Figure 1.7. Schematic of p-n junction (a) before diffusion of carriers and (b) after diffusion of carriers

In addition, when thermal equilibrium is reached, the energy band at the p-n interface changes owing to the alignment of the Fermi levels of the n- and p-type materials. In general, the empirical relations for the Fermi energy levels of p-type material ($E_{P,p}$) and n-type material ($E_{F,n}$) are given by[172]

$$E_{F,p} = E_{Fi}^p - kTln\left(\frac{N_a}{n_i^2}\right), \qquad (1.2)$$

$$E_{F,n} = E_{Fi}^n - kTln\left(\frac{N_d}{n_i^2}\right), \qquad (1.3)$$

where k is the Boltzmann's constant, T is the absolute temperature, N_a is the hole doping densities on the p-type side, N_d is the electron doping densities on the n-type side and n_i is the intrinsic carrier density, E_{Fi}^p and E_{Fi}^n are the intrinsic Fermi levels. When there is no contact between the two types of materials, then there is no influence on their band structures. On contact and at thermal equilibrium, the Fermi levels of the two materials align i.e., $E_{F,p} = E_{F,n} = E_F$, where E_F is the aligned Fermi energy level. Whereas, their intrinsic Fermi energy levels will separate with an energy offset

$$E_{Fi}^p - E_{Fi}^n = kTln\left(\frac{N_a N_d}{n_i^2}\right). \qquad (1.4)$$

This results in band bending across the p-n interface as shown in figure 1.8(a). Dividing both sides by electron charge q, the equation (1.3) becomes

$$\frac{E_{Fi}^p}{q} - \frac{E_{Fi}^n}{q} = V_p - V_n = \frac{kT}{q}ln\left(\frac{N_a N_d}{n_i^2}\right), \qquad (1.5)$$

where $V_p - V_n = V_{Bin}$ is equivalent to the electrostatic potential across the p-n junction and is known as the built-in potential (V_{Bin}). The fundamental relation between the built-in electric field $E(x)$ and the built-in potential V_{Bin} is given by

$$E(x) = \frac{dV_{Bin}(x)}{dx}. \qquad (1.6)$$

Outside the depletion region, $E(x) = 0$ because V_p and V_n are constant. Under thermal equilibrium and at zero external bias, only the built-in potential V_{Bin} across the junction exists. However, when an external potential (V_{ext}) is applied, the potential across the junction varies and in turn, the band bending changes. In the case of forward biasing, the potential across the junction decreases to $V_{Bin} - V_{ext}$, which in turn, decreases the depletion region width and further reduces the band bending. On the other hand, under reverse bias the potential across the junction increases to $V_{Bin} + V_{ext}$. Consequently, the depletion region width and the band bending also increase. The band diagrams of a p-n junction under reverse and forward biases are shown in figure 1.8(b-c). Depending on the application, p-n junction diodes require different biasing conditions. For example, LED applications require a forward bias, while as photodiodes work under a reverse bias.
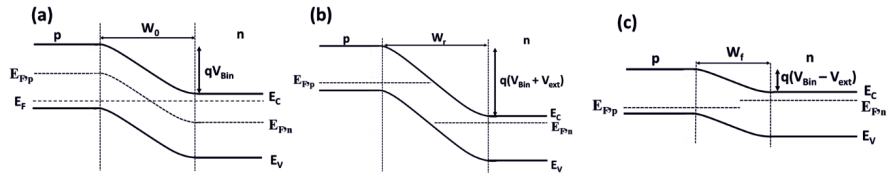
Figure 1.8. Band bending of the p-n junction and the effect on the built-in potential under (a) thermal equilibrium and zero bias ($V_{ext}=0$), (b) reverse bias and (c) forward bias, with applied external potential of V_{ext}.

1.6. Photodiode

1.6.1. Working principle

A photodiode is a p-n junction that converts light into electrical signals [173,174]. The basic operation of a photodiode consists of three steps, including (i) electron-hole generation, (ii) electron-hole transportation, and (iii) output photocurrent. It works on the principle of photoelectric effect under reverse bias. In dark conditions, owing to the strong built-in electric field, there are no free electrons and holes inside the depletion region of a photodiode [175]. When the photodiode is illuminated with photons of higher energy than the band gap of the semiconductor, electron-hole or excitonic separation occurs. Then, under the influence of the applied reverse potential, free holes move towards the p-region and free electrons move towards the n-region, as shown in figure 1.9. This results in the flow of an electric current, called photocurrent [176]. Under

reverse potential, the depletion region width increases by the amount of applied reverse potential. On illumination, the p-n junction produces higher number of electron-hole pairs that contribute to the photocurrent. In general, in order to obtain maximum quantum efficiency from a photodiode, it is necessary to operate it in reverse bias, slightly below the break down potential V_b of the photodiode. Such photodiodes are called avalanche photodiodes and produce a large number of electron-hole pairs for one incident photon, due to the wider depletion region. The quantum efficiency is thus higher compared to photodiodes operating at other reverse biases. In addition, there is also electron-hole generation outside the depletion region. However, these electron-hole pairs can recombine with the minority and majority carriers and therefore, do not contribute to the photocurrent. Moreover, when there is a high number of interfacial defects in the photodiode, the photogenerated carriers are likely to be trapped by them, whereupon reducing the overall quantum efficiency of the photodiode.
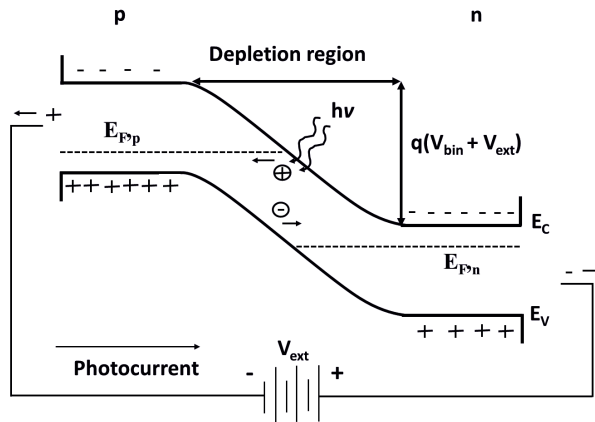
Figure 1.9. Band diagram of a p-n junction under illumination and reverse biasing.

1.6.2. Photodiode characteristics

The electrical characteristics of a photodiode are similar to conventional diodes. The equation of current-voltage characteristics of a diode is

$$ I = I_D \left[exp \left(\frac{V}{\eta V_T} \right) - 1 \right], \tag{1.7} $$

where $V_T = kT/q$ is the thermal voltage and $V_T = 25$ mV at room temperature, η is the ideality factor and $\eta = 1$ for an ideal diode, I_D is the

reverse saturation current, which may range from pA to nA depending on the structure of the device [177]. In fact, an ideality factor of 1 implies that under forward bias, the p-n interface produces only a diffusion current. This is however only possible when there are no defects in the p-n junction. The presence of defects in real cases leads to recombination currents under the forward bias giving an ideality factor of 2 or higher.

On the other hand, under reverse bias and in dark conditions, the current is approximately equal to the reverse saturation current (I_D), also known as the dark current of a photodiode [178]. When a photodiode is illuminated, I_D increases proportionally to the optical power of the light source as shown in figure 1.10 until the limit of the diode breakdown potential (V_B), after which I_D saturates and increases rapidly.
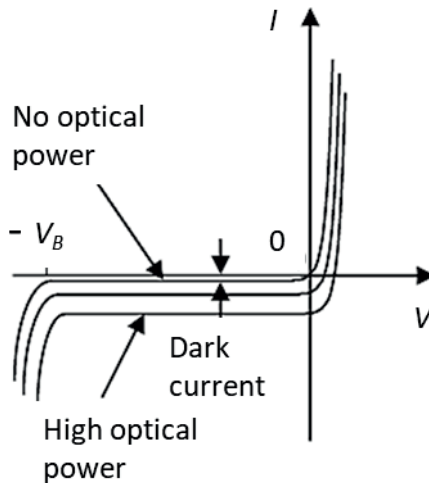

Figure 1.10. I-V characteristics of a photodiode, reproduced with permission from [172].

The figures of merit associated with photodiodes are provided below.

1) **Sensitivity (S)** is defined as the ratio of current, when the UV illumination is switched off (I_{UV}), to the dark current (I_{dark}) [179], and is given by

$$S = \frac{I_{UV}}{I_{dark}}. \qquad (1.8)$$

2) **Responsivity (R)** is defined as the ratio of photocurrent generated to the power of the incident UV light [179], and is given by

$$R = \frac{I_{UV} - I_{dark}}{P_{incident} A_{eff}},$$ (1.9)

Where, $P_{incident}$ is the power of the incident UV light and A_{eff} is the effective area of the incident UV light.

3) **External quantum efficiency (EQE)** is defined as the ratio of number of charge carriers measured at the output detector to the number of incident photons per unit time [180]. *EQE* and responsivity are interrelated by the empirical formula:

$$EQE = R \frac{hc}{q\lambda},$$ (1.10)

where *R* is the responsivity, *h* is Plank's constant, *c* is speed of light, q is the electron charge, and λ is the wavelength of the incident UV light source.

4) **Response time** is defined by two parameters T_{rise} and T_{decay}. In fact, T_{rise} is the time taken to raise the current from 10% to 90% under the UV radiations, while T_{decay} is the time taken for the current to drop from 90% to 10% when UV radiation is turned off [179].

1.6.3. Energy band diagram of the photodiode

Figure 1.11 is the band energy diagram with HOMO/LUMO levels of the ITO/ZnO nanorods/F8BT/PEDOT:PSS/Ag photodiode. Due to differences in the band gaps and work functions of the materials, band bending is inevitable. In fact, n-type ZnO exhibits an upward band bending because electrons as majority carriers migrate to the PEDOT:PSS, leaving behind holes at its surface. PEDOT:PSS, on the other hand, exhibits downward band bending because it accepts these electrons at its surface. These positive and negative charges at the interface give rise to a depletion region, with a built-in electric field directed from ZnO towards PEDOT:PSS. In addition, there is a potential barrier of ~1.8 eV between ZnO valance band and F8BT HOMO level, suggesting that under UV irradiations, the photogenerated holes can be easily transferred from

ZnO valance band to F8BT HOMO level and further transferred to the PEDOT:PSS HOMO level.
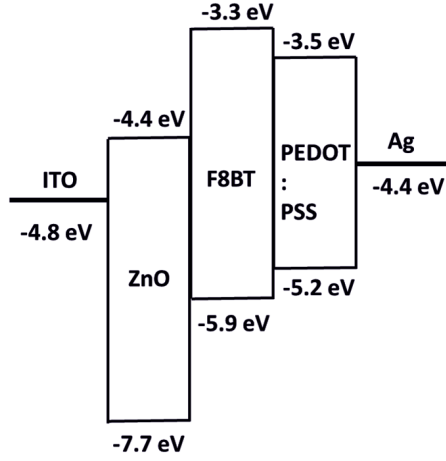
Figure 1.11. Band energy diagram of photodiode fabricated in this work.

1.6.4. Cheung's method for the ideality factor calculations of photodiode

The ideality factor calculations followed Cheung's method [181]. In general, the non-ideal diode current equation is

$$I = I_S[\exp\left(\frac{qV_D}{\eta kT}\right) - 1],\qquad(1.11)$$

where q is the electronic charge, $V_D = V - IR$ is the applied potential across the diode expressed as total voltage drop V across the series recombination of the diode and resistor, k is the Boltzmann's constant, T is the absolute temperature, and I_S is the reverse saturation current. After expressing all the terms and differentiating equation (1.11), as a function of ln(I), the following equation is obtained

$$\frac{d(V)}{d(\ln(I))} = I_S[\exp\left(\frac{q(V-IR)}{\eta kT}\right) - 1.\qquad(1.12)$$

Then the plot of $\frac{d(V)}{d(\ln(I))}$ *vs* V provides a slope of $\frac{\eta kT}{q}$, from which η, is obtained.

1.7. Aim of the thesis

The aim of this thesis was to develop a systematic approach towards the fabrication of a novel hybrid UV-photodiode device, based on n-type ZnO nanorods and p-type F8BT and PEDOT:PSS polymers. The hydrothermal synthesis route used in this work is a cost-effective route for the synthesis of ZnO nanostructures, as it does not require specialized equipment, high pressures and high temperatures. The synthesis temperature is under 100°C or under the boiling point of water. Moreover, the fabrication of the ZnO nanostructures and photodiodes are carried out in ambient pressures. Additionally, polymers consist of Earth-abundant materials, including C, N, O and S, ensure sustainability of the processes. The energy efficiency of the devices was also studied in terms of the EQE. The effect of synthesis conditions on the characteristics of the ZnO nanostructures allowed understanding the figures of merit of the UV-photodiodes. Therefore, a detailed study of the synthesis and characterization of ZnO nanoparticles and ZnO nanorods was carried out.

2. MATERIALS AND METHODS

2.1. Materials used

All the chemicals used were of analytical reagent grade. Two types of zinc precursors; Zinc acetate dihydrate ($Zn(CH_3COO)_2.2H_2O$) and zinc acetate anhydrous ($Zn(CH_3COO)_2$) with ~99.9% purity were purchased from Fisher Scientific and Alfa Aesar, respectively. Sodium hydroxide (NaOH) with 99.9% purity was purchased from Sigma Aldrich. Zinc nitrate hexahydrate ($Zn(NO_3)_2.6H_2O$) and hexamethylenetetramine ($(CH_2)_6N_4$, HMTA) precursors with 99.9% purity were purchased from Sigma Aldrich. Three different absolute alcohols viz., ethanol, methanol, isopropanol were purchased from Honeywell. An aqueous alcohol, 70% ethanol and 30% water was prepared by dissolving 30% de-ionized (DI) water in absolute ethanol. Non-functionalized NC7000 multi-walled CNT were purchased from Nanocyl. Two grades of PEDOT:PSS polymer, 900181-100G and F HC solar were purchased from Sigma Aldrich and OSSILA, respectively. F8BT polymer of grade 698687 was purchased from Sigma Aldrich. Indium tin oxide (ITO) substrates with 100 nm ITO thickness and 20 Ω/cm^2 resistance were purchased from OSSILA. Toluene with 99.9% purity was purchased from Honeywell. Hydrochloric acid (HCl) with 48% concentration was purchased from Honeywell. Silver (Ag) paste for contacts was purchased from Chemtronics.

2.2. Synthesis of ZnO nanoparticles

2.2.1. General methodology for the syntheses of ZnO nanoparticles

In the general procedure, solutions of 0.05 M of zinc precursor were prepared by adding a fixed amount of 219.5 mg of $Zn(CH_3COO)_2.2H_2O$ or 189.5 mg of $Zn(CH_3COO)_2$ to 20 ml of absolute ethanol, absolute methanol, absolute isopropanol and aqueous ethanol (70%). The solutions were placed in a water bath maintained at 60-70°C and under continuous magnetic stirring until the zinc precursor was completely dissolved. In order to prevent the evaporation of the alcohol, the reaction temperature was maintained below the boiling point of the corresponding alcohol. In addition, NaOH solutions of different concentrations were

prepared by varying the amount of NaOH from 60 mg (0.075 M), 80 mg (0.10 M), 100 mg (0.15 M) to 120 mg (0.20 M) in 20 ml of different alcohols. As prepared NaOH solutions were added dropwise to 0.05 M zinc precursor solutions in order to obtain 1:1.5, 1:2, 1:2.5 and 1:3 of zinc precursor to NaOH molar ratios. Subsequently, the mixtures were magnetically stirred at 600 revolutions per minute (rpm) for 2 h as shown in figure 2.1(a-b). Thereafter, the final solutions were cooled to room temperature during which, the resulting ZnO nanoparticles settled at the bottom of the beaker in the form of white precipitates as shown in figure 2.1(c). Centrifugation at 4500 rpm for 6 minutes further isolated these nanoparticles, which were then air-dried at 60°C for 24 h. The centrifugation and drying resulted in the agglomeration of ZnO precipitates in the form of pellets, as shown in figure 2.1(d-e). These pellets were then crushed gently using a mortar and pestle to obtain a very fine powder of ZnO nanoparticles. An image of typical ZnO nanopowder obtained after gentle crushing is shown in figure 2.1(f).
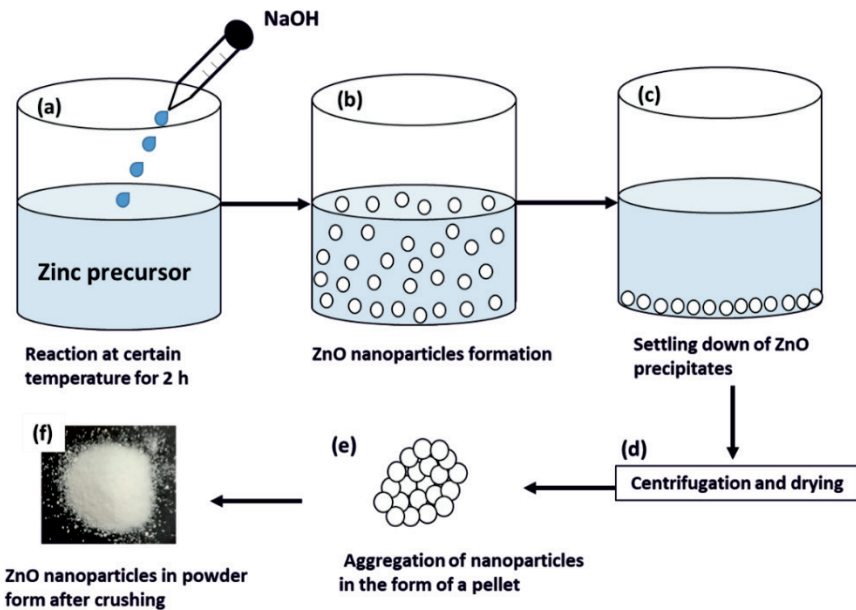

Figure 2.1. Schematic of the general methodology used for the syntheses of ZnO nanoparticles.
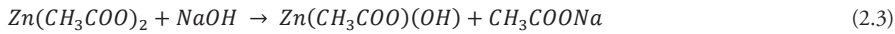
2.2.2. Synthesis reactions

The formation of ZnO nanoparticles, using two different zinc precursors along with NaOH, in four alcoholic solvents is described by the following chemical reactions [182]

1. Reaction of Zn(CH$_3$COO)$_2$.2H$_2$O with NaOH in alcoholic solvent

$$Zn(CH_3COO)_2(2H_2O) + NaOH \rightarrow Zn(CH_3COO)(OH) + CH_3COONa + 2H_2O \qquad (2.1)$$

$$Zn(CH_3COO)(OH) + NaOH \rightarrow ZnO + CH_3COONa + H_2O \qquad (2.2)$$

2. Reaction of Zn(CH$_3$COO)$_2$ with NaOH in alcoholic solvent

$$Zn(CH_3COO)_2 + NaOH \rightarrow Zn(CH_3COO)(OH) + CH_3COONa \qquad (2.3)$$

$$Zn(CH_3COO)(OH) + NaOH \rightarrow ZnO + CH_3COONa + H_2O \qquad (2.4)$$

Equations (2.1)-(2.4) indicate that the formation of ZnO nanoparticles depends on the quantity of NaOH that controls the reaction kinetics. In fact, the amount of NaOH also controls the pH of the solution, which in turn, also controls the reaction kinetics. Lower amounts of NaOH lead to slower reaction kinetics causing incomplete reactions between NaOH and zinc precursor, leading to the presence of Zn(CH$_3$COO)(OH) in the final product (I). On the other hand, a higher amount of NaOH increases the reaction kinetics, but may lead to the presence of Na or NaOH in the final product (I). Thus, it is important to use an optimum ratio of zinc acetate precursors to NaOH for the synthesis of ZnO nanoparticles, in order to produce highly crystalline nanoparticles without reaction by-products. Different types of ZnO nanoparticles, following chemical reactions 2.1 or 2.2, were synthesized by varying the synthesis conditions, such as the quantities of NaOH, zinc precursor and alcoholic solvents, as described in the following sections.

2.2.3. Nomenclature of samples

1. Nomenclature followed for labelling the ZnO nanoparticle samples and their hybrids

The general nomenclature for labelling the ZnO samples synthesized in this work is

ZPSRHx

Here, Z stands for ZnO and P is the precursor. For the anhydrous zinc acetate precursor, P=A. furthermore, S is for the solvent and corresponds to ethanol (E), aqueous ethanol (E_a), Methanol (M), Isopropanol (I). R is molar ratio of the zinc acetate precursor to NaOH and is expressed as 1.5, 2, 2.5, 3 indicating 1:1.5, 1:2, 1:2.5 and 1:3 molar ratios, respectively. Then, H is for the hybrid ZnO samples, representing the organic counterpart, and can be replaced by C or p, where C is for CNT and p is for PEDOT:PSS polymer. Also, x is for ex-situ synthesized hybrid samples. If x is absent, it implies the hybrid samples were prepared by in-situ growth of ZnO on CNT. Similarly, when a precursor is not mentioned in the nomenclature then it refers to a sample that has been synthesized using zinc dihydrate precursor. For example, a ZnO nanoparticle (Z) sample prepared using zinc acetate anhydrous precursor (A) with absolute ethanol solvent (E) for 1:2 molar ratio of zinc precursor to NaOH (2), is labelled as ZAE2. Similarly, for the same sample synthesized using zinc dihydrate precursor the label is ZE2. In the case of an in-situ synthesized ZnO sample (Z) with CNT (C) and zinc dihydrate acetate precursor using absolute ethanol solvent (E) for 1:2 molar ratio (2) has the label ZE2C. Finally, an ex-situ (x) synthesized ZnO-PEDOT:PSS (p) hybrid sample using zinc acetate anhydrous precursor (A), with the same molar ratio and solvent is labelled as ZAE2px. A schematic representation defining different symbols of the nomenclature is represented in figure 2.2.
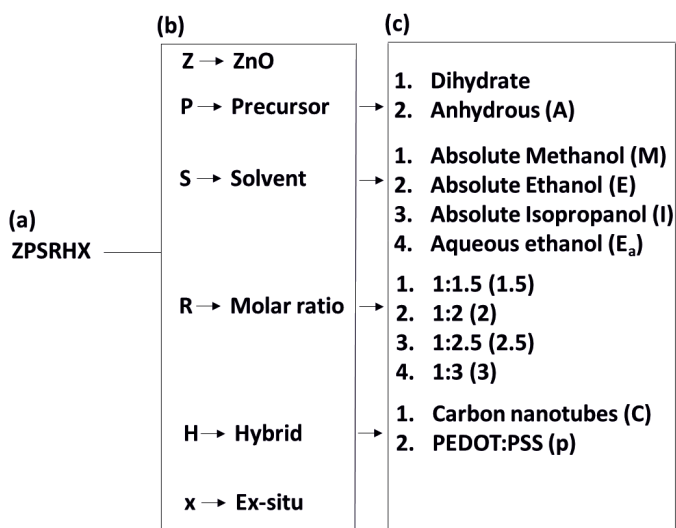

Figure 2.2. Schematic description of the nomenclature ZPSRHx adapted for the samples synthesized in this thesis.

2. Nomenclature followed for labelling ZnO nanorod samples

The general nomenclature for labelling the ZnO nanorod samples prepared in this work is

ZNR-S

Here, similar to ZnO nanoparticles, Z stands for ZnO and S for the four solvents used in the seed layer i.e., absolute ethanol (E), aqueous ethanol (E_a), absolute methanol (M) and absolute isopropanol (I) and NR for nanorods. As an example, ZnO nanorod samples prepared using absolute methanol are labelled as ZNR-M.

3. Nomenclature followed for labelling of p-n heterojunction photodiode devices

The general nomenclature for ZnO nanorod samples prepared in this work is

PD-S

Here, PD stands for photodiode and S for the seeding solvents, similar to ZnO nanoparticles and ZnO nanorods samples. Therefore, for absolute ethanol (E), aqueous ethanol (E_a), absolute methanol (M) and absolute isopropanol (I), the photodiodes are labelled as PD-E, PD-E_a, PD-M and PD-I, respectively.

2.2.4. Synthesis procedure

Case 1: Study of the influence of NaOH concentration in absolute ethanol

For this study, 0.075 M, 0.10 M, 0.15 M, and 0.02 M solutions of NaOH were added drop-by-drop to 0.05 M solution of $Zn(CH_3COO)_2.2H_2O$, prepared in absolute ethanol solvent. The reaction temperature was fixed to 65°C and reaction time to 2 h. Molar ratios of $Zn(CH_3COO)_2.2H_2O$:NaOH of 1:1.5, 1:2, 1:2.5 and 1:3 were obtained for the final solutions. ZnO nanoparticles were obtained by following the procedure described in section 2.2.1. According to the nomenclature described in section 2.2.3, the samples of case 1 are

labelled as ZE1.5, ZE2, ZE2.5 and ZE3, respectively. The results based on ZE2 are published in the orginal publication (III).

Case 2: Study of the influence of water in ethanol/aqueous ethanol

To evaluate the effect of water in the synthesis, aqueous ethanol containing 70% ethanol was used as solvent. Similar to case 1, four samples with molar ratio of 1:1.5, 1:2, 1:2.5 and 1:3 were prepared by dropwise addition of 0.075 M, 0.10 M, 0.15 M, and 0.02 M solutions of NaOH to 0.05 M solution of $Zn(CH_3COO)_2.2H_2O$. The temperature was maintained at 65°C for 2 h. According to the nomenclature, the samples prepared in this case are labelled as $ZE_a1.5$, ZE_a2, $ZE_a2.5$ and ZE_a3, respectively. The results of these nanoparticles are published in the original publication (I).

Case 3: Study of the influence of hydrates in the precursor

In cases 1 and 2, $Zn(CH_3COO)_2.2H_2O$ precursor was used to synthesize ZnO nanoparticles in absolute and aqueous ethanol, respectively. In this study, $Zn(CH_3COO)_2$ anhydrous precursor i.e., without any additional hydrates was used. An absolute alcohol solvent was selected in order to completely eliminate water at the beginning of the synthesis. Similar to case 1 and case 2, in the first step, four samples of $Zn(CH_3COO)_2$:NaOH ratio were prepared. The reaction temperature was fixed to 65°C and reaction time to 2 h and the as-synthesized samples are labelled as ZAE1.5, ZAE2, ZAE2.5 and ZAE3, respectively. The results of ZAE2 are published in the original publication (II).

Case 4: Study of the influence of solvents for 1:2 ratio and without water

In this study, two additional absolute alcohol solvents, methanol and isopropanol, were selected and a molar ratio of zinc precursor to NaOH of 1:2 was fixed. For the synthesis, a 0.10 M solution of NaOH, prepared in 20 ml of absolute methanol and absolute isopropanol was dropwise added to 20 mL of 0.05 M $Zn(CH_3COO)_2.2H_2O$ precursor solution prepared in the same solvents. The temperature was maintained at 60°C and 70°C, for absolute methanol and isopropanol, respectively and the reaction time was fixed to 2 h. However, before the synthesis, it was necessary to sonicate the solution for 5 minutes in order to dissolve the

Zn(CH$_3$COO)$_2$.2H$_2$O precursor in absolute isopropanol, after having magnetically stirred the solution for 15 minutes at 70ºC. This step was necessary, as the precursor did not dissolve completely by the standard procedure followed for other alcohols. The samples prepared in this case are labelled as ZM2 and ZI2, respectively. The results based on these ZnO nanoparticles are published in the original publication (III).

Case 5: Green-synthesis of ZnO nanoparticles for antimicrobial application

For this study, the ZnO nanoparticles were synthesized by using a green synthesis route using thuja tincture. To prepare a thuja tincture, 2 g of grounded thuja leaves were dissolved in 50 ml of absolute ethanol which was covered with aluminium foil and stored in dark for 24 h. After 24 h, the mixture was manually shaken and stored in dark for another 24 h. The final solution was filtered to remove the plant residues and impurities. Subsequetntly, similar to case 1 and case 3, two ZnO nanoparticles with 1:2 zinc precursor: NaOH molar ratio were prepared by using Zn(CH$_3$COO)$_2$.2H$_2$O and Zn(CH$_3$COO)$_2$ precurosrs. However, in this case, 20 ml thuja tincture was used to dissolve the zinc precurosrs but NaOH as similar to case 1 and 3 was dissolved in absolute ethanol. Similar to case 1 and case 3, the synthesis was carried out for 2 h reaction at 65 ºC. The final green mixture obtained were ZnO nanoparticles covered organic moieties from the thuja tincture. Antimicrobial properties of these ZnO nanoparticles were evaluated and results were published in the original publication (V). However, the optical properties of such ZnO nanoparticles were not beneficial for practical applications in this thesis and therefore, the optical results of green-synthesized ZnO nanoparticles are not discussed in this thesis.

2.3. Synthesis of ZnO-CNT nanohybrids

To study the influence of CNT on the optical properties and defect states of ZnO nanoparticles, two types of ZnO-CNT nanohybrids were synthesized by using ex-situ and in-situ approaches. In total, four different types of ZnO-CNT nanohybrid samples were synthesized: two ex-situ and two in-situ.

2.3.1. Ex-situ synthesis

For the ZnO-CNT nanohybrid synthesis, 2 mg of NANOCYL NC700 multi-walled CNT (non-functionalized) was mixed with 10 mg of samples ZEa1.5 and ZEa3. The mixture was then added to ~1 ml of absolute ethanol and sonicated for 5 minutes. Thereafter, the resulting black mixture was dried at 60°C for 24 h, which resulted in the agglomeration of the mixture in the form of a pellet. The pellet was then gently crushed using a mortar and pestle to obtain a fine powder of ZnO-CNT nanohybrids, which were labelled as $ZE_a1.5Cx$ and ZE_a3Cx, respectively. The results of these ZnO-CNT nanohybrids are published in the original publication (I).

2.3.2. In-situ synthesis

Firstly, a CNT solution was prepared by mixing 4 mg of CNT in 50 ml of absolute ethanol and sonicating until a homogenous mixture was obtained. Similar to ZnO nanoparticles of cases 1 and 3, a 0.05 M solutions of $Zn(CH_3COO)_2.2H_2O$ and $Zn(CH_3COO)_2$ were prepared in 20 ml of absolute ethanol, respectively. To prepare a 0.10 M NaOH solution, ~80 mg of NaOH was added to 19 ml of absolute ethanol in which, 1 ml of CNT mixture (~0.08 mg) was added. The NaOH and CNT mixture was sonicated before being added drop wise to the zinc precursor solutions. The reaction was completed at 65°C for 2 h, and ZnO-CNT nanohybrid pellets were obtained, as described earlier. The pellets were gently crushed to obtain a black ZnO-CNT nanohybrid powder and the nanohybrids were labelled as ZE2C and ZAE2C, respectively. The results of these ZnO-CNT nanohybrids are published in the original publication (II).

2.4. Ex-situ synthesis of ZnO-PEDOT:PSS nanohybrids

For the preparation of ZnO-PEDOT:PSS nanohybrids, an ex-situ approach was considered. Two ZnO nanoparticle samples i.e., ZE2 and ZAE2 as described in cases 1 and 3, were selected. Here, 400 ml of PEDOT:PSS (900181-100G, Sigma Aldrich) was added to 20 mg of samples ZE2 and ZAE2. The mixture was sonicated for 1 h, after which it was dried at 70°C for 24 h in air ambient. Thereafter, the dried mixtures were crushed to obtain a blue powder of agglomerated ZnO-PEDOT:PSS nanohybrids, which are labelled as ZE2px and ZAE2px,

respectively. The results of these ZnO-PEDOT:PSS nanohybrids are published in the original publication (II).

2.5. Synthesis of ZnO nanorods

The goal of synthesizing ZnO nanorods was to investigate their electrical characteristics, photoresponse and persistent photoconductivity. The synthesis of ZnO nanorods were carried out on etched and non-etched indium tin oxide (ITO) substrates of 20 mm X 15 mm size, 100 nm ITO thickness and 20 Ω/square resistance. The results based on ZnO nanorod samples are presented in the original publication (III). Following are the various procedures used for the synthesis of ZnO nanorods.

Step 1: Etching and cleaning of ITO substrate

In the first step, ITO coated on the glass substrate (figure 2.3(a)) was etched in the center using 12 M hydrochloric acid (HCl). The rest of the substrate was covered with copper tape, which protected it from etching and also limited the etching width to ~4 mm as shown in figure 2.3(b). After etching, the copper tape was removed as shown in figure 2.3(c) and the etched ITO substrate was washed with DI water. These substrates were then further cleaned with acetone, isopropanol and DI water via sonication for 10 minutes in each solvent.

Step 2: Seed layer solution preparation and seeding: alcoholic solvent dependent

Four different seed layer solutions were prepared using the same four different alcoholic solvents used for ZnO nanoparticle synthesis. The goal of this study was to investigate the influence of solvent-dependent seeding on the shape, size and defect states of ZnO nanorods. To prepare the seed layer solution, 0.11 mg of the $Zn(CH_3COO)_2.2H_2O$ precursor was dissolved in absolute methanol, absolute ethanol, absolute isopropanol and aqueous ethanol, in a beaker placed in a water bath. The water bath was maintained at 60°C, 65°C, 65°C and 70°C, respectively under continuous magnetic stirring until the zinc precursor was completely dissolved (~2 h). After cooling the seeding solution, 2 µL of the solution was drop-cast onto the etched ITO substrate maintained at 60°C on a hot plate. During drop casting, the dropped solution completely covered the etched part and partially covered the non-etched part of

the substrate, as shown in figure 2.3(d). The procedure was repeated 25 times; thus, a total of 50 μl of solution was drop casted. Thereafter, the seeded ITO substrate was washed with the corresponding solvent and immediately annealed at 275°C on a hot plate for 15 minutes. Then the seeded substrate was cooled to room temperature in ambient, after which it was prepared for the growth of nanorods by covering the non-seeded part of the substrate with Teflon tape as shown in figure 2.3(e). Teflon tape was used to prevent the growth of nanorods on the unetched area of the substrate.

Step 3: Growth of ZnO nanorods

For the growth of the ZnO nanorods, 0.595 g of $Zn(NO_3)_2.6H_2O$ was dissolved in 40 ml of DI water, which was maintained under continuous magnetic stirring for 30 minutes at room temperature. Thereafter, 0.28 g HMTA was added to the $Zn(NO_3)_2.6H_2O$ precursor solution and the mixture was magnetically stirred for another 30 minutes. The Teflon covered seeded ITO substrate was horizontally immersed with the etched side facing down in the growth solution contained in a beaker that was placed in a Teflon autoclave and tightly sealed. Subsequently, the Teflon autoclave was maintained at 93°C for 4 h in an oven, after which it was cooled to ambient temperature. After cooling, the Teflon tape was removed and the substrate was washed with DI water and dried at 55°C for 2 h in an oven. The resulting ZnO nanorods on the substrate in figure 2.3(f), were characterized by XRD and cross-sectional SEM.

Step 4: Ag electrodes

For the electrical measurements, Ag (paste) electrodes were deposited on ITO on adjacent sides of the ZnO nanorods with the help of a very fine wire as shown in figure 2.3(g-h).
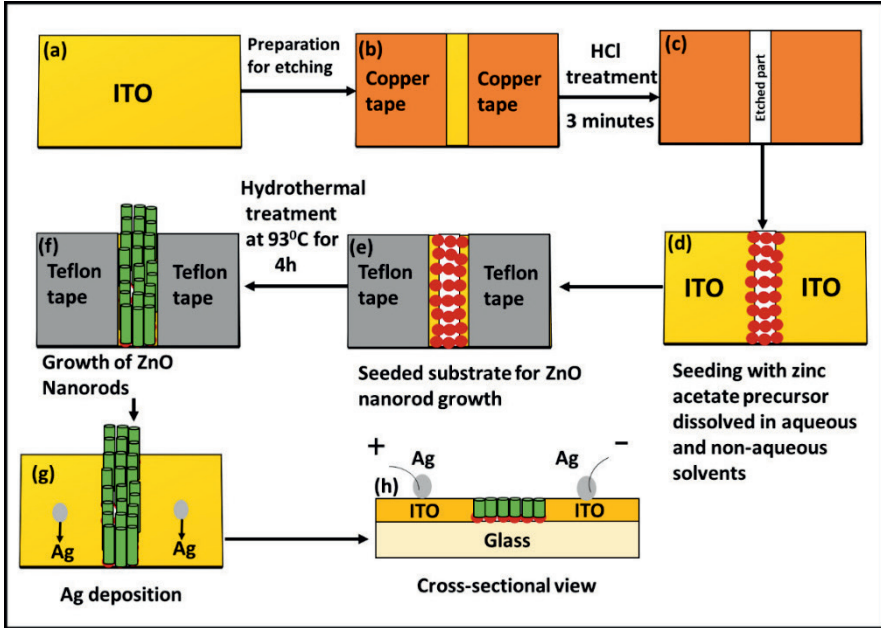
Figure 2.3. Schematic of the process followed for the synthesis of ZnO nanorods and for deposition of Ag contacts (III).

2.6. Fabrication of p-n heterojunction photodiodes

In total, four p-n heterojunction photodiodes were fabricated in order to evaluate their electrical characteristics in dark and under UV illumination (VI). The device structure was ITO (anode)/ZnO NR (n-type)/F8BT (p-type)/PEDOT:PSS (p-type)/Ag (electrode). A schematic for the fabrication of the device is shown in figure 2.4 and a step-by-step description for the fabrication of the device is provided as follows.

Step 1: Cleaning of ITO substrates

Firstly, ITO substrates were cleaned in acetone, isopropanol and DI water with 10 minutes sonication in each solvent. A schematic of cleaned ITO substrate is shown in figure 2.4(a).

Step 2: Growth of ZnO nanorods

The growth of ZnO nanorods was carried out in a manner similar to that described previously in section 2.5. ZnO nanorods were grown on non-etched or full ITO substrates in order to obtain a better charge transportation through the different layers of the device, as shown in

figure 2.4(b). The area of ZnO nanorod growth was limited to ~4-5 mm by covering the rest of the ITO with Teflon tape during the growth of nanorods.

Step 3: Spin coating of F8BT polymer

Firstly, a solution of the as-purchased p-type F8BT polymer (698687, Sigma Aldrich) was prepared by dissolving 20 mg of F8BT polymer in 2 ml of toluene in a glove box. Then, 20 µl of the solution was spin coated at 2000 rpm for 30 seconds over the ZnO nanorods layer in figure 2.4(c). Thereafter, the substrate was annealed at 110°C for 15 minutes to ensure molecular bonding between the ZnO nanorods and F8BT polymer.

Step 4: Spin coating of PEDOT:PSS polymer

Subsequently, 20 µL of as-purchased PEDOT:PSS polymer (F HC solar cells, OSSILA) was spin coated on top of the F8BT polymer layer at 3000 rpm for 50 seconds as shown in figure 2.4(d). The as-purchased PEDOT:PSS did not contain any lumps and therefore, no filtration of the polymer was required before spin coating. After spin coating, the substrate was annealed at 110°C for 15 minutes.

Step 5: Deposition of Ag contacts

For the contacts, Ag was deposited on top of the PEDOT:PSS layer (upper contact) and on ITO coating (bottom contact), as shown in figure 2.4(e). Ag was left to set in ambient conditions for 40-45 minutes. The device was then characterized electrically.
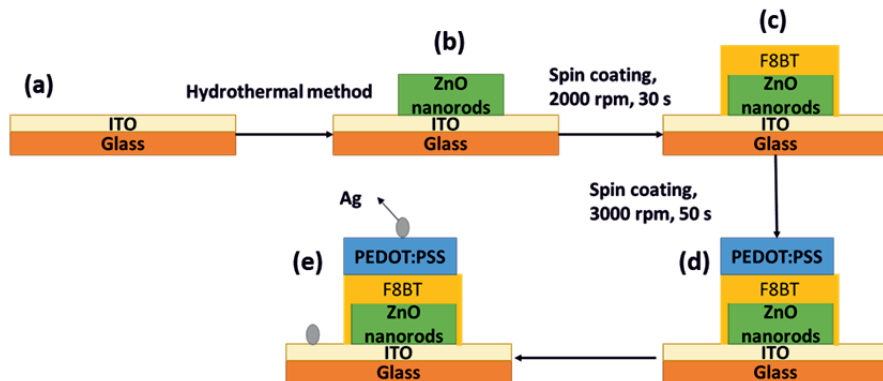

Figure 2.4. A step-by-step schematic for the preparation of the device ITO (anode)/ ZnO nanorods (n-type)/F8BT (p-type)/PEDOT:PSS (p-type)/Ag (electrode).

2.7. Characterization techniques

X-ray diffraction (XRD) patterns for both ZnO nanoparticles and ZnO nanorods were collected in Bragg–Brentano geometry using a Bruker D8 Discover diffractometer (Bruker AXS, Germany) with CuKα1 radiation (λ = 0.15406 nm) selected by a Ge (111) monochromator and LynxEye detector which has a resolution of 0.04 2θ.

Transmission electron microscopy (TEM) studies of ZnO nanoparticles and ZnO nanohybrids were carried out using two different TEM microscopes. The first microscope was JEOL 2010 LaB$_6$ TEM (JEOL, Japan) operating at 200 kV in TEM mode and providing a point-to-point resolution of 1.9 Å. The second microscope was a Tecnai G2 F20 (Netherlands) field emission gun (FEG) at an acceleration voltage of 200 kV with a point-to-point resolution of 2.4 Å.

Scanning electron microscopy (SEM) studies of ZnO nanorods was carried out on ZEISS EVO MA15 SEM (ZEISS, Germany) in secondary electron mode and a FEI QUANTA 250 environmental SEM FEG operating at 15 kV with resolution of 0.5 nm. The cross-sectional SEM on photodiodes was carried out on a FEI QUANTA 250 environmental SEM FEG operating at 15 kV with resolution of 0.5 nm.

Fourier transform infra-red spectroscopy (FTIR) was performed on ZnO nanoparticles and ZnO-CNT nanohybrids using spectrometer (Nicolet is^{10} Thermo Scientific, Germany) with frequency resolution of 0.25 cm^{-1}. The spectrometer was cooled with liquid nitrogen for FTIR measurements in the range of 540–4000 cm^{-1} and the measurements were taken at a step size of 2 cm^{-1}.

X-Ray photon electron spectroscopy (XPS) measurements of ZnO nanoparticles and ZnO nanohybrids were performed at room temperature with a SPECS PHOIBOS 150 hemispherical analyzer (SPECS GmbH, Berlin, Germany)). A base pressure of 5×10^{-10} mbar and monochromatic Al K alpha radiation (1486.74 eV) was used as excitation source operated at 300 W. The energy resolution as measured by the full width half maximum (FWHM) of the Ag 3d$_{5/2}$ peak for a sputtered silver foil was 0.62 eV. The spectra were calibrated with respect to the C1s at 284.8 eV for all ZnO nanoparticle and ZnO nanohybrid samples.

Raman spectra of ZnO nanoparticles and ZnO nanohybrids were collected using a WITec Confocal Raman Microscope System alpha 300R (WITec Inc., Ulm, Germany). The excitation was generated by a frequency-doubled Nd:YAG laser (New-port, Irvine, CA, USA) at a wavelength of 532 nm, with 50 mW maximum laser output power in a single longitudinal mode. The system was equipped with a Nikon (Otawara, Japan) objective with a X20 magnification and a numerical aperture NA = 0.46. The acquisition time of a single spectrum was set to 0.5 s.

UV-Vis absorbance study of ZnO nanoparticles and ZnO nanohybrids was carried out using a NANOCOLOR UV-VIS II spectrometer (MACHEREY-NAGEL, Germany) in 200–900 nm region. For other ZnO nanoparticles and ZnO nanorods samples, the optical absorbance was determined using an UV-Vis UV-1600PC spectrophotometer (VWR, US) in the 300–700 nm region. The scan resolutions were 2 nm and 5 nm.

Photoluminescence (PL) spectra of ZnO nanoparticles, ZnO nanohybrids and ZnO nanorods were collected at room temperature with an excitation wavelength of 365 nm of an LSM-365A LED (Ocean Insight, USA) with a specified output power of 10 mW. The emission was collected by FLAME ES UV-Vis spectrometer (Ocean optics, USA) with a spectral resolution 1.34 nm.

Electrical measurements on ZnO nanorods and photodiodes were carried out using two source measure units (Agilent 4156) with a step size of 20 mV and maximum compliance of 100 mA.

Photoresponse of ZnO nanorods and photodiodes was collected by using a 125 W Hg lamp with an output wavelength of 365 nm through an optical fiber of diameter 4 mm with irradiance of ~15 mW/cm^2.

Tauc plots of all samples were plotted to calculate the band gap of samples by using a direct band gap equation

$$(\alpha h\nu)^2 = \beta(h\nu - E_g), \qquad (2.5)$$

where α is absorption coefficient, h is Plank's constant, ν is frequency of light source, β is a band tailoring parameter, and E_g is the optical band gap of material.

Size distribution histograms were obtained from TEM images of ZnO nanoparticles, in-situ ZnO-CNT nanohybrids and SEM images of ZnO nanorod samples. The average sizes and standard deviations were obtained from size distribution histograms.

OriginPro software was used to plot the graphs in this work.

3. RESULTS

In this chapter, the structural, chemical, optical and electrical properties of ZnO nanoparticles, nanohybrids, nanorods and photodiodes are presented. This chapter is divided into three sections.

3.1. ZnO nanoparticles and their nanohybrids

For ZnO nanoparticles, results are discussed based on three synthesis parameters, (1) effect of solvents for 1:2 molar ratio, (2) effect of molar ratios of zinc precursor to NaOH, and (3) effect of hydrates in the zinc precursor. For ZnO nanohybrids, results are discussed for three types of ZnO nanohybirds (1) ex-situ synthesized ZnO-CNT nanohybrids, (2) in-situ synthesized ZnO-CNT nanohybrids and (3) ex-situ synthesized ZnO-PEDOT:PSS nanohybrids.

3.2. ZnO nanorods

For ZnO nanorods, results are discussed in terms of the seeding solvents i.e., (1) effect of absolute alcohols and (2) effect of aqueous alcohol, as seeding solvents.

3.3. Photodiodes

The photodiode section consists of incorporating ZnO nanorods of section 3.2., in a ZnO-polymer hybrid diode. Therefore, differences in the photodiodes arise directly from differences in the seed-layer solvent in the ZnO nanorod growth.

3.1. ZnO nanoparticles and their nanohybrids

3.1.1. Crystalline structure

The crystalline properties of ZnO nanoparticle samples were studied by XRD. The technique provided insight on their phase, crystallite size, as well as the presence of secondary phases and unreacted precursor. In general, all the samples show diffraction peaks (100), (002), (101), (102) and (110) corresponding to the hexagonal wurtzite ZnO structure (a

= 3.25 Å and c = 5.20 Å) of ZnO, as provided by standard powder diffraction database (JCPDS, Card Number 36-1451)[183].

(1) Effect of absolute alcohol solvents for 1:2 molar ratio of zinc precursor to NaOH on ZnO nanoparticle synthesis

Figure 3.1 is the XRD patterns of samples ZM2, ZI2, ZE2, and ZE_a2 that were synthesized using $Zn(CH_3CO_2)_2.2H_2O$ precursor, as described in chapter 2. The indexed diffraction peaks of samples ZM2, ZE2, and ZI2 are broader compared to sample ZE_a2. This suggests that ZnO synthesized using absolute alcohol are smaller in size. The Debye-Scherrer equation was applied to estimate the particle sizes of all the ZnO nanoparticles.

$$D = \frac{0.9\,\lambda}{\beta\cos\theta}, \qquad\qquad (3.1)$$

Where, D is the particle size, λ (= 0.154 nm) is the wavelength of the incident X-ray beam, β is FWHM in radians and θ is the Bragg's diffraction angle. Nanoparticle size calculations were carried out using (100), (002) and (101) reflections. The estimated average particle sizes of all samples are listed in table 3.1. For samples ZM2, ZE2, and ZI2, particle size in the range of ∼5-10 nm was estimated. On the other hand, for sample ZE_a2, the estimated particle size was ∼47 nm with significant differences in particle sizes, when considering (001), (002) and (101) reflections, suggesting that the nanoparticles of this sample are not spherical. The Debye-Scherrer equation is only applicable to spherically shaped nanoparticles. Nevertheless, it does provide important information about nanoparticle sphericity, including a preliminary qualitative assessment of particle size and deviation from spherical morphology.

Diffraction peaks indicating the presence of secondary phases are absent in the XRD patterns of ZE2 and ZE_a2. However, the XRD patterns of ZM2, and ZI2 show additional peaks that are more prominent in ZI2. These additional peaks are related to the presence of unreacted zinc acetate precursor (marked X), NaOH (marked Y), and Na metal (marked Z) [181]. Isopropanol is a longer carbon-chain alcohol (C_3H_7OH) compared to ethanol (C_2H_5OH) and methanol (CH_3OH). The dilution of zinc precursor and NaOH depends on the carbon chain length and polarity of the alcoholic solvent and the synthesis reaction time [184]. In addition, NaOH has a low solubility in isopropanol alcohol, which

implies that a reaction time of 2 h may not be sufficient for the complete reaction of zinc precursor with NaOH in isopropanol. This induces the presence of unreacted precursor by-products in the ZnO nanopowder prepared with isopropanol. A small amount of residual zinc acetate precursor is also visible with the methanol solvent samples, but in a lower amount than for ZI2 samples. The lower amount of unreacted precursor in ZM2 is therefore due to methanol being a shorter carbon chain alcohol. Therefore, these results suggest that absolute ethanol is an optimal solvent among the absolute alcohols in this study for the synthesis of ZnO for 2 h of synthesis time.
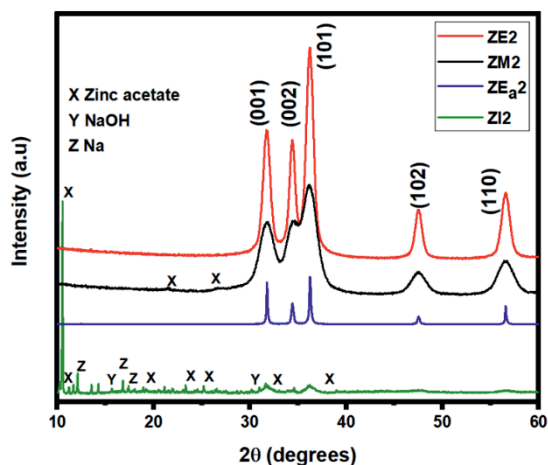
Figure 3.1. XRD patterns of ZnO nanoparticle samples ZE2, ZM2, ZEa2 and ZI2 (III).

(2) Effect of aqueous ethanol on ZnO nanoparticle synthesis

The effect of aqueous solvent on the ZnO nanoparticle synthesis was studied in order to understand the reaction kinetics of the synthesis. To that end, two different solvents were considered. The first solvent was absolute ethanol and the second solvent was aqueous ethanol containing 30% water. The precursor to NaOH ratio was varied as explained below. Figure 3.2(a) shows the XRD patterns of samples ZE1.5, ZE2.5 and ZE3. These samples were prepared with $Zn(CH_3CO_2)_2.2H_2O$ precursor using absolute ethanol and by varying the NaOH amount. No secondary phase is visible in the XRD patterns of these samples, which indicates that single-phase ZnO nanoparticles were synthesized. Additionally, a significant difference in the peak widths with different amounts of NaOH are observed, suggesting that the crystallite size varies

by varying the NaOH amount as listed in table 3.1. This is because pH or the amount of hydroxyl groups varies with variable NaOH quantities [185]. This, in turn affects the reaction kinetics and modifies the ZnO nanoparticle morphology, size and defects.

A solvent containing 70% absolute ethanol and 30% distilled water was used for the synthesis of ZnO nanoparticles, while keeping all other synthesis parameters the same as for absolute ethanol. Compared to absolute ethanol-synthesized samples, the XRD pattern of aqueous ethanol-synthesized samples show additional unreacted $Zn(CH_3CO_2)_2 \cdot 2H_2O$ precursor peaks marked X and Na peak marked Z in figure 3.2(b). In fact, dihydrate acetate precursor is highly soluble in water and therefore dissolves more quickly in aqueous ethanol than absolute ethanol. In addition, NaOH also dissolves in water quickly and dissociates into Na ions and OH ions. Thus, the lack of water in the solvent leads to unreacted precursor and Na peaks in aqueous ethanol-synthesized samples. The sample $ZE_a1.5$ was prepared using the lowest amount of NaOH and its XRD pattern shows both $Zn(CH_3CO_2)_2$ precursor and Na peaks. In this sample, the presence of unreacted precursor is likely because of insufficient amount of NaOH leading to incomplete reaction between acetate precursor and NaOH. On the other hand, sample ZE_a2 did not show reflections corresponding to unreacted precursor in figure 3.1, indicating optimum zinc precursor to NaOH ratio. However, on further increasing the NaOH amount, there is a reappearance of the Na peak for samples $ZE_a2.5$ and ZE_a3, which may be because of excess NaOH. In addition, compared to samples synthesized with absolute ethanol, the peak widths of aqueous ethanol-synthesized samples are much narrower, indicating a larger particle size for the latter. Therefore, the presence of water leads to the growth of larger nanoparticles due the condensation reaction that takes place in the presence of water molecules.
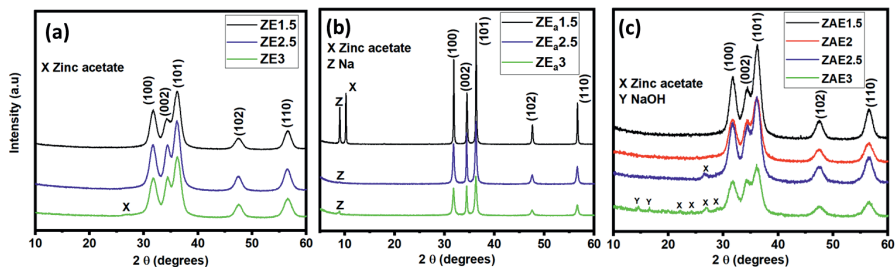

Figure 3.2. XRD patterns of samples (a) ZE1.5, ZE2.5 and ZE3, (b) $ZE_a1.5$, $ZE_a2.5$ and ZE_a3, and (c) ZAE1.5, ZAE2 ZAE2.5 and ZAE3, respectively.

(3) Effect of hydrates and molar ratio on the ZnO nanoparticle synthesis

To understand the role of hydrates in the synthesis of ZnO nanoparticles, samples ZAE1.5, ZAE2, ZAE2.5 and ZAE3 were prepared using anhydrous acetate precursor and absolute ethanol solvent. Similar to dihydrate acetate precursor-synthesized samples, the ZnO-A-based samples did not show any secondary phases, as observed in figure 3.2(c). However, additional XRD peaks are visible for highest NaOH ratios and they are marked X and Y in figure 3.2(c). In fact, the anhydrous acetate precursor does not contain hydrate molecules contrary to dihydrate acetate precursor. Therefore, the reaction kinetics of anhydrous acetate precursor with NaOH in absolute ethanol is comparatively slower than dihydrate acetate precursor, which leads to the formation of smaller nanoparticles. Furthermore, it also leads to an incomplete dissolution and reaction between $Zn(CH_3CO_2)_2$ precursor with NaOH in samples ZAE2.5. Similarly, sample ZAE3 shows both NaOH and acetate related reflections in the XRD pattern marked Y and X, respectively, due to further increase of undissolved NaOH quantity and incomplete reaction between anhydrous acetate precursor and NaOH. On the other hand, samples ZAE1.5 and ZAE2, do not show any unreacted precursor peaks owing to low amounts of NaOH. Therefore, the XRD results of anhydrous acetate-synthesized samples indicate that lower quantities of NaOH are optimal for the synthesis of these samples within a synthesis time of 2 h.

3.1.2. Nanostructures and morphology

TEM study was carried out on the ZnO nanoparticle samples and their nanohybrids, in order to gain information on their morphology and particles sizes. The average particle size of the ZnO nanoparticles obtained from the TEM studies and from the equation (3.1) of XRD studies, is listed in table 3.1. In addition, table 3.1 is also lists the morphology and shape of ZnO nanoparticles obtained from their TEM images.

(1) Effect of absolute alcohol solvents for 1:2 zinc precursor to NaOH molar ratio on ZnO nanoparticle synthesis

Figure 3.3(a-h) are the TEM images and size distribution histograms of samples ZM2, ZE2, ZE_a2, and ZI2, respectively. The ZnO nanoparticles

of ZM2, ZE2, and ZI2 that were synthesized using absolute methanol, ethanol and isopropanol, respectively are spherical. The size distribution histograms of samples ZM2, ZE2 and ZI2 revealed an average size of ~4.8 nm, ~5.2 nm and ~4.2 nm, respectively, as shown in in figure 3.3(e-g) and also listed in table 3.1. On the other hand, sample ZE_a2 that was synthesized using aqueous ethanol shows a needle-like morphology along with several hexagonally shaped nanoparticles in figure 3.3(c) and has an average size of ~48 nm estimated using equation (3.1). Considering the varying morphology, size distribution histograms were not plotted for this sample. This indicates that absolute alcohol plays an important role in controlling the morphology and size of ZnO nanoparticles. The presence of water in the solvent induces an uncontrollable growth owing to condensation with the water molecules. In addition, nanoparticles of ZM2 and ZE2 agglomerate as seen in the TEM images of figure 3.3(a-b), while the nanoparticles of sample ZI2 in figure 3.3(h) are monodispersed. This supports a possible coverage of ZnO nanoparticles by isopropoxide groups for ZI2 sample. The low magnification TEM image of sample ZI2 in figure 3.3(d), reveals the presence of unreacted zinc precursor with rice-like morphology, also identified by XRD. The dark dots in the background of the TEM grid in figure 3.3(d) correspond to ZnO nanoparticles. In addition, the presence of organic moieties, such as isopropoxide groups are likely to act as surfactants that prevent the agglomeration of the nanoparticles.
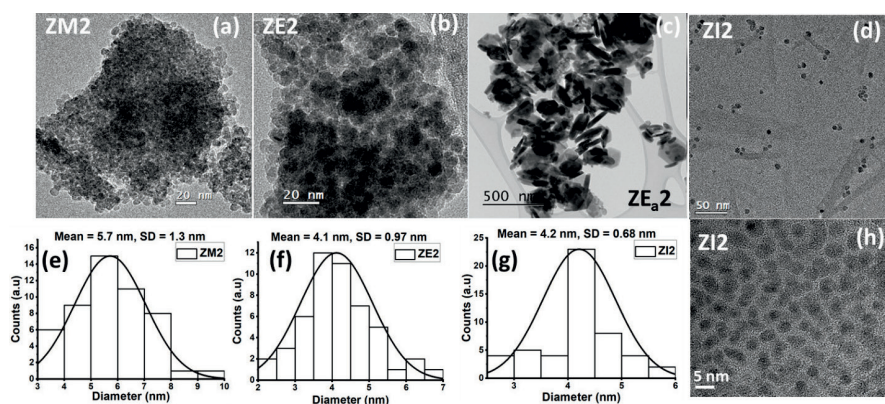

Figure 3.3. High magnification TEM micrographs of samples (a) ZM2, (b) ZE2, with their corresponding size distribution histograms in (e) and (f), respectively, (c) High magnification TEM image of ZE_a2, (d) Low magnification and (h) High magnification TEM image of ZI2 with its corresponding size distribution histogram in (g).

(2) Effect of aqueous alcohol on the synthesis of ZnO nanoparticles

Figure 3.4(a-c) are the TEM micrographs of samples ZE3, ZE2.5, and ZE1.5, respectively. These nanoparticles are spherically shaped along with a small difference in their sizes. In addition, the nanoparticles of samples ZE3 and ZE2.5 are agglomerated, as observed from TEM images in figure 3.4(a-b), respectively. Whereas, the nanoparticles of samples ZE1.5 are monodispersed in some areas and form aggregates in other areas in the higher magnification TEM image of figure 3.4(c). This indicates that too high an amount of NaOH promotes the agglomeration of ZnO nanoparticles, while a lower amount of NaOH tends to produce monodispersed nanoparticles. The size distribution histograms of these sample in figure 3.4(d-f) estimate an average size of ~4.7 nm, ~4.7 nm and ~6.9 nm for samples ZE3, ZE2.5 and ZE3, respectively and are also listed in table 3.1. On the other hand, for samples $ZE_a1.5$, $ZE_a2.5$ and ZE_a3, synthesized using aqueous ethanol, the nanoparticles are larger than for absolute ethanol. The presence of water inevitably promotes a condensation reaction and a better dissolution of NaOH in the alcoholic solvent. The trend observed consists of a decrease in nanoparticle size with the increase of NaO quantities in figure 3.4(g-i). For instance, in figure 3.4(i), the largest ZnO nanoparticles with hexagonal, rod and rectangular shapes are obtained for sample $ZE_a1.5$ that was synthesized using the lowest quantity of NaOH. An increase in NaOH resulted in the production of smaller nanoparticles with variable shapes for samples $ZE_a2.5$ in figure 3.4(h). The highest quantity of NaOH i.e., ZE_a3 produced the smallest sized nanoparticles with both, spherical and facetted morphologies in figure 3.4(g). The decrease in particle size with increase of the NaOH quantity is attributed to the increase in the reactivity of the zinc precursor $Zn(CH_3CO_2)_2.2H_2O$ with NaOH. From the reaction 2.1, described in chapter 2, it is clear that the reaction between $Zn(CH_3CO_2)_2.2H_2O$ and NaOH consists of a rapid conversion of $Zn(CH_3CO_2)_2.2H_2O$ to an intermediate phase $Zn(CH_3COO)(OH)$ and then to ZnO. Increasing the quantity of NaOH leads to an increase in the amount of hydroxide ions in the solution, which results in the transformation of the shape of the nanoparticles. When the NaOH quantity is increased to a certain limit, the ZnO nanoparticles no longer follow their preferential growth along c-axis due to excess of hydroxide ions, resulting in nanoparticles of smaller sizes with smoother facets as seen for sample ZE_a3 in figure 3.4(g). Thus, the TEM study of ZnO nanoparticles synthesized by varying NaOH quantities in aqueous ethanol solvent provides an important insight on the control of the

shape, size and morphology of ZnO nanoparticles in aqueous media. In fact, additional and rapid hydrolysis does not allow efficient control of the nanoparticle morphological characteristics compared to absolute alcohol solvents.
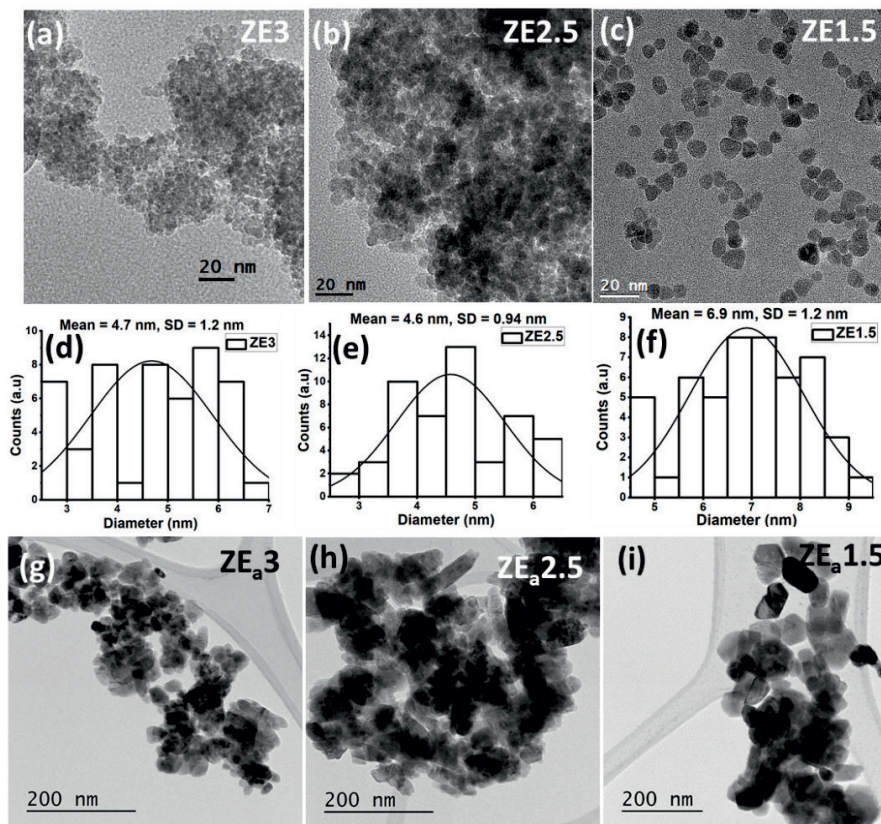
Figure 3.4. Low magnification TEM micrographs of samples (a) ZE3, and (b) ZE2.5, and high magnification TEM micrograph of sample (c) ZE1.5. The size distribution histograms of samples (d) ZE3, (e) ZE2.5 and (f) ZE1.5. Low magnification TEM micrograph of sample (g) ZE_a3, and high magnification TEM micrographs of samples (h) $ZE_a2.5$, and (i) $ZE_a1.5$.

(3) Effect of hydrates on the ZnO nanoparticle synthesis

Figure 3.5(a-d) are the low magnification and overview TEM images of samples ZAE1.5, ZAE2, ZAE2.5 and ZAE3, respectively. In general, the nanoparticles exhibit uniform spherical morphologies with small variations in size as a function of NaOH quantities. Similar to samples ZE2, ZE2.5 and ZE3 synthesized using the dihydrate acetate precursor, the nanoparticles of samples ZAE2, ZAE2.5 and ZAE3 tend to agglomerate.

Whereas, for the lowest amount of NaOH, the nanoparticles of sample ZAE1.5 are monodispersed as observed in figure 3.5(a). This again suggests that the lowest amount of NaOH prevents the agglomeration of nanoparticles. On the other hand, the TEM image of sample ZAE1.5 in figure 3.5(e) consists of flakes, attributed to the unreacted anhydrous acetate precursor. The dark dots in the background on the carbon grid consist of ZnO nanoparticles. In addition, the HRTEM image of sample ZAE2.5 in figure 3.5(f), clearly shows the spherical nanoparticles and samples ZAE2 and ZAE3 in figure 3.5(g-h), illustrate the lattice fringes of the crystalline nanoparticles. In general, the spherical morphology for both dihydrate acetate and anhydrous acetate-synthesized samples corroborate with each other, suggesting absolute ethanol plays a crucial role in the formation of uniform spherical shaped nanoparticles regardless of the presence of hydrates in the precursor. However, the lack of hydrates produces a high amount of synthesis by-product with a lower ZnO nanoparticle yield. The sizes of the nanoparticles ZAE2, ZAE2.5 and ZAE3 were estimated in the range of 4 nm to 7 nm from their size distribution histograms as shown in figure 3.5(i-k).
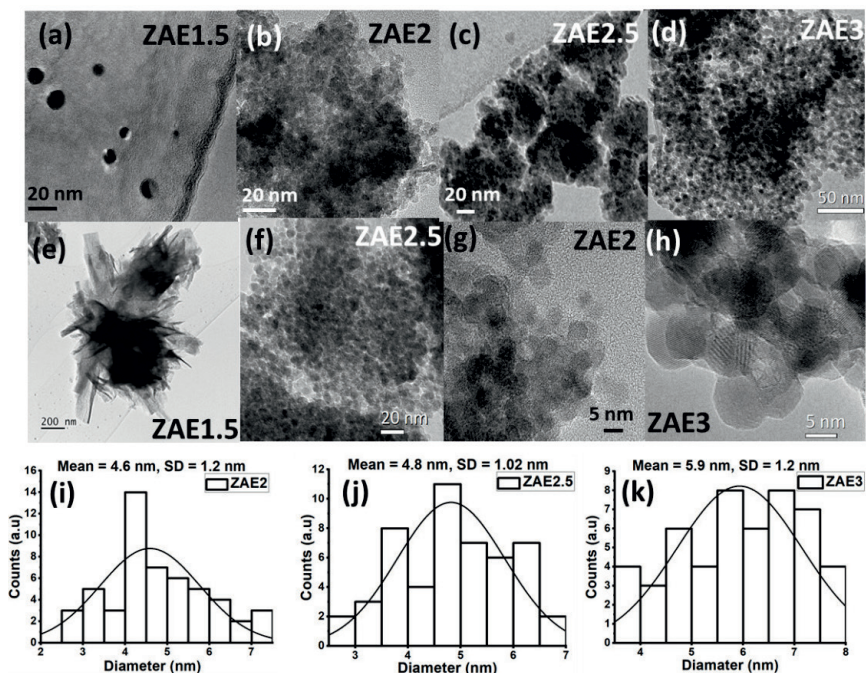

Figure 3.5. Overview and low magnification TEM micrographs of samples (a) ZAE1.5, (b) ZAE2, (c) ZAE2.5 and (d) ZAE3. High magnification TEM micrographs of samples (e) ZAE1.5 and (f) ZAE2.5, and high-resolution TEM micrographs of samples (g) ZAE2 and (h) ZAE3, respectively, (i), (j) and (k) are size distribution histograms of ZAE2, ZAE2.5 and ZAE3.

(4) In-situ synthesized ZnO-CNT nanohybrids

For the in-situ synthesis of ZnO-CNT nanohybrids, a molar ratio of 1:2 of zinc precursor to NaOH for both zinc precursors i.e., hydrated and anhydrous, were chosen. The solvent was absolute ethanol in both cases. From the XRD study, the 1:2 molar ratio tends to be optimal for both ZE2 and ZAE2 nanoparticle samples, which motivated the choice of this particular molar ratio for the preparation of in-situ ZnO-CNT nanohybrid samples.

Figures 3.6(a) and 3.6(d) are the TEM images of samples ZAE2C and ZE2C, respectively, where ZnO nanoparticles are dominant. This is because of the low wt% (~1 wt%) of CNT used during the synthesis. The high-resolution TEM images of samples ZAE2C and ZE2C are presented in figures 3.6(c) and 3.6(f), where sidewalls of CNT are clearly visible. In addition, ZnO nanoparticles decorating the walls of CNT indicate successful formation of the ZnO-CNT nanohybrids. To synthesize these samples, the CNT were functionalized by sonication in ethanol. Thus, carboxyl (COOH) functional groups are present on the walls of the CNT that can be broken down into carbonyl (C-O) and hydroxyl (OH). These functional groups promote the covalent bonding between CNT and ZnO nanoparticles, necessary for the decoration of nanoparticles on the CNT sidewalls. The presence of CNT does not alter the crystallinity nor the size distribution of the ZnO nanoparticles, and average sizes of ~4.7 nm and ~5.7 nm were calculated for ZAE2C and ZE2C, respectively, from their size distribution histograms as shown in figures 3.6(b) and 3.6(e), respectively.
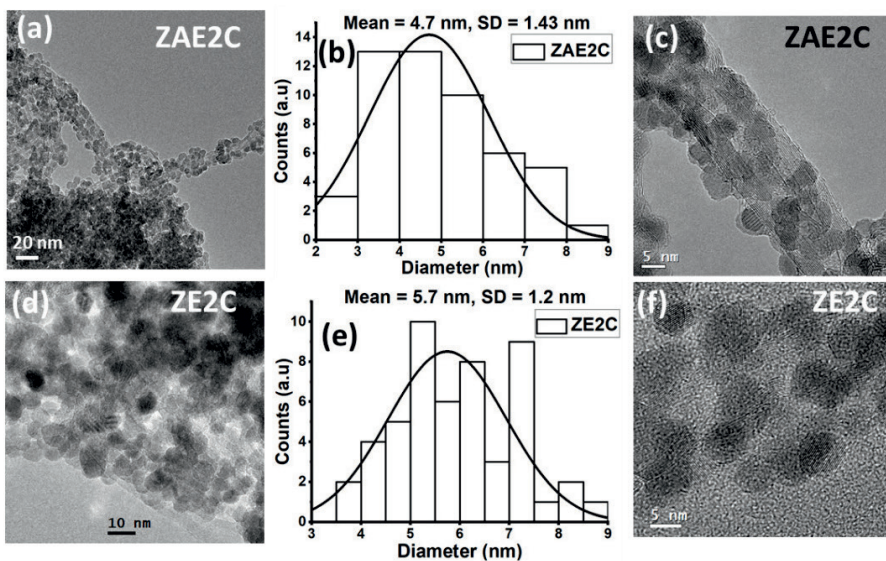
Figure 3.6. (a), (d) Low magnification and high magnification TEM images of samples ZAE2C and ZE2C (b), (e) size distribution histograms of their ZnO nanoparticles ZAE2 and ZE2, and (c), (f) high resolution TEM images of samples ZAE2C and ZE2C.

(5) Ex-situ synthesized ZnO-PEDOT:PSS nanohybrids

Similar to in-situ ZnO-CNT nanohybrids, a molar ratio of 1:2 was considered for ex-situ synthesis of ZnO-PEDOT:PSS nanohybrid samples, prepared using the anhydrous and dihydrate zinc precursors and absolute ethanol solvents.

Figure 3.7(a-b) are the low magnification and overview TEM images of samples ZE2px and ZAE2px. Here, PEDOT:PSS appears as flakes for both samples, without any noticeable agglomeration of ZnO nanoparticles in the polymer matrix. For sample ZAE2px, all areas of PEDOT:PSS are densely packed with ZnO nanoparticles, as observed in figure 3.7(b). Whereas, some areas of PEDOT:PSS are less densely packed with ZnO nanoparticles for sample ZE2px, as observed in figure 3.7(a). The high magnification TEM images of samples ZE2px and ZAE2px are shown in figure 3.7(c-d). Therefore, TEM images in general confirm the successful formation of ZnO-PEDOT:PSS nanohybrids.
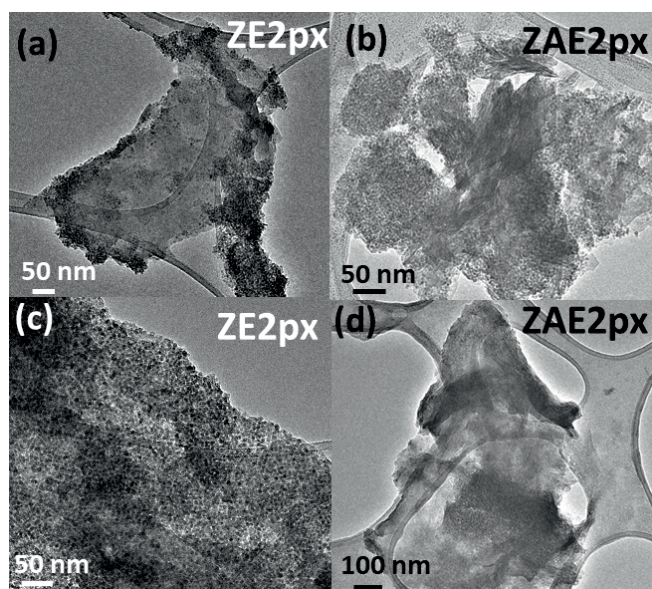
Figure 3.7. Low magnification and overview TEM images of samples (a) and (c) ZE2px, (b) and (d) ZAE2px.

Table 3.1. List of average particle sizes of all ZnO nanoparticle samples, calculated from Debye Scherrer equation and size distribution histograms and morphologies obtained from TEM images.

Sample name	XRD particle size (nm)	TEM particle size (nm)	Morphology from TEM
ZM2	10	5.7 ± 1.3 nm	Spherical
ZI2	7.3	4.2 ± 0.68 nm	Spherical
ZE1.5	6.1	4.7 ± 1.2 nm	Spherical
ZE2	9.9	5.2 ± 0.97 nm	Spherical
ZE2.5	6.6	4.6 ± 0.94 nm	Spherical
ZE3	6	6.9 ± 1.2 nm	Spherical
$ZE_a1.5$	43.1	----	Hexagonal, rod and rectangular
ZE_a2	47.5	----	Hexagonal and needle-like
$ZE_a2.5$	26.2	----	variable
ZE_a3	20.5	----	Spherical and facetted
ZAE1.5	5.9	4.6	Spherical
ZAE2	5	4.6 ± 1.2 nm	Spherical
ZAE2.5	5.5	4.8 ± 1.02 nm	Spherical
ZAE3	3.7	5.9± 1.2 nm	Spherical

3.1.3. Chemical bonding

FTIR spectroscopy was performed on ZnO nanoparticles and ex-situ synthesized ZnO-CNT nano hybrids in order to gain information on their chemical bonding.

(1) Effect of absolute alcohol solvents for 1:2 zinc precursor to NaOH molar ratio on ZnO nanoparticle synthesis

Figure 3.8 is the FTIR spectra of samples ZM2, ZE2, ZI2 and ZE$_a$2 synthesized by varying the alcoholic solvent. The band located between 700 cm^{-1}-500 cm^{-1} corresponds to the Zn-O stretching bond, which is the characteristics of ZnO [186]. In the region 1700-500 cm^{-1}, all these samples tend to show similar FTIR peak structures with differences only in the intensities of some peaks. In addition, samples ZM2, ZE2 and ZE$_a$2 tend to show a broad band near 3300 cm^{-1} corresponding to OH-stretching which originates from water and NaOH. Remarkably, for sample ZI2, the band at 3300 cm^{-1} is of low intensity. The bands between 1000 cm^{-1}-800 cm^{-1} are attributed to Zn-OH. Sample ZE$_a$2 presents the highest intensity for Zn-OH band compared to other samples due to the presence of water during its synthesis. These bands are almost not visible in the case of ZI2, confirming the possible coating of ZnO nanoparticles with isopropoxide groups. Furthermore, the bands situated between 1600 cm^{-1} and 1100 cm^{-1} correspond to several acetate groups (-COOH) [187]. These groups are adsorbed on the surfaces of the ZnO nanoparticles during the synthesis. In particular, the bands located between 1600 cm^{-1} and 1500 cm^{-1} correspond to symmetric stretching vibrations of C=O bond. Whereas, the bands between 1500 cm^{-1} and 1400 cm^{-1} correspond to asymmetric stretching vibrations of the C=O bond. The broad peak at around 1350 cm^{-1} corresponds to C–O bonds. Finally, a band between 3000 cm^{-1} and 2800 cm^{-1} corresponding to CH-stretching of alkane groups, is observed in all of these samples.
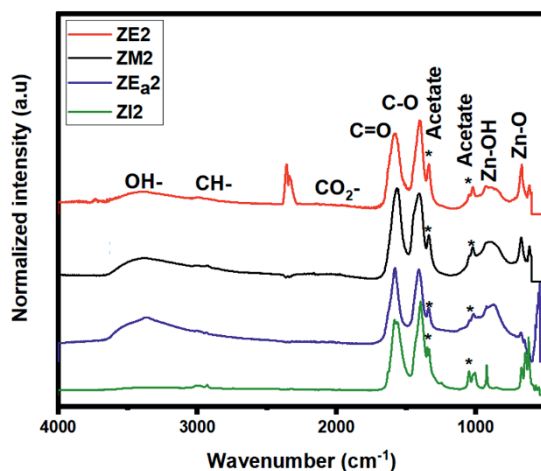
Figure 3.8. FTIR spectra of samples ZE2, ZM2, ZE$_a$2 and ZI2, respectively.

(2) Effect of aqueous ethanol on the ZnO nanoparticle synthesis

Figure 3.9(a) shows the FTIR spectra of samples ZE1.5, ZE2.5 and ZE3 and figure 3.9(b) shows the FTIR spectra of samples ZE$_a$1.5, ZE$_a$2.5 and ZE$_a$3, prepared using absolute and aqueous ethanol, respectively. For both types of samples, the Zn-O vibration bands tend to downshift from ~680 cm^{-1} to 640 cm^{-1} and the intensity of the band decreases with increasing NaOH quantities. This suggests a change in the size and morphology of ZnO nanoparticles with increase of NaOH quantity, analogous to TEM results [188]. In addition, all the ZnO nanoparticles show a broad band near 3300 cm^{-1} corresponding to OH-stretching. It originates from water and NaOH for samples synthesized using aqueous ethanol and only from NaOH for samples of absolute ethanol. The width of this band tends to increase in the presence of water and also with the increase of NaOH, suggesting an increase in the adsorption of hydroxyl groups on the surface of nanoparticles. In addition, for all samples the OH$^-$ functional groups bonded to Zn are located between 1000 cm^{-1} and 800 cm^{-1}. The intensity of Zn-OH bonds also tends to increase with the increase of NaOH quantity and is a little higher for samples prepared using aqueous ethanol, further supporting the increase in the number of hydroxyl groups on the surface of the nanoparticles.
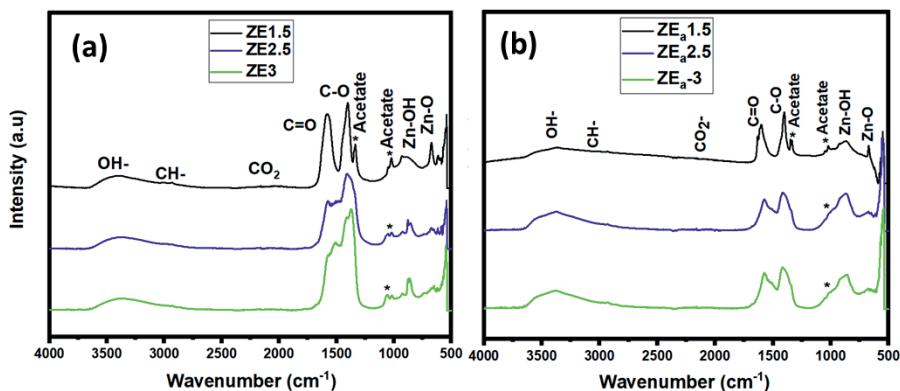
Figure 3.9. FTIR spectra of samples (a) ZE1.5, ZE2.5 and ZE3, and (b) $ZE_a1.5$, $ZE_a2.5$ and ZE_a3.

(3) Effect of hydrates on the ZnO nanoparticle synthesis

Figure 3.10(a) shows FTIR spectra of samples ZAE1.5, ZAE2, ZAE2.5 and ZAE3 prepared using anhydrous acetate precursor. For a corresponding zinc precursor to NaOH molar ratio, the ZnO-A samples show similar peak structures and frequency localizations to dihydrate acetate-based samples. However, the intensity of the -OH band near 3300 cm^{-1} and of Zn-OH band between 1000 cm^{-1} and 800 cm^{-1}, tends to be relatively higher for anhydrous acetate-based samples. This suggest that anhydrous acetate-based samples possess relatively higher amounts of surface defects than dihydrate acetate-based samples that chemisorb a higher number of hydroxyl groups.

(4) Ex-situ synthesized ZnO-CNT nanohybrids

Figure 3.10(b) shows the FTIR spectra of samples $ZE_a1.5Cx$, ZE_a3Cx, and pristine CNT. The FTIR spectra of these nanohybrid samples contain similar bonds to their free-standing counterparts i.e., $ZE_a1.5$ and ZE_a3. However, a broad peak at 2130 cm^{-1} is present for the ex-situ synthesized ZnO-CNT nanohybrid samples that is absent for freestanding nanoparticles. This peak is also visible for pristine CNT and therefore can be safely attributed to CO_2 peak.
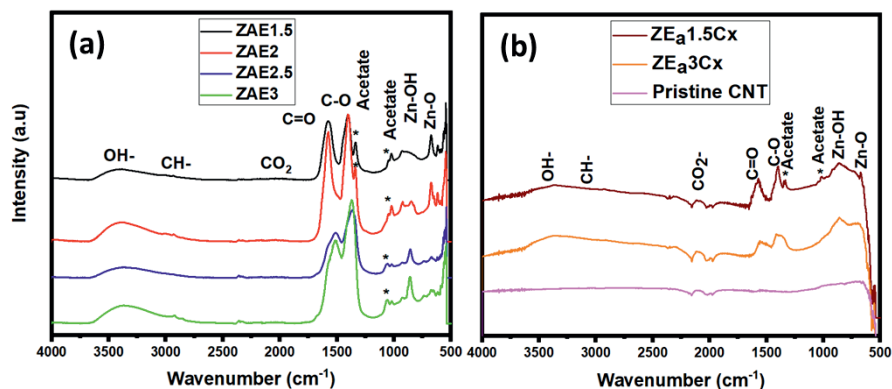
Figure 3.10. FTIR spectra of samples (a) ZAE1.5, ZAE2, ZAE2.5 and ZAE3, and (b) ZE$_a$1.5Cx, ZE$_a$3Cx, and pristine CNT, respectively.

3.1.4. X-ray photoelectron spectroscopy

The surface chemistry of ZnO nanoparticles, ZnO-CNT nanohybrid (in-situ) and ZnO-PEDOT:PS nanohybrid (ex-situ) samples synthesized using 1:2 molar ratios of zinc precursor to NaOH were studied by XPS, by collecting C1s and O1s spectra.

(a) C1s spectra of ZnO nanoparticles and their nanohybrids

Figure 3.11(a-i) show the high resolution C1s spectra of samples ZE$_a$2, ZI2, ZE2, ZM2, ZE2C, ZE2px, ZAE2, ZAE2C, and ZAE2px, respectively. In all samples, the C-C bond at 284.8 eV corresponds to adventitious carbon.

(1) Effect of solvents for 1:2 molar ratio of zinc precursor to NaOH on the ZnO chemical states

Figure 3.11(a-d) are the C1s XPS spectra of samples ZM2, ZI2, ZE$_a$2 and ZE2. In general, the C1s peak intensity varies for samples prepared using different solvents indicating changes in the surface chemistry of these samples. For instance, the C1s spectrum of sample ZI2 manifests the highest relative contributions from C-OH and O=C-O bonds, as shown in figure 3.11(b). This confirms the presence of unreacted zinc acetate precursor and NaOH on the surface of ZI2 nanoparticles, corroborating with XRD, TEM and FTIR studies, due to anchoring of isopropoxide groups on the surface of ZnO through oxygen bonding.

On the other hand, in the case of methanol and ethanol solvents, organic moities do not anchor to the surface of ZnO nanoparticles. Therefore, samples ZM2 and ZE2 show relatively lower contributions from C-OH and O=C-O bonds, as seen in figures 3.11(a) and 3.11(d) respectively, compared to sample ZI2. However, for sample ZE_a2, due the presence of water, the dissolution of zinc precursor and nucleation rate of ZnO nanoparticles are the quickest. Therefore, sample ZE_a2 shows the lowest relative contribution of zinc acetate-related C-OH and O=C-O bonds in the C1s XPS spectra in figure 3.11(c).

(2) Effect of hydrates in the zinc precursor on the chemical states of ZnO

Figure 3.11(g) shows the C1s XPS spectra of sample ZAE2. Compared to ZE2 of figure 3.11(d), ZAE2 show higher intensity of O=C-O bonds, suggesting the presence of a higher amount of unreacted acetate precursor on the surface of ZAE2. This result corroborates with the XRD analysis.

(3) In-situ synthesized ZnO-CNT nanohybrids

Figure 3.11(e) and 3.11(h) are the C1s XPS spectra of ZE2C and ZAE2C, respectively. For these samples, an additional peak corresponding to sp^2 hybridization of C atoms of CNT at binding energy of 283 eV is present. Furthermore, the relative intensities of C-OH peaks for both ZnO-CNT nanohybrid samples are slightly higher compared to their corresponding ZnO nanoparticle samples, which could indicate an increase in the amount of hydroxyl groups [189]. In fact, before the synthesis, the CNT was sonicated in ethanol, which engendered a breakdown of sidewalls and produced C-dangling bonds [190]. In addition, during the synthesis process the sonicated CNT were mixed in the NaOH solution, which was added drop-by-drop to the zinc precursor solution. Subsequently, the final mixture was maintained at 65°C for 2 h. Considering the OH-rich conditions, OH groups attach to C-dangling bonds during the synthesis process leading to a relatively higher intensity of C-OH peaks in ZnO-CNT nanohybrid samples.

(4) Ex-situ syntheszied ZnO-PEDOT:PSS nanohybrids

Figures 3.11(f) and 3.11(i) are the C1s XPS spectra of samples ZE2px and ZAE2px, respectively. In sample ZAE2px, a decrease in O=C-O and

C-OH peak intensities relative to C-C peak is observed in figure 3.11(i). This indicates an oxygen-deficient or a reduced PEDOT:PSS polymer. However, for sample ZE2px, the relative intensities of all the C1s peaks are similar, owing to the additional pair of water molecules present in the $Zn(CH_3CO_2)_2.2H_2O$ precursor used for the synthesis of sample ZE2px.
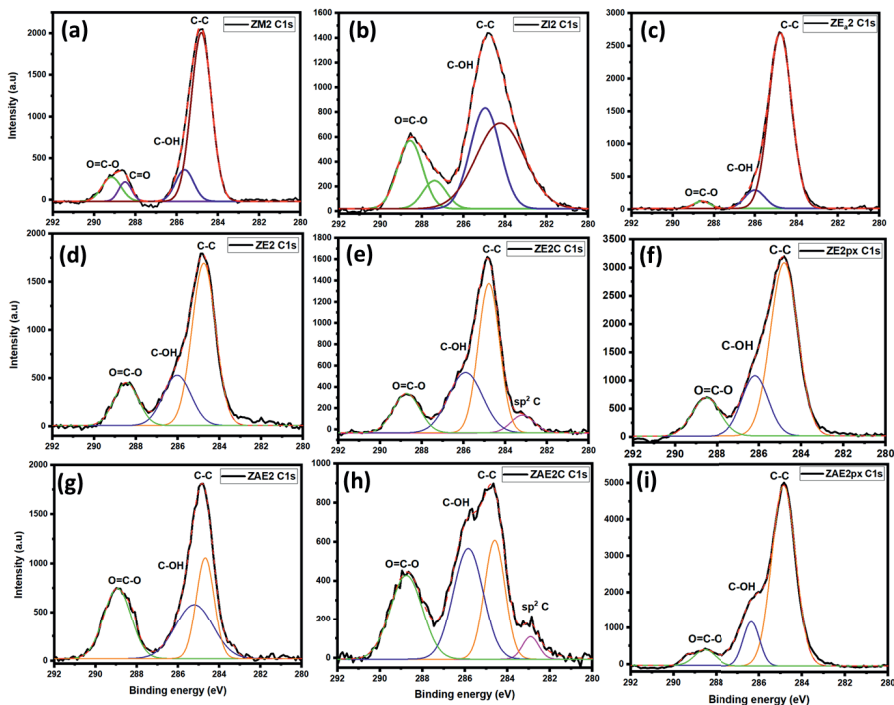
Figure 3.11. C1s XPS spectra of samples (a) ZM2, (b) ZI2, (c) ZE_a2, (d) ZE2, (e) ZE2C, (f) ZE2px, (g) ZAE2, (h) ZAE2C and (i) ZAE2px.

(b) O1s spectra of ZnO nanoparticles and their nanohybrids

Figures 3.12(a-i) show the high resolution O1s spectra of ZM2, ZE_a2, ZI2, ZE2, ZE2C, ZE2px, ZAE2, ZAE2C, and ZAE2px, respectively. For all samples, the main peak at ~529 eV is the lattice oxygen corresponding to Zn-O bond that is characteristic of ZnO nanoparticles. Additionally, the peak at ~531.5 eV corresponds to the presence of OH groups that are bonded to the ZnO nanoparticle surface indicating Zn-OH bonds. However, this peak can also be related to oxygen defects or surface oxygen vacancies [191]. Also, the TEM study highlighted small sized nanoparticles of ~5 nm for samples ZM2, ZE2 and ZI2 and ~50 nm for sample ZE_a2, supporting the presence of surface oxygen defects due to a high surface-to-volume ratio, especially in the ~5 nm sized nanoparticles.

(1) Effect of solvents for 1:2 molar ratio of precursor to NaOH on ZnO chemical states

Figure 3.12(a-d) are the O1s XPS spectra of samples ZM2, ZI2, ZE$_a$2 and ZE2, respectively. For samples ZM2, ZE$_a$2, and ZE2 in figures 3.12(a), 3.12(c) and 3.12(d), the O1s peak structure is similar with only differences in their relative intensities, implying comparable surface chemistry. However, for sample ZI2 in figure 3.12(b), the O1s peak structure is different and the intensity of Zn-OH peak is higher than the lattice Zn-O peak, indicating a higher amount of adsorbed OH groups and unreacted Zn precursor. In addition, there is an extra Na peak at 536 eV present for sample ZI2 as observed in figure 3.12(b), also confirmed by XRD. Therefore, the chemical states of sample ZI2 obtained from C1s and O1s spectra suggest that the surface of this sample is covered with isopropyl groups from isopropanol, acetate groups from Zn precursor and OH groups from NaOH.

(2) Effect of hydrates in precursor on the chemical states of ZnO

Figure 3.12(g) shows the O1s XPS spectra of sample ZAE2. Compared to sample ZE2 in figure 3.12(d) the intensities of C-O and Zn-OH peaks are higher for sample ZAE2. The origin of C-O peak is associated with the dihydrate and anhydrous acetate precursors used for the synthesis of samples ZE2 and ZAE2, respectively. Therefore, higher C-O peak intensity in case of sample ZAE2 suggests the presence of a higher amount of unreacted precursor on the surface of this sample, corroborating with the C1s, XRD and TEM results. This is because the solubility of anhydrous acetate precursor in absolute ethanol is relatively low compared to dihydrate acetate precursor. Similarly, the high intensity of ZnO-OH peak indicates higher amount of surface defects in sample ZAE2 compared to sample ZE2.

(3) In-situ synthesized ZnO-CNT nanohybrids

Figures 3.12(e) and 3.12(h) show the high resolution O1s spectra of samples ZE2C and ZAE2C, respectively. Since both C1s and O1s spectra of these samples contain hydroxyl components, it therefore suggests that the hydroxyl groups are responsible for the decoration of CNT with ZnO enabling the anchoring of ZnO on CNT sidewalls through Zn-O-C covalent bonds (Zn-OH/C-OH). Therefore, the O1s spectra indicates

that Zn-O/OH-C bonding is responsible for nanohybrid synthesis, which allows decoration of ZnO nanoparticles on the sidewalls of the CNT.

(4) Ex-situ synthesized ZnO-PEDOT:PSS nanohybrids

The O1s XPS spectra of samples ZE2px and ZAE2px are shown in figures 3.12(f) and 3.12(i), respectively. In addition to the peak corresponding to Zn-O bond, these nanohybrids show additional characteristic peaks of PEDOT:PSS. The peak at 532.7 eV corresponds to the C-O-C bond of PEDOT and the peak at 531.7 eV is the O=S bond of PSS. From the figures 3.12(f) and 3.12(i), it is clear that the PEDOT:PSS character is more dominant than ZnO in both samples. In addition, the O1s region of sample ZAE2px of figure 3.12(i) consists of a relatively less intense C-O-C peak and a more intense O=S peak compared to sample ZE2px. Therefore, either PEDOT was removed or degraded as a result of the anhydrous precursor, indicated by the loss in relative intensity of the C-O-C.
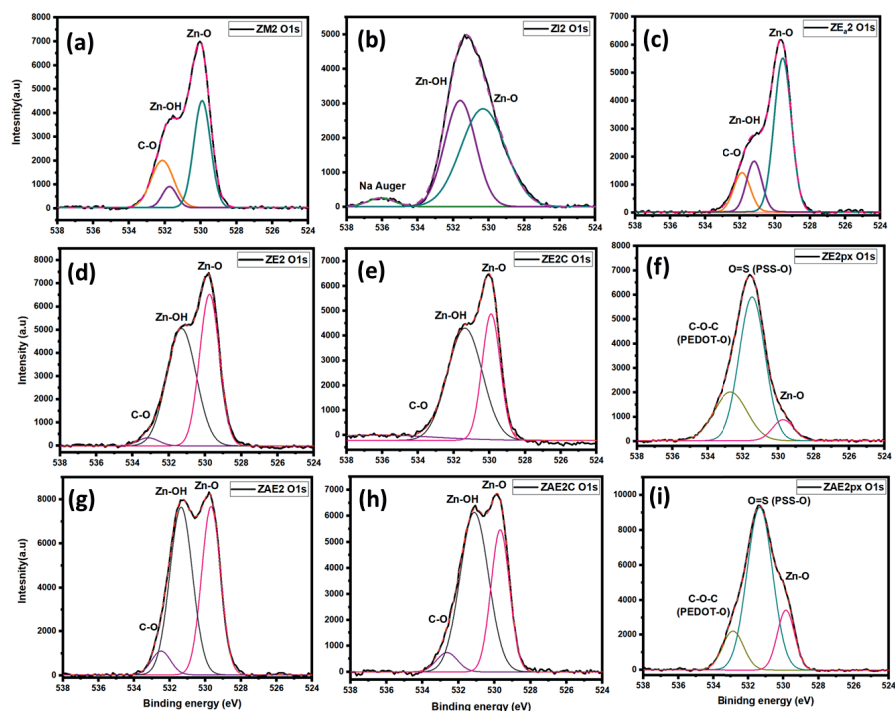

Figure 3.12. O1s XPS spectra of samples (a) ZM2, (b) ZI2, (c) ZE$_a$2, (d) ZE2, (e) ZE2C, (f) ZE2px, (g) ZAE2, (h) ZAE2C and (i) ZAE2px.

3.1.5. Raman spectroscopy

Raman spectroscopy was performed in order to attain information on the vibrational properties, chemical structure and molecular interactions of ZnO nanoparticles, in-situ ZnO-CNT and ex-situ ZnO-PEDOT:PSS nanohybrids. Figure 3.13 compares the different vibrational modes obtained for samples ZM2, ZE$_a$2, ZI2, ZE2, and ZAE2, in the range of 100-800 cm^{-1}. The modes visible at ~440 cm^{-1}, ~585 cm^{-1}, and 667 cm^{-1} correspond to E$_{2H}$, E$_1$(LO) and E$_2$(TO) modes, respectively. The modes visible at ~320 cm^{-1} and 506 cm^{-1} correspond to E$_{2H}$-E$_{2L}$ and E$_1$(TO) + E$_{2L}$ modes and are known as multi-phonon scattering modes. In particular, the E$_{2H}$ mode at ~440 cm^{-1} is the Zn-O vibrational bond, which corresponds to lattice oxygen and confirms the formation of ZnO [192]. Whereas, the mode E$_1$(LO) corresponds to oxygen related defects. In general, the modes below 300 cm^{-1} are Zn-related defects, whereas the modes above 300 cm^{-1} are related to both Zn or oxygen-related complex defects [192].

(1) Effect of alcoholic solvents for 1:2 zinc precursor to NaOH molar ratio on the vibrational modes of ZnO nanoparticles

In figure 3.13, sample ZE2 has the highest E$_{2H}$ mode intensity compared to samples ZM2 and ZE$_a$2. On the other hand, for sample ZI2, the E$_{2H}$ mode intensity has diminished and shifted slightly to a higher wave number. Several factors may be responsible for the same, including the presence of organic contaminants, unreacted zinc precursor or NaOH that affect the phonon confinement of ZI2 nanoparticles. Besides, XRD and TEM clearly indicate the presence of very small ZI2 nanoparticles that are covered by isopropoxide groups that dampen the phonon vibrational modes. On the other hand, the E$_1$(LO) band indicates the presence of oxygen vacancies, zinc interstitials or complexes of both. The relative intensities of E$_{2H}$ band to E$_1$(LO) band therefore suggests that samples ZE2 has the lowest amount of oxygen vacancies compared to other samples.

(2) Effect of hydrates in the zinc precursor for 1:2 zinc precursor to NaOH molar ratio

In figure 3.13, The E$_{2H}$ peak of ZAE2 has a relatively higher intensity than sample ZE2, which suggests that sample ZAE2 has a more stable

lattice configuration than sample ZE2. In addition, the ratio of E_{2H} band to E_1(LO) band is higher for sample ZAE2 than sample ZE2 indicating a lower amount of oxygen vacancies in this sample.
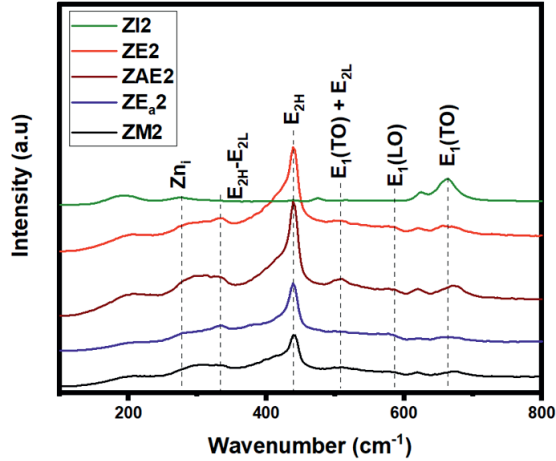
Figure 3.13. Raman spectra of samples (a) ZI2, ZE2, ZAE2, ZE_a2, and ZM2, in the range of 100-800 cm^{-1}.

(3) In-situ synthesized ZnO-CNT nanohybrids

Figure 3.14(a) shows the Raman spectra of samples ZE2C and ZAE2C in the range 100-800 cm^{-1}. The intensity of E_{2H} mode for these samples has been preserved on hybridizing with CNT. Whereas, the relative intensity of E_1(LO) bands and E_{2H}-E_{2L} bands increases in both samples compared to their corresponding ZnO nanoparticles, indicating an increased number of surface defects in these samples [193].

To further investigate the surface defects in ZnO-CNT nanohybrids, the bands from 1200-1800 cm^{-1} corresponding to D anG bands of CNT are compared with those of pristine CNT, as shown in figure 3.14(b). The (*) marked peaks in these samples are attributed to C-O bond vibrations from the acetate precursor used during synthesis [194]. In addition, there is a redshift to ~1351 cm^{-1} in the D-band of ZnO-CNT nanohybrid samples compared to D-band at 1341 cm^{-1} of pristine CNT. Similarly, G-band is also redshifted from 1579 cm^{-1} to ~1592 cm^{-1} for the ZnO-CNT nanohybrid samples compared to the pristine CNT. These redshifts also indicate the presence of oxygen or OH groups on the CNT surface [193].

(4) Ex-situ synthesized ZnO-PEDOT:PSS nanohybrids

Figure 3.14(a) shows the Raman spectra of samples ZE2px and ZAE2px, in the range 100-800 cm^{-1}. In these samples, due to the chemical interactions between PEDOT:PSS polymer and ZnO nanoparticles, the E_{2H} peak for ZnO-PEDOT:PSS nanohybrid samples is shifted to a higher wavenumber of 445 cm^{-1}. This peak is observed to be relatively more intense for sample ZAE2px than ZE2px. Additionally, there is a peak at 275 cm^{-1} related to Zn_i or Zn_i clustering. For both samples i.e., ZE2px and ZAE2px, the intensity of mode at 275 cm^{-1} is relatively higher compared to other modes and is the highest for sample ZAE2px. This suggests in general, there is a higher amount of Zn_i related defects in these two nanohybrid samples, which are relatively higher for sample ZAE2px.

The Raman spectra of ZnO-PEDOT:PSS nanohybrid samples was also analyzed in the range 900-1700 cm^{-1}, where detailed information on PEDOT and PSS vibrational modes exist, as shown in figure 3.14(c). The vibrational modes at 988 cm^{-1} and 1097 cm^{-1} are typical PSS vibrational modes [195]. Whereas, the vibrational modes at 1263 cm^{-1}, 1369 cm^{-1}, 1436 cm^{-1} and 1517 cm^{-1} correspond to C_α-C_α, C_β-C_β, symmetrical C_α=C_β and asymmetrical C_α=C_β stretching vibrational modes, respectively for PEDOT [195]. The symmetrical vibrational bond at 1436 cm^{-1} is observed to be redshifted for sample ZE2px compared to pristine PEDOT:PSS at 1440 cm^{-1} [196]. This mode is slightly more redshifted in sample ZAE2px, suggesting a slightly higher benzoid (coil) to quinoid (linear) structural transition [196]. On the other hand, the asymmetrical C_α=C_β modes at 1517 cm^{-1} is more intense for ZAE2px sample compared to ZE2px sample. The higher shifts and higher intensities in sample ZAE2px imply that the bonds in PEDOT chain have undergone structural modification, which in turn suggests that PEDOT was degraded or removed from the macromolecule upon combining with ZAE2 nanoparticles, as also demonstrated by XPS studies.
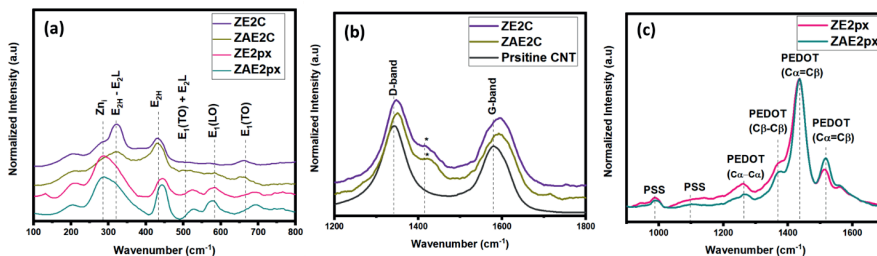
Figure 3.14. Normalized Raman spectra of samples (a) ZE2C, ZAE2C, ZE2px, and ZAE2px, in the range of 100-800 cm⁻¹ (b) ZE2C, ZAE2C, and pristine CNT in the range of 1200-1800 cm⁻¹, and (c) ZE2px and ZAE2px, in the range of 900-1700 cm⁻¹.

3.1.6. Band gaps

The band gaps of ZnO nanoparticle, ZnO-CNT nanohybrids and ZnO-PEDOT:PSS nanohybrid samples are obtained from UV-Vis absorption spectroscopy followed by Tauc plots. Table 3.2 is the list of band gap calculated for these samples.

Figure 3.15(a-d) are the Tauc plots of the ZnO nanoparticles synthesized by varying solvents, molar ratios and precursor. The band gaps of the samples range from 3.05 eV to 3.4 eV, as listed in table 3.2 and are within the theoretical band gap of ZnO [197,198]. The variations in the band gap of these samples are an effect of the synthesis conditions that include solvents, NaOH amount and hydrates in the zinc precursor. For all ZnO nanoparticle samples, the absorption spectra revealed a sharp shoulder at 3.3 eV, stretching down to ~2.0 eV. Shoulders related to defect level absorption (DLA) are absent.

Table 3.2. List of band gap values calculated for ZnO nanoparticle samples and their nanohybrids with CNT and PEDOT:PSS

Sample name	Band gap (eV) ± 0.1 eV
ZM2	3.1
ZI2	3.23
ZE1.5	3.34
ZE2	3.28
ZE2.5	3.3
ZE3	3.14
$ZE_a1.5$	3.19
ZE_a2	3.16
$ZE_a2.5$	3.27
ZE_a3	3.29
ZAE1.5	3.08
ZAE2	3.11
ZAE2.5	3.14
ZAE3	3.05
ZE2C	3.11
ZAE2C	3.18
$ZE_a1.5Cx$	3.18
ZE_a3Cx	3.17
ZE2px	3.2
ZAE2px	3.21

Figure 3.15(e) is the Tauc plots of both ex-situ and in-situ ZnO-CNT nanohybrid samples and figure 3.15(f) is the Tauc plots of ex-situ ZnO-PEDOT:PSS nanohybrid samples. The four ZnO-CNT and two ZnO-PEDOT:PSS nanohybrid samples exhibit slightly lower band gaps than their corresponding ZnO nanoparticles. Nevertheless, these values are in good agreement with the theoretical band gaps of ZnO, implying that the absorbance in ZnO-nanohybrids is dominated by ZnO. Metallic CNT generally absorb in the infra-red region owing to Van Hove singularities and PEDOT:PSS absorbs in the near infra-red region [199]. Therefore, no contribution of CNT or PEDOT:PSS to the ZnO band-to-band absorption is likely for both ZnO-CNT and ZnO-PEDOT:PSS nanohybrids that is restricted to the near UV region.
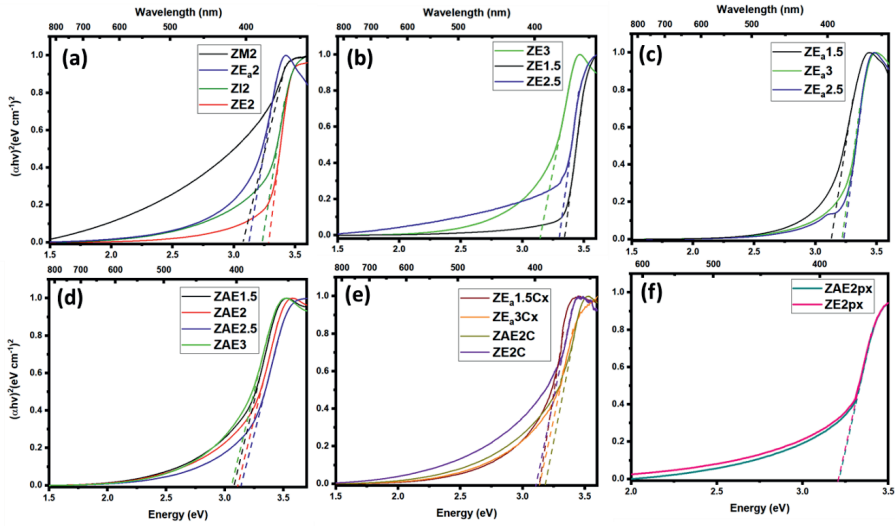
Figure 3.15. Tauc plots of ZnO nanoparticle samples (a) ZM2, ZE2, ZI2, and ZE$_a$2, (b) ZE1.5, ZE2.5 and ZE3, (c) ZE$_a$1.5, ZE$_a$2.5 and ZE$_a$3, (d) ZAE1.5, ZAE2 ZAE2.5 and ZAE3, (e) ZE2C, ZAE2C, ZE$_a$1.5Cx, and ZE$_a$3Cx, (f) ZE2px and ZAE2px, respectively. The dashed lines are the tangents to the Tauc plot and its x-intercept is the band gap.

3.1.7. Photoluminescence emission spectroscopy

PL spectroscopy was carried out on the ZnO nanoparticles and their nanohybrid samples. It revealed the defect states and the optical emission properties of the samples. In order to incite band-to-band transitions in these samples, a 365 nm (3.4 eV) excitation source, which has an energy slightly higher than the band gap of ZnO (~3.3 eV) was chosen. The PL study provided the NBE and DLE that varied as a function of synthesis conditions and defect states. The origin of DLE has been attributed to the combination of several point defects, such as O_i, V_O, V_{Zn}, Zn_i, and their complexes [200]. Whereas, the NBE originates from the recombination of excitons due to band-to-band transitions.

(1) Effect of solvents on the PL emission properties of ZnO nanoparticles

Figure 3.16(a) shows the normalized PL spectra of samples ZM2, ZI2, ZE2 and ZE$_a$2, respectively. The samples synthesized using absolute alcohols tend to show similar PL emission properties due their small size of ~ 5 nm. The DLE of these samples have well-defined peaks owing to

their high surface-to-volume ratio or the presence of higher amounts of surface defects. Nevertheless, they have differences in the overall PL quantum yield. In general, the NBE of all these samples lies between 383 nm and 388 nm, corresponding to band-to-band transitions. On the other hand, sample ZE_a2 shows a negligible DLE compared to the other three samples, due to a smaller specific surface or a lower amount of surface defects. In addition, the NBE-to-DLE ratio of sample ZE_a2 is the highest compared to the other three samples, indicating the best crystalline quality, attributed to the presence of water in the synthesis mixture that provided proper oxidizing conditions during synthesis. In turn, precipitation of larger sizes of nanoparticles of ~50 nm with high crystallinity and lower surface defects is engendered. However, the NBE of sample ZE_a2 is red-shifted to ~392 nm, suggesting the presence of shallow donor states in the sample.

Furthermore, for all these samples, the dominant DLE emission peak is at 2.2 eV is related to the doubly ionized oxygen vacancy or the surface oxygen vacancy V_O^{++}. The second dominant emission peak at ~2.5 eV is attributed to the singly ionized oxygen vacancy or volume oxygen vacancy V_O^+. These two vacancies are responsible for the green luminescence in ZnO. The intensity of the green emission is influenced by chemisorbed species on the surface of the nanoparticles with small sizes of ~5-10 nm, especially when PL measurements are performed in air ambient. The chemisorbed oxygen species induce an upward band bending in the ZnO nanoparticles, which allows V_O^+ to convert into V_O^{++} and subsequently emit at 2.2 eV [98]. Therefore, the observed dominant green emission in all of these samples is mainly surface related with differences arising from different solvents. Besides, for sample ZI2, the intense DLE suggests that the presence of unreacted precursor and isopropoxide groups does not passivate the surface defects of ZnO nanoparticles.

(2) Effect of molar ratios on the PL emission properties of ZnO nanoparticles

Figure 3.16(b) is the normalized PL spectra of ZnO nanoparticle samples ZE1.5, ZE2.5, and ZE3 and figure 3.16(c) is the normalized PL spectra of samples $ZE_a1.5$, $ZE_a2.5$ and ZE_a3, respectively. The NBE-to-DLE ratio tends to increase for samples ZE2.5, followed by ZE1.5 and ZE3. Whereas, the NBE-to-DLE ratio tends to decrease with the increase of NaOH amount for samples synthesized using aqueous ethanol.

In addition, the NBE of samples prepared using aqueous ethanol is redshifted and lies between 393 nm and 397 nm, corresponding to the transitions from Zn shallow donor levels to the valance band. However, unlike samples synthesized using absolute ethanol, the samples prepared using aqueous ethanol show an increase in DLE for the highest amount of NaOH i.e., for ZE_a3. Therefore, in order to further investigate the effect of water and molar ratio, a detailed analysis of DLE of samples $ZE_a1.5$ and ZE_a3 was carried out as shown in the figure 3.17(a). These two samples present the lowest and highest band gaps from Tauc plots, the largest and smallest particle sizes from TEM study, and the least and the most intense DLE. The Gaussian deconvolution of the DLE for ZE_a3 reveals the most significant emission peaks corresponding to green emission component at ~2.2 eV, followed by yellow-orange emission component at ~2.1 eV and red emission component at ~1.95 eV. In general, the surface oxygen vacancy V_O^{++} at ~2.2 eV and the volume oxygen vacancy V_O^{+} at ~2.5 eV are responsible for green emission in ZnO. However, the emission due to volume-related oxygen vacancy (V_O^{+} at ~2.5 eV) is absent in these samples. This implies that the use of aqueous ethanol has ensured an appropriate oxygenation of the ZnO nanoparticles, within their volume that suppresses V_O^{+}. Therefore, V_O^{++} at ~2.2 eV or the surface oxygen vacancy is the major component of the green emission of DLE for samples synthesized using aqueous ethanol, but is nevertheless negligible compared to the intense NBE.

(3) Effect of hydrates in the precursor on the PL emission properties of ZnO nanoparticles

Figure 3.16(d) shows the PL emission spectra of samples ZAE1.5, ZAE2, ZAE2.5 and ZAE3, prepared using anhydrous acetate precursor and absolute ethanol. For a similar zinc precursor to NaOH molar ratio, the PL spectra of these samples show similar emission peak localizations to that of samples prepared using the dihydrate acetate precursor. However, there are differences in the relative intensities of the emission peaks. In general, the DLE of anhydrous acetate-synthesized samples is higher than the dihydrate acetate samples, suggesting a higher amount of surface defects in the former. However, in particular, samples ZAE2 and ZE2 tend to show the highest NBE-to-DLE ratios compared to samples of other solvents, as well as their corresponding different molar ratios. These two samples therefore possess the highest amount of surface defects, which corroborate with TEM and XPS studies.
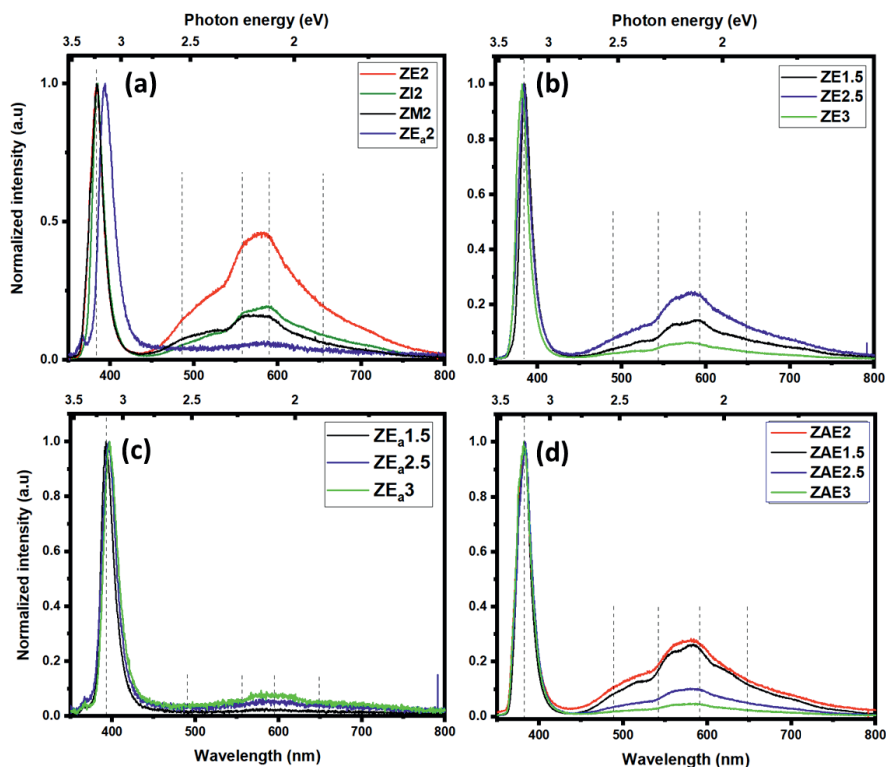
Figure 3.16. Normalized PL spectra of ZnO nanoparticle samples (a) ZE2, ZI2, ZM2 and ZE$_a$2, (b) ZE1.5, ZE2.5 and ZE3, (c) ZE$_a$1.5, ZE$_a$2.5 and ZE$_a$3 and (d) ZAE1.5, ZAE2, ZAE2.5 and ZAE3.

(4) Ex-situ synthesized ZnO-CNT nanohybrids

Figure 3.17(b) shows the PL spectra of samples ZE$_a$1.5Cx and ZE$_a$3Cx. A ~5-fold enhancement in the NBE has been obtained from the nanohybrid samples ZE$_a$1.5Cx and ZE$_a$3Cx, compared to their corresponding nanoparticle samples ZE$_a$1.5 and ZE$_a$3. Furthermore, the NBE-to-DLE ratio increases for nanohybrid samples indicating a reduction or passivation in the surface defects on conjoining with CNT. In addition, compared to their corresponding ZnO nanoparticle samples ZE$_a$1.5 and ZE$_a$3, the NBE of the ZnO-CNT nanohybrid samples is blue-shifted and lies between 383 nm and 387 nm. These transitions correspond to the band-to-band transitions in ZnO. The blue-shift in the NBE further supports the fact that CNT passivate the surface defects, making them optically inactive, due to which the NBE is blueshifted owing to reduction in surface trap states. A comparison of the DLE of ZE$_a$3Cx with its corresponding nanoparticle samples is shown in figure 3.17(a).

The $ZE_a1.5Cx$ did not show any DLE and was not included in the figure 3.17(a). On the other hand, ZE_a3Cx clearly manifests a decrease in all components of DLE compared to sample ZE_a3. In fact, the CNT cover the surface of the nanoparticles and block the adsorption of hydroxyl groups and oxygen molecules responsible for the DLE. Nevertheless, a hint of DLE is visible in sample ZE_a3Cx owing to the higher surface-to-volume ratio of sample ZE_a3. This suggest that a higher quantity of CNT may be required to passivate the surface defects of ZE_a3.

(5) In-situ synthesized ZnO-CNT nanohybrids

Figure 3.17(c) shows the PL spectra of samples ZE2C and ZAE2C, prepared using absolute alcohol via an in-situ approach. For the synthesis of these samples, CNT were functionalized by sonicating them in absolute ethanol, which resulted in hydroxyl and carbonyl functional groups. The PL spectra of these ZnO-CNT nanohybrid samples show similarities in all the emission peak localizations to those of their corresponding ZnO nanoparticles, indicating the origin of emission is mainly from ZnO nanoparticles. However, there are significant changes in the overall quantum yield of certain emission peaks owing to the interfacial bonding between ZnO nanoparticles and CNT via hydroxyl groups. Since the PL measurements on these ZnO-CNT nanohybrid samples were performed in air, the adsorption of moisture and oxygen molecules on ZnO surface is inevitable. Thus, the dominant emission in these ZnO-CNT nanohybrid samples is also the green emission, similar to their corresponding freestanding ZnO nanoparticles. In addition, the functional hydroxyl groups of CNT enhance the upward band bending in these ZnO-CNT nanohybrid samples, which further leads to an increase in the size of depletion region. Therefore, the probability to capture electron at the defect sites is higher for these ZnO-CNT nanohybrid samples compared to their corresponding ZnO nanoparticle samples, resulting in higher DLE from the ZnO-CNT nanohybrid samples. This mechanism also reduces the probability of band-to-band transitions, which results in the reduction of NBE intensities in the samples ZE2C and ZAE2C. The NBE of these ZnO-CNT nanohybrid samples is redshifted compared to ZnO nanoparticles, suggesting an increase in the amount of Zn_i, which corroborates with their Raman spectroscopy results.
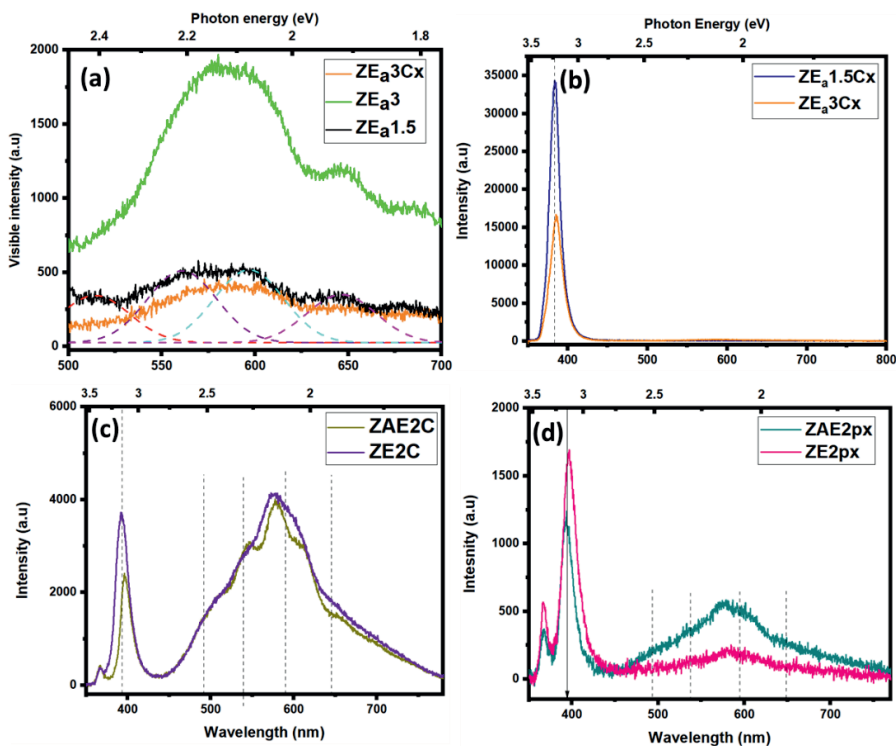
Figure 3.17. Visible PL emission spectra of samples (a) ZE_a3, $ZE_a1.5$ and ZE_a3Cx in the visible emission range only, where dotted lines are deconvolution of the peaks of sample ZE_a3, PL spectra of samples (b) $ZE_a1.5Cx$ and ZE_a3Cx, (c) ZAE2C and ZE2C, and (c) ZAE2px and ZE2px, respectively.

(6) Ex-situ-synthesized ZnO-PEDOT:PSS nanohybrids

Figure 3.17(d) provides the PL emission spectra of samples ZE2px and ZAE2px. These ZnO-PEDOT:PSS nanohybrid samples tend to show similarities in the PL emission peak localizations to their corresponding free-standing nanoparticle samples i.e., ZE2 and ZAE2, respectively. This indicates that the origin of emission from ZnO-PEDOT:PSS nanohybrid samples is again from free-standing ZnO nanoparticles. In fact, the ZnO-PEDOT:PSS nanohybrid samples were synthesized ex-situ, where 95 wt% PEDOT:PSS and 5 wt% ZnO nanoparticles were used. In addition, the complete coverage of PEDOT:PSS as seen from the TEM image of figure 3.7(a-d) hinders the adsorption of species from the ambient. Therefore, the NBE-to-DLE ratio is higher in the ZnO-PEDOT:PSS nanohybrid samples compared to their corresponding nanoparticle samples. An increase in DLE for sample ZAE2px can be attributed to the higher amount of hydroxyl groups or surface defects

present on the free-standing ZAE2 nanoparticles, as assessed by XPS studies. Additionally, the NBE of the ZnO-PEDOT:PSS nanohybrid samples is redshifted, suggesting an increased amount of Zn_i, further corroborating the Raman spectroscopy results.

3.2. ZnO nanorods

Four ZnO nanorod samples, ZNR-M, ZNR-E, ZNR-I and ZNR-E$_a$ were grown on etched ITO substrates. The seeding solvents were varied i.e., absolute methanol, absolute ethanol, absolute isopropanol and aqueous ethanol. The use of different alcoholic solvents in the nanorod seed layer or creation of ZnO nucleation sites produces similar defects in the nucleation layer, as in the ZnO nanoparticles that would then have an influence on the type and quality of defects in the ZnO nanorods. The ZnO nanorod morphology and defect states would in turn be modified by the presence of these defects that affect the opto-electrical properties of the ZnO nanorods. The as-grown ZnO nanorods were characterized morphologically, optically and electrically. Furthermore, these ZnO nanorod samples were examined for suitability in photo response, persistent photoconductivity and UV sensing applications.

3.2.1. Crystalline structure

The XRD analyses were performed on the ZnO nanorod samples in order to obtain insights on their crystallinity on nanorod growth direction. Since samples were grown on etched ITO substrates, the XRD patterns of the ITO substrate were also collected simultaneously by default and used as a reference as shown in figure 3.18. The presence of typical ZnO diffraction peaks (100), (002) and (001) in the XRD patterns of these samples confirms the hexagonal wurtzite structure of the ZnO nanorods (JCPDS, Card Number 36-1451). In addition, the sharp peak at ~34.5^0, which is an out-of-plane reflection, suggests that nanorods were grown along c-axis [201]. In addition, the XRD peaks (222) and (400) corresponding to the ITO coated on glass marked (*) are visible.
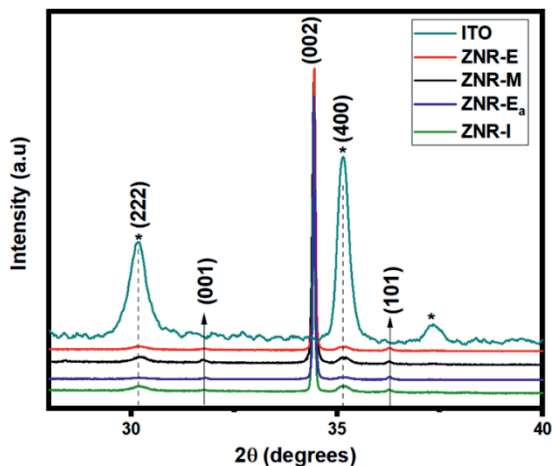
Figure 3.18. XRD spectra of ITO substrate and samples ZNR-E, ZNR-M, ZNR-E$_a$ and ZNR-I. The (*) marked peaks are the XRD characteristics peaks of ITO (III).

3.2.2. Morphology

SEM study was performed on the ZnO nanorod samples to study their morphology and the uniformity of the nanorod layer on the substrates. The low magnification SEM images of figures 3.19(a-d) provide information on the uniformity of nanorod growth, while the higher magnification SEM images of figure 3.19(e-f) provide information on their morphology and diameters. The diameters of the ZnO nanorods calculated from the size distribution histograms of their SEM images are listed in table 3.3.

(1) Effect of absolute alcohol seeding solvents on the growth of ZnO nanorods

Samples prepared using absolute alcohol i.e., ZNR-M, ZNR-E and ZNR-I show differences in the nanorod surface coverage of the substrate, as observed in the top-view low-magnification SEM images in figure 3.19(a-d). In figure 3.19(a), sample ZNR-M tends to exhibit the best surface uniformity of nanorods. Whereas, for samples ZNR-E and ZNR-I, areas without nanorods are clearly visible, observed in figure 3.19(b-c). On the other hand, higher magnification SEM images of figures 3.19(e-g) show the nanorod morphology and provide information on the morphological homogeneity of nanorods. The nanorods of ZNR-M and ZNR-E present homogenous morphology, observed in figure 3.19(e-f).

Whereas, ZNR-I has a non-homogeneous growth of nanorods compared to ZNR-M and ZNR-I, as observed in figure 3.19(g). The diameters of ZnO nanorod samples were obtained through size distribution histograms and are listed in table 3.3. The three nanorod samples prepared using absolute alcohols present similar diameters of ~80 nm - 90 nm.

In addition, HMTA used during the synthesis of nanorods, reduces the growth in the radial direction and favors the growth in the direction of the polar c-plane [72]. However, the nucleation layer defines the size of the nuclei, which in turn depends on the solvent used. As previously observed with ZnO nanoparticles, absolute alcohol solvents produce small nanoparticles. In fact, HMTA acts as a surfactant and covers the side walls or non-polar surfaces with OH groups, leading to reduction in the radial growth of nanorods [202]. Studies show that HMTA is a pH buffer that ensures a continuous vertical growth of ZnO nanorods by regulating the release of hydroxyl ions. Moreover, the concentration of HMTA in the reaction mixture modifies the nucleation process by interacting with the seed layer, thus increasing the density of nanorods [203].

(2) Effect of aqueous alcohol seeding solvent on the growth of ZnO nanorods

Unlike other ZnO nanorod samples, the sample ZNR-E_a exhibits the least uniformity in terms of surface coverage and consists of several voids, as observed from its low magnification SEM image in figure 3.19(d). In addition, due to the presence of 30% water in the seeding solvent, sample ZNR-E_a also exhibits the largest diameter of ~110 nm among all samples, observed in its high magnification SEM image in figure 3.19(h). Therefore, the presence of water in the seeding solvent has produced nanorods with the largest diameter and the lowest uniformity compared to nanorods grown with an absolute alcohol seeding solvent.
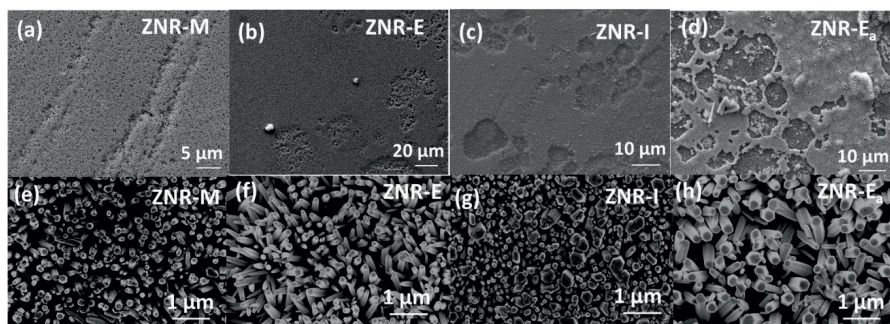
Figure 3.19. Low magnification SEM images of samples (a) ZNR-M, (b) ZNR-E, (c) ZNR-I and (d) ZNR-E$_a$, showing the surface coverage. Higher magnification SEM images of samples (e) ZNR-M, (f) ZNR-E, (g) ZNR-I and (h) ZNR-E$_a$ (III).

Table 3.3. List of nanorods diameter obtained from SEM.

Sample	Diameter (nm) from SEM
ZNR-M	85 ± 20.3 nm
ZNR-I	80 ± 14.6 nm
ZNR-E	90 ± 30.5 nm
ZNR-E$_a$	110 ± 33.3 nm

3.2.3. Optical properties

(a) UV-Vis spectroscopy and band gaps of ZnO nanorods

The band gaps of the ZnO nanorod samples are calculated through UV-Vis absorption spectroscopy followed by Tauc plots presented in figure 3.20(a). The band gaps of these samples lie between ~3.1 eV to 3.2 eV, which is within the theoretical band gap range of ZnO. Similar to ZnO nanoparticles, the absorption spectra of all ZnO nanorods revealed a sharp shoulder at ~3.3 eV stretching down to 2 eV, without any shoulders related to defect level absorption.
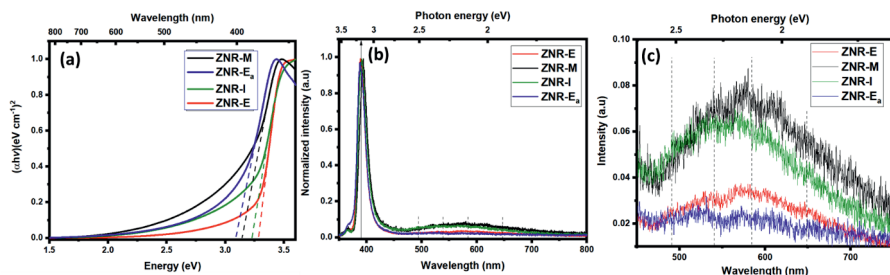
Figure 3.20. (a) Tauc plot, (b) normalized PL spectra and (c) magnified view of the visible PL emission spectra of all ZnO nanorod samples (III). The dashed lines in (a) are the tangent to the Tauc plots curve, showing the band gaps at the x-intercept.

(b) PL emission spectroscopy of ZnO nanorods

The PL spectra of ZnO-nanorod samples are shown in figure 3.20(b). Similar to ZnO-nanoparticle samples, the PL spectra of ZnO-nanorod samples consist of the typical NBE and DLE of ZnO. The PL spectra show negligible DLE due to their high aspect ratio or low specific surface. For ZnO nanorods, the PL spectra are normalized in order to emphasize on the low DLE and secondly, because the surface of all ZnO nanorod layers have a roughness as seen from their SEM images. These samples show a high NBE-to-DLE ratio and therefore, harbor lower intrinsic defects. The NBE of these samples are between 388 nm and 393 nm, corresponding to the transitions from Zn shallow donor levels or from conduction band to the valance band.

Figure 3.20(b) shows a hint of DLE for samples ZNR-M and ZNR-I, suggesting slightly higher number of surface defects in these samples compared to the others. The figure 3.20(c) emphasizes on only the DLE emission peak, indicating that sample ZNR-M shows the highest DLE, followed by sample ZNR-I, and ZNR-E. The ZnO nanorod samples were prepared in oxygen-rich conditions, i.e., water was used during their synthesis, resulting in larger nanorod diameters due to larger nuclei in the seed layer. The dominant emission peak in the ZnO nanorod samples is the green emission corresponding to the presence of V_O. In particular, the surface oxygen vacancy V_O^{++} at ~2.2 eV is the major green emission component in these samples. Whereas, the other green component at ~2.5 eV related to the volume oxygen vacancy V_O^+ is absent in the ZnO nanorod samples, shown in figure 3.20(c). The other emission components in the DLE of ZnO nanorods are yellow-orange at ~2.1 eV and red at ~1.95 eV. The yellow-orange emission at ~2.1 eV is

due to the transitions from Zn_i to O_i [204]. Whereas, the red emission at ~1.95 eV is attributed to the transitions related to Zn_i, usually observed in oxygen rich conditions [204]. However, these defect emissions are negligible in the ZnO nanorods.

3.2.4. Electrical properties studied by I-V and I-t measuremesnts

(a) I-V characteristics of ZnO nanorods on etched ITO substrates

Electrical properties of the four ZnO nanorod samples were studied using room temperature current-voltage (I-V) and current-time (I-t) measurements in dark and under UV illumination with Ag contacts on ITO, which is shown in figure 2.3(h) of chapter 2. The goal of the measurements was to study the effect of UV light on the current and photoresponse of the ZnO nanorod samples. Figure 3.21(a) shows the I-V characteristics of four ZnO nanorod samples in dark and under UV light in the range from -3 V to +3 V. From these measurements, ohmic I-V characteristics with differences in their output currents are obtained.

(1) Effect of absolute alcohol seeding solvent on I-V characteristics of ZnO nanorods on etched ITO substrates

In dark conditions, the magnitude of the overall output current for samples prepared using absolute alcohols decreases in descending order for ZNR-M, ZNR-E and ZNR-I, indicated by dashed lines in figure 3.21(a). In general, factors such as uniformity of the nanorods and defects affect the conductivity of ZnO nanorods. From SEM images, sample ZNR-M shows the highest uniformity, followed by sample ZNR-E and ZNR-I, which explains highest output currents from sample ZNR-M.

(2) Effect of aqueous alcohol seeding solvent on I-V characteristics of ZnO nanorods on etched ITO substrates

For sample ZNR-E$_a$, the presence of water results in the growth of nanorods of larger diameters with low surface coverage. In addition, the surface of sample ZNR-E$_a$ consists of the highest number of voids compared to samples grown using absolute alcohol seeding solvent. Therefore, in dark conditions, sample ZNR-E$_a$ produces the lowest output current due, as observed by the dashed line in figure 3.21(a). In addition, figure 3.21(a) also shows I-V characteristics of all ZnO nanorod

samples under UV light. Under UV light, an increase in the magnitude of the output current for all samples compared to dark conditions, is observed. However, the overall increase in output current is the lowest for sample ZNR-E$_a$ compared to other samples under UV radiation.
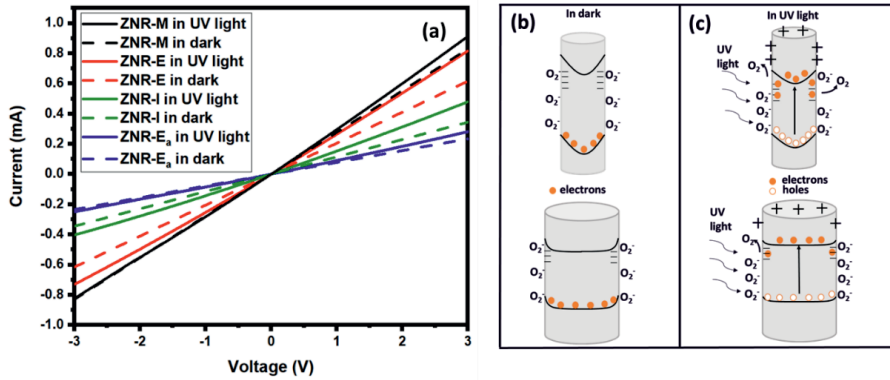
Figure 3.21. (a) I-V characteristics of all ZnO nanorod samples measured in dark (dashed lines) and under UV light (solid lines) from -3 V to +3 V. Schematic of the band bending and oxygen ion adsorption-desorption mechanism of smaller and larger nanorods in (b) dark and (c) UV irradiation (III).

(b) I-t measurements of the photoresponse characteristics of ZnO nanorods on etched ITO substrates under UV irradiations

To evaluate the UV photoresponse of the four ZnO nanorod samples, several on-off cycles were performed under UV radiation and the I-t characteristics are shown in figure 3.22(a). The UV light was turned on and off five times at intervals of 10s and 350 s each, with possible errors of 1 s due to manual operation. In general, for all samples, the current increases by 15-25 % for all cycles during the on-cycle. The increase in current under UV radiation is attributed to the generation of holes in the valance band on excitation and transfer of electrons to the conduction band. This in turn, reduces the overall band bending and thus, the depletion region width reduces under UV radiation, as shown in figure 3.21(c). Nevertheless, due to the remnant upward band bending of ZnO, some holes are still accumulated on the surface [205]. Simultaneously, some of the electrons are trapped at the surface of nanorods, while others travel to the volume of the nanorods and contribute to their conductivity. The surface accumulated holes subsequently combine with the adsorbed oxygen radicals that then desorb from the ZnO nanorod surface in the form of oxygen molecules leaving behind a free electron, which in turn,

contributes to the increase of the conductivity of ZnO nanorods [206]. After every UV on-cycle, the samples were maintained in dark for 50 s, where a decrease in current was observed in figure 3.22(a), attributed to the increase in band bending of the ZnO nanorods, as shown in figure 3.21(b). Ideally, during the off-cycle, the current should drop to its dark current [207]. However, the dark current recovery depends on the rate at which photo-excited carriers recombine, which in turn, depends on the size of the depletion region. In fact, larger the depletion region, slower is the recombination, leading to a slow decay of the current that persists even in dark [208]. The remnant dark current is known as persistent photo conductivity (PPC) of ZnO nanorods [208], observed for the ZnO nanorod samples during the off-cycles (50 s).

(1) Effect of absolute alcohol seeding solvent on the persistent photoconductivity of ZnO nanorods on etched ITO substrates

The samples ZNR-M, ZNR-E and ZNR-I, prepared using absolute alcohols exhibit similar PPC behaviors, which has been attributed to their similar diameters. In addition, these three samples exhibit higher amounts of surface defects as observed from their DLE in figure 3.20(c). Therefore, the decay of current is slower in these samples, which in turn gives a higher PPC.

(2) Effect of aqueous alcohol seeding solvent on the persistent photoconductivity of ZnO nanorods on etched ITO substrates

On the other hand, for sample ZNR-E$_a$, the current decay is quicker during the UV off-cycle compared to the other samples, which can be attributed to its lower number of surface defects. In fact, the relatively limited depletion region, owing to the larger diameters of nanorods, reduces the number of surface defects.
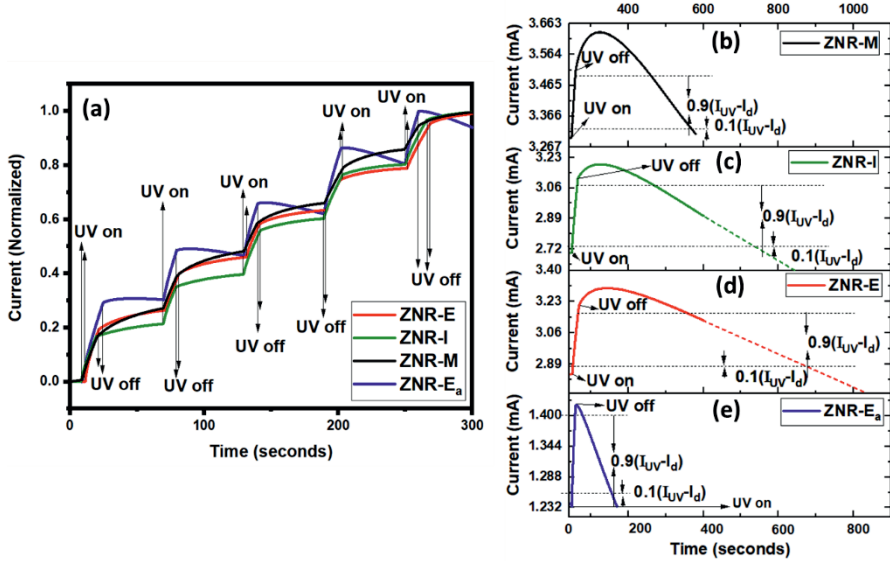
Figure 3.22. (a) I-t characteristics of all ZnO nanorod samples under UV on-off cycles with total measurement for 300 s at a constant bias of 3 V. Single on-off cycle of samples (b) ZNR-M, (c) ZNR-I, (d) ZNR-E and (e) ZNR-E$_a$ at a constant bias of 3 V. The dashed lines in the figures (c) and (d) are the extrapolations of the current decay to the X-intercept (III).

(c) Photoresponse parameters of ZnO nanorods on etched ITO substrates

The UV photoresponse properties of all ZnO nanorod samples were assessed by calculating their responsivity, sensitivity and response time [179], as shown in figure 3.22(b-e). All these figures of merit are defined in chapter 1. To that end, the ZnO nanorods were irradiated with UV light at different intervals ($T_{UV-light}$) as listed in table 3.4. After UV irradiation, the UV off cycle was maintained for 350 s. The sensitivities of the ZnO nanorods are similar, ranging from ~1.1 to 1.5, as listed in table 3.4. These values suggest that regardless of differences in I_{dark} and total UV radiation time ($T_{UV-light}$), the increase of photocurrent with respect to the dark current is approximately the same for all the samples. In addition, for samples ZNR-M and ZNR-E$_a$, the current returned to the dark current value during the UV off-interval of 50 s. However, samples ZNR-E and ZNR-I did not reach their dark current value within the UV off-interval. Therefore, the necessary time to reach dark current during the UV off-cycle was estimated by extrapolation as shown by dotted lines in figure 3.22(c-d). The other two parameters i.e.,

responsivity and response time exhibit a high dependence on the seeding solvent, discussed in the following section.

(1) Effect of absolute alcohol seeding solvent on the current rise and decay times of ZnO nanorods on etched ITO substrates

Among the ZnO nanorod samples synthesized using absolute alcohols, the highest responsivity was calculated for sample ZNR-I, followed by samples ZNR-E, and ZNR-M. In addition, the response times was calculated with two parameters including, rise time (T_{rise}) and decay time (T_{decay}). In general, T_{rise} is directly dependent on the $T_{UV\text{-}light}$ as listed in table 3.4. Whereas, T_{decay} is the intrinsic property of the ZnO nanorod samples which depends on their surface defects, oxygen adsorption and band bending. In addition, T_{decay} provided information on the figures of merit for photoresponse or UV sensor applicability.

In figure 3.22(b-d), after switching off the UV radiation, two phenomena occur. The first phenomenon is related to charge de-trapping, due to which samples ZNR-M, ZNR-E and ZNR-I show a rapid increase in current rather than an immediate decay, after switching off the UV radiation. The second phenomenon is related to PPC and is observed in all samples. Due to this phenomenon, T_{decay} takes over 100 s to descend to the dark current values. For samples ZNR-E and ZNR-I, the T_{decay} was estimated to be ~320 s and ~265 s, respectively, by extrapolation. This suggests that PPC is the most dominant in these two samples. On the other hand, T_{decay} of ~110 s was calculated for sample ZNR-M and no extrapolation was needed as the sample decayed to its dark current within the UV-off time.

(2) Effect of aqueous alcohol seeding solvent on the current rise and decay time of ZnO nanorod sample on etched ITO substrates

Figure 3.22(e) shows the photoresponse of sample ZNR-E$_a$, which was grown using aqueous ethanol. Unlike ZnO nanorod samples prepared using absolute alcohols, only the PPC phenomenon and not the charge de-trapping phenomenon was observed in sample ZNR-E$_a$. As a result, the fastest T_{decay} of ~80 s was calculated for sample ZNR-E$_a$ with an immediate decay after switching off the UV radiation. Since sample ZNR-E$_a$ shows an immediate decay in current after switching off the UV

radiation with the fastest T_{decay} of ~80 s, it has potential as a UV sensor with low heating effects owing to low charge trapping.

Table 3.4. List of photoresponse parameters of ZnO nanorods samples.

Sample	S	R (mA/w)	T_{rise} (s)	I_{rise} (µA/s)	T_{decay} (s)	I_{decay} (µA/s)	$T_{UV-light}$ (s)
ZNR-M	1.067	116.8	8.4	20.5	107.5	1.6	10.9
ZNR-I	1.153	220.2	13.3	25.3	264.4	1.29	14.8
ZNR-E	1.129	193.7	14.2	20.2	318.1	0.92	17.3
ZNR-E$_a$	1.145	95.5	7.9	18	77.8	1.84	11.6

3.3. Photodiodes

The third and final part of this thesis consists of the fabrication of a hybrid p-n junction photodiode. To that end, the four nanorod samples grown with different seed-layer solvents described in the previous section, were combined with polymers in order to fabricate hybrid photodiodes. Even though the bare nanorods exhibit photoresponse under UV light, their figures of merit are rather low. Therefore, in order to improve their figures of merit, diode configurations are required, as they allow better control of the I-V characteristics. Hence, four hybrid p-n heterojunction devices with configurations of ITO/ZnO NR (n-type)/F8BT (p-type)/ PEDOT:PSS (p-type)/Ag(electrodes) were fabricated (VI). These devices are labelled as PD-M, PD-E, PD-I and PD-E$_a$, as described in chapter 3.

3.3.1. Morphology

Figure 3.23(a-d) are the cross-sectional SEM images of the four photodiodes with individual layers visible in figure 3.23(a). The ZnO nanorod layer has a thickness of ~1 µm and the combined F8BT and PEDOT:PSS polymer layer has a thickness of ~135 nm. The bottom-most layer of ~110 nm observed in SEM images, is the ITO layer coated glass substrate. For PD-M, PD-E and PD-E$_a$, the nanorods tend to grow vertically on the ITO layer in figures 3.23(a), 3.23(b) and 3.23(d), respectively. Whereas, nanorods of PD-I display random orientations, along with some vertical growth in figure 3.23(c). For the other samples, the polymer layers were detached from the nanorod layers during SEM sample preparation and are therefore not visible.
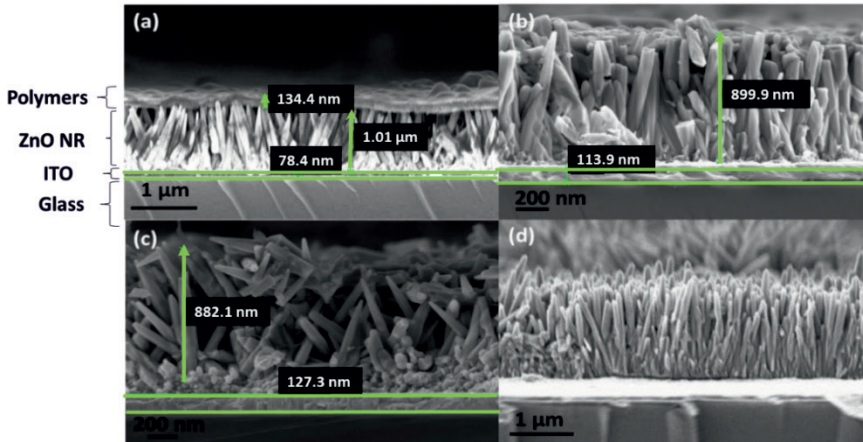
Figure 3.23. Cross sectional SEM images of device (a) PD-M, (b) PD-E, (c) PD-I and (d) PD-E$_a$ (VI).

3.3.2. I-V characteristics in dark

Figure 3.24(a) shows the I-V characteristics of the four photodiodes in dark and under UV light from -3 V to +3 V. The I-V curves of the photodiodes exhibit diode rectification features, with a forward turn-on voltage in the range of 0.2 V to 0.8 V. Rectification ratios i.e., $I_{forward}/I_{reverse}$ were calculated for all the photodiodes at ±3 V, where $I_{forward}$ is the current during forward bias i.e., at positive voltages and $I_{reverse}$ is the current during reverse bias or at negative voltages. A higher rectification ratio allows a more precise control of the diode current. The highest rectification ratio of 640 was calculated for PD-M, followed by almost similar rectification ratios of 80 and 78 for PD-E and PD-I, respectively. Finally, the lowest rectification ratio of 44 was calculated for PD-E$_a$. The semi-log plots of the I-V curves i.e., log(I)-V plots are provided in figure 3.24(b). In particular, PD-M possesses the lowest $I_{reverse}$ of ~1 nA and PD-E$_a$ possesses the highest $I_{reverse}$ of ~10 μA. These differences in the reverse or leakage currents in dark conditions are attributed to the uniformity of the ZnO-nanorod surface coverage. In the top-view SEM images of ZnO nanorods shown in figure 3.19(a-d), the highest to lowest nanorod surface coverage was ZNR-M, ZNR-E, ZNR-I and ZNR-E$_a$. Therefore, a more uniform surface coverage of the ZnO nanorods produces a lower leakage current in dark conditions. In addition, the $I_{reverse}$ current in dark increases with increasing reverse bias. This can be attributed to the passivation of the interfacial defects at the p-n heterojunction at reverse bias [209]. From the PL study in section 3.2.3., bare ZnO nanorods harbor some amount

of surface defects that were responsible for their PPC. These defects also affect the rectification ratios of the diodes.

3.3.3. Ideality factor calculations

The ideality factor (η) of ~1.8, ~2.0, ~2.4 and ~3.2 were calculated for PD-I, PD-M, PD-E and PD-E$_a$, respectively, by using Cheung's method[181] as described in section 1.6.4 of chapter 1. Theoretically, in a non-ideal diode, when the current flows in the p-n heterojunction, the charges are trapped at the defects in the initial stages. The trapped charges can recombine producing η= 2, characteristic of recombination currents. Subsequently, the diffusion current increases rapidly, once all the defects are filled with charges. At this stage, recombination is no longer the dominant process and η=1. For an intermediate current range, where both the charge diffusion and recombination contribute, $1 \leq \eta \leq 2$ [210]. Therefore, the ideality factors of ~2.0 and ~1.8 for PD-M and PD-I, respectively, indicate that the current generation mechanism in these two devices, is firstly dominated by recombination of the carriers followed by their diffusion. On the other hand, a high ideality factor of η>2 is generally attributed to non-linear shunts due to which, the charge recombination current flows inhomogenously in the device [211]. Moreover, ZNR-E$_a$ has the most non-uniform surface with several voids; therefore, the local non-liner shunts are most plausible in PD-E$_a$, leading to a high ideality factor of ~3.2.

3.3.4. I-V characteristics under UV irradiations

Under UV radiation, The I-V characteristics in figure 3.24(a) indicate a significant enhancement in the photocurrent, attributed to the depletion region formed at the interface of n-type ZnO nanorods and p-type F8BT/PEDOT:PSS. Within the depletion region, the built-in electric field is directed from ZnO nanorods to F8BT/PEDOT:PSS and provides a driving force for the separation of e-h pairs under UV radiation. The excitons are then collected by the external load, resulting in the enhancement of the total output current compared to dark conditions [212]. Such an enhancement is more prominent in reverse bias because the depletion region width increases with the applied negative voltage, whereupon increasing the excitonic cross-section. In figure 3.24(b), PD-M and PD-I tend to produce an output current enhancement of 3 orders of magnitude under UV irradiation. Whereas, PD-E and PD-E$_a$

exhibit one order of magnitude increase in the output current under UV irradiation. For PD-M and PD-I, their corresponding bare ZnO nanorods ZNR-M and ZNR-I exhibit higher number of surface defects than bare nanorods of PD-E and PD-E$_a$ i.e., ZNR-E and ZNR-E$_a$. In fact, oxygen vacancies trap photogenerated electrons; therefore, the increase in the number of oxygen vacancies leads to the improvement in the excitonic separation [213,214]. Therefore, a higher number of surface defects in PD-M and PD-I tend to promote excitonic separation, leading to higher photocurrents. However, there is a decay in the reverse photocurrent for voltages lower than -1 V for PD-M and -2 V for device PD-I in figure 3.24(b). This suggests that below a certain negative voltage, the defects at the interface of these two samples become inactive under UV radiation. On the other hand, the depletion region width decreases under forward bias and therefore, the effect of UV radiation is almost similar for devices PD-M, PD-I and PD-E. Nevertheless, due to the presence of oxygen vacancies on their surfaces, a small depletion layer will still persist, leading to the trapping of excitons and subsequently, to the lowering the output current. However, device PD-E$_a$ tends to show the highest increase in the photocurrent, under forward biasing, likely due to the negligible number of defects they harbor. Therefore, this study demonstrates that for defective ZnO nanorod hybrid diodes, a reverse bias is required to compensate for the positively charged surface oxygen vacancies in order to produce higher photocurrents.
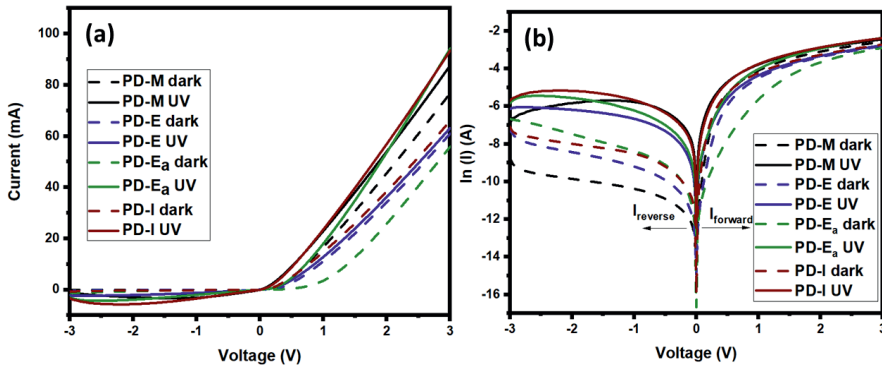

Figure 3.24. (a) I-V and (b) log(I)-V characteristics of p-n heterojunction photodiodes PD-M, PD-E, PD-I and PD-E$_a$ (VI).

3.3.5. I-t characteristics: UV on/off cycles

Figure 3.25(a-p) are the I-t characteristics of the devices PD-M, PD-E, PD-I and PD-E$_a$, respectively demonstrating the photoresponse behavior of the devices under different reverse biases of -0.1 V, -0.5 V, -1 V and -2 V. Photoresponses of the devices were examined under a series of UV-on/off cycles. The UV-on cycle interval was fixed at 10 s, while the UV-off cycle was fixed at 140 s, with plausible error of 1 s due to manual operation.

In general, the magnitude of the photocurrent increases with increasing reverse bias, owing to the increase in the width of the depletion region. The stability of the photoresponses was evaluated in the on and off cycles. Firstly, PD-E tends to show the most stable photoresponse at all four reverse biases, in figures 3.25(b), 3.25(f), 3.25(j) and 3.25(n). Similar tendencies are observed for device PD-E$_a$ for reverse biases of -2 V, -1 V and -0.5 V, in figures 3.25(d), 3.25(h) and 3.25(i), respectively. However, there are some instabilities in the photoresponse at reverse bias of -0.1 V, as shown in figure 3.25(p). In addition, the photocurrents at reverse biases of -0.1 V, -0.5 V and -1 V are relatively higher for device PD-E$_a$ than PD-E, owing to slight differences in the surface defects of bare ZnO nanorods ZNR-E$_a$ and ZNR-E of the two photodiodes. Whereas, at a reverse bias of -2 V, both devices show similar maximum photocurrents, indicating that a reverse bias of -2 V is able to compensate for the defects in these two photodiodes. On the other hand, PD-M shows instabilities in photoresponse at -0.5 V and -0.1 V as shown in figures 3.25(i) and 3.25(m), respectively. However, at biases of -2 V and -1 V of figures 3.25(a) and 3.25(e), the photocurrents are stable. Whereas, photoresponse of PD-I is unstable for all biases in figures 3.25(g), 3.25(k) and 3.25(o), except at -2 V reverse bias in figure 3.25(c). The overall photocurrent of PD-M is higher than PD-I and is also the highest among all the devices. In addition, an increase in the maximum photocurrent with number of UV-on/off cycles, has been observed for PD-I at -1 V, -0.5 V and -0.1 V, as shown in figures 3.25(g), 3.25(k) and 3.25(o), respectively. A similar behavior is also shown by PD-M at a reverse bias of -0.5 V, in figure 3.25(i). In fact, the bare ZnO nanorods of device PD-I exhibit high surface defects suggesting a high probability of charge trapping in ZnO nanorods of PD-I. Furthermore, these nanorods are randomly orientated, instead of the ideal vertical orientation, whereupon generating a defective p-n interface of ZnO nanorods and

polymers. Moreover, charge transfer processes are deteriorated due to incomplete interfacial contact. Therefore, the increase in onset currents at every on-cycle for reverse biases of -0.1 V, -0.5 V and -1 V, suggests that the trapped charges contribute to the photocurrent, along with excitons and that these voltages are therefore not sufficient to compensate for the defect states. However, at a reverse bias of -2 V, a stable maximum photocurrent during the four UV on-off cycles is obtained, implying -2 V is an optimum working bias for PD-I. On the other hand, at a reverse bias of -0.1 V, the PD-M tends to show a drop in photocurrent as the UV-on/off cycles progress, as shown in figure 3.25(m). A similar drop in current is also observed for PD-E$_a$ at reverse bias of -0.1 V, as shown in figure 3.25(p) and is attributed to the trapping of photo generated carriers in the ZnO nanorod defect states.
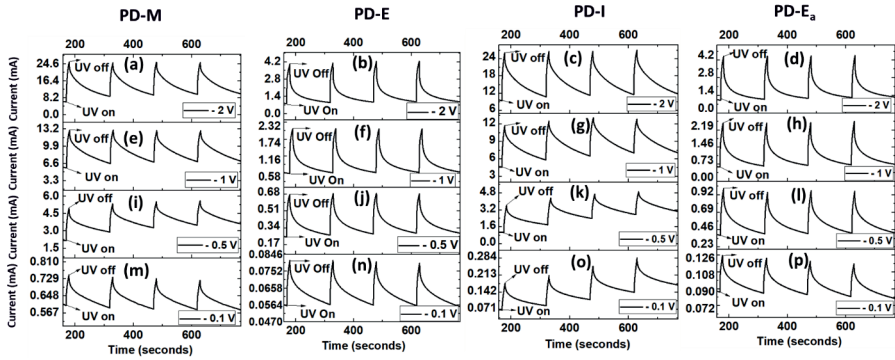
Figure 3.25. Photoresponse under several UV on-off cycles of devices (a) PD-M, (b) PD-E, (c) PD-I and (d) PD-E$_a$ at reverse bias of -0.1 V, -0.5 V, -1 V and -2 V (VI).

3.3.6. Figures of merit

The figures of merit of the photodiodes were evaluated in terms of their sensitivity (S), responsivity (R), and external quantum efficiencies (EQE), response time T_{rise} and T_{decay}, defined in chapter 2. Table 3.5 lists the parameters calculated for all the devices.

The responsivity and external quantum efficiency of the devices increase with reverse bias, as listed in table 3.5. However, compared to bare ZnO nanorods, the responsivity of the photodiodes is higher by three orders of magnitude. Figure 3.25 is also the basis of comparison for the responsivity and EQE of the four photodiodes at the four voltages. In fact, the performances of PD-M and PD-I are almost similar at the same

reverse bias. For instance, EQE of PD-M and PD-I at a reverse bias of -2 V is ~2760%. Similarly, devices PD-E and PD-E$_a$ show similar performances with similar EQE of ~600% at the same reverse bias of -2 V. Therefore, EQE is much higher for devices PD-M and PD-I than PD-E and PD-E$_a$, listed in table 3.5. In addition, PD-M and PD-I possess better ideality factors of ~2.0 and ~1.8, respectively. They demonstrate a higher increase in $I_{reverse}$ under UV irradiations as obtained from their *log(I)-V* characteristics in figure 3.24(b), along with higher photocurrents. These parameters contribute to their higher responsivity and EQE in comparison to the other two devices.

Another important figure of merit of a photodiode is its response time i.e., T_{rise} and T_{decay}. In fact, T_{rise} is directly dependent on the total UV irradiation time, which was fixed to 10 s. Therefore, the photodiodes show almost similar T_{rise} for a particular voltage. T_{rise} decreases from ~7.7 s at -0.1 V to 6.2 s at -2 V for the four photodiodes. On the other hand, T_{decay} is the intrinsic property of the device and depends on various parameters, such as defects at the p-n interface, probability of recombination of excitons, charge trapping in the defects of bare ZnO nanorods and width of the depletion region. Also, higher the applied voltage, quicker is the T_{decay}. Devices PD-E and PD-E$_a$ display a quick decay with T_{decay} of ~90 s at -0.1 V and of ~60 s at -2.0 V, compared to the slower decay of T_{decay} of PD-I of ~225 s at -0.1 V and of 108 s at -2.0 V. On the other hand, device PD-M shows T_{decay} of ~100 s to 125 s, at different voltages. However, when selecting the best photodiode, a compromise between the different figures of merit is required. In that regard, PD-M appears to have a better ZnO nanorod surface coverage and the highest rectification ratio. It also exhibits relatively stable on/off-cycles, an ideality factor of 2, good sensitivity, responsivity and EQE. Therefore, PD-M appears to be the most suitable candidate for photodiode applications among the four photodiodes.

Table 3.5. List of figures of merit, including S, R (A/W), T_{rise} (s), T_{decay} (s), and EQE (%) of photodiodes PD-M, PD-E, PD-I and PD-E$_a$ (VI).

	Voltage (V)	S	R (A/W)	T_{rise} (s)	T_{decay} (s)	EQE (%)
PD-M						
	0.1	1.24	0.08	7.7	97.1	25.2
	0.5	1.6	1.2	7.3	125.4	379.8
	1	1.9	3.15	6.6	111.8	1071.8
	2	2.5	8.14	6.6	108.3	2764.4
PD-E						
	0.1	1.4	0.01	7.6	90.2	4.2
	0.5	2.4	2.1	6.8	84.2	71.5
	1	3.5	0.8	6.2	70.6	268
	2	4.4	1.7	6.4	62.6	590
PD-I						
	0.1	2	0.08	7.5	225.1	25.8
	0.5	1.8	1.15	7.5	147.7	391.5
	1	1.83	3.11	7.2	109.8	1054.8
	2	2.3	8.16	7.6	108.5	2773.2
PD-E$_a$						
	0.1	1.4	0.02	7.6	81	6.3
	0.5	2.3	0.3	6.7	90	99.4
	1	3.6	1	7.0	80.7	335.1

4. DISCUSSION

In this thesis, a systematic study of the synthesis and characterization of ZnO nanostructures has been performed. The goal of this work was the polymer encapsulation of ZnO nanostructures for the fabrication of hybrid UV photodiodes. On their own, bare ZnO nanostructures, such as 1D ZnO nanorods, nanowires etc., are capable of detecting UV radiations due to their wide band gap of 3.37 eV and high excitonic energy of 60 meV. However, combining n-type ZnO nanostructures with other p-type materials provides additional advantages. In effect, the p-n junction between such materials leads to higher photogeneration of e-h pairs and external bias controllable I-V characteristics. Herein, we focused on the growth of 1D ZnO nanorods by varying the seeding solvents of the ZnO-nanorod seed layers. The four alcohol seeding solvents, i.e., absolute methanol, absolute ethanol, absolute isopropanol and aqueous ethanol had a clear influence on the physical and opto-electrical properties of the ZnO nanorods. Subsequently, four hybrid photodiodes with configurations of ITO/ZnO NR/F8BT/PEDOT:PSS/ Ag were successfully fabricated by spin coating p-type polymers F8BT and PEDOT:PSS on the hydrothermally grown n-type ZnO nanorods.

We highlighted that the solvents played a crucial role on the surface-defect generation, ZnO nanorod lengths and diameters, as well as ZnO-nanorod surface coverages. In general, the bare ZnO nanorods with absolute alcohol seeding solvents exhibit diameters of less than 100 nm and display a more uniform surface coverage. Whereas, the ZnO nanorods grown with aqueous alcohol seed layers exhibit larger diameter ~110 nm and the lowest surface coverage with several voids visible in the SEM images. In addition, the PL studies on bare ZnO nanorods showed differences in surface defects, depending on the alcohol of the seed layer. The most visible components of surface defects in these nanorods correspond to the surface oxygen vacancies V_O^{++} at ~2.2 eV. Whereas, the component related to volume oxygen vacancies V_O^{+} at ~2.5 eV was not visible in the photoluminescence emission studies of the nanorods, owing to the high oxygen content during sol-gel and hydrothermal syntheses.

Furthermore, the I-V characteristics of the as-grown ZnO nanorods present an ohmic behavior with different output currents. Under UV radiations, increase in the output current of bare nanorods is due to the

oxygen adsorption-desorption mechanism at their surfaces. However for photodiodes, the enhancement in current is attributed to the depletion region formed at the interface of n-type ZnO nanorods and p-type F8BT/PEDOT:PSS and the built-in electric field. In reverse bias, the depletion region width increases, which in turn, increases the excitonic cross-section and therefore, the photogenerated current. Moreover, the I-V characteristics of the photodiodes display a rectifying behavior with differences in their rectification ratios. The highest rectification ratio of ~640 was obtained for the absolute methanol seed layer solvent, followed by lower rectification ratios of ~80 and ~78 for absolute isopropanol and ethanol seeding solvents. The lowest rectification ratio of ~44 was obtained for the aqueous ethanol seeding solvent with an ideality factor of ~3.2. The ideality factors of the ZnO nanorods grown on absolute alcohol seeding layers were between 1.8 and 2.4.

The I-t characteristics of bare ZnO nanorods grown on isopropanol solvent seed layer display the highest responsivity of 220 mA/w, followed by absolute ethanol, methanol and aqueous ethanol. In addition, the bare ZnO nanorods show persistent photoconductivity, which is a defect- and ambient-mediated phenomenon. In fact, persistent photoconductivity produces a slow decay of the current during the UV-off cycles in the nanorods. The differences in persistent photoconductivity are directly corelated to the ZnO-nanorod defect states, as the ambient conditions were the same for the samples in this case. The production of these defect states is controlled by the seeding solvent used that in turn, tailors the diameters of the nanorod. In that regard, ZNR-E$_a$ with the largest nanorod diameter, is a potential candidate for UV sensor applications considering the fastest response time T_{decay} of 78 s compare to the others ZnO nanorods (> 107 s). Nevertheless, ZnO nanorods with smaller diameters grown with absolute alcohol seed layers have potential for photocapacitors applications, owing to more pronounced persistent photoconductivity effects. Nonetheless, bare nanorods of this study present rather low responsivities that need improvement if further applications are envisaged.

Therefore, the diode architecture was selected, and the photoresponse of these photodiodes were assessed from I-t characteristics under several UV on-off cycles, at different reverse biases. The first improvement was the visible decrease in the persistent photoconductivity during the off-cycle. This is attributed to the polymer layer that passivates the nanorod

surface, preventing oxygen adsorption-desorption related decay current in the dark cycles. However, there is slight current decay or persistent photoconductivity arising from some of the non-passivated defects present on the surface of ZnO nanorods. Nevertheless, the responsivity of the photodiodes shows a marked improvement with almost three orders of magnitude increase compared to bare ZnO nanorods. In addition, we show that the seeding alcohol influenced the EQE of the photodiodes. The methanol and isopropanol seed layers had the highest and similar EQE of ~2760% at -2 V, ~1060% at -1 V, ~380% at -0.5 V and 25% at -0.1 V. On the other hand, the ethanol and aqueous ethanol seed layers possessed a similar EQE of 600% at -2 V, ~300% at -1 V, ~80% at - 0.5 V and ~5% at - 0.1 V. This suggests that low reverse biases are insufficient for proper working of the photodiodes considering the instabilities of the I-t characteristics. This also implies that higher the number of defects in nanorods, higher is the EQE at higher reverse bias that in fact compensates for the presence of these defects, allowing more functional photodiodes. On the other hand, higher number of defects leads to a higher decay current in dark conditions or during off-cycles. Therefore, the lowest response times were estimated for the absolute ethanol and aqueous ethanol seed layer solvents. At a reverse bias of -2 V, T_{decay} of ~108 s for absolute methanol and isopronanol and of ~65 s for absolute ethanol and aqueous ethanol ZnO-nanorod seed layers were obtained. In addition to the high responsivity and EQE, low response time is also an important photodiode parameter. Therefore, a compromise between the different figures of merit was sought in order to designate the best photodiode of this work. Since photodiodes are UV-detection devices, their maximum output current is an important factor, which is already considered in their responsivity and EQE. In that regard, the absolute methanol ZnO-nanorod seed layer stands out, along with the isopropanol ZnO-seed layer. Nevertheless, other characteristics of the absolute methanol ZnO-nanorod seed layer are also attractive, including a better ZnO-nanorod surface coverage, the highest rectification ratio, relatively stable on/off cycles, an ideality factor of 2, good sensitivity, responsivity and EQE. Therefore, PD-M outperforms PD-I and appears to be the best candidate for photodiode applications among the four photodiodes.

Since the seed layer used to grow ZnO nanorods plays an important part in the photodiode characteristics, the type of defects present in the seed layer need further evaluation. Therefore, the seed layer solvents were used

to synthesize ZnO nanoparticles using sol-gel synthesis routes before the nanorod study itself, in order to identify these defects. Sol-gel synthesis is a cost-effective route that precipitates ZnO nanoparticles exhibiting the same defects as the ZnO nuclei present in the ZnO-nanorod seed layer. For the absolute alcohol synthesis, the ZnO nanoparticles had the same uniform spherical morphology with average diameters of ~5 nm. On the other hand, the aqueous ethanol solvent generated nanoparticles having random morphologies with much larger nanoparticle sizes, suggesting that the presence of water leads to uncontrolled reaction kinetics. Photoluminescence spectroscopy performed on the absolute alcohol-synthesized ZnO nanoparticles indicated that the green component, which originates from the combination of surface oxygen vacancy V_O^{++} at 2.2 eV and volume oxygen vacancy V_O^+ at 2.5 eV were the dominant components. However, the presence of unreacted precursors was also detected depending on the solvents and the molar ratios of Zn precursor to NaOH. In fact, the absolute isopropanol solvent produces ZnO nanoparticles, but organic moieties such as isopropoxide groups cannot be eliminated from the sample. Nevertheless, these by-products do not alter the defect states of the ZnO nanoparticles. On the other hand, the green emission component related to V_O^+ at 2.5 eV is absent for ZnO nanoparticles synthesized using aqueous ethanol, owing to the oxygenated synthesis conditions. These defects are also visible in ZnO nanorods, even though in negligible amounts owing to the high aspect ratios of these hierarchical ZnO nanorods. Therefore, the defects in the nanorods can be correlated to the defects present in the seed layer studied via nanoparticle precipitation. The choice of the precursor to NaOH molar ratio of 1:2 was influenced by several nanoparticle properties. In fact, a molar ratio of 1:2 provided ZnO nanoparticles with interesting optical properties or a more intense DLE, probably due to lower quantities of by-products related to zinc precursor, Na and NaOH in these samples. For a lower amount of NaOH, the amount of reaction by-products was higher for absolute alcohol solvents. For the aqueous ethanol solvent, the number and quantities of by-products was lower; however, the lack of control of the growth process renders the morphology of the nanoparticles unpredictable. In addition, an anhydrous precursor was also selected to synthesize ZnO nanoparticles that showed higher amounts of surface defects and slightly smaller nanoparticle sizes. Green synthesis routes were also applied for ZnO-nanoparticle synthesis but were discontinued due to less interesting optical properties. However, the anhydrous precursor was not used for ZnO-nanorod growth, as the

influence of the higher number of defects would have been negligible on the nanorod growth considering the hydrothermal synthesis conditions.

Nevertheless, the ability to control these defects is also important via post-synthesis treatments. Therefore hybrid nanoparticles consisting of ZnO combined with CNT and PEDOT:PSS polymers were studied. Both, ex-situ and in-situ syntheses of these hybrid nanocomposites were carried out. In fact, ex-situ synthesis of ZnO-CNT and ZnO-PEDOT:PSS brought about a passivation of these surface defects, as CNT and PEDOT:PSS blocked the adsorption and desorption of oxygen radicals. On the other hand, the DLE of in-situ ZnO-CNT hybrids was enhanced, compared to their corresponding ZnO nanoparticles due to an enhancement in the upward band bending, arising from hydroxyl groups at the surface of ZnO and CNT. For the photodiode fabrication, the ZnO nanorods were covered with polymers F8BT and PEDOT:PSS. Therefore, the defect states of ZnO nanorods combined with polymers can be correlated to the defect states of ZnO nanoparticles combined with polymers. These transpositions of the defect states allow understanding the I-V characteristics, such as the abrupt drop of current or current decay for UV on-off cycles in photodiodes and bare ZnO nanorods, which are in fact mediated by defects in ZnO. All the other figures of merit of the photodiodes i.e., responsivity, EQE, response time as a function of ZnO-nanorod seed layer and effect of polymer coating can therefore be interpreted in terms of seeding solvent-mediated defects.

5. CONCLUSION

In conclusion, we have successfully prepared ZnO-nanorod-based hybrid photodiode devices for UV radiation detection and photocurrent generation. Four seeding alcohol solvents were selected for the ZnO-nanorod growth in order to fabricate four hybrid photodiodes. It was demonstrated that the seeding solvent had a clear influence of the photodiode functionalities, owing to the various defect states in the ZnO nanorods. The photodiode containing the ZnO nanorods grown by the absolute methanol seed layer exhibited the best compromises among the figures of merit for photodiode applications. Solvents control the size, morphology, uniformity and defect generation in bare ZnO nanorods that are useful for applications, such as charge storage studied by the I-V characteristics and I-t characteristics. However, their responsivity under UV radiation is quite low for application purposes. In fact, charge storage via the phenomenon of persistent photoconductivity is a defect- and ambient-mediated phenomenon and has transversal applications in gas sensing, piezo and bio-sensing. Therefore, bare ZnO nanorods display potential for wide range of applications, not limited to UV sensing. Nevertheless, their low UV responsivities need to be improved if future applications are envisaged. Therefore, the strategy of fabricating photodiodes was opted for in this thesis. The configuration allowed better control of the current-voltage characteristics, in turn enhancing their figures of merit, such as responsivity, sensitivity, external quantum efficiency and response time. Therefore, based on these factors, the absolute methanol seed layer-based photodiode stood out as the best candidate. To the best of our knowledge, this work is the first to demonstrate via a systematic study, the effect of the seed-layer solvents on the properties of ZnO nanorods and subsequently, on the photodiodes. Therefore, this thesis provides a new methodology to fabricate UV photodiodes and provides a detailed analysis of the influence of defects in ZnO nanorods on the figure of merits of these UV photodiodes.

Our approach to fabricate UV photodiodes is analyzed and compared to the commercial UV photodiodes, which are mainly based on GaN, 4H-SiC or AlGaN. The main advantage of the photodiodes of this work, is the cost-effective and low-temperature hydrothermal synthesis of ZnO nanorods. Whereas, other materials are usually synthesized using state-of-the-art and high-cost thin film techniques, such as metal-

organic chemical vapor deposition and physical vapor deposition. These techniques allow synthesizing a defect-free material, due to which commercial UV photodiodes have very fast responses of pico-seconds. The data herein demonstrates that a lower number of defect states produces a lower photodiode responsivity, similar to commercial photodiodes. For example, responsivity of GaN UV photodiode manufactured by APA optics Inc. is 0.9-0.7 A/W for a wavelength of 310 nm and effective area of 0.2-20 mm^2 [215]. On the other hand, we calculated a responsivity of ~ 8 A/W at wavelength of 365 nm, and reverse bias of - 2 V for the best performing PD-M photodiode with effective area of ~12.5 mm^2. Nevertheless, PD-M has a disadvantage of a slow T_{decay} response time of ~110 s at - 2 V, owing to PPC of ZnO nanorods. Another attractive advantage of our work is the fabrication of an energy-efficient photodiode with high EQE of ~2760%, calculated for PD-M at - 2 V. An important feature of an energy-efficient photodiode is the operation of self-powered photodiodes or at 0 V external bias, as they do not consume external energy for their operation. The operation mode of a zero-bias photodiode is via the photovoltaic mode, but the output current is suppressed due to the lack of bias. As a result, self-powered photodiode present low EQE, often less than 100%. In that regard, the photodiode in this study can be considered energy-efficient owing to a high EQE of ~2760% for PD-M at a relatively low bias of -2 V.

In general, photodiodes are the most important link between the optical and electronic fields as they work on the basic principle of converting light signals into electrical current, which is also the working principle for solar cells, communications, automobiles, aerospace and other applications. Due the wide applications of photodiodes, the related market is expected to grow from USD 3B in 2022 to USD 6B in 2032. The current research on photodiodes focuses on exploring advanced materials including, semiconductors, perovskites and organic materials in a hybrid configuration in order to enhance their figures of merits. In addition, improving the flexibility of the photodiodes is another aspect that has widened their applications to biomedical and wearable optoelectronic devices. However, most of the current commercial photodiodes are rather expensive for daily use. Therefore, there is a high demand for the development of photodiodes that are energy-efficient, cost-effective, and flexible with a high sensitivity towards low intensity light signals, quick responsivity and high EQE.

Our study explored some of the key challenges in photodiode research, such as their cost-effective synthesis and has added scientific insights to the field. In fact, inserting a p-type F8BT polymer layer in between n-type ZnO nanorods and p-type PEDOT:PSS layer in this work is a novel configuration for UV photodiodes that has never been investigated and has shown promising results. Nevertheless, some improvements in the device, such as using flexible conducting substrates instead of rigid ITO and control of device configurations, such as area and thickness of different layers, needs to be explored before technology transfer. Other perspectives of future research include increasing the range of applications by evaluating the figures of merit of the photodiodes at different UV wavelengths, including the detectivity and signal-to-noise ratio

REFERENCES

1. Nakamura, S.; Krames, M.R. History of Gallium–Nitride-Based Light-Emitting Diodes for Illumination. *Proceedings of the IEEE* **2013**, *101*, 2211-2220, doi:10.1109/JPROC.2013.2274929.

2. Jafar, N.; Jiang, J.; Lu, H.; Qasim, M.; Zhang, H. Recent Research on Indium-Gallium-Nitride-Based Light-Emitting Diodes: Growth Conditions and External Quantum Efficiency. *Crystals* **2023**, *13*, 1623.

3. Zhao, Y.; Xu, M.; Huang, X.; Lebeau, J.; Li, T.; Wang, D.; Fu, H.; Fu, K.; Wang, X.; Lin, J.; et al. Toward high efficiency at high temperatures: Recent progress and prospects on InGaN-Based solar cells. *Materials Today Energy* **2023**, *31*, 101229, doi:https://doi.org/10.1016/j.mtener.2022.101229.

4. Chapter 3 - The Current Situation in Ultra-Precision Technology – Silicon Single Crystals as an Example. In *Advances in CMP Polishing Technologies*, Doi, T., Marinescu, I.D., Kurokawa, S., Eds.; William Andrew Publishing: Oxford, 2012; pp. 15-111.

5. Wan, J.; Song, T.; Flox, C.; Yang, J.; Yang, Q.-H.; Han, X. Advanced Nanomaterials for Energy-Related Applications. *Journal of Nanomaterials* **2015**, *2015*, 564097, doi:10.1155/2015/564097.

6. Triana, M.A.; Hsiang, E.-L.; Zhang, C.; Dong, Y.; Wu, S.-T. Luminescent Nanomaterials for Energy-Efficient Display and Healthcare. *ACS Energy Letters* **2022**, *7*, 1001-1020, doi:10.1021/acsenergylett.1c02745.

7. Tegart, G. Nanotechnology: the technology for the twenty-first century. *Foresight* **2004**, *6*, 364-370, doi:10.1108/14636680410569948.

8. Malik, S.; Muhammad, K.; Waheed, Y. Nanotechnology: A Revolution in Modern Industry. *Molecules* **2023**, *28*, 661.

9. Christian, F.; Edith; Selly; Adityawarman, D.; Indarto, A. Application of nanotechnologies in the energy sector: A brief and short review. *Frontiers in Energy* **2013**, *7*, 6-18, doi:10.1007/s11708-012-0219-5.

10. Sun, Y.; Liu, N.; Cui, Y. Promises and challenges of nanomaterials for lithium-based rechargeable batteries. *Nature Energy* **2016**, *1*, 16071, doi:10.1038/nenergy.2016.71.

11. Nasiri, N.; Tricoli, A. Chapter 5 - Nanomaterials-based UV photodetectors. In *Industrial Applications of Nanomaterials*, Thomas, S., Grohens, Y., Pottathara, Y.B., Eds.; Elsevier: 2019; pp. 123-149.

12. Gour, A.; Jain, N.K. Advances in green synthesis of nanoparticles. *Artificial Cells, Nanomedicine, and Biotechnology* **2019**, *47*, 844-851, doi:10.1080/21691401.2019.1577878.

13. Gutierrez, R.M.P.; Mendez, J.V.M.; Vazquez, I.A. Chapter 2 - A novel approach to the oral delivery of bionanostructures for systemic disease. In *Nanostructures for Oral Medicine*, Andronescu, E., Grumezescu, A.M., Eds.; Elsevier: 2017; pp. 27-59.

14. Joudeh, N.; Linke, D. Nanoparticle classification, physicochemical properties, characterization, and applications: a comprehensive review for biologists. *Journal of Nanobiotechnology* **2022**, *20*, 262, doi:10.1186/s12951-022-01477-8.

15. Sharma, P.; Hasan, M.R.; Mehto, N.K.; Deepak; Bishoyi, A.; Narang, J. 92 years of zinc oxide: has been studied by the scientific community since the 1930s- An overview. *Sensors International* **2022**, *3*, 100182, doi:https://doi.org/10.1016/j.sintl.2022.100182.

16. Kołodziejczak-Radzimska, A.; Jesionowski, T. Zinc Oxide—From Synthesis to Application: A Review. *Materials* **2014**, *7*, 2833-2881.

17. Wang, Z.L. Nanostructures of zinc oxide. *Materials Today* **2004**, *7*, 26-33, doi:https://doi.org/10.1016/S1369-7021(04)00286-X.

18. Mishra, Y.K.; Adelung, R. ZnO tetrapod materials for functional applications. *Materials Today* **2018**, *21*, 631-651, doi:https://doi.org/10.1016/j.mattod.2017.11.003.

19. Shen, G.; Chen, D. One-dimensional nanostructures for electronic and optoelectronic devices. *Frontiers of Optoelectronics in China* **2010**, *3*, 125-138, doi:10.1007/s12200-010-0001-4.

20. Ding, M.; Guo, Z.; Zhou, L.; Fang, X.; Zhang, L.; Zeng, L.; Xie, L.; Zhao, H. One-Dimensional Zinc Oxide Nanomaterials for Application in High-Performance Advanced Optoelectronic Devices. *Crystals* **2018**, *8*, 223.

21. Albiter, E.; Barrera-Andrade, J.M.; Rojas-García, E.; Valenzuela, M.A. 17 - Recent advances of nanocarbon-inorganic hybrids in photocatalysis. In *Nanocarbon and its Composites*, Khan, A., Jawaid,

M., Inamuddin, Asiri, A.M., Eds.; Woodhead Publishing: 2019; pp. 521-588.

22. Rezaie, M.N.; Mohammadnejad, S.; Ahadzadeh, S. Hybrid inorganic-organic light-emitting heterostructure devices based on ZnO. *Optics & Laser Technology* **2021**, *138*, 106896, doi:https://doi.org/10.1016/j.optlastec.2020.106896.

23. Sarma, B.K.; Rajkumar, P. Al-doped ZnO transparent conducting oxide with appealing electro-optical properties – Realization of indium free transparent conductors from sputtering targets with varying dopant concentrations. *Materials Today Communications* **2020**, *23*, 100870, doi:https://doi.org/10.1016/j.mtcomm.2019.100870.

24. Fortunato, E.; Barquinha, P.; Pimentel, A.; Gonçalves, A.; Marques, A.; Pereira, L.; Martins, R. Recent advances in ZnO transparent thin film transistors. *Thin Solid Films* **2005**, *487*, 205-211, doi:https://doi.org/10.1016/j.tsf.2005.01.066.

25. Wibowo, A.; Marsudi, M.A.; Amal, M.I.; Ananda, M.B.; Stephanie, R.; Ardy, H.; Diguna, L.J. ZnO nanostructured materials for emerging solar cell applications. *RSC Advances* **2020**, *10*, 42838-42859, doi:10.1039/D0RA07689A.

26. Huang, J.; Yin, Z.; Zheng, Q. Applications of ZnO in organic and hybrid solar cells. *Energy & Environmental Science* **2011**, *4*, 3861-3877, doi:10.1039/C1EE01873F.

27. Ong, C.B.; Ng, L.Y.; Mohammad, A.W. A review of ZnO nanoparticles as solar photocatalysts: Synthesis, mechanisms and applications. *Renewable and Sustainable Energy Reviews* **2018**, *81*, 536-551, doi:https://doi.org/10.1016/j.rser.2017.08.020.

28. Deka Boruah, B. Zinc oxide ultraviolet photodetectors: rapid progress from conventional to self-powered photodetectors. *Nanoscale Advances* **2019**, *1*, 2059-2085, doi:10.1039/C9NA00130A.

29. Inamdar, S.I.; Ganbavle, V.V.; Rajpure, K.Y. ZnO based visible–blind UV photodetector by spray pyrolysis. *Superlattices and Microstructures* **2014**, *76*, 253-263, doi:https://doi.org/10.1016/j.spmi.2014.09.041.

30. Jangir, L.K.; Kumari, Y.; Kumari, P. 13 - Zinc oxide-based light-emitting diodes and lasers. In *Nanostructured Zinc Oxide*, Awasthi, K., Ed.; Elsevier: 2021; pp. 351-374.

31. Rahman, F. Zinc oxide light-emitting diodes: a review. *Opt. Eng.* **2019**, *58*, 010901, doi:10.1117/1.OE.58.1.010901.

32. da Silva-Neto, M.L.; de Oliveira, M.C.A.; Dominguez, C.T.; Lins, R.E.M.; Rakov, N.; de Araújo, C.B.; Menezes, L.d.S.; de Oliveira, H.P.; Gomes, A.S.L. UV random laser emission from flexible ZnO-Ag-enriched electrospun cellulose acetate fiber matrix. *Scientific Reports* **2019**, *9*, 11765, doi:10.1038/s41598-019-48056-w.

33. Lu, Y.J.; Shi, Z.F.; Shan, C.X.; Shen, D.Z. Chapter 4 - ZnO nanostructures and lasers. In *Nanoscale Semiconductor Lasers*, Tong, C., Jagadish, C., Eds.; Elsevier: 2019; pp. 75-108.

34. Krishna, K.G.; Umadevi, G.; Parne, S.; Pothukanuri, N. Zinc oxide based gas sensors and their derivatives: a critical review. *Journal of Materials Chemistry C* **2023**, *11*, 3906-3925, doi:10.1039/D2TC04690C.

35. Xuan, J.; Zhao, G.; Sun, M.; Jia, F.; Wang, X.; Zhou, T.; Yin, G.; Liu, B. Low-temperature operating ZnO-based NO2 sensors: a review. *RSC Advances* **2020**, *10*, 39786-39807, doi:10.1039/D0RA07328H.

36. Liu, K.; Sakurai, M.; Aono, M. ZnO-Based Ultraviolet Photodetectors. *Sensors* **2010**, *10*, 8604-8634.

37. Mitra, A.; Thareja, R.K.; Ganesan, V.; Gupta, A.; Sahoo, P.K.; Kulkarni, V.N. Synthesis and characterization of ZnO thin films for UV laser. *Applied Surface Science* **2001**, *174*, 232-239, doi:https://doi.org/10.1016/S0169-4332(01)00171-4.

38. Das, S.N.; Moon, K.-J.; Kar, J.P.; Choi, J.-H.; Xiong, J.; Lee, T.I.; Myoung, J.-M. ZnO single nanowire-based UV detectors. *Applied Physics Letters* **2010**, *97*, doi:10.1063/1.3464287.

39. Raha, S.; Ahmaruzzaman, M. ZnO nanostructured materials and their potential applications: progress, challenges and perspectives. *Nanoscale Advances* **2022**, *4*, 1868-1925, doi:10.1039/D1NA00880C.

40. Chauhan, R.; Kumar, A.; Tripathi, R.; Kumar, A. Advancing of Zinc Oxide Nanoparticles for Cosmetic Applications. In *Handbook of Consumer Nanoproducts*, Mallakpour, S., Hussain, C.M., Eds.; Springer Nature Singapore: Singapore, 2022; pp. 1057-1072.

41. Kuo, C.-L.; Wang, C.-L.; Ko, H.-H.; Hwang, W.-S.; Chang, K.-m.; Li, W.-L.; Huang, H.-H.; Chang, Y.-H.; Wang, M.-C. Synthesis of zinc oxide nanocrystalline powders for cosmetic applications. *Ceramics International* **2010**, *36*, 693-698, doi:https://doi.org/10.1016/j.ceramint.2009.10.011.

42. Foudi, H.; Soukeur, A.; Rekhila, G.; Trari, M.; Amara, M. Synthesis and characterization of ZnO nanoparticles for antibacterial paints. *Chemical Papers* **2023**, *77*, 1489-1496, doi:10.1007/s11696-022-02565-7.

43. Lallo da Silva, B.; Caetano, B.L.; Chiari-Andréo, B.G.; Pietro, R.C.L.R.; Chiavacci, L.A. Increased antibacterial activity of ZnO nanoparticles: Influence of size and surface modification. *Colloids and Surfaces B: Biointerfaces* **2019**, *177*, 440-447, doi:https://doi.org/10.1016/j.colsurfb.2019.02.013.

44. Abebe, B.; Zereffa, E.A.; Tadesse, A.; Murthy, H.C.A. A Review on Enhancing the Antibacterial Activity of ZnO: Mechanisms and Microscopic Investigation. *Nanoscale Research Letters* **2020**, *15*, 190, doi:10.1186/s11671-020-03418-6.

45. Youn, S.-M.; Choi, S.-J. Food Additive Zinc Oxide Nanoparticles: Dissolution, Interaction, Fate, Cytotoxicity, and Oral Toxicity. *International Journal of Molecular Sciences* **2022**, *23*, 6074.

46. Vanmaekelbergh, D.; van Vugt, L.K. ZnO nanowire lasers. *Nanoscale* **2011**, *3*, 2783-2800, doi:10.1039/C1NR00013F.

47. Djurišić, A.B.; Ng, A.M.C.; Chen, X.Y. ZnO nanostructures for optoelectronics: Material properties and device applications. *Progress in Quantum Electronics* **2010**, *34*, 191-259, doi:https://doi.org/10.1016/j.pquantelec.2010.04.001.

48. Pearton, S.J.; Norton, D.P.; Heo, Y.W.; Tien, L.C.; Ivill, M.P.; Li, Y.; Kang, B.S.; Ren, F.; Kelly, J.; Hebard, A.F. ZnO spintronics and nanowire devices. *Journal of Electronic Materials* **2006**, *35*, 862-868, doi:10.1007/BF02692541.

49. Park, C.H.; Zhang, S.B.; Wei, S.-H. Origin of p-type doping difficulty in ZnO: The impurity perspective. *Physical Review B* **2002**, *66*, 073202, doi:10.1103/PhysRevB.66.073202.

50. Narayanan, N.; Kannoth, D.N. Exploring p type conductivity in ZnO thin films by In–N codoping for homo-junction devices.

Journal of Materials Science: Materials in Electronics **2017**, *28*, 5962-5970, doi:10.1007/s10854-016-6270-y.

51. Ryu, Y.R.; Kim, W.J.; White, H.W. Fabrication of homostructural ZnO p–n junctions. *Journal of Crystal Growth* **2000**, *219*, 419-422, doi:https://doi.org/10.1016/S0022-0248(00)00731-4.

52. Lu, J.G.; Ye, Z.Z.; Yuan, G.D.; Zeng, Y.J.; Zhuge, F.; Zhu, L.P.; Zhao, B.H.; Zhang, S.B. Electrical characterization of ZnO-based homojunctions. *Applied Physics Letters* **2006**, *89*, doi:10.1063/1.2245221.

53. Liang, F.-X.; Gao, Y.; Xie, C.; Tong, X.-W.; Li, Z.-J.; Luo, L.-B. Recent advances in the fabrication of graphene–ZnO heterojunctions for optoelectronic device applications. *Journal of Materials Chemistry C* **2018**, *6*, 3815-3833, doi:10.1039/C8TC00172C.

54. Bader, B.A.; Khashan, K.S. Optoelectronic properties of ZnO/Si heterojunction prepared by laser ablation. *AIP Conference Proceedings* **2022**, *2437*, doi:10.1063/5.0092288.

55. Vempati, S.; Mitra, J.; Dawson, P. One-step synthesis of ZnO nanosheets: a blue-white fluorophore. *Nanoscale Research Letters* **2012**, *7*, 470, doi:10.1186/1556-276X-7-470.

56. Zeghoud, S.; Hemmami, H.; Ben Seghir, B.; Ben Amor, I.; Kouadri, I.; Rebiai, A.; Messaoudi, M.; Ahmed, S.; Pohl, P.; Simal-Gandara, J. A review on biogenic green synthesis of ZnO nanoparticles by plant biomass and their applications. *Materials Today Communications* **2022**, *33*, 104747, doi:https://doi.org/10.1016/j.mtcomm.2022.104747.

57. Lee, S.; Jeong, S.; Kim, D.; Hwang, S.; Jeon, M.; Moon, J. ZnO nanoparticles with controlled shapes and sizes prepared using a simple polyol synthesis. *Superlattices and Microstructures* **2008**, *43*, 330-339, doi:https://doi.org/10.1016/j.spmi.2008.01.004.

58. Bulcha, B.; Leta Tesfaye, J.; Anatol, D.; Shanmugam, R.; Dwarampudi, L.P.; Nagaprasad, N.; Bhargavi, V.L.N.; Krishnaraj, R. Synthesis of Zinc Oxide Nanoparticles by Hydrothermal Methods and Spectroscopic Investigation of Ultraviolet Radiation Protective Properties. *Journal of Nanomaterials* **2021**, *2021*, 8617290, doi:10.1155/2021/8617290.

59. Lupan, O.; Emelchenko, G.A.; Ursaki, V.V.; Chai, G.; Redkin, A.N.; Gruzintsev, A.N.; Tiginyanu, I.M.; Chow, L.; Ono, L.K.;

Roldan Cuenya, B.; et al. Synthesis and characterization of ZnO nanowires for nanosensor applications. *Materials Research Bulletin* **2010**, *45*, 1026-1032, doi:https://doi.org/10.1016/j.materresbull.2010.03.027.

60. Wirunchit, S.; Gansa, P.; Koetniyom, W. Synthesis of ZnO nanoparticles by Ball-milling process for biological applications. *Materials Today: Proceedings* **2021**, *47*, 3554-3559, doi:https://doi.org/10.1016/j.matpr.2021.03.559.

61. Worasawat, S.; Masuzawa, T.; Hatanaka, Y.; Neo, Y.; Mimura, H.; Pecharapa, W. Synthesis and characterization of ZnO nanorods by hydrothermal method. *Materials Today: Proceedings* **2018**, *5*, 10964-10969, doi:https://doi.org/10.1016/j.matpr.2018.01.010.

62. Espitia, P.J.P.; Soares, N.d.F.F.; Coimbra, J.S.d.R.; de Andrade, N.J.; Cruz, R.S.; Medeiros, E.A.A. Zinc Oxide Nanoparticles: Synthesis, Antimicrobial Activity and Food Packaging Applications. *Food and Bioprocess Technology* **2012**, *5*, 1447-1464, doi:10.1007/s11947-012-0797-6.

63. Zhang, Y.; Ram, M.K.; Stefanakos, E.K.; Goswami, D.Y. Synthesis, Characterization, and Applications of ZnO Nanowires. *Journal of Nanomaterials* **2012**, *2012*, 624520, doi:10.1155/2012/624520.

64. Motana, S.; Shariq, M.; Alajlani, Y.; Pamu, D.; Chowdhury, R.; Jayaganthan, R.; Mohammed, T. Structural and Optical Properties of Pure Wurtzite ZnO under Uniaxial Strain Based on First-Principles Study. *Acta Physica Polonica A* **2020**, *137*, 361-367, doi:10.12693/APhysPolA.137.361.

65. Reeber, R.R. Lattice parameters of ZnO from 4.2° to 296°K. *Journal of Applied Physics* **1970**, *41*, 5063-5066, doi:10.1063/1.1658600.

66. Soni, H.; Singh, A.; Mishra, A.K. Biaxial strain induced tunable electronic properties study of ZnO nanoparticles via first-principles density functional theory. *Materials Science and Engineering: B* **2023**, *288*, 116186, doi:https://doi.org/10.1016/j.mseb.2022.116186.

67. Ashok, K.S.; Zhong Lin, W.; Dennis, L.P.; Nibir, K.D.; Tariq, M.; Anwar, A.F.M. ZnO Nanostructures for Optoelectronic Applications. In *Optoelectronic Devices and Properties*, Oleg, S., Ed.; IntechOpen: Rijeka, 2011; p. Ch. 9.

68. Consonni, V.; Lord, A.M. Polarity in ZnO nanowires: A critical issue for piezotronic and piezoelectric devices. *Nano Energy* **2021**, *83*, 105789, doi:https://doi.org/10.1016/j.nanoen.2021.105789.

69. Koster, R.S.; Fang, C.M.; Dijkstra, M.; van Blaaderen, A.; van Huis, M.A. Stabilization of Rock Salt ZnO Nanocrystals by Low-Energy Surfaces and Mg Additions: A First-Principles Study. *The Journal of Physical Chemistry C* **2015**, *119*, 5648-5656, doi:10.1021/jp511503b.

70. Bates, C.H.; White, W.B.; Roy, R. New High-Pressure Polymorph of Zinc Oxide. *Science* **1962**, *137*, 993-993, doi:doi:10.1126/science.137.3534.993.a.

71. Yang, J.; Wang, J.; Li, X.; Lang, J.; Liu, F.; Yang, L.; Zhai, H.; Gao, M.; Zhao, X. Effect of polar and non-polar surfaces of ZnO nanostructures on photocatalytic properties. *Journal of Alloys and Compounds* **2012**, *528*, 28-33, doi:https://doi.org/10.1016/j.jallcom.2012.02.162.

72. Gerbreders, V.; Krasovska, M.; Sledevskis, E.; Gerbreders, A.; Mihailova, I.; Tamanis, E.; Ogurcovs, A. Hydrothermal synthesis of ZnO nanostructures with controllable morphology change. *CrystEngComm* **2020**, *22*, 1346-1358, doi:10.1039/C9CE01556F.

73. Liu, Y.; Xu, W.; Shan, Y.; Xu, H. High Reactivity of the ZnO(0001) Polar Surface: The Role of Oxygen Adatoms. *The Journal of Physical Chemistry C* **2017**, *121*, 15711-15718, doi:10.1021/acs.jpcc.7b03326.

74. Cui, J. Zinc oxide nanowires. *Materials Characterization* **2012**, *64*, 43-52, doi:https://doi.org/10.1016/j.matchar.2011.11.017.

75. Mohammadzadeh, A.; Azadbeh, M.; Shokriyan, B.; Khalil Abad, S.N. Synthesis of ZnO nanocombs and tetrapods by catalyst-free oxidation of alpha brass powders in air atmosphere. *Ceramics International* **2020**, *46*, 2552-2557, doi:https://doi.org/10.1016/j.ceramint.2019.09.112.

76. Hong, M.; Meng, J.; Yu, H.; Du, J.; Ou, Y.; Liao, Q.; Kang, Z.; Zhang, Z.; Zhang, Y. Ultra-stable ZnO nanobelts in electrochemical environments. *Materials Chemistry Frontiers* **2021**, *5*, 430-437, doi:10.1039/D0QM00709A.

77. Newton, M.C.; Warburton, P.A. ZnO tetrapod nanocrystals. *Materials Today* **2007**, *10*, 50-54, doi:https://doi.org/10.1016/S1369-7021(07)70079-2.

78. Vogel, D.; Krüger, P.; Pollmann, J. Ab initio electronic-structure calculations for II-VI semiconductors using self-interaction-corrected pseudopotentials. *Physical Review B* **1995**, *52*, R14316-R14319, doi:10.1103/PhysRevB.52.R14316.

79. Vogel, D.; Krüger, P.; Pollmann, J. Self-interaction and relaxation-corrected pseudopotentials for II-VI semiconductors. *Physical Review B* **1996**, *54*, 5495-5511, doi:10.1103/PhysRevB.54.5495.

80. Goh, E.S.; Mah, J.W.; Yoon, T.L. Effects of Hubbard term correction on the structural parameters and electronic properties of wurtzite ZnO. *Computational Materials Science* **2017**, *138*, 111-116, doi:https://doi.org/10.1016/j.commatsci.2017.06.032.

81. Harun, K.; Mansor, N.; Ahmad, Z.A.; Mohamad, A.A. Electronic Properties of ZnO Nanoparticles Synthesized by Sol-gel Method: A LDA+U Calculation and Experimental Study. *Procedia Chemistry* **2016**, *19*, 125-132, doi:https://doi.org/10.1016/j.proche.2016.03.125.

82. Zwicker, G.; Jacobi, K. Experimental band structure of ZnO. *Solid State Communications* **1985**, *54*, 701-704, doi:https://doi.org/10.1016/0038-1098(85)90591-5.

83. King, P.D.C.; Veal, T.D.; Schleife, A.; Zúñiga-Pérez, J.; Martel, B.; Jefferson, P.H.; Fuchs, F.; Muñoz-Sanjosé, V.; Bechstedt, F.; McConville, C.F. Valence-band electronic structure of CdO, ZnO, and MgO from x-ray photoemission spectroscopy and quasi-particle-corrected density-functional theory calculations. *Physical Review B* **2009**, *79*, 205205, doi:10.1103/PhysRevB.79.205205.

84. Meyer, B.K.; Alves, H.; Hofmann, D.M.; Kriegseis, W.; Forster, D.; Bertram, F.; Christen, J.; Hoffmann, A.; Straßburg, M.; Dworzak, M.; et al. Bound exciton and donor–acceptor pair recombinations in ZnO. *physica status solidi (b)* **2004**, *241*, 231-260, doi:https://doi.org/10.1002/pssb.200301962.

85. Galdámez-Martinez, A.; Santana, G.; Güell, F.; Martínez-Alanis, P.R.; Dutt, A. Photoluminescence of ZnO Nanowires: A Review. *Nanomaterials* **2020**, *10*, 857.

86. Hariwal, Rajesh V.; Malik, H.K.; Negi, A.; Kandasami, A. Controlling room temperature ferromagnetism and band gap in ZnO nanostructured thin films by varying angle of implantation. *RSC Advances* **2018**, *8*, 6278-6287, doi:10.1039/C7RA10615G.

87. Granerød, C.S.; Galeckas, A.; Johansen, K.M.; Vines, L.; Prytz, Ø. The temperature-dependency of the optical band gap of ZnO measured by electron energy-loss spectroscopy in a scanning transmission electron microscope. *Journal of Applied Physics* **2018**, *123*, doi:10.1063/1.5023316.

88. Look, D.C.; Reynolds, D.C.; Sizelove, J.R.; Jones, R.L.; Litton, C.W.; Cantwell, G.; Harsch, W.C. Electrical properties of bulk ZnO. *Solid State Communications* **1998**, *105*, 399-401, doi:https://doi.org/10.1016/S0038-1098(97)10145-4.

89. Hammer, M.S.; Rauh, D.; Lorrmann, V.; Deibel, C.; Dyakonov, V. Effect of doping- and field-induced charge carrier density on the electron transport in nanocrystalline ZnO. *Nanotechnology* **2008**, *19*, 485701, doi:10.1088/0957-4484/19/48/485701.

90. Carofiglio, M.; Barui, S.; Cauda, V.; Laurenti, M. Doped Zinc Oxide Nanoparticles: Synthesis, Characterization and Potential Use in Nanomedicine. *Applied Sciences* **2020**, *10*, 5194.

91. Alexandrov, A.; Zvaigzne, M.; Lypenko, D.; Nabiev, I.; Samokhvalov, P. Al-, Ga-, Mg-, or Li-doped zinc oxide nanoparticles as electron transport layers for quantum dot light-emitting diodes. *Scientific Reports* **2020**, *10*, 7496, doi:10.1038/s41598-020-64263-2.

92. Kim, Y.-S.; Park, C.H. Rich Variety of Defects in ZnO via an Attractive Interaction between O Vacancies and Zn Interstitials: Origin of n-Type Doping. *Physical Review Letters* **2009**, *102*, 086403, doi:10.1103/PhysRevLett.102.086403.

93. Look, D.C.; Hemsky, J.W.; Sizelove, J.R. Residual Native Shallow Donor in ZnO. *Physical Review Letters* **1999**, *82*, 2552-2555, doi:10.1103/PhysRevLett.82.2552.

94. Gurylev, V.; Perng, T.P. Defect engineering of ZnO: Review on oxygen and zinc vacancies. *Journal of the European Ceramic Society* **2021**, *41*, 4977-4996, doi:https://doi.org/10.1016/j.jeurceramsoc.2021.03.031.

95. Zhu, Q.; Xie, C.; Li, H.; Yang, C.; Zhang, S.; Zeng, D. Selectively enhanced UV and NIR photoluminescence from a degenerate ZnO

nanorod array film. *Journal of Materials Chemistry C* **2014**, *2*, 4566-4580, doi:10.1039/C4TC00011K.

96. Liao, Z.-M.; Zhang, H.-Z.; Zhou, Y.-B.; Xu, J.; Zhang, J.-M.; Yu, D.-P. Surface effects on photoluminescence of single ZnO nanowires. *Physics Letters A* **2008**, *372*, 4505-4509, doi:https://doi.org/10.1016/j.physleta.2008.04.013.

97. Nagpal, K.; Rauwel, E.; Estephan, E.; Soares, M.R.; Rauwel, P. Significance of Hydroxyl Groups on the Optical Properties of ZnO Nanoparticles Combined with CNT and PEDOT:PSS. *Nanomaterials* **2022**, *12*, 3546.

98. Vanheusden, K.; Warren, W.L.; Seager, C.H.; Tallant, D.R.; Voigt, J.A.; Gnade, B.E. Mechanisms behind green photoluminescence in ZnO phosphor powders. *Journal of Applied Physics* **1996**, *79*, 7983-7990, doi:10.1063/1.362349.

99. Khranovskyy, V.; Lazorenko, V.; Lashkarev, G.; Yakimova, R. Luminescence anisotropy of ZnO microrods. *Journal of Luminescence* **2012**, *132*, 2643-2647, doi:https://doi.org/10.1016/j.jlumin.2012.04.048.

100. Bekeny, C.; Voss, T.; Gafsi, H.; Gutowski, J.; Postels, B.; Kreye, M.; Waag, A. Origin of the near-band-edge photoluminescence emission in aqueous chemically grown ZnO nanorods. *Journal of Applied Physics* **2006**, *100*, doi:10.1063/1.2390548.

101. Borade, P.A.; Sant, T.; Gokarna, A.; Joshi, K.U.; Panat, R.P.; Jejurikar, S.M. Role of defects in modulating the near band edge emissions of sub-micron ZnO crystals. *Optical Materials* **2020**, *109*, 110348, doi:https://doi.org/10.1016/j.optmat.2020.110348.

102. Ahn, C.H.; Kim, Y.Y.; Kim, D.C.; Mohanta, S.K.; Cho, H.K. A comparative analysis of deep level emission in ZnO layers deposited by various methods. *Journal of Applied Physics* **2009**, *105*, doi:10.1063/1.3054175.

103. Gong, Y.; Andelman, T.; Neumark, G.F.; O'Brien, S.; Kuskovsky, I.L. Origin of defect-related green emission from ZnO nanoparticles: effect of surface modification. *Nanoscale Research Letters* **2007**, *2*, 297, doi:10.1007/s11671-007-9064-6.

104. Willander, M.; Nur, O.; Sadaf, J.R.; Qadir, M.I.; Zaman, S.; Zainelabdin, A.; Bano, N.; Hussain, I. Luminescence from Zinc

Oxide Nanostructures and Polymers and their Hybrid Devices. *Materials* **2010**, *3*, 2643-2667.

105. Polsongkram, D.; Chamninok, P.; Pukird, S.; Chow, L.; Lupan, O.; Chai, G.; Khallaf, H.; Park, S.; Schulte, A. Effect of synthesis conditions on the growth of ZnO nanorods via hydrothermal method. *Physica B: Condensed Matter* **2008**, *403*, 3713-3717, doi:https://doi.org/10.1016/j.physb.2008.06.020.

106. Dakhlaoui, A.; Jendoubi, M.; Smiri, L.S.; Kanaev, A.; Jouini, N. Synthesis, characterization and optical properties of ZnO nanoparticles with controlled size and morphology. *Journal of Crystal Growth* **2009**, *311*, 3989-3996, doi:https://doi.org/10.1016/j.jcrysgro.2009.06.028.

107. Tiwari, S.K.; Kumar, V.; Huczko, A.; Oraon, R.; Adhikari, A.D.; Nayak, G.C. Magical Allotropes of Carbon: Prospects and Applications. *Critical Reviews in Solid State and Materials Sciences* **2016**, *41*, 257-317, doi:10.1080/10408436.2015.1127206.

108. Rathinavel, S.; Priyadharshini, K.; Panda, D. A review on carbon nanotube: An overview of synthesis, properties, functionalization, characterization, and the application. *Materials Science and Engineering: B* **2021**, *268*, 115095, doi:https://doi.org/10.1016/j.mseb.2021.115095.

109. Manoj Kumar, R.; Sharma, S.K.; Manoj Kumar, B.V.; Lahiri, D. Effects of carbon nanotube aspect ratio on strengthening and tribological behavior of ultra high molecular weight polyethylene composite. *Composites Part A: Applied Science and Manufacturing* **2015**, *76*, 62-72, doi:https://doi.org/10.1016/j.compositesa.2015.05.007.

110. Ma, R.; Wei, B.; Xu, C.; Liang, J.; Wu, D. Development of supercapacitors based on carbon nanotubes. *Science in China Series E: Technological Sciences* **2000**, *43*, 178-182, doi:10.1007/BF02916888.

111. Iijima, S.; Brabec, C.; Maiti, A.; Bernholc, J. Structural flexibility of carbon nanotubes. *The Journal of Chemical Physics* **1996**, *104*, 2089-2092, doi:10.1063/1.470966.

112. Robertson, J. Realistic applications of CNTs. *Materials Today* **2004**, *7*, 46-52, doi:https://doi.org/10.1016/S1369-7021(04)00448-1.

113. Tsukagoshi, K.; Yoneya, N.; Uryu, S.; Aoyagi, Y.; Kanda, A.; Ootuka, Y.; Alphenaar, B.W. Carbon nanotube devices for nanoelectronics. *Physica B: Condensed Matter* **2002**, *323*, 107-114, doi:https://doi.org/10.1016/S0921-4526(02)00993-6.

114. Schroeder, V.; Savagatrup, S.; He, M.; Lin, S.; Swager, T.M. Carbon Nanotube Chemical Sensors. *Chemical Reviews* **2019**, *119*, 599-663, doi:10.1021/acs.chemrev.8b00340.

115. Yan, Y.; Miao, J.; Yang, Z.; Xiao, F.-X.; Yang, H.B.; Liu, B.; Yang, Y. Carbon nanotube catalysts: recent advances in synthesis, characterization and applications. *Chemical Society Reviews* **2015**, *44*, 3295-3346, doi:10.1039/C4CS00492B.

116. Anzar, N.; Hasan, R.; Tyagi, M.; Yadav, N.; Narang, J. Carbon nanotube - A review on Synthesis, Properties and plethora of applications in the field of biomedical science. *Sensors International* **2020**, *1*, 100003, doi:https://doi.org/10.1016/j.sintl.2020.100003.

117. Aval, L.F.; Ghoranneviss, M.; Pour, G.B. High-performance supercapacitors based on the carbon nanotubes, graphene and graphite nanoparticles electrodes. *Heliyon* **2018**, *4*, e00862, doi:https://doi.org/10.1016/j.heliyon.2018.e00862.

118. Kanoun, O.; Bouhamed, A.; Ramalingame, R.; Bautista-Quijano, J.R.; Rajendran, D.; Al-Hamry, A. Review on Conductive Polymer/CNTs Nanocomposites Based Flexible and Stretchable Strain and Pressure Sensors. *Sensors* **2021**, *21*, 341.

119. Maheswaran, R.; Shanmugavel, B.P. A Critical Review of the Role of Carbon Nanotubes in the Progress of Next-Generation Electronic Applications. *Journal of Electronic Materials* **2022**, *51*, 2786-2800, doi:10.1007/s11664-022-09516-8.

120. Fakhri, N.; Tsyboulski, D.A.; Cognet, L.; Weisman, R.B.; Pasquali, M. Diameter-dependent bending dynamics of single-walled carbon nanotubes in liquids. *Proceedings of the National Academy of Sciences* **2009**, *106*, 14219-14223, doi:doi:10.1073/pnas.0904148106.

121. Su, W.; Li, X.; Li, L.; Yang, D.; Wang, F.; Wei, X.; Zhou, W.; Kataura, H.; Xie, S.; Liu, H. Chirality-dependent electrical transport properties of carbon nanotubes obtained by experimental measurement. *Nature Communications* **2023**, *14*, 1672, doi:10.1038/s41467-023-37443-7.

122. Zhang, F.; Hou, P.-X.; Liu, C.; Wang, B.-W.; Jiang, H.; Chen, M.-L.; Sun, D.-M.; Li, J.-C.; Cong, H.-T.; Kauppinen, E.I.; et al. Growth of semiconducting single-wall carbon nanotubes with a narrow band-gap distribution. *Nature Communications* **2016**, *7*, 11160, doi:10.1038/ncomms11160.

123. Wang, Y.; Lu, Z.; Hu, Q.; Qi, X.; Li, Q.; Wu, Z.; Zhang, H.-L.; Yu, C.; Wang, H. Mass-produced metallic multiwalled carbon nanotube hybrids exhibiting high N-type thermoelectric performances. *Journal of Materials Chemistry A* **2021**, *9*, 3341-3352, doi:10.1039/D0TA10113C.

124. Shah, K.A.; Tali, B.A. Synthesis of carbon nanotubes by catalytic chemical vapour deposition: A review on carbon sources, catalysts and substrates. *Materials Science in Semiconductor Processing* **2016**, *41*, 67-82, doi:https://doi.org/10.1016/j.mssp.2015.08.013.

125. Arora, N.; Sharma, N.N. Arc discharge synthesis of carbon nanotubes: Comprehensive review. *Diamond and Related Materials* **2014**, *50*, 135-150, doi:https://doi.org/10.1016/j.diamond.2014.10.001.

126. Baddour, C.E.; Fadlallah, F.; Nasuhoglu, D.; Mitra, R.; Vandsburger, L.; Meunier, J.-L. A simple thermal CVD method for carbon nanotube synthesis on stainless steel 304 without the addition of an external catalyst. *Carbon* **2009**, *47*, 313-318, doi:https://doi.org/10.1016/j.carbon.2008.10.038.

127. Hou, G.; Chauhan, D.; Ng, V.; Xu, C.; Yin, Z.; Paine, M.; Su, R.; Shanov, V.; Mast, D.; Schulz, M.; et al. Gas phase pyrolysis synthesis of carbon nanotubes at high temperature. *Materials & Design* **2017**, *132*, 112-118, doi:https://doi.org/10.1016/j.matdes.2017.06.070.

128. Salah, L.S.; Ouslimani, N.; Bousba, D.; Huynen, I.; Danlée, Y.; Aksas, H. Carbon Nanotubes (CNTs) from Synthesis to Functionalized (CNTs) Using Conventional and New Chemical Approaches. *Journal of Nanomaterials* **2021**, *2021*, 4972770, doi:10.1155/2021/4972770.

129. Ma, P.-C.; Siddiqui, N.A.; Marom, G.; Kim, J.-K. Dispersion and functionalization of carbon nanotubes for polymer-based nanocomposites: A review. *Composites Part A: Applied Science and Manufacturing* **2010**, *41*, 1345-1367, doi:https://doi.org/10.1016/j.compositesa.2010.07.003.

130. Norizan, M.N.; Moklis, M.H.; Ngah Demon, S.Z.; Halim, N.A.; Samsuri, A.; Mohamad, I.S.; Knight, V.F.; Abdullah, N. Carbon nanotubes: functionalisation and their application in chemical sensors. *RSC Advances* **2020**, *10*, 43704-43732, doi:10.1039/D0RA09438B.

131. Mc Carthy, B.; Coleman, J.N.; Czerw, R.; Dalton, A.B.; Carroll, D.L.; Blau, W.J. Microscopy studies of nanotube-conjugated polymer interactions. *Synthetic Metals* **2001**, *121*, 1225-1226, doi:https://doi.org/10.1016/S0379-6779(00)00906-1.

132. Hu, L.; Song, J.; Yin, X.; Su, Z.; Li, Z. Research Progress on Polymer Solar Cells Based on PEDOT:PSS Electrodes. *Polymers* **2020**, *12*, 145.

133. Jäckle, S.; Liebhaber, M.; Gersmann, C.; Mews, M.; Jäger, K.; Christiansen, S.; Lips, K. Potential of PEDOT:PSS as a hole selective front contact for silicon heterojunction solar cells. *Scientific Reports* **2017**, *7*, 2170, doi:10.1038/s41598-017-01946-3.

134. Li, Z.; Liang, Y.; Zhong, Z.; Qian, J.; Liang, G.; Zhao, K.; Shi, H.; Zhong, S.; Yin, Y.; Tian, W. A low-work-function, high-conductivity PEDOT:PSS electrode for organic solar cells with a simple structure. *Synthetic Metals* **2015**, *210*, 363-366, doi:https://doi.org/10.1016/j.synthmet.2015.11.006.

135. Shahrim, N.A.A.; Ahmad, Z.; Wong Azman, A.; Fachmi Buys, Y.; Sarifuddin, N. Mechanisms for doped PEDOT:PSS electrical conductivity improvement. *Materials Advances* **2021**, *2*, 7118-7138, doi:10.1039/D1MA00290B.

136. Xiong, Z.; Liu, C. Optimization of inkjet printed PEDOT:PSS thin films through annealing processes. *Organic Electronics* **2012**, *13*, 1532-1540, doi:https://doi.org/10.1016/j.orgel.2012.05.005.

137. Wang, G.-F.; Tao, X.-M.; Wang, R.-X. Fabrication and characterization of OLEDs using PEDOT:PSS and MWCNT nanocomposites. *Composites Science and Technology* **2008**, *68*, 2837-2841, doi:https://doi.org/10.1016/j.compscitech.2007.11.004.

138. Kim, J.C.; Rahman, M.M.; Ju, M.J.; Lee, J.-J. Highly conductive and stable graphene/PEDOT:PSS composite as a metal free cathode for organic dye-sensitized solar cells. *RSC Advances* **2018**, *8*, 19058-19066, doi:10.1039/C8RA02668H.

139. Alemu, D.; Wei, H.-Y.; Ho, K.-C.; Chu, C.-W. Highly conductive PEDOT:PSS electrode by simple film treatment with methanol for ITO-free polymer solar cells. *Energy & Environmental Science* **2012**, *5*, 9662-9671, doi:10.1039/C2EE22595F.

140. Khasim, S.; Pasha, A.; Badi, N.; Lakshmi, M.; Mishra, Y.K. High performance flexible supercapacitors based on secondary doped PEDOT–PSS–graphene nanocomposite films for large area solid state devices. *RSC Advances* **2020**, *10*, 10526-10539, doi:10.1039/D0RA01116A.

141. Cheng, T.; Zhang, Y.-Z.; Yi, J.-P.; Yang, L.; Zhang, J.-D.; Lai, W.-Y.; Huang, W. Inkjet-printed flexible, transparent and aesthetic energy storage devices based on PEDOT:PSS/Ag grid electrodes. *Journal of Materials Chemistry A* **2016**, *4*, 13754-13763, doi:10.1039/C6TA05319J.

142. Salar-Garcia, M.J.; Montilla, F.; Quijada, C.; Morallon, E.; Ieropoulos, I. Improving the power performance of urine-fed microbial fuel cells using PEDOT-PSS modified anodes. *Applied Energy* **2020**, *278*, 115528, doi:https://doi.org/10.1016/j.apenergy.2020.115528.

143. Luo, R.; Li, H.; Du, B.; Zhou, S.; Zhu, Y. A simple strategy for high stretchable, flexible and conductive polymer films based on PEDOT:PSS-PDMS blends. *Organic Electronics* **2020**, *76*, 105451, doi:https://doi.org/10.1016/j.orgel.2019.105451.

144. Döbbelin, M.; Marcilla, R.; Salsamendi, M.; Pozo-Gonzalo, C.; Carrasco, P.M.; Pomposo, J.A.; Mecerreyes, D. Influence of Ionic Liquids on the Electrical Conductivity and Morphology of PEDOT:PSS Films. *Chemistry of Materials* **2007**, *19*, 2147-2149, doi:10.1021/cm070398z.

145. Khasim, S.; Pasha, A.; Roy, A.S.; Parveen, A.; Badi, N. Effect of Secondary Doping Using Sorbitol on Structure and Transport Properties of PEDOT–PSS Thin Films. *Journal of Electronic Materials* **2017**, *46*, 4439-4447, doi:10.1007/s11664-017-5437-5.

146. Yamaguchi, H.; Aizawa, K.; Chonan, Y.; Komiyama, T.; Aoyama, T.; Sakai, E.; Qiu, J.; Sato, N. Highly Flexible and Conductive Glycerol-Doped PEDOT:PSS Films Prepared Under an Electric Field. *Journal of Electronic Materials* **2018**, *47*, 3370-3375, doi:10.1007/s11664-018-6292-8.

147. Xu, B.; Gopalan, S.-A.; Gopalan, A.-I.; Muthuchamy, N.; Lee, K.-P.; Lee, J.-S.; Jiang, Y.; Lee, S.-W.; Kim, S.-W.; Kim, J.-S.; et al. Functional solid additive modified PEDOT:PSS as an anode buffer layer for enhanced photovoltaic performance and stability in polymer solar cells. *Scientific Reports* **2017**, *7*, 45079, doi:10.1038/srep45079.

148. Meen, T.-H.; Chen, K.-L.; Chen, Y.-H.; Chen, W.-R.; Chou, D.-W.; Lan, W.-H.; Huang, C.-J. The Effects of Dilute Sulfuric Acid on Sheet Resistance and Transmittance in Poly(3,4-thylenedioxythiophene): Poly(styrenesulfonate) Films. *International Journal of Photoenergy* **2013**, *2013*, 843410, doi:10.1155/2013/843410.

149. Jang, H.; Kim, M.S.; Jang, W.; Son, H.; Wang, D.H.; Kim, F.S. Highly conductive PEDOT:PSS electrode obtained via post-treatment with alcoholic solvent for ITO-free organic solar cells. *Journal of Industrial and Engineering Chemistry* **2020**, *86*, 205-210, doi:https://doi.org/10.1016/j.jiec.2020.03.005.

150. Adekoya, G.J.; Sadiku, R.E.; Hamam, Y.; Ray, S.S.; Mwakikunga, B.W.; Folorunso, O.; Adekoya, O.C.; Lolu, O.J.; Biotidara, O.F. Pseudocapacitive material for energy storage application: PEDOT and PEDOT:PSS. *AIP Conference Proceedings* **2020**, *2289*, doi:10.1063/5.0028340.

151. Ma, J.H.; Kim, M.G.; Jeong, J.H.; Park, M.H.; Ha, H.J.; Kang, S.J.; Kang, S.J. Highly Efficient ITO-Free Quantum-Dot Light Emitting Diodes via Solution-Processed PEDOT:PSS Semitransparent Electrode. *Materials* **2023**, *16*, 4053.

152. Liu, L.; Li, S.; Wu, L.; Chen, D.; Cao, K.; Duan, Y.; Chen, S. Enhanced flexibility and stability of PEDOT:PSS electrodes through interfacial crosslinking for flexible organic light-emitting diodes. *Organic Electronics* **2021**, *89*, 106047, doi:https://doi.org/10.1016/j.orgel.2020.106047.

153. Youn, H.; Jeon, K.; Shin, S.; Yang, M. All-solution blade–slit coated polymer light-emitting diodes. *Organic Electronics* **2012**, *13*, 1470-1478, doi:https://doi.org/10.1016/j.orgel.2012.04.008.

154. Sinha, S.K.; Noh, Y.; Reljin, N.; Treich, G.M.; Hajeb-Mohammadalipour, S.; Guo, Y.; Chon, K.H.; Sotzing, G.A. Screen-Printed PEDOT:PSS Electrodes on Commercial Finished Textiles for Electrocardiography. *ACS Applied Materials & Interfaces* **2017**, *9*, 37524-37528, doi:10.1021/acsami.7b09954.

155. Tseng, S.-R.; Meng, H.-F.; Lee, K.-C.; Horng, S.-F. Multilayer polymer light-emitting diodes by blade coating method. *Applied Physics Letters* **2008**, *93*, doi:10.1063/1.2999541.

156. Donley, C.L.; Zaumseil, J.; Andreasen, J.W.; Nielsen, M.M.; Sirringhaus, H.; Friend, R.H.; Kim, J.-S. Effects of Packing Structure on the Optoelectronic and Charge Transport Properties in Poly(9,9-di-n-octylfluorene-alt-benzothiadiazole). *Journal of the American Chemical Society* **2005**, *127*, 12890-12899, doi:10.1021/ja051891j.

157. Cong, S.; Creamer, A.; Fei, Z.; Hillman, S.A.J.; Rapley, C.; Nelson, J.; Heeney, M. Tunable Control of the Hydrophilicity and Wettability of Conjugated Polymers by a Postpolymerization Modification Approach. *Macromolecular Bioscience* **2020**, *20*, 2000087, doi:https://doi.org/10.1002/mabi.202000087.

158. He, Y.; Gong, S.; Hattori, R.; Kanicki, J. High performance organic polymer light-emitting heterostructure devices. *Applied Physics Letters* **1999**, *74*, 2265-2267, doi:10.1063/1.123862.

159. Chua, L.-L.; Zaumseil, J.; Chang, J.-F.; Ou, E.C.W.; Ho, P.K.H.; Sirringhaus, H.; Friend, R.H. General observation of n-type field-effect behaviour in organic semiconductors. *Nature* **2005**, *434*, 194-199, doi:10.1038/nature03376.

160. Alehdaghi, H.; Marandi, M.; Irajizad, A.; Taghavinia, N. Influence of cathode roughness on the performance of F8BT based organic–inorganic light emitting diodes. *Organic Electronics* **2015**, *16*, 87-94, doi:https://doi.org/10.1016/j.orgel.2014.10.038.

161. Mbarek, M.; Sagaama, L.; Alimi, K. New copolymer involving PVK and F8BT for organic solar cells applications: Design, synthesis, characterization and theoretical studies. *Optical Materials* **2019**, *91*, 447-454, doi:https://doi.org/10.1016/j.optmat.2019.03.053.

162. Shu, S.; Xu, T.; Su, J. A flexible floating-gate based organic field-effect transistor non-volatile memory based on F8BT/PMMA integrated floating-gate/tunneling layer. *Physica Scripta* **2023**, *98*, 045402, doi:10.1088/1402-4896/acbdce.

163. Mamada, M.; Komatsu, R.; Adachi, C. F8BT Oligomers for Organic Solid-State Lasers. *ACS Applied Materials & Interfaces* **2020**, *12*, 28383-28391, doi:10.1021/acsami.0c05449.

164. Faria, J.C.D.; Campbell, A.J.; McLachlan, M.A. Fluorene copolymer bilayers for emission colour tuning in inverted hybrid light emitting diodes. *Journal of Materials Chemistry C* **2015**, *3*, 4945-4953, doi:10.1039/C5TC00263J.

165. Noebels, M.; Cross, R.E.; Evans, D.A.; Finlayson, C.E. Characterization of spray-coating methods for conjugated polymer blend thin films. *Journal of Materials Science* **2014**, *49*, 4279-4287, doi:10.1007/s10853-014-8123-5.

166. Kim, J.-S.; Lu, L.; Sreearunothai, P.; Seeley, A.; Yim, K.-H.; Petrozza, A.; Murphy, C.E.; Beljonne, D.; Cornil, J.; Friend, R.H. Optoelectronic and Charge Transport Properties at Organic–Organic Semiconductor Interfaces: Comparison between Polyfluorene-Based Polymer Blend and Copolymer. *Journal of the American Chemical Society* **2008**, *130*, 13120-13131, doi:10.1021/ja803766j.

167. Lattante, S.; Cretí, A.; Lomascolo, M.; Anni, M. On the correlation between morphology and Amplified Spontaneous Emission properties of a polymer: Polymer blend. *Organic Electronics* **2016**, *29*, 44-49, doi:https://doi.org/10.1016/j.orgel.2015.11.027.

168. Bolink, H.J.; Coronado, E.; Repetto, D.; Sessolo, M. Air stable hybrid organic-inorganic light emitting diodes using ZnO as the cathode. *Applied Physics Letters* **2007**, *91*, doi:10.1063/1.2809387.

169. C, A.; Pahlevani, M.; Welch, G.C. Organic light emitting diodes (OLEDs) with slot-die coated functional layers. *Materials Advances* **2021**, *2*, 628-645, doi:10.1039/D0MA00903B.

170. Sun, K.; Zhang, S.; Li, P.; Xia, Y.; Zhang, X.; Du, D.; Isikgor, F.H.; Ouyang, J. Review on application of PEDOTs and PEDOT:PSS in energy conversion and storage devices. *Journal of Materials Science: Materials in Electronics* **2015**, *26*, 4438-4462, doi:10.1007/s10854-015-2895-5.

171. Choi, S.; Kim, W.; Shin, W.; Oh, J.; Jin, S.; Jung, Y.M.; Ryu, M.-Y.; Lee, H. Effects of UV-ozone treatment on the electronic structures of F8BT and PFO polymeric thin films. *Current Applied Physics* **2020**, *20*, 1359-1365, doi:https://doi.org/10.1016/j.cap.2020.08.015.

172. Hui, R. Chapter 4 - Photodetectors. In *Introduction to Fiber-Optic Communications*, Hui, R., Ed.; Academic Press: 2020; pp. 125-154.

173. Hariharan, P. Chapter 7 - Detectors. In *Basics of Interferometry*, Hariharan, P., Ed.; Academic Press: San Diego, 1992; pp. 57-65.

174. Anderson, L.K.; McMurtry, B.J. High-speed photodetectors. *Appl Opt* **1966**, *5*, 1573-1587, doi:10.1364/ao.5.001573.

175. Marghany, M. Chapter 3 - Quantization of Maxwell's equations. In *Synthetic Aperture Radar Imaging Mechanism for Oil Spills*, Marghany, M., Ed.; Gulf Professional Publishing: 2020; pp. 41-60.

176. García, J.; Delgado, F.J.; Ortega, P.R.; Bermejo, S. 17 - Photovoltaic and fuel cells in power microelectromechanical systems for smart energy management. In *Smart Sensors and MEMs (Second Edition)*, Nihtianov, S., Luque, A., Eds.; Woodhead Publishing: 2018; pp. 461-498.

177. Asadi, F. A simple method for accurate modeling of diode parameters. *Energy Reports* **2022**, *8*, 155-162, doi:https://doi.org/10.1016/j.egyr.2022.05.136.

178. Stiff-Roberts, A.D. 6.11 - Quantum-Dot Infrared Photodetectors. In *Comprehensive Semiconductor Science and Technology*, Bhattacharya, P., Fornari, R., Kamimura, H., Eds.; Elsevier: Amsterdam, 2011; pp. 452-485.

179. Komatsu, H.; Kawamoto, Y.; Ikuno, T. Freestanding Translucent ZnO–Cellulose Nanocomposite Films for Ultraviolet Sensor Applications. *Nanomaterials* **2022**, *12*, 940.

180. Mousavi, S.S.; Sajad, B.; Majlesara, M.H. Fast response ZnO/PVA nanocomposite-based photodiodes modified by graphene quantum dots. *Materials & Design* **2019**, *162*, 249-255, doi:https://doi.org/10.1016/j.matdes.2018.11.037.

181. Cheung, S.K.; Cheung, N.W. Extraction of Schottky diode parameters from forward current-voltage characteristics. *Applied Physics Letters* **1986**, *49*, 85-87, doi:10.1063/1.97359.

182. Imran, M.; Haider, S.; Ahmad, K.; Mahmood, A.; Al-masry, W.A. Fabrication and characterization of zinc oxide nanofibers for renewable energy applications. *Arabian Journal of Chemistry* **2017**, *10*, S1067-S1072, doi:https://doi.org/10.1016/j.arabjc.2013.01.013.

183. Arefi, M.R.; Rezaei-Zarchi, S. Synthesis of Zinc Oxide Nanoparticles and Their Effect on the Compressive Strength and Setting Time of

Self-Compacted Concrete Paste as Cementitious Composites. *Int. J. Mol. Sci.* **2012**, *13*, 4340-4350.

184. Hu, Z.; Escamilla Ramírez, D.J.; Heredia Cervera, B.E.; Oskam, G.; Searson, P.C. Synthesis of ZnO Nanoparticles in 2-Propanol by Reaction with Water. *The Journal of Physical Chemistry B* **2005**, *109*, 11209-11214, doi:10.1021/jp0506033.

185. Ha, T.T.; Canh, T.D.; Tuyen, N.V. A Quick Process for Synthesis of ZnO Nanoparticles with the Aid of Microwave Irradiation. *ISRN Nanotechnology* **2013**, *2013*, 497873.

186. Sharma, D.; Jha, R. Analysis of structural, optical and magnetic properties of Fe/Co co-doped ZnO nanocrystals. *Ceram. Int.* **2017**, *43*, 8488-8496.

187. Xiong, G.; Pal, U.; Serrano, J.G. Correlations among size, defects, and photoluminescence in ZnO nanoparticles. *J. Appl. Phys.* **2007**, *101*, 024317.

188. Wahab, R.; Ansari, S.G.; Kim, Y.S.; Song, M.; Shin, H.-S. The role of pH variation on the growth of zinc oxide nanostructures. *Applied Surface Science* **2009**, *255*, 4891-4896, doi:https://doi.org/10.1016/j.apsusc.2008.12.037.

189. Aïssa, B.; Fauteux, C.; El Khakani, M.A.; Daniel, T. Structural and photoluminescence properties of laser processed ZnO/carbon nanotube nanohybrids. *Journal of Materials Research* **2009**, *24*, 3313-3320, doi:10.1557/jmr.2009.0421.

190. Rossell, M.D.; Kuebel, C.; Ilari, G.; Rechberger, F.; Heiligtag, F.J.; Niederberger, M.; Koziej, D.; Erni, R. Impact of sonication pretreatment on carbon nanotubes: A transmission electron microscopy study. *Carbon* **2013**, *61*, 404-411, doi:https://doi.org/10.1016/j.carbon.2013.05.024.

191. Sahai, A.; Goswami, N. Probing the dominance of interstitial oxygen defects in ZnO nanoparticles through structural and optical characterizations. *Ceramics International* **2014**, *40*, 14569-14578, doi:https://doi.org/10.1016/j.ceramint.2014.06.041.

192. Aljawfi, R.N.; Alam, M.J.; Rahman, F.; Ahmad, S.; Shahee, A.; Kumar, S. Impact of annealing on the structural and optical properties of ZnO nanoparticles and tracing the formation of clusters via DFT calculation. *Arabian Journal of Chemistry* **2020**, *13*, 2207-2218, doi:https://doi.org/10.1016/j.arabjc.2018.04.006.

193. Montanheiro, T.L.d.A.; de Menezes, B.R.C.; Ribas, R.G.; Montagna, L.S.; Campos, T.M.B.; Schatkoski, V.M.; Righetti, V.A.N.; Passador, F.R.; Thim, G.P. Covalently γ-aminobutyric acid-functionalized carbon nanotubes: improved compatibility with PHBV matrix. *SN Applied Sciences* **2019**, *1*, 1177, doi:10.1007/s42452-019-1224-7.

194. Sharma, A.; Singh, B.P.; Dhar, S.; Gondorf, A.; Spasova, M. Effect of surface groups on the luminescence property of ZnO nanoparticles synthesized by sol–gel route. *Surface Science* **2012**, *606*, L13-L17, doi:https://doi.org/10.1016/j.susc.2011.09.006.

195. Chang, S.H.; Chiang, C.H.; Kao, F.S.; Tien, C.L.; Wu, C.G. Unraveling the Enhanced Electrical Conductivity of PEDOT:PSS Thin Films for ITO-Free Organic Photovoltaics. *IEEE Photonics Journal* **2014**, *6*, 1-7, doi:10.1109/JPHOT.2014.2331254.

196. Lee, H.; Kim, Y.; Cho, H.; Lee, J.-g.; Kim, J.H. Improvement of PEDOT:PSS linearity via controlled addition process. *RSC Advances* **2019**, *9*, 17318-17324, doi:10.1039/C9RA03040A.

197. Davis, K.; Yarbrough, R.; Froeschle, M.; White, J.; Rathnayake, H. Band gap engineered zinc oxide nanostructures via a sol–gel synthesis of solvent driven shape-controlled crystal growth. *RSC Advances* **2019**, *9*, 14638-14648, doi:10.1039/C9RA02091H.

198. Jafarova, V.N.; Orudzhev, G.S. Structural and electronic properties of ZnO: A first-principles density-functional theory study within LDA(GGA) and LDA(GGA)+U methods. *Solid State Communications* **2021**, *325*, 114166, doi:https://doi.org/10.1016/j.ssc.2020.114166.

199. Rauwel, P.; Galeckas, A.; Salumaa, M.; Ducroquet, F.; Rauwel, E. Photocurrent generation in carbon nanotube/cubic-phase HfO2 nanoparticle hybrid nanocomposites. *Beilstein J Nanotechnol* **2016**, *7*, 1075-1085, doi:10.3762/bjnano.7.101.

200. Janotti, A.; Van de Walle, C.G. Native point defects in ZnO. *Physical Review B* **2007**, *76*, 165202, doi:10.1103/PhysRevB.76.165202.

201. Zhou, Q.; Wen, J.Z.; Zhao, P.; Anderson, W.A. Synthesis of Vertically-Aligned Zinc Oxide Nanowires and Their Application as a Photocatalyst. *Nanomaterials* **2017**, *7*, 9.

202. Murillo, G.; Leon-Salguero, E.; Martínez-Alanis, P.R.; Esteve, J.; Alvarado-Rivera, J.; Güell, F. Role of aluminum and HMTA in

the hydrothermal synthesis of two-dimensional n-doped ZnO nanosheets. *Nano Energy* **2019**, *60*, 817-826, doi:https://doi.org/10.1016/j.nanoen.2019.04.017.

203. Parize, R.; Garnier, J.; Chaix-Pluchery, O.; Verrier, C.; Appert, E.; Consonni, V. Effects of Hexamethylenetetramine on the Nucleation and Radial Growth of ZnO Nanowires by Chemical Bath Deposition. *The Journal of Physical Chemistry C* **2016**, *120*, 5242-5250, doi:10.1021/acs.jpcc.6b00479.

204. Alvi, N.H.; ul Hasan, K.; Nur, O.; Willander, M. The origin of the red emission in n-ZnO nanotubes/p-GaN white light emitting diodes. *Nanoscale Research Letters* **2011**, *6*, 130, doi:10.1186/1556-276X-6-130.

205. Liao, Z.-M.; Xu, J.; Zhang, J.-M.; Yu, D.-P. Photovoltaic effect and charge storage in single ZnO nanowires. *Applied Physics Letters* **2008**, *93*, doi:10.1063/1.2957470.

206. Saxena, R.S. Study on Photoconductivity in Air and Vacuum of ZnO Prepared by different materials. *International Journal for Research in Applied Science and Engineering Technology* **2018**, *6*, 2466-2471.

207. Kushwaha, A.; Aslam, M. Defect induced high photocurrent in solution grown vertically aligned ZnO nanowire array films. *Journal of Applied Physics* **2012**, *112*, doi:10.1063/1.4749808.

208. Hullavarad, S.; Hullavarad, N.; Look, D.; Claflin, B. Persistent Photoconductivity Studies in Nanostructured ZnO UV Sensors. *Nanoscale Research Letters* **2009**, *4*, 1421, doi:10.1007/s11671-009-9414-7.

209. Hwang, J.D.; Lee, K.S. A High Rectification Ratio Nanocrystalline p–n Junction Diode Prepared by Metal-Induced Lateral Crystallization for Solar Cell Applications. *Journal of The Electrochemical Society* **2008**, *155*, H259, doi:10.1149/1.2840618.

210. Lee, G.W.; Shim, J.-I.; Shin, D.-S. On the ideality factor of the radiative recombination current in semiconductor light-emitting diodes. *Applied Physics Letters* **2016**, *109*, doi:10.1063/1.4959081.

211. Breitenstein, O.; Altermatt, P.; Ramspeck, K.; Schenk, A. *The Origin of Ideality factors n > 2 of Shunts and Surfaces in the Dark I-V Curves of Si Solar Cells*; 2006.

212. Lin, Y.; Zou, J.; Wang, W.; Liu, X.; Gao, J.; Lu, Z. High-performance self-powered ultraviolet photodetector based on PEDOT:PSS/CuO/ZnO nanorod array sandwich structure. *Applied Surface Science* **2022**, *599*, 153956, doi:https://doi.org/10.1016/j.apsusc.2022.153956.

213. Wang, X.; Xu, H.; Zhang, Y.; Ji, X.; Zhang, R. Fructose-regulated ZnO single-crystal nanosheets with oxygen vacancies for photodegradation of high concentration pollutants and photocatalytic hydrogen evolution. *Ceramics International* **2021**, *47*, 16170-16177, doi:https://doi.org/10.1016/j.ceramint.2021.02.193.

214. Zhang, J.; Li, J. The Oxygen Vacancy Defect of ZnO/NiO Nanomaterials Improves Photocatalytic Performance and Ammonia Sensing Performance. *Nanomaterials* **2022**, *12*, 433.

215. Monroy, E.; Omnès, F.; Calle, F. Wide-bandgap semiconductor ultraviolet photodetectors. *Semiconductor Science and Technology* **2003**, *18*, R33, doi:10.1088/0268-1242/18/4/201.

SUMMARY

This thesis demonstrates the fabrication of cost-effective and energy-efficient photodiodes for UV detection applications. It focuses on the growth of 1D ZnO nanorods and their role in UV detection, on their own and in a diode configuration. The produced photodiodes were fabricated by cost-effective methods and were evaluated in terms of their external quantum efficiencies (EQE). Four alcohol seeding solvents were used for the ZnO-nanorod growth that influenced the generation of defects within. The latter was studied by precipitating freestanding ZnO-nanoparticles via hydrothermal sol-gel routes using the same seeding solvents, as well as by optimizing synthesis conditions. In fact, for a similar solvent the ZnO nanorods show similar defects as ZnO nanoparticles, with significant differences in their optical emission intensities. Therefore, the novelty of the thesis lies in correlating the defect states in the nanorods to the figures of merit of the photodiodes, as a function of seeding solvents applied for their growth. Furthermore, ZnO nanorods on their own have shown charge storage and UV sensing properties, owing to the defect-related phenomenon of persistent photoconductivity and due to the wide band gap of ZnO (~3.3 eV), respectively. Persistent photoconductivity is an asset for charge storage, but detrimental for UV detection. Therefore, the UV sensing properties were enhanced by devising a hybrid p-n junction, consisting of n-type ZnO nanorods and p-type F8BT and PEDOT:PSS polymers. Subsequently, the effect of persistent photoconductivity was reduced through the passivation of defects by the polymers. Nevertheless, the remnant defect states in ZnO nanorods have shown a significant influence on the figures of merit of the photodiodes. This work enabled identifying the best performing photodiode, which was grown with the absolute methanol seeding layer. This photodiode exhibited this best surface coverage of ZnO nanorods, the highest rectification ratio of ~640 with a negligible dark current, a good ideality factor of 2, a high sensitivity of 2.4 and responsivity of 8.14 A/w. The very high EQE of ~2760% at a bias of -2 V, denotes a highly energy-efficient photodiode. To the best of our knowledge, no other study demonstrates the effect of seeding solvents on the production of defects in ZnO nanorods and subsequently, on the figures of merit of the photodiodes. In addition, the incorporation of p-type F8BT polymer with n-type ZnO nanorods and p-type PEDOT:PSS polymer within a diode configuration itself is novel for UV photodiode applications. Therefore, this approach has

contributed to not only a new scientific understanding of the working of ZnO-polymer based hybrid photodiodes, but it also unfolds a new route to fabricate UV photodiodes with an additional F8BT interlayer. A further understanding of the photodiode configuration, such as thickness of different layers and their surface areas is now necessary to improve their figures of merit or the photodiode performance.

KOKKUVÕTE

Doktoritöös uuriti kulutõhusate ja energiasäästlike fotodioodide valmistamist ultraviolettkiirguse (UV-kiirguse) tuvastamise jaoks. Uurimuses keskenduti ühemõõtmeliste tsinkoksiidist (ZnO) nanovarraste valmistamisele ja nende kasutamisele UV-kiirguse tuvastuses eraldi ning fotodioodi konfiguratsioonis. Fotodioodid valmistati kulutõhusate meetoditega ning hinnati välise kvantefektiivsuse (ingl *external quantum efficiencies*, EQE) järgi. ZnO-nanovarda valmistamiseks kasutati nelja alkohoolset külvilahust, mis mõjutasid defektide teket varrastel. Samuti uuriti ZnO-nanoosakeste sadestamist hüdrotermilise sool-geel meetodi abil, kasutades samu külvilahuseid ning optimeerides sünteesitingimusi. Sama lahuse puhul on ZnO-nanovarrastel ja ZnO-nanoosakestel ühesugused defektid, erinev on vaid nende optilise emissiooni intensiivsus. Seetõttu seisneb uurimistöö uudsus nanovarraste defektiseisundite korreleerimises fotodioodide väärtusnäitajatega, sõltuvalt varraste valmistamiseks kasutatud külvilahustest. Lisaks ilmnesid ZnO-nanovarrastel laengu salvestamise ja UV-kiirgustundlikkuse omadused, mis on tingitud püsiva fotojuhtivuse defektiga seotud nähtusest ning ZnO suurest ribalaiusest (~3,3 eV). Püsiv fotojuhtivus on laengu salvestamise eelis, kuid ebasobiv UV-kiirguse tuvastamisel. Seetõttu muudeti varda UV-kiirgustundlikkust hübriidse p-n-ülemineku väljatöötamisega, mis koosnes n-tüüpi ZnO-nanovarrastest ning p-tüüpi F8BT ja PEDOT: PSS polümeeridest. Polümeeride defektide passiivistamisega püsiva fotojuhtivuse mõju vähenes. Sellegipoolest on ZnO-nanovarraste jääkdefektidel oluline mõju fotodioodide omadustele.

Uurimistöö võimaldas tuvastada kõige paremini toimiva fotodioodi, mida kasvatati absoluutse metanooli külvikihiga. Sellel fotodioodil oli ZnO-nanovarraste parim pinnakate, kõrgeim alaldussuhe ~640 tühise tumevooluga, hea ideaalsustegur 2, kõrge tundlikkus 2,4 ja reageerimistase 8,14 A/W. Kõrge EQE (~2760%) viitab fotodioodi energiasäästlikkusele. Meie teadmiste kohaselt ei näita ükski teine uuring külvilahuse mõju ZnO-nanovarraste defektide tekkele ja seejärel fotodioodide omadustele. Lisaks on uudne p-tüüpi F8BT polümeeri lisamine n-tüüpi ZnO-nanovarrastesse ning p-tüüpi PEDOT: PSS polümeeri lisamine dioodikonfiguratsioonis UV-kiirguse fotodiioodirakenduste jaoks. Uurimuses kirjeldatud lähenemine aitab kaasa uuele teaduslikule arusaamale ZnO-polümeeril põhinevate hübriidfotodioodide tööst ning

avab ka uue tee kulutõhusate, täiendava F8BT vahekihiga UV-kiirguse fotodioodide valmistamiseks.

Edaspidi on vajalik fotodioodide konfiguratsiooni, näiteks erinevate kihtide paksuse ja pindala mõju täiendav uurimine fotodioodi väärtusnäitajate ja jõudluse parandamiseks.

ACKNOWLEDMENTS

I

ORIGINAL PUBLICATIONS

K. Nagpal, L. Rapenne, D. S. Wragg, E. Rauwel, P. Rauwel, "The role of CNT in surface defect passivation and UV emission intensification of ZnO nanoparticles" Nanomaterials and Nanotechnology, **12**, 1–10 (2022)

The role of CNT in surface defect passivation and UV emission intensification of ZnO nanoparticles

Keshav Nagpal[1] [iD], Laetitia Rapenne[2], David S Wragg[3] [iD], Erwan Rauwel[1] [iD] and Protima Rauwel[1] [iD]

Abstract

We report on the controlled enhancement of the UV emission from ZnO nanoparticles synthesized via hydrothermal sol-gel routes. Various characterization techniques were used in this study to determine the crystal structure, defect formation, morphology and size of the ZnO nanoparticles. Firstly, the crystallinity of the ZnO nanoparticles was assessed by X-ray diffraction. The role of the precursor quantities on their morphology and bandgap states was investigated via transmission electron microscopy and photoluminescence spectroscopy, respectively. Subsequently, the impurity content and related bonds were evaluated by Fourier-transform infrared spectroscopy. In this work, the ZnO nanoparticles manifest a sharp UV emission along with a subdued green emission in the visible region. Conjoining ZnO with carbon nanotubes (CNT) suppressed the visible emission, as well as blueshifted and intensified the UV emission by ~5-fold. These results suggest that CNT are effective in passivating the surface states of ZnO nanoparticles.

Introduction

ZnO is a semiconductor material that has attracted interest for a wide range of applications, such as solar cells,[1] light emitting diodes[2,3] and other optoelectronic devices.[4,5] Its most significant properties are a wide bandgap of 3.36 eV along with a high exciton binding energy of 60 meV at room temperature.[6] ZnO is therefore considered suitable for a variety of short-wavelength devices, viz. Ultraviolet (UV) light emitting diodes, UV lasers and tuneable UV photodetectors.[7,8] For the preceding devices, nanostructures, especially nanoparticles of ZnO have been widely studied.[9,10] However, obtaining pure UV emission from nanoparticles of ZnO is challenging due to the large quantities of surface and volume defects they harbour. These defects tend to augment the visible emission at the detriment of the UV emission. Their photoluminescence (PL) spectrum is composed of two main emission peaks: a near band-edge emission (NBE) in the UV region and defect level emission (DLE) in the visible region.

[1]Institute of Forestry and Engineering Sciences, Estonian University of Life Sciences, Tartu, Estonia
[2]Univ. Grenoble Alpes, CNRS, Grenoble Institute of Engineering, Grenoble, France
[3]Department of Chemistry and SMN, University of OSLO, Norway

Corresponding author:
Protima Rauwel, Institute of Technology, Estonian University of Life Sciences, Kreutzwaldi 56-1, Tartu 51014, Estonia.
Email: protima.rauwel@emu.ee

The NBE originates from the recombination of free excitons due to band-to-band transitions, whereas the DLE arises from surface or volume defect states, such as oxygen vacancies (Vo) and zinc interstitials (Zn_i).[11] In effect, surface defects or impurities trap a large number of photogenerated electrons. Furthermore, the NBE diminishes when the particle size reduces or the surface to volume ratio increases, whereupon the DLE dominates the emission spectrum owing to a higher amount of surface defects.[12–15] Therefore, strategies to enhance the NBE consist of supressing defect formation during synthesis or post-growth.[16,17] Several, methods have been investigated to that end, which include surface state modification of ZnO by TiO_2 and Al_2O_3 capping layers; hydrogenation[18–20]; annealing under N_2 and O_2[21–23]; controlling defects during synthesis itself[24,25]; and conjoining them with metal nanoparticles displaying surface plasmon resonance.[26,27]

Organic and inorganic materials have witnessed enhancements in physical, chemical and structural properties when combined with CNT. For instance, $CoFe_2O_4$-CNT present higher electromagnetic shielding, while as Sn–Ag–Cu composites benefit from better structural and electrical properties in solder joints for certain concentrations of CNT.[28,29] Similarly, for flexible electronics, polyaniline-CNT hydrogels have demonstrated excellent electrical conductivity owing to their high dispersion in hydrogel-based matrices.[30] Furthermore, combining CNT with rubber increases the resistance-strain response of the composite.[31] CNT are produced by several different synthesis routes such as chemical vapour deposition, electric arc discharge and laser ablation.[32] Due to their inertness, functionalizing CNT, that is, attaching functional organic moieties to the walls of the CNT is a prerequisite to combining them with other organic and inorganic materials. Functional moieties include amine, ester, carboxyl, carbonyl and hydroxyl groups.[32,33] Sonication is also a viable method of activating the CNT walls and rendering them receptive to inorganic nanoparticles.[15,34–36]

In a previous work, the influence of hydrated precursors on the surface defects of ZnO nanoparticles synthesized via non-aqueous sol-gel routes was investigated. The results demonstrated that the hydrates present in ZnO tend to enhance the NBE and diminish the green emission component of the DLE due to improved oxidation of ZnO during synthesis.[37] However, even though hydrated precursors are efficient at suppressing volume-related defects, surface-related defects nevertheless persist. Subsequently, the ZnO nanoparticles were combined with carbon nanotubes (CNT) in order to passivate residual defect states,[38] which then enhance the UV emission. Lastly, enhancing the UV emission from ZnO-CNT nanohybrids could also be beneficial for other applications, including photocatalysis,[39] charge separation,[40] field electron emission,[41] photoresponse,[42] gas or electrochemical sensors[43,44] and other optoelectronic devices.[45]

This manuscript reports on the effect of varying NaOH and Zn precursor ratio on the properties of ZnO nanoparticles prepared via hydrothermal sol-gel routes. In addition, these ratios provide an approach to controlling the size of the nanoparticles and consequently, the formation of surface defects. Moreover, by combining the as-synthesized ZnO nanoparticles with CNT, it is further possible to reduce the residual surface states in order to obtain a notable enhancement in the UV emission. The optical properties are discussed in terms of the synthesis conditions, crystal structure, chemical properties and morphology of the samples.

Materials and methods

Synthesis

ZnO. All the chemicals used for the syntheses of ZnO nanoparticles were of analytical reagent grade. In order to prepare a 0.05 M solution, 219.5 mg of zinc acetate dihydrate $(Zn(CH_3CO_2)_2.2H_2O)$ (99.9%, Aldrich) was dissolved in 20 ml of aqueous ethanol (70%) in a beaker placed in a water bath. The solution was maintained at 60^0C under continuous magnetic stirring until a transparent solution was obtained. Further, 0.075 M, 0.10 M, 0.125 M and 0.15 M solutions of NaOH (99.9%, Aldrich) in 20 ml of aqueous ethanol (70%) were prepared and added drop wise to 0.05 M precursor solutions to obtain 1:1.5, 1:2, 1:2.5 and 1:3 ratios, respectively. Thereafter, the mixtures were maintained at 60^0C for 2 h and cooled to ambient temperature. After cooling, white ZnO precipitates settled at the bottom of the reaction vessel. The resulting solutions containing ZnO nanoparticles were then centrifuged at 4500 r/min for 6 min and dried for 24 h in air at 60^0C. This resulted in an agglomeration of ZnO nanoparticles in the form of a porous pellet, which is typical after drying nanoparticles synthesized via sol-gel and hydrothermal synthesis routes. These pellets were thereafter gently crushed using a pestle and mortar to obtain very fine nanopowders of ZnO nanoparticles. Nanopowders consist of well-dispersed ZnO nanoparticles that are necessary to create ZnO-CNT hybrids.

ZnO-CNT nanohybrids. For the preparation of ZnO-CNT nanohybrids (16.66 wt%), 2 mg of NANOCYL NC7000 multi-walled carbon nanotubes (MWCNT) were mixed with 10 mg of ZnO nanoparticles synthesized with precursor to NaOH molar ratios of 1:1.5 and 1:3. Absolute ethanol was added to the mixture and the solution was sonicated for 5 min. Thereafter, the ZnO-CNT mixtures were dried in air at 60^0C for 24 h. The resulting ZnO-CNT pellets were further crushed to obtain a very fine black powder.

Characterization

X-ray diffraction patterns were collected in Bragg–Brentano geometry using a Bruker D8 Discover diffractometer (Bruker AXS, Germany) with CuKα1 radiation (λ = 0.15,406 nm)

Table 1. List of ZnO samples and ZnO-CNT nanohybrids synthesized in this work. The quantity of the $Zn(CH_3CO_2)_2.2H_2O$ precursor was fixed at 0.2195 g.

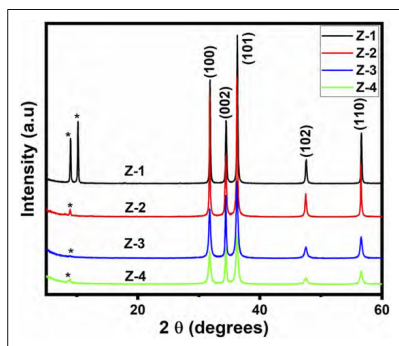| Sample	NaOH quantity (g)	Molar ratio	CNT quantity (mg)
Z–1	0.0599	1:1.5	—
Z–2	0.0799	1:2	—
Z–3	0.0999	1:2.5	—
Z–4	0.1199	1:3	—
Z–1–CNT	0.0599	1:1.5	2
Z–4–CNT	0.1199	1:3	2

Figure 1. XRD patterns of ZnO samples Z–1, Z–2, Z–3 and Z–4. The peaks marked with (*) indicate the presence of unreacted precursor.

selected by a Ge (111) monochromator and LynxEye detector. Transmission electron microscopy (TEM) was carried out on a JEOL 2010 LaB$_6$ TEM (JEOL, Japan) operating at 200 kV in TEM mode and providing a point-to-point resolution of 1.9 Å. Fourier-transform infrared (FTIR) spectrometer (Nicolet is[10] Thermo Scientific, Germany) was cooled with liquid nitrogen for FTIR measurements in the range of 540–4000 cm^{-1}. The optical absorbance of ZnO and ZnO-CNT nanohybrids were determined using a NANOCOLOR UV-VIS II spectrometer (MACHEREY-NAGEL, Germany) in 200–900 nm region. The bandgap of ZnO and ZnO-CNT nanohybrids were subsequently calculated with Tauc plots. PL spectroscopy was carried out at room temperature with an excitation wavelength of 365 nm of a LSM-365A LED (Ocean insight, USA) with a specified output power of 10 mW. The emission was collected by FLAME UV-–Vis spectrometer (Ocean optics, USA) with spectral resolution 1.34 nm. Optical images of ZnO were taken under UV lamp ZLUV220 with an excitation source of 365 nm.
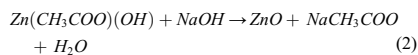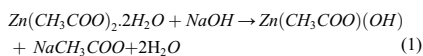
Result and discussion

Table 1 provides a list of ZnO samples and ZnO-CNT nanohybrids synthesized in this work. Samples Z–1, Z–2,

Z–3 and Z–4 correspond to molar ratio 1:1.5, 1:2, 1:2.5 and 1:3 of $Zn(CH_3CO_2)_2.2H_2O$ to NaOH, respectively. Samples Z–1–CNT and Z–4–CNT correspond to ZnO-CNT nano-hybrids. In this study, the term 'ZnO samples' refers to samples Z–1, Z–2, Z–3 and Z–4 and the term ZnO-CNT refers to the hybrid samples of Z–1–CNT and Z–4–CNT.

Structure and morphology

XRD patterns of the ZnO samples are shown in Figure 1. The peaks (100), (002), (101), (102) and (110) correspond to the hexagonal wurtzite structure (a = 3.25 Å and c = 5.20 Å) of ZnO (JCPDS, Card Number 36–1451).[46,47] The spectra also indicate the presence of unreacted precursor $Zn(CH_3CO_2)_2.2H_2O$ (marked with *). The precipitation of ZnO nanoparticles are described by the following chemical reactions[48]:

$$Zn(CH_3COO)_2.2H_2O + NaOH \rightarrow Zn(CH_3COO)(OH) + NaCH_3COO + 2H_2O \quad (1)$$

$$Zn(CH_3COO)(OH) + NaOH \rightarrow ZnO + NaCH_3COO + H_2O \quad (2)$$

The reactions of equations (1) and (2) indicate that the formation of ZnO nanoparticles depends on the quantity of NaOH that controls the reaction kinetics.[49] Varying the pH via the NaOH content is commonly used in non-aqueous or hydrolytic sol-gel routes for ZnO nanoparticle synthesis. In hydrothermal synthesis, increasing the quantity of NaOH for a fixed concentration of $Zn(CH_3CO_2)_2.2H_2O$ precursor, increases the pH of the solution and the reaction kinetics, which in turn, decreases the particle size and modifies the surface defects. Additionally, the presence of $Zn(CH_3COO)(OH)$ suggests an incomplete reaction, which can therefore be attributed to an insufficient quantity of NaOH. The XRD pattern of sample Z–1 exhibits the most intense diffraction peaks of the unreacted precursor followed by Z–2. A less intense peak is also visible for the sample with the highest quantity of NaOH, that is, Z–4. On the other hand, for sample Z–3, this peak is the least intense. Co-workers

Table 2. List of particle sizes estimated from the Scherrer equation with their corresponding shapes obtained from TEM.

Ratio of precursor to NaOH	XRD (estimated particle size from Scherrer equation)	T, nmEM (nanoparticle shape)
1:1.5 (Z–1)	43.09	Hexagonal, rod and rectangular
1:2 (Z–2)	47.52	Hexagonal and needle-like
1:2.5 (Z–3)	26.15	No defined shape
1:3 (Z–4)	20.53	Spherical and facetted
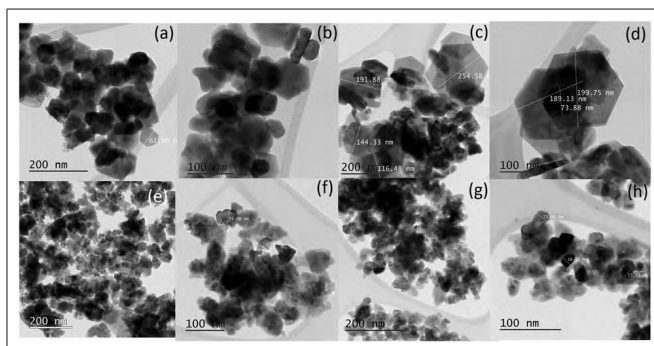
Figure 2. TEM images of the as-synthesized ZnO samples. Overview images: (a) Z–1 (c) Z–2 (e) Z–3 and (f) Z–4. High magnification TEM images: (b) Z–1 (d) Z–2 (f) Z–3 and (h) Z–4.

usually calcine the ZnO sample in order to remove impurities and unreacted precursors.[48] However, calcination changes the defect states of ZnO. Our aim is to evaluate the properties of the as-synthesized ZnO nanoparticles.

Furthermore, a qualitative idea of the size of ZnO nanoparticles was obtained by calculating the full width at half maximum (FWHM) of the (002) reflection for all the ZnO samples. These FWHM values are 0.193°, 0.175°, 0.318° and 0.405° for samples Z–1, Z–2, Z–3 and Z–4, respectively. The FWHM tends to increase with the NaOH quantity implying that the average size of the nanoparticles decreases. Subsequently, the FWHM values were applied to the Scherrer formula in equation (3) in order to obtain ZnO nanoparticle sizes[50] (Table 2). The Scherrer equation gives a single size value based on the assumption that the crystallites are spherical. Since TEM analyses reveal several nanoparticle morphologies, the Scherrer equation therefore provides only limited insight into the nanoparticle sizes. Nevertheless, it does indicate a general tendency of reduction in particle size as a function of increase in NaOH quantities.

$$D = \frac{0.9\lambda}{\beta \cos\theta} \quad (3)$$

where D is particle size, λ (= 0.15,406 nm) is the wavelength of incident X-ray beam, β is FWHM in radians and θ is Bragg's diffraction angle.

TEM analysis on the as-synthesized ZnO nanoparticles confirmed their actual size and shape. ZnO-CNT samples were not characterized by TEM, as conjoining ZnO with CNT does not produce any changes to shape, size or morphology of the nanoparticles as shown in previous studies.[34–36] Figure 2 provides an overview of the sizes and morphologies of ZnO nanoparticles summarized in Table 2. Different nanoparticle morphologies are visible, including hexagonal, rectangular, needle-like and spherical (Table 2). Hexagonal, rod and rectangular shaped ZnO nanoparticles are obtained for sample Z–1 synthesized with the lowest NaOH (Figures 2(a) and (b)). On increasing the NaOH quantity, ZnO nanoparticles of Z–2 display a needle-like morphology (Figure 2(c)) along with several hexagonally shaped nanoparticles (Figure 2(d)). An additional increase in the NaOH quantity in Z–3 produced smaller nanoparticles (Figures 2(e) and (f)) with variable shapes. The highest NaOH quantity of Z–4 led to the smallest nanoparticles (Figures 2(g) and (h)). The decrease in the particle size with increase in NaOH quantity is attributed to an increase in the reactivity of the precursors. The reaction consists of a rapid conversion of $Zn(CH_3COO)_2.2H_2O$ to an intermediate phase of $Zn(CH_3COO)(OH)$ and then to ZnO, with relatively low aggregation with a reduced average particle size.[51] On the other hand, the transformation in the shape of the nanoparticles can be attributed to an excess of
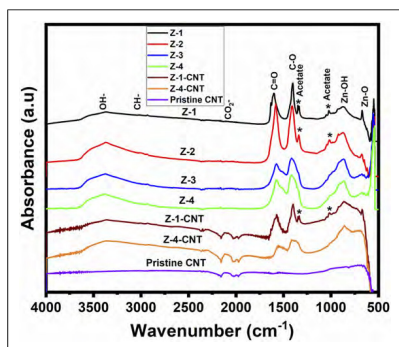
Figure 3. FTIR spectra of ZnO nanoparticles (labelled Z–1, Z–2, Z–3 and Z–4), ZnO–CNT nanohybrids (labelled Z–1–CNT and Z–4–CNT) and pristine CNT.

hydroxyl ions in the solution due to increase in the NaOH quantity. These additional hydroxyl ions are adsorbed on the surfaces of the ZnO nanoparticles, blocking their growth along the c-axis and in turn, leading to an unselective and uncontrolled hydrolysis nucleation.[52] With the increase of NaOH quantities, the ZnO nanoparticles no longer follow their preferential growth along the c-axis and are transformed into nanoparticles with smoother facets, for example, Z–4.

In Figure 3, the FTIR spectra provide information on various vibrational bonds produced during the synthesis of ZnO, ZnO-CNT nanohybrids and pristine CNT. The band located between 700-500 cm^{-1} corresponds to the Zn-O stretching bond, which confirms the formation of ZnO.[53] The vibration band of ZnO downshifts from ~680 cm^{-1} to 640 cm^{-1} for increasing NaOH quantities, suggesting changes in the morphology of ZnO nanoparticles, analogous to TEM results.[52] The broad band near 3300 cm^{-1} corresponds to OH-stretching, originating from water and NaOH.[54] The OH-stretching band appears to be less intense and narrower for sample Z–1, but more intense and broader for samples Z–2, Z–3 and Z–4. This variation in band broadness and intensity is attributable to unequal quantities of OH$^-$ functional groups chemisorbed on the ZnO nanoparticle surfaces. In addition, the OH$^-$ functional groups bonded to Zn, thart is, the Zn-OH bonds[55] are located between 1000 and 800 cm^{-1}. Bands between 3000 and 2800 cm^{-1} correspond to CH-stretching of alkane groups. Furthermore, the bands situated between 1600 and 1100 cm^{-1} comprise of several acetate groups (-COOH).[56] These groups are adsorbed on the surfaces of the ZnO nanoparticles during synthesis. In particular, the bands located between 1600 and 1500 cm^{-1} and 1500 and

1400 cm^{-1} correspond to symmetric and asymmetric stretching vibrations of the C=O bond, respectively.[53,57,58] The broad peak at around 1350 cm^{-1} corresponds to C–O bonds. With variations in the NaOH quantities, the vibration peaks of C=O and C–O bonds manifest changes in their band intensities, owing to morphological changes of the nanoparticles. The bands (marked as *) between 1300 and 1100 cm^{-1} are attributed to the carboxylate (COO$^-$) functional group originating from unreacted $Zn(CH_3CO_2)_2.2H_2O$ precursor, analogous to XRD results.

The FTIR spectra of ZnO-CNT nanohybrids, that is, samples Z–1–CNT and Z–4–CNT contain similar bonds to the as-synthesized ZnO samples. However, a broad peak at 2130 cm^{-1} is present for the ZnO-CNT samples. This peak is also visible for pristine CNT and can therefore be safely attributed to CO_2 peak.[59]

Optical properties

The bandgaps of ZnO and ZnO-CNT hybrids were calculated through UV–Vis absorption spectroscopy followed by Tauc plots presented in Figure 4. The absorption properties of ZnO-CNT are similar to the as-grown ZnO nanoparticles. In fact, MWCNT are prone to bundling, suppressing their optical signals. In addition, they absorb in the infrared region owing to Van Hove singularities. Therefore, no contribution to the near band absorption of ZnO is expected.[36] The bandgaps of these ZnO samples range from 3.16 eV to 3.29 eV. Bandgaps of 3.27 eV have also been observed for ZnO samples with a high concentration of surface defects.[37] These variations in the bandgap are a result of syntheses via sol-gel routes .[60,61] The absorption spectra of the ZnO samples revealed a sharp shoulder at 3.3 eV, stretching down to 2 eV–2.5 eV. However, shoulders related to defect level absorption were absent. For samples Z–1–CNT and Z–4–CNT in Figures 4(a) and 4(d), (a), broader absorption shoulder starting at 3.3 eV and extending below 2 eV is visible. The presence of metallic MWCNT therefore has an effect on the near infrared absorption of the hybrid samples as explained above. In both ZnO-CNT samples, a slight decrease in bandgap is observable, suggesting modifications to specific defect states investigated in the next section by PL spectroscopy.

The emission properties of the as-synthesized ZnO and ZnO-CNT nanohybrids were examined through room temperature PL measurements. The 365 nm (3.4 eV) excitation source was used to incite band-to-band transitions in ZnO and ZnO-CNT samples with bandgaps between 3.17 eV and 3.29 eV. The PL spectra of Figure 5 manifest typical PL emission characteristics of ZnO nanoparticles comprising of the NBE and DLE. It is noteworthy that the unreacted acetate precursor does not produce any PL emission under 365 nm excitation; the PL emissions emanating from
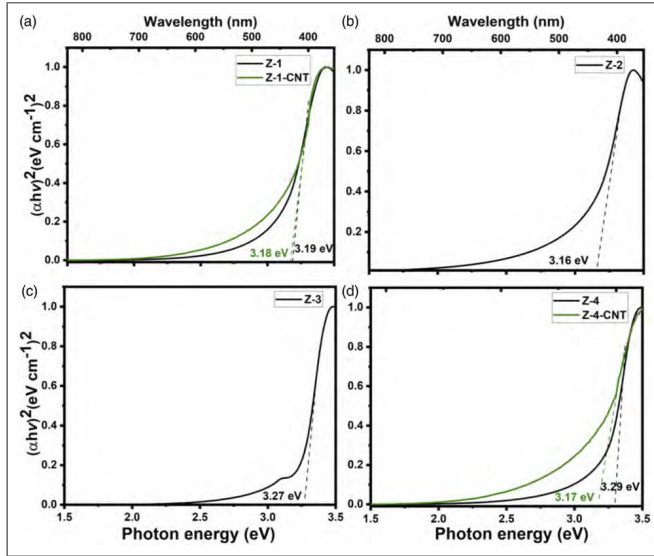
Figure 4. Tauc plots of samples (a) Z–1 and Z–1–CNT, (b) Z–2, (c) Z–3 and (d) Z–4 and Z–4–CNT.
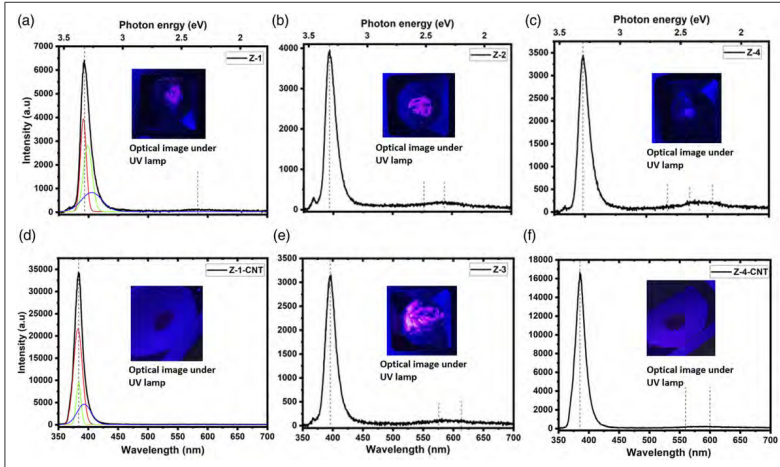

Figure 5. PL emission spectra of samples (a) Z–1, (b) Z–2, (c) Z–4 (d) Z–1–CNT, (e) Z–3 and (f) Z–4–CNT. Vertical marked dashed lines indicate major emission components. The insets are optical images taken under 365 nm illumination.

the samples therefore originate from the ZnO nanoparticles alone. Additionally, the ratio of the NBE to DLE provides a qualitative measure of the crystallinity of the ZnO samples; a higher ratio signifies a lower number of intrinsic defects.

The major emission wavelengths are deconvoluted with the Gaussian function in Figure 5. In general, all the samples exhibited similar PL emission tendencies; however, differences in quantum yield are observed with variations in NaOH quantities. For example, the quantum yield of the NBE for sample Z–4 is ∼50% lower than Z–1. This suggests that the increase in NaOH tends to create non-radiative defect centres within the ZnO nanoparticles, which in turn lower the UV emission intensity. Furthermore, the increase in the DLE or a lower NBE to DLE ratio also supports the presence of surface defects. Other factors, such as shape, size and post-synthesis treatment also modify surface defects.[37] The varied morphologies and size distributions of the ZnO nanoparticles have therefore an important influence on the NBE to DLE ratios. However, for samples combined with CNT, that is, Z–1–CNT and Z–4–CNT, a ∼5-fold increase of the UV emission intensity is observed along with a slight blueshift compared to Z–1 and Z–4, respectively. These preceding modifications clearly suggest that sonication is effective in creating ZnO-CNT nanohybrids. The sonication time of 5 min was optimized in other studies by the authors,[15,36] where the mechanism behind nanoparticle decoration on CNT was also explained. Defective areas of CNT, including kinks, bends or zones where C-C bonds break down, are active sites for anchorage of nanoparticles. The advantage of sonicating CNT in ethanol is 2-fold. Firstly, ethanol allows a homogeneous dispersion of CNT; secondly, sonication breaks down C-C bonds on the outer walls of the CNT, facilitating their decoration with nanoparticles.

The NBE to DLE ratios are the highest for these CNT-based samples, confirming a notable reduction or passivation of defects. The UV emission peaks for ZnO samples in Figure 5 lie between 393 nm and 397 nm and correspond to the transitions from Zn shallow donor levels to the valance band.[47–49] Only samples Z–1 and Z–4 were combined with CNT as they were synthesized with the lowest and highest quantities of NaOH. These samples also present the lowest and highest bandgaps from Tauc plots, the largest and smallest particle sizes from TEM study and the least to most intense DLE. Therefore, understanding the effect of surface passivation by CNT for these two samples will help elucidate the mechanism of UV emission enhancement as a function of synthesis parameters. For ZnO-CNT nanohybrids, the blueshifted UV emission peaks situated between 383 nm and 386 nm correspond to the band-to-band transitions of ZnO. This implies that the defects in these samples are surface related and therefore, CNT clearly play a role in their passivation, whereupon they turn optically inactive. On the other hand, Z–4–CNT still manifests a hint
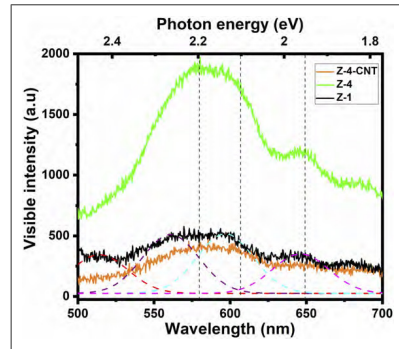

Figure 6. Visible PL emission of samples Z–4–CNT, Z–4 and Z–1. The dashed curves are the Gaussian deconvolution of the most significant peaks of sample Z–1.

of DLE even though its intensity has largely reduced. The insets of Figure 5 display optical images of the ZnO and ZnO-CNT samples under 365 nm UV light illumination. A violet-blue hue corresponding to surface and bulk Zn interstitials mainly emanates from the ZnO samples. The emission is the most significant for sample Z–3 (inset of Figure 5(e)) and less intense for other samples (insets of Figure 5(a), 5(b) and 5(c)). On the other hand, ZnO-CNT samples emanate only in the UV; in the insets of Figures 5(d) and (f), visible PL emission is absent.

A more detailed analysis was carried out for the DLE component of samples Z–1, Z–4, Z–1–CNT and Z–4–CNT in Figure 6. The DLE is a combination of optically active point defects, such as oxygen vacancies (V_O), zinc vacancies (V_{ZN}), oxygen interstitials (O_i) and antisites (O_{ZN}), zinc interstitials (Zn_i), as well as their complexes.[62] It is noteworthy to mention that Z–1–CNT did not produce any visible luminescence. On the other hand, Z–4–CNT manifested a clear decrease in the visible luminescence. The Gaussian deconvolution of sample Z–4 in Figure 6, provides the most significant emission peaks, such as the green emission at ∼2.2 eV, yellow-orange emission at ∼2.1 eV and red emission at ∼1.95 eV. DLE of the samples is dominated by a yellow-green emission in addition to a less significant red component at 1.95 eV. Besides, the highly intense UV emission of the ZnO-CNT samples overwhelms the DLE, which is therefore not discernible in the PL photographs in the insets of Figure 5 (c) and 5(f). The yellow-green component is related to Vo; in particular, Vo$^+$ at 2.5 eV due to volume related oxygen vacancies is absent or negligible in our samples. The use of aqueous ethanol has therefore ensured an appropriate oxygenation of ZnO leading to the suppression of Vo$^{+\cdot}$ However, the emission at

~2.2 eV is related to the surface oxygen vacancies or Vo^{++}. In this study, it is the major emission component of the DLE. PL was carried out in air ambient; therefore, the likelihood of adsorption of OH^- and O_2 is high. Chemisorbed oxygen species provoke an upward band bending of ZnO, boosting electron-hole pair separation and in turn, delaying excitonic recombination. Subsequently, the surface trapped holes tunnel to deep levels i.e. to Vo^+ and convert them into Vo^{++}. Eventually, an electron from the conduction band then recombines with the Vo^{++} and emits the DLE at 2.2 eV. On conjoining with CNT, the adsorption of O_2 and OH^- is hindered; thereupon, the upward band bending is reduced. Thus, the tunnelling of holes to deep levels is suppressed and the probability of NBE increases.[63]

Furthermore, variations in the ZnO nanoparticle morphologies engender changes in their defect states. Rod-like or bean-like ZnO tend to harbour lower amounts of Vo, while as in spherical ZnO nanoparticles, it is the major emission component of the DLE.[64] On the other hand, hexagonal ZnO is made up of six facets: four polar and two non-polar.[65] The latter has tendencies to adsorb oxygen species from air. However, polar facets are either O or Zn terminated and therefore harbour related point defects. Cubic or rectangular shaped ZnO has two polar and two non-polar surfaces.[66]

Additionally, the size of Z–4 nanoparticles was the smallest, implying the highest surface to volume ratio among the as-produced ZnO samples. The increase in the surface to volume ratio therefore explains the more intense 2.2 eV emission for sample Z–4. On combining with CNT, the Vo^{++} emission significantly recedes (Z–4) or disappears (Z–1). Furthermore, the red emission at 1.95 eV also diminishes for both ZnO-CNT samples. This emission has been regarded as transitions related to Zn_i, usually observed in ZnO samples synthesized in oxygen rich conditions.[67,68] The yellow-orange emission at around 2.1 eV relates to the transitions from Zn_i to O_i.[69] The residual DLE of Z–4–CNT is likely due to the incomplete passivation of the ZnO surface. The peak intensities of the NBE for samples Z–1–CNT and Z–4–CNT are at ~383 nm and ~385.5 nm, respectively. Therefore, a difference of ~2.5 nm between the peak NBE intensities exists for these two samples. Since the Z–4 nanoparticle sizes are smaller, signifying that their surface is larger, a higher quantity of CNT would therefore be necessary to ensure optimum surface coverage. The latter would ascertain passivation of surface defects and a further blueshift of the NBE for Z–4–CNT.

Conclusion

We have demonstrated a feasible route to control the UV emission from the ZnO nanoparticles via the suppression of both volume and surface defects. The ZnO nanoparticles were prepared via hydrothermal sol-gel routes by varying Zn precursor to NaOH ratios. In effect, the quantity of NaOH was instrumental in determining the kinetics of the ZnO precipitation reaction. Furthermore, the morphology and sizes of the ZnO nanoparticles are dependent on these ratios. Various morphologies of ZnO nanoparticles i.e. hexagonal, rectangular, needle-like and spherical were obtained as a result of the synthesis conditions. TEM study revealed that for the highest NaOH quantity generated the smallest ZnO nanoparticles. Additionally, the use of aqueous ethanol supported the synthesis of well-oxygenated ZnO nanoparticles as volume related defects were essentially absent in the PL emission spectra. In all cases, the ZnO nanoparticles manifested an intense UV emission and a negligible surface related DLE. The DLE was suppressed and the NBE was blueshifted and further amplified ~5-fold on conjoining with CNT.

ORCID iDs

Keshav Nagpal   https://orcid.org/0000-0003-0040-9984
Erwan Rauwel   https://orcid.org/0000-0001-8950-1415
Protima Rauwel   https://orcid.org/0000-0001-5393-2352

References

1. Zhou C, Ghods A, Yunghans K, et al. *ZnO for Solar Cell and Thermoelectric Applications*. Bellingham, WA: SPIE, 2017.
2. Pearton SJ and Ren F. Advances in ZnO-based materials for light emitting diodes. *Curr Opin Chem* 2014; 3: 51–55.
3. Norek M. Approaches to enhance UV light emission in ZnO nanomaterials. *Curr Appl Physs* 2019; 19: 867–883.
4. Tsukazaki A, Ohtomo A, Onuma T, et al. Repeated temperature modulation epitaxy for p-type doping and light-emitting diode based on ZnO. *Nat Mater* 2005; 4: 42–46.
5. Djurišić AB, Ng AMC, and Chen XY. ZnO nanostructures for optoelectronics: material properties and device applications. *Prog Quan Electron* 2010; 34: 191–259.
6. Lin B, Fu Z, and Jia Y. Green luminescent center in undoped zinc oxide films deposited on silicon substrates. *Appl Phys Lett* 2001; 79: 943–945.

7. Pearton SJ, Lim WT, Wright JS, et al. ZnO and related materials for sensors and light-emitting diodes. *J Electron Mater* 2008; 37: 1426–1432.

8. Dai T-F, Hsu W-C, and Hsu H-C. Improvement of photo-luminescence and lasing properties in ZnO submicron spheres by elimination of surface-trapped state. *Opt Express* 2014; 22: 27169–27174.

9. Sasani Ghamsari M, Alamdari S, Han W, et al. Impact of nanostructured thin ZnO film in ultraviolet protection. *Int J Nanomedicine* 2017; 12: 207–216.

10. Sawyer S, Qin L, and Shing C. Zinc oxide nanoparticles for ultraviolet photodetection. *Int J High Speed Electron Syst* 2011; 20: 183–194.

11. Ungula J and Dejene BF. Effect of solvent medium on the structural, morphological and optical properties of ZnO nanoparticles synthesized by the sol-gel method. *Phys B: Condens Matter* 2016; 480: 26–30.

12. Gong Y, Andelman T, Neumark GF, et al. Origin of defect-related green emission from ZnO nanoparticles: effect of surface modification. *Nanoscale Res Lett* 2007; 2: 297.

13. Wang Z, Wang F, Cui Y, et al. Novel method to enhance the visible emission of ZnO nanostructures. *Chem Phys Lett* 2014; 614: 53–56.

14. Li XL, Li C, Zhang Y, et al. Atomic layer deposition of ZnO on multi-walled carbon nanotubes and its use for synthesis of CNT-ZnO heterostructures. *Nanoscale Res Lett* 2010; 5: 1836–1840.

15. Rauwel E, Galeckas A, Soares MR, et al. Influence of the interface on the photoluminescence properties in ZnO carbon-based nanohybrids. *J Phys Chem C* 2017; 121: 14879–14887.

16. Bazargan AM, Sharif F, Mazinani S, et al. Integrated synthesis and surface passivation of ZnO nanoparticles to enhance UV spectrum selectivity. *J Mater Sci Mater Electron* 2016; 27: 8221–8226.

17. Qin L, Shing C, Sawyer S, et al. Enhanced ultraviolet sensitivity of zinc oxide nanoparticle photoconductors by surface passivation. *Opt Mater* 2011; 33: 359–362.

18. Sharma A, Singh BP, Dhar S, et al. Effect of surface groups on the luminescence property of ZnO nanoparticles synthesized by sol-gel route. *Surf Sci* 2012; 606: L13–L17.

19. Hofmann DM, Hofstaetter A, Leiter F, et al. Hydrogen: a relevant shallow donor in zinc oxide. *Phys Rev Lett* 2002; 88: 045504.

20. Dev A, Niepelt R, Richters JP, et al. Stable enhancement of near-band-edge emission of ZnO nanowires by hydrogen incorporation. *Nanotechnology* 2010; 21: 065709.

21. Lapp J, Thapa D, Huso J, et al. Enhancement of the ultraviolet photoluminescence of ZnO films: coatings, annealing, and environmental exposure studies. *AIP Adv* 2020; 10: 085217.

22. Thapa D, Huso J, Morrison JL, et al. Achieving highly-enhanced UV photoluminescence and its origin in ZnO nanocrystalline films. *Opt Mater* 2016; 58: 382–389.

23. Zhang CY. The influence of post-growth annealing on optical and electrical properties of p-type ZnO films. *Mater Sci Semicond Process* 2007; 10: 215–221.

24. Nie Y, Wang Z, Wang J, et al. Synthesis and structure-dependent optical properties of ZnO nanocomb and ZnO nanoflag. *J Phys Chem C* 2017; 121: 26076–26085.

25. Musa I, Qamhieh N, and Mahmoud ST. Synthesis and length dependent photoluminescence property of zinc oxide nano-rods. *Results Phys* 2017; 7: 3552–3556.

26. Guidelli EJ, Baffa O, and Clarke DR. Enhanced UV emission from silver/ZnO and gold/ZnO core-shell nanoparticles: photoluminescence, radioluminescence, and optically stimulated luminescence. *Sci Rep* 2015; 5: 14004.

27. Jiang T, Qin X, Sun Y, et al. UV photocatalytic activity of Au@ZnO core-shell nanostructure with enhanced UV emission. *RSC Adv* 2015; 5: 65595–65599.

28. Wang M, Zhang Y, Dong C, et al. Preparation and electro-magnetic shielding effectiveness of cobalt ferrite nanoparticles/carbon nanotubes composites. *Nanomater Nanotechnol* 2019; 9: 1847980419837821.

29. Ismail N, Jalar A, Afdzaluddin A, et al. Electrical resistivity of Sn–3.0 Ag–0.5 Cu solder joint with the incorporation of carbon nanotubes. *Nanomater Nanotechnol* 2021; 11: 1847980421996539.

30. Kalakonda P, Kalakonda PB, and Banne S. Studies of electrical, thermal, and mechanical properties of single-walled carbon nanotube and polyaniline of nanoporous nanocomposites. *Nanomater Nanotechnol* 2021; 11: 18479804211001140.

31. Liu X, Guo R, Lin Z, et al. Resistance-strain sensitive rubber composites filled by multiwalled carbon nanotubes for structuraldeformation monitoring. *Nanomater Nanotechnol* 2021; 11: 18479804211011384.

32. Rathinavel S, Priyadharshini K, and Panda D. A review on carbon nanotube: an overview of synthesis, properties, functionalization, characterization, and the application. *Mater Sci Eng B* 2021; 268: 115095.

33. Basiuk EV, Ramírez-Calera IJ, Meza-Laguna V, et al. Solvent-free functionalization of carbon nanotube bucky-paper with amines. *Appl Surf Sci* 2015; 357: 1355–1368.

34. Rauwel P, Galeckas A, and Rauwel E. Time evolution of ZnO-CNT photoluminescence under variable ambient and temperature conditions. *IOP Conf Ser Mater Sci Eng* 2019; 613: 012031.

35. Rauwel P, Galeckas A, and Rauwel E. Enhancing the UV emission in ZnO-CNT hybrid nanostructures via the surface Plasmon resonance of Ag nanoparticles. *Nanomaterials* 2021; 11: 452.

36. Rauwel P, Galeckas A, Salumaa M, et al. Photocurrent generation in carbon nanotube/cubic-phase HfO2 nanoparticle hybrid nanocomposites. *Beilstein J Nanotechnol* 2016; 7: 1075–1085.

37. Rauwel E, Galeckas A, Rauwel P, et al. Precursor-dependent blue-green photoluminescence emission of ZnO nano-particles. *J Phys Chem C* 2011; 115: 25227–25233.

38. Rauwel P, Salumaa M, Aasna A, et al. A review of the synthesis and photoluminescence properties of hybrid ZnO and carbon nanomaterials. *J Nanomater* 2016; 2016: 5320625.

39. Byrappa K, Dayananda AS, Sajan CP, et al. Hydrothermal preparation of ZnO: CNT and TiO2: CNT composites and their photocatalytic applications. *J Mater Sci* 2008; 43: 2348–2355.

40. Zhang WD, Jiang LC, and Ye JS. Photoelectrochemical study on charge transfer properties of ZnO nanowires promoted by carbon nanotubes. *J Phys Chem C* 2009; 113: 16247–16253.

41. Kennedy J, Fang F, Futter J, et al. Synthesis and enhanced field emission of zinc oxide incorporated carbon nanotubes. *Diam Relat Mater* 2017; 71: 79–84.

42. Choi MS, Park T, Kim WJ, et al. High-performance ultraviolet photodetector based on a zinc oxide nanoparticle@single-walled carbon nanotube heterojunction hybrid film. *Nanomaterials* 2020; 10: 395.

43. Barthwal S and Singh NB. ZnO-CNT nanocomposite: a device as electrochemical sensor. *Mater Today Proc* 2017; 4: 5552–5560.

44. Barthwal S, Singh B, Barthwal S, et al. ZnO-CNT nanocomposite based gas sensors-an overview. *Sensor Lett* 2017; 15: 955–969.

45. Singh LT, Sugavaneshwar RP, and Nanda KK. Carbon nanotube-ZnO nanowire hybrid architectures as multifunctional devices. *AIP Adv* 2013; 3: 082106.

46. Arefi MR and Rezaei-Zarchi S. Synthesis of zinc oxide nanoparticles and their effect on the compressive strength and setting time of self-compacted concrete paste as cementitious composites. *Int J Mol Sci* 2012; 13: 4340–4350.

47. Bouzourâa MB, Naciri AE, Moadhen A, et al. Effects of silicon porosity on physical properties of ZnO films. *Mater Chem Phys* 2016; 175: 233–240.

48. Imran M, Haider S, Ahmad K, et al. Fabrication and characterization of zinc oxide nanofibers for renewable energy applications. *Arab J Chem* 2017; 10: S1067–S1072.

49. Ha TT, Canh TD, and Tuyen NV. A quick process for synthesis of ZnO nanoparticles with the aid of microwave irradiation. *ISRN Nanotechnology* 2013; 2013: 497873.

50. Monshi A, Foroughi MR, and Monshi M. Modified scherrer equation to estimate more accurately nano-crystallite size using XRD. *World J Nano Sci Eng* 2012; 2: 154–160.

51. Xu S and Wang ZL. One-dimensional ZnO nanostructures: solution growth and functional properties. *Nano Res* 2011; 4: 1013–1098.

52. Wahab R, Ansari SG, Kim YS, et al. The role of pH variation on the growth of zinc oxide nanostructures. *Appl Surf Sci* 2009; 255: 4891–4896.

53. Sharma D and Jha R. Analysis of structural, optical and magnetic properties of Fe/Co co-doped ZnO nanocrystals. *Ceram Int* 2017; 43: 8488–8496.

54. Xiong G, Pal U, Serrano JG, et al. Photoluminesence and FTIR study of ZnO nanoparticles: the impurity and defect perspective. *Phys Status Solidi C* 2006; 3: 3577–3581.

55. Kołodziejczak-Radzimska A, Markiewicz E, and Jesionowski T. Structural characterisation of ZnO particles obtained by the emulsion precipitation method. *J Nanomater* 2012; 2012: 656353.

56. Xiong G, Pal U, and Serrano JG. Correlations among size, defects, and photoluminescence in ZnO nanoparticles. *J Appl Phys* 2007; 101: 024317.

57. Sowri Babu K, Ramachandra Reddy A, Sujatha C, et al. Synthesis and optical characterization of porous ZnO. *J Adv Ceram* 2013; 2: 260–265.

58. Phoohinkong W, Foophow T, and Pecharapa W. Synthesis and characterization of copper zinc oxide nanoparticles obtained via metathesis process. *Adv Nat Sci Nanosci Nanotechnol* 2017; 8: 035003.

59. Hosseini Largani S and Akbarzadeh Pasha M. The effect of concentration ratio and type of functional group on synthesis of CNT-ZnO hybrid nanomaterial by an in situ sol-gel process. *Int Nano Lett* 2017; 7: 25–33.

60. Davis K, Yarbrough R, Froeschle M, et al. Band gap engineered zinc oxide nanostructures via a sol-gel synthesis of solvent driven shape-controlled crystal growth. *RSC Adv* 2019; 9: 14638–14648.

61. Singh M, Goyal M, and Devlal K. Size and shape effects on the band gap of semiconductor compound nanomaterials. *J Taibah Univ Sci* 2018; 12: 470–475.

62. Janotti A and Van de Walle CG. Native point defects in ZnO. *Phys Rev B* 2007; 76: 165202.

63. Richters JP, Voss T, Kim DS, et al. Enhanced surface-excitonic emission in ZnO/Al2O3 core-shell nanowires. *Nanotechnology* 2008; 19: 305202.

64. Crapanzano R, Villa I, Mostoni S, et al. Morphology related defectiveness in ZnO luminescence: from bulk to nano-size. *Nanomaterials* 2020; 10: 1983.

65. Wang X, Yin L, Liu G, et al. Polar interface-induced improvement in high photocatalytic hydrogen evolution over ZnO-CdS heterostructures. *Energy Environ Sci* 2011; 4: 3976–3979.

66. Wöll C. The chemistry and physics of zinc oxide surfaces. *Prog Surf Sci* 2007; 82: 55–120.

67. Djurisic A, Leung Y, Tam K, et al. *Defect Emissions in ZnO Nanostructures*. Bellingham, WA: SPIE, 2005.

68. Przezdziecka E, Guziewicz E, Jarosz D, et al. Influence of oxygen-rich and zinc-rich conditions on donor and acceptor states and conductivity mechanism of ZnO films grown by ALD-experimental studies. *J Appl Phys* 2020; 127: 075104.

69. Djurišić AB, Leung YH, Tam KH, et al. Green, yellow, and orange defect emission from ZnO nanostructures: influence of excitation wavelength. *Appl Phys Lett* 2006; 88: 103107.

II

Article

Significance of Hydroxyl Groups on the Optical Properties of ZnO Nanoparticles Combined with CNT and PEDOT:PSS

Keshav Nagpal [1], Erwan Rauwel [1], Elias Estephan [2], Maria Rosario Soares [3] and Protima Rauwel [1,*]

1 Institute of Forestry and Engineering, Estonian University of Life Sciences, 51014 Tartu, Estonia
2 LBN, University of Montpellier, 34193 Montpellier, France
3 CICECO, University of Aveiro, 3810-193 Aveiro, Portugal
* Correspondence: protima.rauwel@emu.ee

Abstract: We report on the synthesis of ZnO nanoparticles and their hybrids consisting of carbon nanotubes (CNT) and polystyrene sulfonate (PEDOT:PSS). A non-aqueous sol–gel route along with hydrated and anhydrous acetate precursors were selected for their syntheses. Transmission electron microscopy (TEM) studies revealed their spherical shape with an average size of 5 nm. TEM also confirmed the successful synthesis of ZnO-CNT and ZnO-PEDOT:PSS hybrid nanocomposites. In fact, the choice of precursors has a direct influence on the chemical and optical properties of the ZnO-based nanomaterials. The ZnO nanoparticles prepared with anhydrous acetate precursor contained a high amount of oxygen vacancies, which tend to degrade the polymer macromolecule, as confirmed from X-ray photoelectron spectroscopy and Raman spectroscopy. Furthermore, a relative increase in hydroxyl functional groups in the ZnO-CNT samples was observed. These functional groups were instrumental in the successful decoration of CNT and in producing the defect-related photoluminescence emission in ZnO-CNT.

Keywords: ZnO; ZnO-CNT; ZnO-PEDOT:PSS; nanoparticles; hybrids; hydroxyl groups; non-aqueous sol–gel; surface defects; photoluminescence

1. Introduction

Hybrid nanocomposites combining organic and inorganic counterparts have a multitude of applications, e.g., light-emitting diodes (LED), solar cells, and photodetectors [1–3]. Organic materials consist of polymers possessing remarkable properties, such as easy processing, flexibility, and good conductivity [4]. However, their high cost and lack of stability are obstacles for practical devices. On the other hand, inorganic materials present higher structural, chemical, and functional stability, as well as a high charge mobility, making them suitable for optoelectronic applications [5]. Therefore, the combination of organic with inorganic materials provides robust multifunctional nanocomposites with applications in flexible electronic and photonic devices [6–8].

Conducting polymers such as poly (3,4-ethylenedioxythiophene) poly(styrenesulfonate) (PEDOT:PSS) are already being incorporated into organic thin film transistors, organic LED, organic solar cells, capacitors, batteries, and thermoelectric devices, as well as technologies such as touch screens and electronic papers [9,10]. In addition, PEDOT:PSS is mechanically stable and highly flexible. Various combinations of PEDOT:PSS with inorganic materials, such as SnO_2, TiO_2, CdS, CdSe, ZnO and metal nanostructures, have been investigated to that end [11,12]. Among these inorganic nanomaterials, ZnO is promising due its wide band gap of 3.37 eV, large exciton binding energy of 60 meV, high chemical stability, and remarkable electrical and optical properties [13]. Moreover, the high surface-to-volume ratio of ZnO nanoparticles implies a spontaneous presence of surface defects, including oxygen vacancies (V_O), oxygen interstitials (O_i), and zinc interstitials (Zn_i). Therefore, in addition to the UV emission, known as the near-band emission (NBE), ZnO nanoparticles

emit within the entire visible spectrum, also known as defect-level emission (DLE) [14]. The latter depends on both the surface and the volume defects introduced during the synthesis of the nanoparticles [15,16]. For example, ZnO nanoparticles prepared by aqueous sol–gel routes tend to emit higher NBE and a negligible DLE [17]. On the other hand, for ZnO nanoparticles prepared by non-aqueous sol–gel routes, the emission depends on the presence of hydrates in the precursor [18,19]. In fact, hydrates in the precursor contribute to the enhancement of NBE due to improved oxidation of ZnO during synthesis [18]. On the other hand, adsorption of hydroxyl groups on the surface of ZnO nanoparticles has been shown to increase the visible PL emission [20]. The chemisorption of oxygen radicals from air on the surface of ZnO nanoparticles also augments green emission from them [21]. In general, small nanoparticles possess a high surface-to-volume ratio, and therefore harbor higher amounts of surface defects. For larger ZnO nanoparticles, defects can be both surface and volume related [22].

Recently, ZnO-CNT nanohybrids have attracted considerable interest due to their high stability and superior photonic, electrochemical and electromagnetic properties, which originate from interfacial effects. In a previous study, we successfully passivated ZnO surface states by combining them with CNT via sonication [17]. In this work, we carry out ZnO nanoparticle synthesis via a non-aqueous sol–gel route with hydrated (zinc acetate dihydrate ($Zn(CH_3CO_2)_2.2H_2O$) and anhydrous (zinc acetate anhydrous ($Zn(CH_3CO_2)_2$) precursors. In a study by Šarić et al., it was shown that with similar precursors, ZnO precipitation could be promoted through an esterification reaction that generates water upon the addition of acetic acid [23]. In our reaction, only absolute ethanol is used as a solvent. It plays a crucial role in controlling the size and shape of ZnO nanoparticles, and consequently, in the formation of various surface defects. Due to the addition of sodium hydroxide in this work, the basic character of the solution prevents any esterification reaction and in turn, no water molecules are formed. This route therefore enables the formation of very small ZnO nanoparticles functionalized with hydroxyl groups, promoting the decoration of CNT with ZnO. We then decorated CNT with ZnO nanoparticles in order to create a hybrid nanocomposite. Subsequently, we fabricated a second type of hybrid nanocomposite consisting of ZnO-PEDOT:PSS and compared the evolution of the surface defects to ZnO-CNT. These optical properties are discussed in terms of synthesis conditions, crystal structure, chemical properties, and the morphology of ZnO nanoparticles and their hybrids. The objective is to use these hybrid materials in LED. Therefore, finding a way to control these surface defects or trap states for LED applications is a priority, as they are detrimental to device properties.

2. Materials and Methods

2.1. Synthesis

2.1.1. ZnO

Two different zinc precursors, $Zn(CH_3CO_2)_2.2H_2O$ (99.5%, Fisher Scientific, Loughborough, UK) and $Zn(CH_3CO_2)_2$ (99.9%, Alfa Aesar, Kandel, Germany), were used for the synthesis of ZnO nanoparticles via non-aqueous sol–gel routes. Sodium hydroxide (NaOH) (99.9%, Aldrich) was used as a reducing agent. All the chemicals used were of analytic reagent grade. To prepare 0.05 M solutions of zinc precursors, 219.5 mg of $Zn(CH_3CO_2)_2.2H_2O$ or 183.48 mg of $Zn(CH_3CO_2)_2$ were dissolved in 20 mL absolute ethanol in a beaker placed in a water bath. The solutions were maintained at 65 °C under continuous magnetic stirring until the precursors were completely dissolved in absolute ethanol. Furthermore, a solution of 0.10 M NaOH in 20 mL absolute ethanol was prepared. The NaOH solution was added dropwise to the zinc precursor solutions. Thereafter, the mixtures were maintained at 65 °C for 2 h after which they were cooled to ambient temperature. White ZnO precipitates settled at the bottom of the reaction vessel. The resulting solutions containing ZnO nanoparticles were then centrifuged at 4500 rpm for 6 min, followed by drying for 24 h in air at 60 °C. This resulted in an agglomeration of ZnO nanoparticles in the form of a pellet, which is typical after drying nanoparticles synthesized

via sol–gel routes. These pellets were thereafter crushed using a pestle and mortar to obtain a very fine powder of ZnO nanoparticles.

2.1.2. ZnO-CNT Hybrids

For the preparation of ZnO-CNT hybrids, firstly, a solution of CNT was prepared by mixing 4 mg of CNT in 50 mL absolute ethanol and sonicating until a homogenous mixture was obtained. As before, 0.05 M zinc precursor solutions were prepared in 20 mL absolute ethanol. To prepare 0.10 M NaOH solutions, ~80 mg of NaOH was added to 19 mL absolute ethanol, in which 1 mL CNT mixture (~0.08 mg) was added. The final mixtures were sonicated and added dropwise to zinc precursor solutions. Thereafter, the reaction was completed as described earlier, and ZnO-CNT hybrid pellets were obtained. These pellets were gently crushed to obtain fine black powders of ZnO-CNT nanohybrids.

2.1.3. ZnO-PEDOT:PSS Hybrids

For the preparation of ZnO-PEDOT:PSS hybrids, 20 mg of the as-synthesized ZnO nanoparticles were taken, to which 400 mg of PEDOT:PSS (as purchased) was added. The mixtures were sonicated for 1 h and dried at 70 °C for 24 h. The dried mixtures were further gently crushed to obtain blue powders with agglomerated particles of ZnO-PEDOT:PSS nanohybrids.

2.2. Characterization

X-ray diffraction patterns were collected in Bragg–Brentano geometry using a Bruker D8 Discover diffractometer (Bruker AXS, Germany) with CuKα1 radiation (λ = 0.15406 nm) selected by a Ge (111) monochromator and LynxEye detector. Transmission electron microscopy (TEM) was carried out on a Tecnai G2 F20 (Netherlands) is a 200 kV field emission gun (FEG) for high-resolution and analytical TEM/STEM. It provided a point-to-point resolution of 2.4 Å. XPS measurements were performed at room temperature with a SPECS PHOIBOS 150 hemispherical analyzer (SPECS GmbH, Berlin, Germany)) with a base pressure of 5×10^{-10} mbar using monochromatic Al K alpha radiation (1486.74 eV) as excitation source operated at 300 W. The energy resolution as measured by the FWHM of the Ag $3d_{5/2}$ peak for a sputtered silver foil was 0.62 eV. The spectra were calibrated with respect to the C1s at 284.8 eV. The optical absorbance of ZnO, ZnO-CNT and ZnO-PEDOT:PSS nanohybrids was determined using a NANOCOLOR UV-VIS II spectrometer (MACHEREY-NAGEL, Germany) in the 200–900 nm region. The band gap of ZnO, ZnO-CNT and ZnO-PEDOT:PSS nanohybrids was subsequently calculated using Tauc plots. PL spectroscopy was carried out at room temperature with an excitation wavelength of 365 nm of an LSM-365A LED (Ocean Insight, USA) with a specified output power of 10 mW. The emission was collected by FLAME UV-Vis spectrometer (Ocean optics, USA) with a spectral resolution 1.34 nm. Optical images of ZnO were taken under a UV lamp ZLUV220 (China) with an excitation source of 365 nm. Raman spectra were collected using a WITec Confocal Raman Microscope System alpha 300R (WITec Inc., Ulm, Germany). Excitation in confocal Raman microscopy is generated by a frequency-doubled Nd:YAG laser (New-port, Irvine, CA, USA) at a wavelength of 532 nm, with 50 mW maximum laser output power in a single longitudinal mode. The system was equipped with a Nikon (Otawara, Japan) objective with a X20 magnification and a numerical aperture NA = 0.46. The acquisition time of a single spectrum was set to 0.5 s.

3. Results

Table 1 provides a list of ZnO, ZnO-CNT and ZnO-PEDOT:PSS samples synthesized in this work. Samples ZnO-D and ZnO-A correspond to ZnO nanoparticles synthesized from $Zn(CH_3CO_2)_2.2H_2O$ and $Zn(CH_3CO_2)_2$ precursors, respectively. Samples ZnO-D-CNT, ZnO-A-CNT, ZnO-D-PEDOT:PSS and ZnO-A-PEDOT:PSS correspond to the hybrids of samples ZnO-D and ZnO-A with CNT and PEDOT:PSS, respectively. In this study, the terms ZnO samples refer to samples ZnO-D and ZnO-A; ZnO-CNT hybrids refer to

samples ZnO-D-CNT and ZnO-A-CNT and ZnO-PEDOT:PSS hybrids refer to samples ZnO-D-PEDOT:PSS and ZnO-A-PEDOT:PSS.

Table 1. List of ZnO-CNT hybrids and ZnO-PEDOT:PSS hybrids synthesized in this work.

Sample Name	CNT (wt%)	PEDOT:PSS (wt%)
ZnO-D-CNT	~1	-
ZnO-A-CNT	~1	-
ZnO-D-PEDOT:PSS	-	~95
ZnO-A-PEDOT:PSS	-	~95

3.1. Structure and Morphology

The XRD patterns of ZnO samples ZnO-D and ZnO-A are shown in Figure 1. The peaks (100), (002), (101), (102), and (110) correspond to the hexagonal Wurtzite structure (a = 3.25 Å and c = 5.20 Å) of ZnO (JCPDS, Card Number 36-1451). No secondary phases are visible in the XRD patterns, indicating that single-phase ZnO nanoparticles were formed. In addition, XRD patterns illustrate that both samples ZnO-D and ZnO-A exhibit very small particle sizes due to broader XRD peaks. The size of nanoparticles was estimated using the Scherrer equation [24].

$$D = \frac{0.9\lambda}{\beta \cos\theta} \quad (1)$$

where D is particle size, λ (=0.15406 nm) is the wavelength of incident X-ray beam, β is FWHM in radians, and θ is Bragg's diffraction angle. Size calculation was carried out by considering the highest-intensity (101) peak. The calculated ZnO nanoparticle sizes of samples ZnO-D and ZnO-A were ~9 nm and ~5 nm, respectively. However, the actual size and shape of ZnO nanoparticles were confirmed from TEM studies as discussed below.
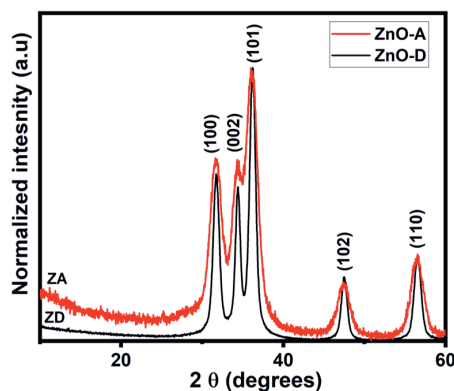
Figure 1. Normalized XRD patterns of samples ZnO-D and ZnO-A.

The morphological features of the as-synthesized ZnO samples, ZnO-CNT hybrids and ZnO-PEDOT:PSS hybrids were studied by TEM, as shown in Figure 2. TEM images in Figure 2a,b consist of overviews of the as-grown samples ZnO-D and ZnO-A, respectively. The micrographs reveal spherical nanoparticles of uniform size that tend to agglomerate. With the help of size distribution histograms of the as-synthesized ZnO samples, we estimate an average nanoparticle size of ~5.2 nm and ~4.8 nm for ZnO-D and ZnO-A, respectively. Figure 2c is a high-resolution TEM (HRTEM) image of sample ZnO-A, where

two ZnO nanoparticles are oriented along the [0001] zone axis of the basal plane of the Wurtzite structure. Figure 2d,e are low-magnification TEM images of the samples ZnO-D-CNT and ZnO-A-CNT, respectively. ZnO nanoparticles dominate the TEM images due to the low wt% (~1 wt%) of CNT in the samples. HRTEM images of ZnO-CNT are presented in Figure 2g,h. The walls of the CNT are clearly visible along with nanoparticles decorating them. We observe that the presence of CNT does not alter the crystallinity or the size distribution of the nanoparticles, and average sizes of ~5.7 nm and ~4.7 nm were retained. The micrographs therefore clearly indicate successful decoration of the nanoparticles on the walls of the CNT. In our study, the nanotubes were functionalized by sonication in pure ethanol; hence, the most likely functional groups present are carboxyl (COOH) that can be broken down into carbonyl (C-O) and hydroxyl (OH) [25]. These functional groups promote a covalent bonding between the CNT and ZnO nanoparticles, necessary for the decoration of CNT. Figure 2f,i are the TEM and scanning transmission electron microscopy (STEM) images of ZnO-D-PEDOT:PSS and ZnO-A-PEDOT:PSS samples, respectively. PE-DOT:PSS appears as flakes without any noticeable agglomeration of ZnO nanoparticles in the polymer layer. However, some areas of PEDOT:PSS are more densely packed with ZnO nanoparticles. The insets of Figure 2f,i are high-magnification TEM images of the samples emphasizing on their homogeneous distribution in the PEDOT:PSS matrix.
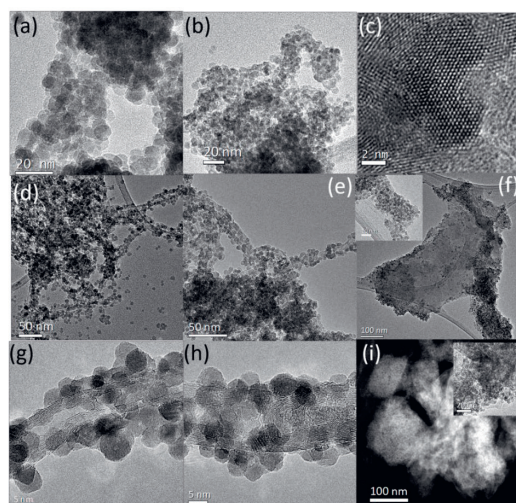
Figure 2. Overview TEM images of samples (**a**) ZnO-D, (**b**) ZnO-A, (**c**) HRTEM image of ZnO-A nanoparticles. Overview TEM images of (**d**) ZnO-D-CNT, (**e**) ZnO-A-CNT, (**f**) ZnO-D-PEDOT:PSS. HRTEM images of (**g**) ZnO-D-CNT, (**h**) ZnO-A-CNT and (**i**) STEM image of ZnO-A-PEDOT:PSS.

The high-resolution XPS spectra of the C 1s and O 1s regions of the as-synthesized and hybrid ZnO nanoparticles are shown in Figures 3 and 4, respectively. For the C 1s spectra of the as-synthesized samples in Figure 3a,d, the photoelectron peak at 284.8 eV corresponds to adventitious carbon [26]. Several carbon bonds are present in the samples, such as C-OH, O=C-O originating from the NaOH and acetate precursors used in the syntheses [27]. Both ZnO-A and ZnO-D contain oxygen and hydroxyl groups that are chemisorbed. The C 1s region of ZnO-CNT in Figure 3b,e manifests an additional peak corresponding to sp^2

hybridization of C atoms in the CNT at a binding energy of 283 eV. In addition, the C-OH peak is relatively more intense for the ZnO-A-CNT sample compared to the as-synthesized ZnO sample in Figure 3d, which could indicate an increase of hydroxyl groups or oxygen vacancies [18]. In fact, sonication of CNT in ethanol engenders a breakdown of the sidewalls, which then produces C-dangling bonds [28]. After sonication and during the initial stages of synthesis, CNT were mixed in ethanol and heated to a temperature of 65 °C for 2 h during which a solution of NaOH was added dropwise. Considering the hydroxyl rich conditions, the attachment of OH groups to C-dangling bonds is likely. For the ZnO-D-based samples, in Figure 3a–c, the relative intensities of the various peaks in the C1s region are similar, unlike the ZnO-A-based samples. In addition, in Figure 3f, a decrease in the O=C-O and C-OH peak intensities relative to the C-C peak for sample ZnO-A-PEDOT:PSS is observed, indicating an oxygen-deficient or -reduced PEDOT:PSS polymer.
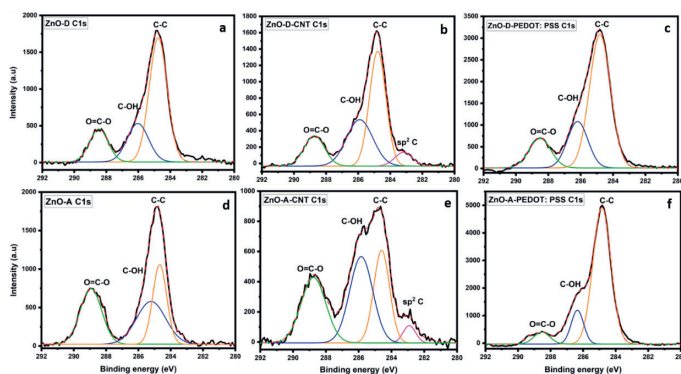
Figure 3. High-resolution XPS spectra of the C1s region of (**a**) ZnO-D, (**b**) ZnO-D-CNT, (**c**) ZnO-D-PEDOT:PSS, (**d**) ZnO-A, (**e**) ZnO-A-CNT and (**f**) ZnO-A-PEDOT:PSS.

The high-resolution spectra of the O 1s region of the ZnO samples, ZnO-CNT hybrids and ZnO-PEDOT:PSS hybrids in Figure 4 consist of several peaks, including lattice oxygen peak of ZnO or the Zn-O bond. Additionally, for the samples ZnO-D (Figure 3a), ZnO-D-CNT (Figure 3b), ZnO-A (Figure 3d) and ZnO-A-CNT (Figure 3e), photoelectron peaks that correspond to hydroxyl groups are also visible. In particular, the photoelectron peak at around 531.5 eV is attributed to Zn-OH bonds as well as oxygen vacancies [22]. TEM analysis estimated an average ZnO nanoparticle size of 5 nm, implying a very high surface-to-volume ratio. In such small nanoparticles, surface oxygen vacancies are prevalent. Since the C 1s region contains oxygen or hydroxyl components and the O 1s region contains carbon and hydroxyl components, it therefore suggests that hydroxyl groups are responsible for the decoration of CNT with ZnO. This directly implies that hydroxyl groups enable the anchoring of ZnO on CNT surface through covalent bonding with carbon, as there is no indication of Zn-C bonds. TEM images clearly indicate that ZnO nanoparticles grow directly on the CNT sidewalls through Zn-O/OH-C bonds. Furthermore, the O 1s region of the ZnO-PEDOT:PSS hybrids of Figure 4c,f display additional peaks, along with differences in relative intensities of peaks compared to ZnO and ZnO-CNT hybrids. In these samples, the characteristics of the PEDOT:PSS polymer is more dominant. In fact, two peaks—C-O-C of PEDOT at 532.7 eV and O=S of PSS at 531.7 eV—are visible as well as a third peak of Zn-O [29]. In general, the ZnO-D lattice, i.e., as-synthesized ZnO-D or ZnO-D in the nanohybrids, shows a more stable oxygen component, when considering the C 1s spectra of Figure 5a–c, where the relative intensities of O=C-O, C-OH and C-C

peaks are rather constant. However, for the ZnO-A-PEDOT:PSS, the PEDOT peak is less intense than the PSS peak. In fact, PEDOT:PSS macromolecule consists of PEDOT that is positively charged, highly conductive, and hydrophobic. On the other hand, PSS is negatively charged, insulating and hydrophilic. If we consider that the nanoparticles were dispersed in an aqueous solution of PEDOT:PSS, then the adsorption of hydroxyl groups on the surface of the ZnO nanoparticles is inevitable. From the relative intensities of various peaks of the O1s region in Figure 4a,d, ZnO-A tends to adsorb a higher quantity of hydroxyl groups than ZnO-D. Consequently, the surface of ZnO-A is more electronegative with a propensity to the positively charged PEDOT. The O 1s region of ZnO-A-PEDOT:PSS consists of a less intense C-O-C peak and a highly intense O=S peak compared to ZnO-D-PEDOT:PSS. The reduction in the relative intensity of the C-O-C peak suggests that either PEDOT was removed or degraded on adding ZnO-A. In addition, the shift in the Zn-O and C-O-C peaks to higher binding energies confirms the formation of a covalent bond between the C of PEDOT and OH groups present on the ZnO surface. The higher binding energy of the Zn-O peak along with an increase in its intensity indicates that the configuration for the lattice oxygen of ZnO-A becomes more stable.
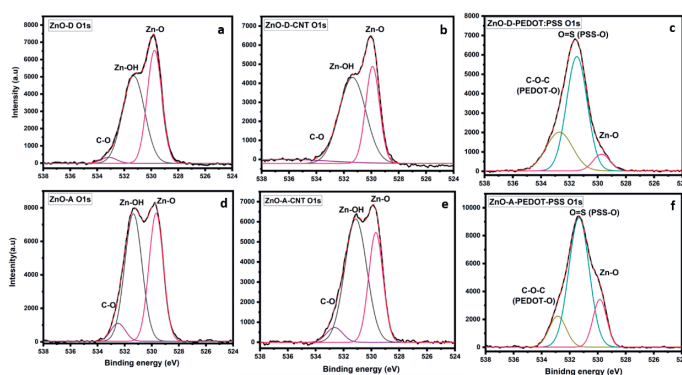
Figure 4. High-resolution XPS spectra of the O 1s region, (**a**) ZnO-D, (**b**) ZnO-D-CNT, (**c**) ZnO-D-PEDOT:PSS, (**d**) ZnO-A, (**e**) ZnO-A-CNT and (**f**) ZnO-A-PEDOT:PSS.

The vibrational properties of the ZnO nanoparticles and their hybrids were investigated using Raman spectroscopy. The results obtained from Raman spectroscopy complement those obtained via XPS. In fact, chemical and structural changes can be evaluated simultaneously on ZnO and CNT or PEDOT:PSS using Raman spectroscopy. Figure 5a compares the different vibrational modes obtained from these samples in the range of 100–800 cm^{-1}. The first-order phonon modes obtained at ~440 cm^{-1}, ~585 cm^{-1} and ~667 cm^{-1}, correspond to E_{2H}, E_1 (LO) and E_2 (TO) modes, respectively [21]. Other modes obtained at ~320 cm^{-1} and 506 cm^{-1} are multiphonon scattering modes that correspond to the E_{2H}–E_{2L} and E_1(TO) + E_{2L} modes, respectively [30]. The E_{2H}, E_{2H}–E_{2L}, E_1 (LO) modes involve the oxygen component of ZnO. More specifically, the E_{2H} at 440 cm^{-1} corresponds to lattice oxygen, whereas the E_1 (LO) corresponds to oxygen-related defects [31]. For all the samples, the E_{2H} mode intensities are high, implying that the ZnO lattice structure is unaffected on hybridizing with CNT or PEDOT:PSS. However, the relative intensity of the E_1 (LO) band increases in the nanocomposites, indicating an increased number of surface defects [32]. The attachment of ZnO on the sidewalls of the CNT through hydroxyl functional groups indicates that the interfacial region and, therefore, the surface of ZnO are highly defective. Additionally, the E_{2H} peak for ZnO-PEDOT:PSS samples has shifted to

a higher wavenumber of 445 cm^{-1} owing to chemical interactions between PEDOT and ZnO. This peak is more intense for ZnO-A-PEDOT:PSS than ZnO-D-PEDOT:PSS, which once again supports that ZnO-A has a more stable lattice configuration in PEDOT:PSS.

Raman signatures lower than 300 cm^{-1} are assigned to the vibrations of Zn_i, and those above 300 cm^{-1} are assigned to the vibrations of oxygen atoms [33]. The peak at 275 cm^{-1} has been attributed to Zn_i or Zn_i clustering [34,35]. The intensity of this mode increases relative to the other modes in the CNT-based nanocomposites and is the highest for PEDOT:PSS-based nanocomposites. This suggests that the amount of Zn_i is higher than Vo in the hybrid samples. Another mode at 526 cm^{-1} is observed for the PEDOT:PSS nanocomposites, corresponding to the combination of Vo and Zn_i [34]. A lower-intensity peak at the same localization is also visible in the ZnO-CNT-based samples. In general, the relative intensity of this combined mode increases in the hybrid samples owing to an increase in Zni. In Figure 5b, Raman bands from 1200–1800 cm^{-1} of pristine CNT are compared to those of ZnO-CNT. The D-band at 1341 cm^{-1} for pristine CNT redshifts for ZnO-CNT to ~1351 cm^{-1}. A similar redshift in the G-band from 1579 cm^{-1} to ~1592 cm^{-1} is also observed. These redshifts further confirm the presence of oxygen or hydroxyl groups on the CNT surface [36]. The (*) marked peaks in ZnO-CNT samples are assigned to C-O bond vibrations from the acetate precursor used during synthesis [21]. Infrared spectroscopy studies of hydrogen adsorption on ZnO suggest that OH and H are adsorbed simultaneously [37]. In fact, the dissociation of hydrogen followed by its adsorption manifests as a change in the corresponding vibrational frequency, including stretching vibrations of Zn-H and O-H, which are very different from the free hydroxyl group vibrational frequency [38]. However, hydrogen adsorption is more likely on prismatic surfaces, implying that facetted ZnO nanoparticles would be more susceptible to hydrogen adsorption [39]. However, for successful hydrogen adsorption, firstly, a more acidic environment is required when working in aqueous media, or a high pressure when working in gaseous media. In addition, the nanoparticles presented in this study are spherical and not facetted. In our case, the NaOH-rich conditions provide a basic environment that is advantageous to the adsorption of hydroxyl groups, further promoted by the presence of V_o.

Figure 5c shows the Raman spectra of ZnO-PEDOT:PSS samples in the range (900–1700 cm^{-1}), where the contributions from PSS and PEDOT vibrational modes are the most significant. Two typical PSS vibrational modes at 988 cm^{-1} and 1097 cm^{-1} are observed [40]. The vibrational modes of PEDOT observed at 1263 cm^{-1}, 1369 cm^{-1}, 1436 cm^{-1} and 1517 cm^{-1} correspond to C_α-C_α, C_β-C_β, symmetrical C_α=C_β and asymmetrical C_α=C_β stretching vibrational modes, respectively. In the ZnO-D-PEDOT:PSS samples, the symmetrical vibrational mode at 1436 cm^{-1} is redshifted compared to the pristine PEDOT:PSS (~1440 cm^{-1}) [41]. However, this mode is slightly more redshifted in the ZnO-A-PEDOT:PSS, suggesting a slightly higher benzoid (coil) to quinoid (linear) structural transition [41,42]. The PEDOT chains of linear conformation tend to increase the conductivity of the polymer due to a stronger covalent bonding with ZnO. Additionally, asymmetrical C_α=C_β bonds of PEDOT have similar intensities for both samples, whereas, C_α-C_α and C_β-C_β bonds for sample ZnO-D-PEDOT:PSS are more intense than sample ZnO-A-PEDOT:PSS. On the other hand, the asymmetrical C_α=C_β bond of PEDOT at 1517 cm^{-1} is more intense for ZnO-A-PEDOT:PSS samples. This implies that the bonds in the PEDOT chain have undergone structural modification provoking a breakdown in symmetry. This again suggests that PEDOT was degraded or removed from the macromolecule upon combining with ZnO-A.
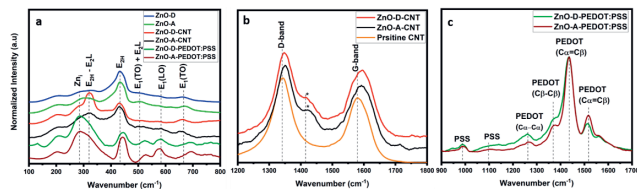
Figure 5. Normalized Raman spectra of (**a**) ZnO-D, ZnO-A, ZnO-D-CNT, ZnO-A-CNT, ZnO-D-PEDOT:PSS and ZnO-A-PEDOT:PSS from 100-800 cm^{-1}, (**b**) pristine CNT, ZnO-D-CNT and ZnO-A-CNT from 1200-1800 cm^{-1}, and (**c**) ZnO-D-PEDOT:PSS and ZnO-A-PEDOT:PSS from 900–1600 cm^{-1}.

3.2. Optical Properties

The band gaps of the ZnO samples, ZnO-CNT hybrids and ZnO-PEDOT:PSS hybrids were calculated via UV-Vis absorption spectroscopy followed by Tauc plots, presented in Figure 6. The band gaps of these samples range from 3.11 to 3.3 eV, which correspond to the theoretical band gap of ZnO, implying that the absorbance in the nanocomposites is dominated by ZnO. Depending on the synthesis routes, variations in the band gaps of ZnO have been observed [43]. The absorption spectra of ZnO samples revealed a sharp shoulder at ~3.3 eV, stretching down to 2.0 eV, whereas a broader shoulder at ~3.3 eV stretching down to ~1.5 eV was observed for the CNT hybrids [44].
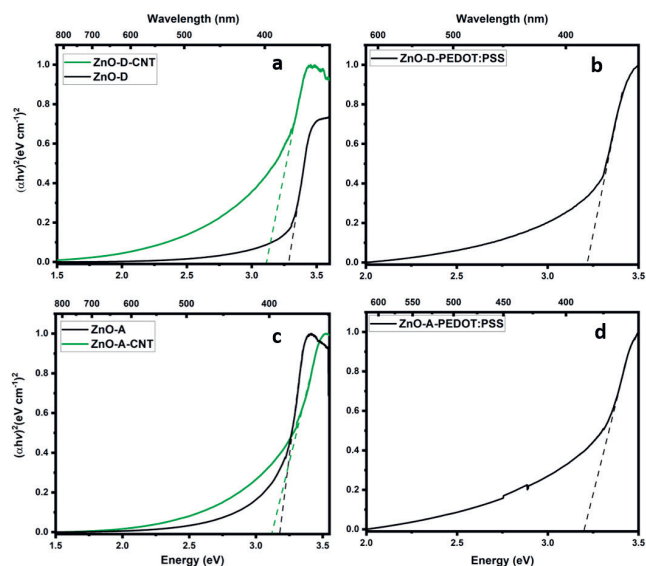
Figure 6. Tauc plot of (**a**) ZnO-D and ZnO-D-CNT, (**b**) ZnO-D-PEDOT:PSS, (**c**) ZnO-A and ZnO-A-CNT, and (**d**) ZnO-A-PEDOT:PSS.

The emission properties of the as-synthesized ZnO samples, ZnO-CNT hybrids, and ZnO-PEDOT:PSS hybrids were investigated at room temperature. A 365 nm (3.4 eV)

excitation source was used to induce band-to-band transitions in these samples with band gaps between 3.11 eV and 3.3 eV. The PL spectra in Figure 7a–f present typical PL emission characteristics of ZnO nanoparticles, consisting of the NBE and DLE [45]. The similarities in emission peak localizations indicate that the emissions mainly originate from ZnO nanoparticles, for both the freestanding and hybrid nanocomposites. However, there are significant changes in the overall quantum efficiencies and intensities of certain emission peaks of the hybrid samples. This suggests that interfacial bonding between ZnO nanoparticles and CNT or PEDOT:PSS via OH groups plays an important role in excitonic separation and recombination. The probable origin of the DLE is the combination of several point defects, such as oxygen interstitials (O_i), oxygen vacancies (V_O), zinc vacancies (V_{Zn}), zinc interstitials (Zn_i), and their complexes [22,46] that are related to the presence of hydrates in the ZnO precursor. In addition, the NBE to DLE ratio is useful in evaluating the crystalline quality of ZnO. Moreover, an average nanoparticle size of 5 nm indicates a high surface-to-volume ratio, which in turn denotes a high amount of surface defects. These surface traps also consist of chemisorbed species, allowing additional radiative or non-radiative recombination mechanisms, which would alter the quantum efficiency of the DLE.

The doubly ionized oxygen vacancy, i.e., V_O^{++}, or surface oxygen vacancy at 2.2 eV is dominant in all the samples due to the high surface-to-volume ratio. The 2.2 eV transition is associated with the capture of a hole by V_O^+ from surface charges to form V_O^{++} [47]. The single ionized oxygen vacancy V_O^+ or volume oxygen vacancy emits at ~2.5 eV. Both types of vacancies produce green luminescence in ZnO. Additionally, the intensity of the green emission can be strongly influenced by free carriers on the surface, especially for nanoparticles with very small sizes [47,48]. Since PL measurements were performed in air, it is likely that hydroxyl groups or oxygen molecules are adsorbed on the surface of the nanoparticles. The chemisorbed oxygen species provoke an upward band bending in the as-synthesized ZnO nanoparticles (Figure 7g), which allows V_O^+ to convert into V_O^{++} through the tunneling of surface-trapped holes to deep levels. Therefore, the observed dominant green emission in ZnO-D and ZnO-A samples is mainly surface related. In a previous study, the chemisorption of hydroxyl groups/oxygen species was suppressed by covering the nanoparticles with CNT [17]. In that study, non-functionalized CNT were used, and a successful passivation of surface states was obtained. In the present case, the CNT were functionalized with OH functional groups, as discussed previously. Therefore, in the present case, the upward band bending is enhanced (Figure 7h). The increased upward band bending leads to further increase in the depletion region size, whereupon the probability of electron capture at the defect sites increases. This mechanism also reduces the probability of band-to-band transitions and the NBE is diminished.

For ZnO-PEDOT:PSS samples, a complete coverage of ZnO with PEDOT:PSS is visible in the TEM images. In general, there is a reduction in the overall emission compared to the as-synthesized and ZnO-CNT samples, due to the low amount of ZnO nanoparticles. However, the NBE-to-DLE ratio is higher in these samples. The increase in NBE can be attributed to the reduced surface hydroxyl groups, relative to the as-synthesized and ZnO-CNT samples, leading to lower upward band bending (Figure 7i). More particularly, the NBE-to-DLE ratio is higher for the ZnO-D-PEDOT:PSS than ZnO-A-PEDOT:PSS. An increase in DLE for the latter can be attributed to the higher amount of hydroxyl groups present on the ZnO-A sample, as assessed on the basis of the XPS studies, leading to a slightly higher upward band bending than for ZnO-D. Additionally, the NBE of both types of hybrid sample, i.e., CNT and PEDOT:PSS, has redshifted, suggesting an increased amount of Zn_i, further corroborating the Raman spectroscopy results. Finally, the red emission at ~1.75 eV is the least significant component in the PL spectra, associated mainly with V_{Zn}-related defects [49].
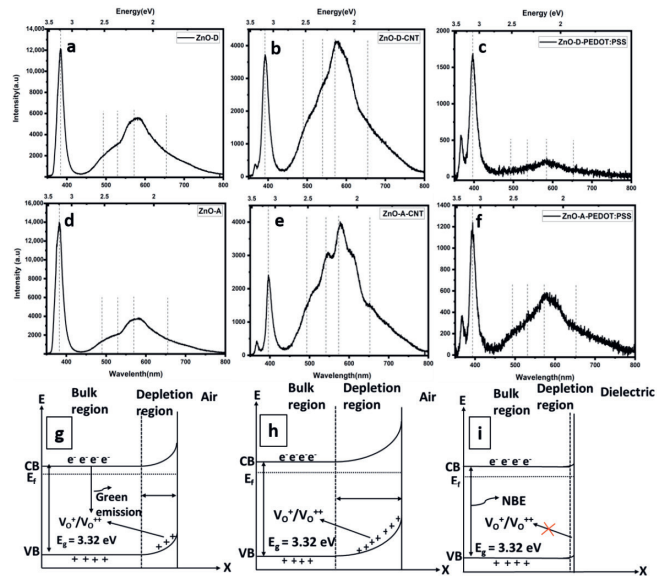
Figure 7. PL emission spectra of (**a**) ZnO-D, (**b**) ZnO-D-CNT, (**c**) ZnO-D-PEDOT:PSS, (**d**) ZnO-A, (**e**) ZnO-A-CNT and (**f**) ZnO-A-PEDOT:PSS. Schematics of upward band bending (**g**) chemisorbed Oxygen species, (**h**) CNT decorated with ZnO through hydroxyl groups, (**i**) ZnO-PEDOT:PSS nanohybrids.

4. Conclusions

In this study, we successfully synthesized ZnO nanoparticles and their hybrids containing CNT and PEDOT:PSS. The effect of hydroxyl groups on the optical properties of ZnO nanoparticles and their hybrids was investigated. The ZnO nanoparticles display optical properties that are both bandgap and defect related. In addition, the choice of precursor immensely influences the overall properties of the nanoparticles and their hybrids. During the synthesis of the hybrid nanocomposites, hydroxyl groups adhere to the surface of the ZnO nanoparticles, and in turn, intensify the defect related emission. These hydroxyl groups are necessary for the successful decoration of the CNT and the incorporation of ZnO in the PEDOT:PSS matrix. Additionally, the linear transformation of PEDOT from the coil structure implies a more conductive polymer, which would enhance the I-V characteristics of the nanocomposite. However, ZnO-A tends to degrade the PEDOT:PSS macromolecule by removing or degrading the conducting PEDOT, which could prove detrimental to the electrical properties of the nanocomposite. Future research consists of incorporating these nanoparticles and their hybrids in LED applications. This present work aids in understanding the modification of the physical and chemical properties of the ZnO nanoparticles when hybridized to PEDOT:PSS and CNT. On the basis of this work, we conclude that ZnO-D and its hybrid nanocomposites, synthesized with hydrate precursors show higher stability and are likely to offer better electrical conductivity when used in LED.

Author Contributions: Conceptualization: K.N., P.R.; methodology: K.N., P.R., E.R.; validation, P.R., E.R. and E.E.; formal analysis, K.N., E.E., M.R.S.; investigation, K.N., P.R., E.R.; resources, E.E., P.R., E.R.; data curation, K.N.; writing—original draft preparation, K.N.; writing—review and editing,

K.N., P.R. and E.R.; supervision, P.R. and E.R.; project administration, P.R.; funding acquisition, P.R. and E.R. All authors have read and agreed to the published version of the manuscript.

Data Availability Statement: Not applicable.

Conflicts of Interest: The authors declare no conflict of interest.

References

1.   Huang, J.; Yin, Z.; Zheng, Q. Applications of ZnO in organic and hybrid solar cells. *Energy Environ. Sci.* **2011**, *4*, 3861–3877. [CrossRef]
2.   Periyayya, U.; Kang, J.H.; Ryu, J.H.; Hong, C.-H. Synthesis and improved luminescence properties of OLED/ZnO hybrid materials. *Vacuum* **2011**, *86*, 254–260. [CrossRef]
3.   Nagpal, K.; Rauwel, E.; Ducroquet, F.; Rauwel, P. Assessment of the optical and electrical properties of light-emitting diodes containing carbon-based nanostructures and plasmonic nanoparticles: A review. *Beilstein J. Nanotechnol.* **2021**, *12*, 1078–1092. [CrossRef] [PubMed]
4.   Shirota, Y.; Kageyama, H. 1—Organic materials for optoelectronic applications: Overview. In *Handbook of Organic Materials for Electronic and Photonic Devices*, 2nd ed.; Ostroverkhova, O., Ed.; Woodhead Publishing: Sawston, UK, 2019; pp. 3–42.
5.   Yu, K.J.; Yan, Z.; Han, M.; Rogers, J.A. Inorganic semiconducting materials for flexible and stretchable electronics. *NPJ Flex. Electron.* **2017**, *1*, 4. [CrossRef]
6.   Könenkamp, R.; Word, R.C.; Godinez, M. Ultraviolet Electroluminescence from ZnO/Polymer Heterojunction Light-Emitting Diodes. *Nano Letters* **2005**, *5*, 2005–2008. [CrossRef]
7.   Biju, V.; Itoh, T.; Anas, A.; Sujith, A.; Ishikawa, M. Semiconductor quantum dots and metal nanoparticles: Syntheses, optical properties, and biological applications. *Anal. Bioanal. Chem.* **2008**, *391*, 2469–2495. [CrossRef]
8.   Yang, P.; Yan, H.; Mao, S.; Russo, R.; Johnson, J.; Saykally, R.; Morris, N.; Pham, J.; He, R.; Choi, H.-J. Controlled Growth of ZnO Nanowires and Their Optical Properties. *Adv. Funct. Mater.* **2002**, *12*, 323–331. [CrossRef]
9.   Huseynova, G.; Hyun Kim, Y.; Lee, J.-H.; Lee, J. Rising advancements in the application of PEDOT:PSS as a prosperous transparent and flexible electrode material for solution-processed organic electronics. *J. Inf. Disp.* **2020**, *21*, 71–91. [CrossRef]
10. Sun, K.; Zhang, S.; Li, P.; Xia, Y.; Zhang, X.; Du, D.; Isikgor, F.H.; Ouyang, J. Review on application of PEDOTs and PEDOT:PSS in energy conversion and storage devices. *J. Mater. Sci. Mater. Electron.* **2015**, *26*, 4438–4462. [CrossRef]
11. Park, Y.; Müller-Meskamp, L.; Vandewal, K.; Leo, K. PEDOT:PSS with embedded TiO2 nanoparticles as light trapping electrode for organic photovoltaics. *Appl. Phys. Lett.* **2016**, *108*, 253302. [CrossRef]
12. Sharma, B.K.; Khare, N.; Ahmad, S. A ZnO/PEDOT:PSS based inorganic/organic hetrojunction. *Solid State Commun.* **2009**, *149*, 771–774. [CrossRef]
13. Lin, B.; Fu, Z.; Jia, Y. Green luminescent center in undoped zinc oxide films deposited on silicon substrates. *Appl. Phys. Lett.* **2001**, *79*, 943–945. [CrossRef]
14. Raji, R.; Gopchandran, K.G. ZnO nanostructures with tunable visible luminescence: Effects of kinetics of chemical reduction and annealing. *J. Sci. Adv. Mater. Devices* **2017**, *2*, 51–58. [CrossRef]
15. Polsongkram, D.; Chamninok, P.; Pukird, S.; Chow, L.; Lupan, O.; Chai, G.; Khallaf, H.; Park, S.; Schulte, A. Effect of synthesis conditions on the growth of ZnO nanorods via hydrothermal method. *Phys. B Condens. Matter* **2008**, *403*, 3713–3717. [CrossRef]
16. Wang, J.; Chen, R.; Xiang, L.; Komarneni, S. Synthesis, properties and applications of ZnO nanomaterials with oxygen vacancies: A review. *Ceram. Int.* **2018**, *44*, 7357–7377. [CrossRef]
17. Nagpal, K.; Rapenne, L.; Wragg, D.S.; Rauwel, E.; Rauwel, P. The role of CNT in surface defect passivation and UV emission intensification of ZnO nanoparticles. *Nanomater. Nanotechnol.* **2022**, *12*, 18479804221079419. [CrossRef]
18. Rauwel, E.; Galeckas, A.; Rauwel, P.; Sunding, M.F.; Fjellvåg, H. Precursor-Dependent Blue-Green Photoluminescence Emission of ZnO Nanoparticles. *J. Phys. Chem. C* **2011**, *115*, 25227–25233. [CrossRef]
19. Niederberger, M. Nonaqueous Sol–Gel Routes to Metal Oxide Nanoparticles. *Acc. Chem. Res.* **2007**, *40*, 793–800. [CrossRef]
20. Kim, S.; Somaratne, R.M.D.S.; Whitten, J.E. Effect of Adsorption on the Photoluminescence of Zinc Oxide Nanoparticles. *J. Phys. Chem. C* **2018**, *122*, 18982–18994. [CrossRef]
21. Sharma, A.; Singh, B.P.; Dhar, S.; Gondorf, A.; Spasova, M. Effect of surface groups on the luminescence property of ZnO nanoparticles synthesized by sol–gel route. *Surf. Sci.* **2012**, *606*, L13–L17. [CrossRef]
22. Sahai, A.; Goswami, N. Probing the dominance of interstitial oxygen defects in ZnO nanoparticles through structural and optical characterizations. *Ceram. Int.* **2014**, *40*, 14569–14578. [CrossRef]
23. Šarić, A.; Gotić, M.; Štefanić, G.; Dražić, G. Synthesis of ZnO particles using water molecules generated in esterification reaction. *J. Mol. Struct.* **2017**, *1140*, 12–18. [CrossRef]

24. Leitão Muniz, F.; Miranda, M.; Morilla-Santos, C.; Sasaki, J. The Scherrer equation and the dynamical theory of X-ray diffraction. *Acta Crystallogr. Sect. A Found. Adv.* **2016**, *72*, 385–390. [CrossRef] [PubMed]
25. Hosseini Largani, S.; Akbarzadeh Pasha, M. The effect of concentration ratio and type of functional group on synthesis of CNT–ZnO hybrid nanomaterial by an in situ sol–gel process. *Int. Nano Lett.* **2017**, *7*, 25–33. [CrossRef]
26. Chen, X.; Wang, X.; Fang, D. A review on C1s XPS-spectra for some kinds of carbon materials. *Fuller. Nanotub. Carbon Nanostructures* **2020**, *28*, 1048–1058. [CrossRef]
27. Aïssa, B.; Fauteux, C.; El Khakani, M.A.; Daniel, T. Structural and photoluminescence properties of laser processed ZnO/carbon nanotube nanohybrids. *J. Mater. Res.* **2009**, *24*, 3313–3320. [CrossRef]
28. Rossell, M.D.; Kuebel, C.; Ilari, G.; Rechberger, F.; Heiligtag, F.J.; Niederberger, M.; Koziej, D.; Erni, R. Impact of sonication pretreatment on carbon nanotubes: A transmission electron microscopy study. *Carbon* **2013**, *61*, 404–411. [CrossRef]
29. Mengistie, D.A.; Ibrahem, M.A.; Wang, P.-C.; Chu, C.-W. Highly Conductive PEDOT:PSS Treated with Formic Acid for ITO-Free Polymer Solar Cells. *ACS Appl. Mater. Interfaces* **2014**, *6*, 2292–2299. [CrossRef]
30. Zeferino, R.S.; Flores, M.B.; Pal, U. Photoluminescence and Raman Scattering in Ag-doped ZnO Nanoparticles. *J. Appl. Phys.* **2011**, *109*, 014308. [CrossRef]
31. Gao, Q.; Dai, Y.; Li, C.; Yang, L.; Li, X.; Cui, C. Correlation between oxygen vacancies and dopant concentration in Mn-doped ZnO nanoparticles synthesized by co-precipitation technique. *J. Alloys Compd.* **2016**, *684*, 669–676. [CrossRef]
32. Naeem, M.; Qaseem, S.; Gul, I.H.; Maqsood, A. Study of active surface defects in Ti doped ZnO nanoparticles. *J. Appl. Phys.* **2010**, *107*, 124303. [CrossRef]
33. Khachadorian, S.; Gillen, R.; Choi, S.; Ton-That, C.; Kliem, A.; Maultzsch, J.; Phillips, M.R.; Hoffmann, A. Effects of annealing on optical and structural properties of zinc oxide nanocrystals. *Phys. Status Solidi B* **2015**, *252*, 2620–2625. [CrossRef]
34. Wang, J.B.; Huang, G.J.; Zhong, X.L.; Sun, L.Z.; Zhou, Y.C.; Liu, E.H. Raman scattering and high temperature ferromagnetism of Mn-doped ZnO nanoparticles. *Appl. Phys. Lett.* **2006**, *88*, 252502. [CrossRef]
35. Gluba, M.A.; Nickel, N.H.; Karpensky, N. Interstitial zinc clusters in zinc oxide. *Phys. Rev. B* **2013**, *88*, 245201. [CrossRef]
36. Montanheiro, T.L.d.A.; de Menezes, B.R.C.; Ribas, R.G.; Montagna, L.S.; Campos, T.M.B.; Schatkoski, V.M.; Righetti, V.A.N.; Passador, F.R.; Thim, G.P. Covalently γ-aminobutyric acid-functionalized carbon nanotubes: Improved compatibility with PHBV matrix. *SN Appl. Sci.* **2019**, *1*, 1177. [CrossRef]
37. Tsyganenko, A.A.; Lamotte, J.; Saussey, J.; Lavalley, J.C. Bending vibrations of OH groups resulting from H$_2$ dissociation on ZnO. *J. Chem. Soc. Faraday Trans. 1 Phys. Chem. Condens. Phases* **1989**, *85*, 2397–2403. [CrossRef]
38. Scarano, D.; Bertarione, S.; Cesano, F.; Vitillo, J.G.; Zecchina, A. Plate-like zinc oxide microcrystals: Synthesis and characterization of a material active toward hydrogen adsorption. *Catal. Today* **2006**, *116*, 433–438. [CrossRef]
39. Dent, A.L.; Kokes, R.J. Hydrogenation of ethylene by zinc oxide. I. Role of slow hydrogen chemisorption. *J. Phys. Chem.* **1969**, *73*, 3772–3780. [CrossRef]
40. Chang, S.H.; Chiang, C.H.; Kao, F.S.; Tien, C.L.; Wu, C.G. Unraveling the Enhanced Electrical Conductivity of PEDOT:PSS Thin Films for ITO-Free Organic Photovoltaics. *IEEE Photonics J.* **2014**, *6*, 1–7. [CrossRef]
41. Lee, H.; Kim, Y.; Cho, H.; Lee, J.-g.; Kim, J.H. Improvement of PEDOT:PSS linearity via controlled addition process. *RSC Adv.* **2019**, *9*, 17318–17324. [CrossRef]
42. Wang, C.; Sun, K.; Fu, J.; Chen, R.; Li, M.; Zang, Z.; Liu, X.; Li, B.; Gong, H.; Ouyang, J. Enhancement of Conductivity and Thermoelectric Property of PEDOT:PSS via Acid Doping and Single Post-Treatment for Flexible Power Generator. *Adv. Sustain. Syst.* **2018**, *2*, 1800085. [CrossRef]
43. Davis, K.; Yarbrough, R.; Froeschle, M.; White, J.; Rathnayake, H. Band gap engineered zinc oxide nanostructures via a sol–gel synthesis of solvent driven shape-controlled crystal growth. *RSC Adv.* **2019**, *9*, 14638–14648. [CrossRef] [PubMed]
44. Rauwel, P.; Galeckas, A.; Salumaa, M.; Ducroquet, F.; Rauwel, E. Photocurrent generation in carbon nanotube/cubic-phase HfO2 nanoparticle hybrid nanocomposites. *Beilstein J. Nanotechnol.* **2016**, *7*, 1075–1085. [CrossRef] [PubMed]
45. Kumar Jangir, L.; Kumari, Y.; Kumar, A.; Kumar, M.; Awasthi, K. Investigation of luminescence and structural properties of ZnO nanoparticles, synthesized with different precursors. *Mater. Chem. Front.* **2017**, *1*, 1413–1421. [CrossRef]
46. Oudhia, A.; Choudhary, A.; Sharma, S.; Aggrawal, S.; Dhoble, S.J. Study of defect generated visible photoluminescence in zinc oxide nano-particles prepared using PVA templates. *J. Lumin.* **2014**, *154*, 211–217. [CrossRef]
47. Vanheusden, K.; Warren, W.L.; Seager, C.H.; Tallant, D.R.; Voigt, J.A.; Gnade, B.E. Mechanisms behind green photoluminescence in ZnO phosphor powders. *J. Appl. Phys.* **1996**, *79*, 7983–7990. [CrossRef]
48. Rauwel, P.; Galeckas, A.; Rauwel, E. Enhancing the UV Emission in ZnO–CNT Hybrid Nanostructures via the Surface Plasmon Resonance of Ag Nanoparticles. *Nanomaterials* **2021**, *11*, 452. [CrossRef]
49. Przezdziecka, E.; Guziewicz, E.; Jarosz, D.; Snigurenko, D.; Sulich, A.; Sybilski, P.; Jakiela, R.; Paszkowicz, W. Influence of oxygen-rich and zinc-rich conditions on donor and acceptor states and conductivity mechanism of ZnO films grown by ALD—Experimental studies. *J. Appl. Phys.* **2020**, *127*, 075104. [CrossRef]

III

K. Nagpal, E. Rauwel, F. Ducroquet, I. Gelard and P. Rauwel, "Relevance of alcoholic solvents in the growth of ZnO nanoparticles and ZnO hierarchical nanorod structures on their optical and opto-electrical properties" , Nanotechnology 34, 485602 (2023)

Relevance of alcoholic solvents in the growth of ZnO nanoparticles and ZnO hierarchical nanorod structures on their optical and opto-electrical properties

Keshav Nagpal[1] ⓘ**, Erwan Rauwel**[1,2] ⓘ**, Frederique Ducroquet**[3] ⓘ**, Isabelle Gélard**[4] ⓘ **and Protima Rauwel**[1,*] ⓘ

[1] Institute of Forestry and Engineering, Estonian University of Life Science, Kreutzwaldi 56/1, Tartu, Estonia
[2] Institute of Veterinary Medicine and Animal Science, Estonian University of Life Science, Kreutzwaldi 62, Tartu, Estonia
[3] Université Grenoble Alpes, IMEP-LaHC, F-38016 Grenoble, France
[4] Université Grenoble Alpes, CNRS, Grenoble INP, LMGP, F-38000 Grenoble, France

E-mail: protima.rauwel@emu.ee

Abstract

We report on the synthesis of ZnO nanoparticles and ZnO hierarchical nanorod structures using four different alcohols i.e. methanol, isopropanol, ethanol, and aqueous ethanol (70% alcohol, 30% water). The syntheses of the nanoparticles were carried out by non-aqueous and hydrothermal routes. In general, absolute alcohol allows a better control of the synthesis reaction and nanoparticles as small as 5 nm were obtained, confirmed by TEM. XPS analysis elucidated the chemical states that were correlated to the synthesis reaction. For the nanorod growth, these four alcohols were used as seeding solvents, followed by hydrothermal ZnO nanorod growth. Here, the seed layer tailored the nanorod diameters and surface defects, which were studied by SEM and photoluminescence spectroscopy. Subsequently, the ZnO nanorods were electrically characterized and exhibited persistent photoconductivity under UV irradiation of 365 nm. The differences in conductivity in dark and under UV irradiation were attributed to the size of the nanorods, defect states, semiconductor band bending and oxygen adsorption–desorption mechanisms. Parameters such as photoresponse and photosensivity are also calculated in order to evaluate their applicability in UV sensors. This work demonstrates optimization of the physical, chemical, electrical and optical properties of both ZnO nanostructures via the use of alcoholic solvents.

Supplementary material for this article is available online

Keywords: ZnO, nanoparticles, nanorods, depletion region, photoresponse, band bending, persistant photoconductivity

(Some figures may appear in colour only in the online journal)

1. Introduction

Metal-oxide-semiconductor nanostructures are suitable candidates for optoelectronic devices, such as chemical sensors,

solar cells, ultra-violet (UV) lasers, UV photodetectors, as well as visible and UV light emitting diodes [1–4]. Among them, the intrinsic n-type ZnO semiconductor has attracted interest due to its wide band gap of 3.37 eV, high excitation binding energy of 60 meV, chemical stability and remarkable electrical and optical properties at the nanoscale [5]. However

---

1

today, the major obstacle in obtaining a ZnO p–n homo-junction diode lies in the difficulty of stabilizing a p-type ZnO semiconductor [6].

The physical and chemical properties of ZnO depend on the synthesis conditions that in turn, control the morphology and defect states of the material. In sol–gel synthesis of ZnO, the polar property and the nature of the organic solvent govern the reaction kinetics that subsequently affect the nucleation and growth of ZnO nanostructures [7]. Also, the presence of water in alcoholic solvents accelerates the growth process, leading to a non-uniform morphology of the nanostructures [8, 9]. In contrast, using absolute alcohol produces spherically shaped nanoparticles (<10 nm) with a uniform size distribution, thus allowing a better control of the reaction kinetics [10]. In general, the synthesis temperature with absolute alcohol solvents is usually restricted to the boiling point of the solvents. For example, the high boiling point of diethylene glycol (DEG) allows synthesis up to temperatures of 245 °C [11, 12]. Moreover, the high dielectric constant of polyol solvents results in a quick dissolution of the inorganic zinc precursors. Besides, ZnO nanoparticles harbor large amounts of surface defects owing to their higher surface-to-volume ratio identified using photoluminescence spectroscopy [13–15].

Other than nanoparticles, ZnO can also be grown as hierarchical structures, such as nanorods that tend to exhibit persistent photoconductivity (PPC) in which, the photo-induced current persists even after the removal of UV radiation [16]. In that regard, PPC widens ZnO-nanorod's applicability to photocapacitors for charge storage applications [16–18]. In fact, PPC is attributed to charge trapping at the various defect states within the band gap of ZnO that in turn, retards the decay of the photocurrent [19]. Studies also demonstrate that adsorption–desorption kinetics of surface oxygen play an important role in the ZnO-nanorod conductivity and PPC [17, 20]. Furthermore, ZnO-nanorod growth methods include chemical vapor growth, electrochemical deposition and vapor–liquid–vapor growth. Nevertheless, hydrothermal synthesis allows cost-effective and low temperature growth of ZnO nanorods. Various substrates, including silicon, sapphire, polystyrene, polyethylene and indium tin oxide (ITO) coated on glass have been utilized for the growth of ZnO nanorods by hydrothermal synthesis [21–23]. Preliminary seeding on a substrate is a crucial step towards creating ZnO nucleation sites in order to promote a high-density growth of ZnO nanorods. Additionally, factors viz., surface roughness, seeding buffer solution and thickness of the seed layer, tailor the morphology of ZnO nanorods [24].

In this work, four types of alcoholic solvents i.e. methanol, ethanol, isopropanol and aqueous ethanol were used for the sol–gel synthesis of ZnO nanoparticles and for the preparation of the seed layer solution to create nucleation sites for ZnO nanorod growth. Depending upon the dimensionality of the ZnO nanostructure i.e. 0D or 1D, the surface defects varied due to the change in the aspect ratio and consequently, the surface-to-volume ratio. In addition, the solvents of the seed layer also alter defects in the nanorod,

which in turn, affect the electrical conductivity and PPC. In order to obtain uniform ZnO nanorod growth, techniques such as chemical vapor deposition and radio frequency magnetron sputtering have been mainly applied for the nucleation of the seeding layer [25, 26]. However, in this study a drop-cast method with the help of a micropipette was employed. This technique is cost-effective and allowed to compare the effect of different alcoholic solvents used for seeding on the uniformity of the ZnO-nanorod growth. Therefore, this study provides new perspectives on the solvent-dependent growth of ZnO nanorods. Subsequently, photoluminescence spectroscopy was used to elucidate the various defects present in these nanoparticles and nanorods. Both, the nanoparticles and nanorods were evaluated by physical and chemical characterization techniques. The nanorods were further evaluated for their current versus voltage (I–V) characteristics and photoconductivity under UV irradiation.

2. Materials and methods

2.1. Synthesis of ZnO nanoparticles

$Zn(CH_3COO)_2.2H_2O$ (99.9%, Aldrich) was used as a zinc precursor for the synthesis of ZnO nanoparticles via sol–gel routes. Sodium hydroxide (NaOH) (99.9%, Aldrich) was used as an oxidizing agent. All the chemicals used were of analytical grade. In order to prepare 0.05 M solutions of zinc precursor, 219.5 mg of $Zn(CH_3COO)_2.2H_2O$ was dissolved in 20 ml of absolute methanol, aqueous ethanol (70% alcohol, 30% water), absolute ethanol and absolute isopropanol. The zinc precursor solutions were placed in a water bath maintained at 60 °C, 65 °C, 65 °C and 70 °C, respectively, controlled by a temperature probe, under continuous magnetic stirring until the zinc salt was completely dissolved in the alcoholic solvent. The temperature was kept below the boiling point of the alcohol in order to prevent its evaporation. In order to dissolve the zinc precursor in isopropanol, the solution was sonicated for 5 min after 10 min of magnetic stirring at 70 °C, after which the solution was again magnetically stirred in a water bath at 70 °C. Further, solutions of 0.10 M NaOH ($\sim$80 mg) in 20 ml of absolute methanol, aqueous ethanol, absolute ethanol and absolute isopropanol were prepared. The NaOH solution was added dropwise to the zinc precursor solutions. Thereafter, the mixtures were maintained at their growth temperatures for 2 h, after which, they were cooled to ambient temperature. The resulting solutions containing ZnO nanoparticles were then centrifuged at 4500 rpm for 6 min and dried for 24 h in air at 60 °C. This resulted in an agglomeration of ZnO nanoparticles in the form of a white pellet that was thereafter crushed in a very fine powder.

2.2. Synthesis of ZnO nanorods

2.2.1. Growth of nanorods. For the growth of ZnO nanorods, ITO coated on a glass substrate was etched at its center for 3 min using 12 M HCL (Honeywell). Copper tape was used to protect the rest of the ITO surface from etching and also to
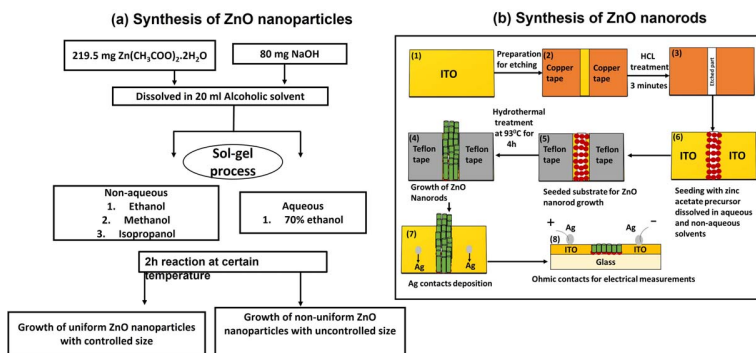
2

Figure 1. (a) Schematic for controlled nanoparticle synthesis. (b)) Schematic of the process followed for the seeding and hydrothermal synthesis of ZnO nanorods, (7) silver paste deposition on ITO for ohmic contacts and (8) schematic of the cross-sectional view of the device with ohmic contacts.

limit the width of the etched zone to ∼4 mm, as shown in figure 1. After etching, the copper tape was removed and the etched substrates were cleaned in acetone, isopropanol and DI water with 10 min of sonication in each solvent.

2.2.2. Seeding. In the first step, four seeding solutions were prepared by dissolving 0.011 g of $Zn(CH_3COO)_2.2H_2O$ in 10 ml of absolute methanol, aqueous ethanol, absolute ethanol and absolute isopropanol. Similar to ZnO nanoparticle synthesis, the seeding solutions were maintained in a water bath at 60 °C, 65 °C, 65 °C and 70 °C under continuous magnetic stirring until the zinc salt was completely dissolved in absolute methanol, aqueous ethanol, absolute ethanol and absolute isopropanol, respectively. After cooling the seeding solutions, $2 \mu l$ of the solution was drop-cast on the etched ITO maintained at 60 °C on a hot plate. The drop-casting procedure was repeated 25 times for a total of $50 \mu l$ of the seeding solution. Thereafter, the seeded ITO was washed with the corresponding solvent and immediately transferred for annealing at 275 °C on a hot plate for 15 min. Then after cooling down the seeded substrate, the non-seeded part of the ITO was covered with Teflon tape to prevent the growth of ZnO nanorods on the non-seeded part as shown in figure 1(b5).

2.2.3. Growth of nanorods. Following the seed layer deposition, the nanorod growth was carried out with 0.595 g of zinc nitrate hexahydrate $(Zn(NO_3)_2.6H_2O)$ dissolved in 40 ml of de-ionized water. The solution was magnetically stirred at room temperature for 30 min. Thereafter, 0.28 g of hexamethylenetetramine $((CH_2)_6N_4, HMTA)$ was added to the solution under constant magnetic stirring for another 30 min. The seeded ITO substrate covered with Teflon tape was then inverted and immersed in the prepared growth solution in a beaker that was then placed in a Teflon autoclave and sealed tightly. The autoclave was then maintained at

93 °C in an oven for 4 h. After which, the autoclave was removed from the oven and cooled down to room temperature. After cooling, the Teflon tape was removed and substrate was thoroughly washed with de-ionized water and dried in an oven maintained at 55 °C for 24 h. For electrical measurements of these nanorods, Ag paste was deposited on each side of the ITO heated on a hot plate at 80 °C for 5 min as shown in figure 1(b7).

2.3. Characterization

X-ray diffraction patterns were collected in Bragg–Brentano geometry using a Bruker D8 Discover diffractometer (Bruker AXS, Germany) with CuKα1 radiation ($\lambda = 0.154\,06$ nm) selected by a Ge (111) monochromator and LynxEye detector. For ZnO nanoparticles prepared using methanol, ethanol and isopropanol, transmission electron microscopy (TEM) was carried out on a Tecnai G2 F20 (Netherlands) field emission gun (FEG) at an acceleration voltage of 200 kV with a point-to-point resolution of 2.4 Å. For the ZnO nanoparticle sample prepared using aqueous ethanol, TEM was carried out on a JEOL 2010 LaB$_6$ (Jeol, Japan) instrument, operating at 200 kV in TEM mode and providing a point-to-point resolution of 1.9 Å. SEM was carried out on ZEISS EVO MA15 SEM (ZEISS, Germany) in secondary electron mode and a FEI QUANTA 250 environmental SEM FEG operating at 15 kV. XPS measurements were performed at room temperature with a SPECS PHOIBOS 150 hemispherical analyzer (SPECS GmbH, Berlin, Germany) in a base pressure of 5×10^{-10} mbar using monochromatic Al K-alpha radiation (1486.74 eV) as an excitation source operated at 300 W. The energy resolution as measured by the FWHM of the Ag 3d5/2 peak for a sputtered silver foil was 0.62 eV. The spectra were calibrated relative to the C 1s at 284.8 eV. The optical absorbance of ZnO nanoparticles and ZnO nanorods were determined using an UV–vis UV-1600PC spectrophotometer (VWR, US) in the 300–700 nm region. The band gap of ZnO
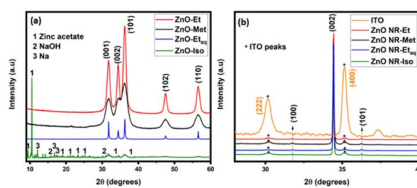
Table 1. List of abbreviations and solvents used for the as-synthesized ZnO nanoparticles and ZnO nanorods.

Sample	Type	Solvent	Seeding solvent
ZnO-Met	Nanoparticles	Methanol	——
ZnO-Et$_{aq}$	Nanoparticles	aqueous ethanol	——
ZnO-Et	Nanoparticles	Ethanol	——
ZnO-Iso	Nanoparticles	Isopropanol	——
ZnO NR-Met	Nanorods	——	Methanol
ZnO NR-Et$_{aq}$	Nanorods	——	aqueous ethanol
ZnO NR-Et	Nanorods	——	Ethanol
ZnO NR-Iso	Nanorods	——	Isopropanol

Figure 2. (a) XRD spectra of samples ZnO-Et, ZnO-Met, ZnO-Et$_{aq}$ and ZnO-Iso. (b) XRD spectra of the ITO substrate (reference) and samples ZnO NR-Et, ZnO NR-Met, ZnO NR-Et$_{aq}$ and ZnO NR-Iso.

samples and ZnO nanorod samples refer to all ZnO nanorod samples.

3.1. Structure and morphology

XRD patterns of ZnO-Met, ZnO-Et$_{aq}$, ZnO-Et and ZnO-Iso are shown in figure 2(a). The peaks (100), (002), (101), (102), and (110) correspond to the hexagonal Wurtzite structure ($a = 3.25$ Å and $c = 5.20$ Å) of ZnO (JCPDS, Card Number 36-1451). Reflections indicating other phases than Wurtzite ZnO are absent in samples ZnO-Met, ZnO-Et$_{aq}$ and ZnO-Et. However, the XRD pattern of sample ZnO-Iso consists of crystalline ZnO nanoparticles of very small sizes. Also, the majority of the additional peaks are related to the zinc acetate precursor (marked 1), others to NaOH (marked 2) and Na metal (marked 3) [27–29]. In fact, for sol–gel synthesis, the reaction time is a crucial parameter for the successful precipitation of crystalline ZnO, which was fixed to 2 h for all four types of ZnO nanoparticles in this study. Hu *et al* demonstrated the formation of highly crystalline ZnO in a long carbon chain solvent medium of 1-butanol (C_4H_9OH) with a longer reaction times of 11–24 h [27]. In our study, due to the longer carbon chain of isopropanol (C_3H_7OH) compared to ethanol (C_2H_5OH) and methanol (CH_3OH), the reaction time of 2 h was clearly not sufficient for the complete reaction of $Zn(CH_3COO)_2.2H_2O$ with NaOH. In addition, NaOH has a low solubility in isopropyl alcohol, which implies that $Zn(CH_3COO)_2.2H_2O$ and NaOH were unable to fully dissolve and react, leading to the presence of by-products, such as unreacted precursors in the ZnO nanopowder. In the XRD patterns, the indexed peaks for samples ZnO-Met and ZnO-Et and for sample ZnO-Iso are broad compared to sample ZnO-Et$_{aq}$. An estimation of the average size of the nanoparticles was carried out by using the full-width-half maximum value in the Scherrer equation (given below) of reflections of ZnO-Met, ZnO-Et and ZnO-Iso.

$$D = \frac{0.9\lambda}{\beta \cos\theta}$$

where D is particle size, λ ($= 0.154\,06$ nm) is the wavelength of incident x-ray beam, β is FWHM in radians and θ is Bragg's diffraction angle. The size calculations were carried out using high index reflections (100) and (002) for samples ZnO-Met, ZnO-Et and ZnO-Et$_{aq}$ and (100) and (101)

nanoparticles and ZnO nanorods were subsequently calculated with Tauc plots. PL spectroscopy was carried out at room temperature on powder samples with an excitation wavelength of 365 nm of LSM-365A LED (Ocean insight, USA) with a specified output power of 10 mW. The emission was collected by FLAME ES UV–vis spectrometer (Ocean optics, USA) with spectral resolution of 1.34 nm. Raman spectra were collected using a WITec Confocal Raman Microscope System alpha 300 R (WITec Inc., Ulm, Germany). Excitation in confocal Raman microscopy is generated by a frequency-doubled Nd:YAG laser (New-port, Irvine, CA, USA) at a wavelength of 532 nm, with 50 mW maximum laser output power in a single longitudinal mode. The system was equipped with a Nikon (Otawara, Japan) objective with a X20 magnification and a numerical aperture NA = 0.46. The acquisition time of a single spectrum was set to 0.5 s. For electrical measurements, ZnO nanorods were grown on 20 mm x 15 mm sized unpatterned ITO glass substrates (OSSILA, UK) with 100 nm ITO thickness and 20 Ω/square resistance. The electrical measurements were carried out using two source measure units (Agilent 4156). The measurements were performed by considering ohmic contacts as shown in figure 1(h). For the photoresponse of ZnO nanorods, a 125 W Hg lamp with an output wavelength of 365 nm was collected by an optical fiber of diameter 4 mm. The irradiance at the outlet of the optical fiber was measured as $\sim$15 mW cm^{-2}.

3. Results

Table 1 provides the list of ZnO nanoparticles and ZnO nanorod samples synthesized in this work. Samples ZnO-Met, ZnO-Et$_{aq}$, ZnO-Et and ZnO-Iso refer to ZnO nanoparticles prepared by using absolute methanol, aqueous ethanol, absolute ethanol and absolute isopropanol as solvents. Whereas, samples ZnO NR-Met, ZnO NR-Et$_{aq}$, ZnO NR-Et and ZnO NR-Iso refer to ZnO nanorod samples prepared by using the same solvents for the seed-layer solution. In this work, terms ZnO samples refer to all ZnO nanoparticle

Figure 3. High magnification TEM micrographs of samples (a) ZnO-Met, (b) ZnO-E$_t$, (c) ZnO-Iso and (d) ZnO-Et$_{aq}$, (e) low magnification TEM image of ZnO-Iso, (f) HRTEM image of single highly crystalline ZnO-Iso nanoparticle. Low magnification SEM images of samples (g) ZnO NR-Met, (h) ZnO NR-Et$_{aq}$, (i) ZnO NR-Et and (j) ZnO NR-Iso, showing the surface morphology. Higher magnification SEM images of samples in titled mode (k) ZnO NR-Met, (l) ZnO NR-Et$_{aq}$, (m) ZnO NR-Et and (n) ZnO NR-Iso, showing hexagonally facetted morphology and density of ZnO nanorods.

reflection for ZnO-Iso. Average nanoparticle diameters of 10 nm, 9 nm and 7.3 nm were obtained, respectively.

XRD patterns of ZnO NR-Et, ZnO NR-Met, ZnO NR-Et$_{aq}$ and ZnO NR-Iso and ITO are shown in figure 2(b). The XRD characteristic peaks (100), (002) and (101) confirm the hexagonal wurtzite structure of ZnO, while the sharp peak at ∼34.5^0, which is the out-of-plane reflection, suggests that nanorods grow along the *c*-axis [30]. The XRD peaks (222) and (400) correspond to ITO coated on glass and are marked (*) in figure 2(b) [31]. More detailed information about the

particle sizes and shapes of the nanoparticles, as well as the diameters of nanorods were obtained via TEM and SEM analyses, described in the following sections.

The morphology and nanoparticle size of the ZnO samples were studied by TEM, as shown in figures 3(a)–(f). For samples ZnO-Met, ZnO-Et and ZnO-Iso in figures 3(a)–(c), the TEM micrographs reveal spherical nanoparticles with a uniform size distribution. However, the nanoparticles of samples ZnO-Met and ZnO-Et tend to agglomerate (figures 3(a) and (b)). Size distribution histograms of samples

5

reveal an average size of ∼4.8 nm, ∼5.2 nm and 4.2 nm for samples ZnO-Met, ZnO-Et and ZnO-Iso, respectively. The nanoparticles of the ZnO-Iso sample are monodispersed, which is likely due to the presence of isopropyl groups ((CH3)$_2$CHO) and other unreacted precursors. Additionally, the low magnification image of ZnO-Iso (figure 3(e)) provides an overview of the nanoparticles. The needle-like structures of low contrast are the unreacted precursor with dark dots corresponding to ZnO nanoparticles magnified in figure 3(c). These organic ligands probably act as a surfactant and prevent ZnO-nanoparticle agglomeration. The HRTEM image of the ZnO-Iso nanoparticles in figure 3(f) provides a point-to-point resolution of a highly crystalline nanoparticle, thus confirming the XRD result of small and crystalline nanoparticles. Sample ZnO-Et$_{aq}$ (figure 3(d)) shows needle-like and hexagonally shaped nanoparticles. In a previous study, the effect of varying the NaOH molar ratio on the morphology of ZnO nanoparticles with an aqueous ethanol solvent was investigated [8]. The authors demonstrated that reaction kinetics leading to the growth of ZnO nanoparticles are accelerated by increasing quantities of OH$^-$ ions in the solution. The increase in hydroxyl ions stimulates the selective and directional growth of nanoparticles, into needle-like structures as well as other irregularly shaped nanoparticles. This suggested that the reaction kinetics are difficult to control in the presence of water. Samples ZnO-Met, ZnO-Et and ZnO-Iso are synthesized with absolute alcohol solvents that are devoid of water and therefore, the reaction rate is slower, which supports the formation of spherically shaped nanoparticles. On the other hand, in the presence of water molecules, the reaction kinetics are quicker, which results in anomalously shaped nanoparticles for sample ZnO-Et$_{aq}$ of figure 3(d). ZnO crystal with a growth direction perpendicular to the [0001] basal planes, contains eight facets. The facets at the 2 ends along are polar, while the other six facets forming the sides of the hexagon are non-polar. More precisely, the ZnO crystal lattice has characteristic polar planes (0001) and (000$\bar{1}$) packed with zinc ions (Zn^{2+}) or oxygen ions (O^{2-}), as well as six non-polar planes belonging to a family of planes [$\bar{1}$ 100], containing both O and Zn ions making them electrically neutral. ZnO polar planes are highly reactive, and are more likely to participate in the chemical reaction of the ZnO nanorod growth process. In addition, one polar plane anchors the nanorod to the substrate, while the other one is exposed to air i.e. (0001), which is Zn-terminated. Furthermore, in ZnO, the growth rate of individual crystallographic planes is determined by the principle of energy minimization according to which, the growth rate of (0001) plane is the highest and (000 $\bar{1}$) plane is the lowest [32]. Therefore, vertical growth along (0001) direction is the most energetically favorable growth axis, which therefore leads to the rod-shaped growth of ZnO. The largest exposed area of the nanorod in the solution corresponds to the non- SEM was performed to study the morphology and distribution of the nanorods on the substrates. SEM images from figures 3(g)–(n) are the top view of ZnO nanorod samples. The low magnification SEM images in figures 3(g)–(j), exhibit zones that are devoid of nanorods, indicating discontinuities in the nanorod layer.

Table 2. List of average particle size of ZnO nanoparticle samples obtained from XRD, and TEM, and average diameter of ZnO nanorods obtained from XRD and SEM. Size distribution histograms are provided in S1 and S2 for nanoparticles and nanorods, respectively.

Sample	Particle size (XRD)	Particle size (TEM)	Nanorod diameter (SEM)
ZnO-Met	10 nm	4.8 nm	——
ZnO-Et$_{aq}$	——	——	——
ZnO-Et	9 nm	5.2 nm	——
ZnO-Iso	7.3 nm	4.2 nm	——
ZnO NR-Met	——	——	85 nm
ZnO NR-Et$_{aq}$	——	——	110 nm
ZnO NR-Et	——	——	90 nm
ZnO NR-Iso	——	——	80 nm

Figure S3 provides additional SEM images depicting the morphology of the nanorods. In figure 3(g), sample ZnO NR-Met exhibits a more uniform nanorod growth compared to sample ZnO NR-Et and sample ZnO NR-Iso that contain zones devoid of nanorods in figures 3(i) and (j). Similarly, sample ZnO NR-Et$_{aq}$ exhibits a non-uniform growth with numerous empty areas (figure 3(h)). Higher magnification images taken with a tilted substrate of the ZnO-nanorod samples in figures 3(k)–(n) exhibit nanorods with diameters listed in table 2. The diameters of ZnO NR-Met, ZnO NR-Et and ZnO NR-Iso samples are similar ∼80–90 nm, obtained from size distribution histograms, most likely due to the absence of water in the seeding solutions. Whereas, due to the presence of 30% water in the seeding solution of the ZnO NR-Et$_{aq}$ sample, the nanorod diameter is the largest (∼110 nm), among the four samples. All nanorod samples present hexagonally facetted nanorods, as visible in figures 3(k)–(n). In fact, a hexagonally facetted polar surfaces, necessary to minimize the energy requirement during growth. In addition, the presence of HMTA during the synthesis process reduces the ZnO growth in the radial direction by restricting it along non-polar m-planes (diametrically) and by favoring the growth in the direction of polar *c*-planes (longitudinally) [32]. In fact, HMTA also covers the surfaces of the non-polar sidewalls with OH groups, similar to a surfactant, whereby it reduces the radial growth of the nanorods [33]. HMTA is a pH buffer that ensures continuous growth of the ZnO nanorod and at the same time regulates the release of OH$^-$ ions. In addition, the concentration of HMTA in the reaction mixture also modifies the nucleation process by interacting with the ZnO seed layer, thus increasing the density of ZnO nanorods [34].

The high-resolution XPS spectra of the C 1s and O 1s regions of the samples ZnO-Met, ZnO-Et$_{aq}$, ZnO-Et and ZnO-Iso are shown in figures 4 and 5, respectively. The C–C bond at 284.8 eV in the C 1s spectra (figure 4), corresponds to adventitious carbon [35]. The bonds C–OH, O=C–O present in these samples are contributions from the NaOH and zinc acetate precursor used during the synthesis [10]. Therefore, C 1s spectra confirm the presence of chemisorbed OH groups on the surface of the nanoparticles. The C 1s spectrum of sample
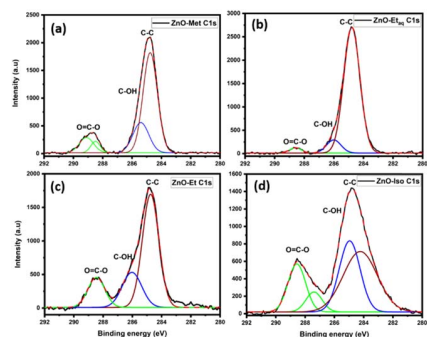
6

Figure 4. C 1s XPS spectra of samples (a) ZnO-Met, (b) ZnO-Et$_{aq}$, (c) ZnO-Et and (d) ZnO-Iso.
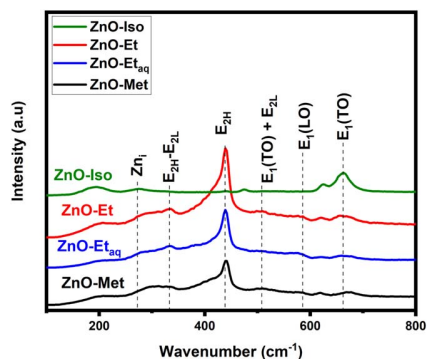

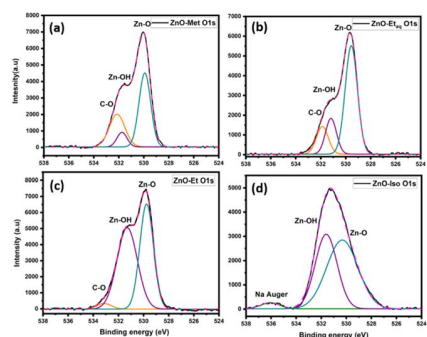**Figure 6.** Raman spectra of samples ZnO-Iso, ZnO-Et, ZnO-Et$_{aq}$, and ZnO-Met.

Figure 5. O 1s XPS spectra of samples (a) ZnO-Met, (b) ZnO-Et$_{aq}$, (c) ZnO-Et and (d) ZnO-Iso.

ZnO-Iso manifests the highest contributions from the O=C–O, C–OH and C=O bonds, which confirm the presence of unreacted zinc acetate precursor and NaOH on the surface ZnO-Iso nanoparticles. Due to the long carbon chain of isopropanol, the dissolution of $Zn(CH_3COO)_2.2H_2O$ salt in isopropanol is very slow and isopropyl groups can anchor easily on the surface of ZnO through oxygen bonding, whereby lowering its solubility. In the case of the other solvents and under similar conditions, $Zn(CH_3COO)_2.2H_2O$ salt dissolution is quicker as the solvent does not anchor on the ZnO nanoparticle surface. This explains the lower contributions from the O=C–O, C–OH and C=O bonds in the case of ZnO-Met and ZnO-Et samples. On the other hand, for sample ZnO-Et$_{aq}$, due the presence of water, the dissolution of the $Zn(CH_3COO)_2.2H_2O$ salt and thus the nucleation rate are the quickest and therefore, the sample shows the lowest contributions from O=C–O, C–OH and C=O bonds. In addition,

the presence of water contributes to by-product and surfactant removal from the surface of ZnO nanoparticles [13].

The high resolution O 1s spectra of samples ZnO-Met, ZnO-Et$_{aq}$, ZnO-Et and ZnO-Iso are shown in figure 5. The main peak is lattice oxygen (Zn–O) bond at ∼529 eV for all samples that is characteristics of ZnO nanoparticles. Additionally, for all samples the peak at ∼531.5 eV corresponds to the presence of hydroxyl groups that are bonded to the ZnO nanoparticle surface. However, this peak can also be related to oxygen defects or surface oxygen vacancies [36]. TEM analysis highlighted the very small size of nanoparticles, supporting the presence of surface oxygen vacancies and C 1s spectra indicated that hydroxyl groups are anchored on the nanoparticle surface. For samples ZnO-Met, ZnO-Et$_{aq}$ and ZnO-Et, O 1s peak structure is similar with only differences in relative intensities of the peaks, implying a comparable surface chemistry. A noticeable difference is the relative increase of the Zn–OH peak to the lattice oxygen peak, which increases with the absolute alcohol chain length. For sample ZnO-Iso, the intensity for the Zn–OH peak is higher than the lattice Zn–O peak, indicating a higher amount of adsorbed OH groups and unreacted Zn precursor. The presence of Na or NaOH is illustrated by the peak at 536 eV in figure 5(d), also confirmed by XRD [37]. Therefore, chemical states of ZnO-Iso obtained from C 1s and O 1s spectra suggest that the surface of sample ZnO-Iso is covered with isopropyl groups from isopropanol, acetate groups from the Zn precursor, and hydroxyl groups from NaOH. Additionally, the Zn 2p spectra are provided in S4. For the ZnO-Iso sample, this further highlights the presence of another phase of Zn with +2 oxidation states at lower binding energies [38]. In our case, the peak at binding energy of ∼1018 eV is most likely related to the unreacted Zn acetate precursor.

The vibrational modes of the ZnO nanoparticles were investigated using Raman spectroscopy. In figure 6, the Raman spectra compare the different vibrational modes from these samples in the range of 100–800 cm^{-1}. The modes
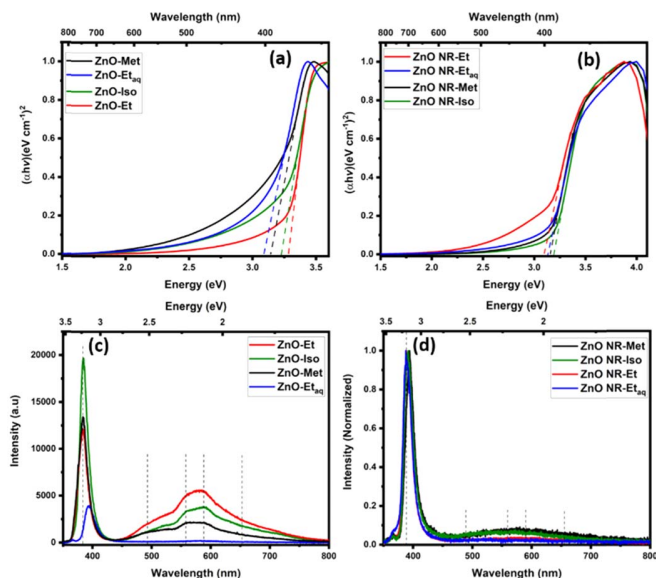
7

175

Figure 7. Tauc plot of samples (a) ZnO-Met, ZnO-Et$_{aq}$, ZnO-Et and ZnO-Iso and (b) ZnO NR-Met, ZnO NR-Et$_{aq}$, ZnO NR-Et, and ZnO NR-Iso, (c) PL spectra of samples ZnO-Met, ZnO-Et, ZnO-Et$_{aq}$ and ZnO-Iso and (d) normalized PL spectra of samples ZnO NR-Met, ZnO NR-Et, ZnO NR-Et$_{aq}$ and ZnO NR-Iso.

visible at $\sim$440 cm^{-1}, $\sim$585 cm^{-1} and $\sim$667 cm^{-1} correspond to E$_{2H}$, E$_1$ (LO) and E$_2$ (TO) modes, respectively and are known as first-order phonon modes. The modes visible at $\sim$320 cm^{-1} and 506 cm^{-1} correspond to the E$_{2H}$–E$_{2L}$ and E$_1$(TO) + E$_{2L}$ modes and are known as multiphonon scattering modes [39, 40]. In particular, the E$_{2H}$ mode at 440 cm^{-1} corresponds to lattice-oxygen or Zn-O vibrations and confirms the formation of ZnO. Whereas, the mode E$_1$ (LO) corresponds to oxygen-related defects [10]. In general, the modes below 300 cm^{-1} are Zn-related defects, while the modes above 300 cm^{-1} are related to oxygen or both, zinc- and oxygen-related complex defects [41]. Sample ZnO-Et shows the highest intensity of E$_{2H}$ mode relative to samples ZnO-Et$_{aq}$ and ZnO-Met. Whereas, for sample ZnO-Iso, the E$_{2H}$ mode has largely diminished. Several factors affect the peak shifts and their intensities, including the presence of secondary phases and inorganic contaminants that modify the phonon confinement of the nanoparticle. Besides, XRD and TEM clearly indicate the presence of very small nanoparticles that are embedded in organic compounds. The latter most likely dampens this particular phonon mode. Further, the high Na:Zn ratio obtained from XPS of 1.5:1 suggests that the presence of Na and NaOH could affect this mode. For e.g. the Raman study of ZnO-CdO based nanocomposite has shown a similar decrease in the E$_{2H}$ mode of ZnO suggesting that the

presence of CdO modifies the phonon confinement of ZnO [42]. Additionally, the E$_1$(TO) band indicates a breakdown in long range ordering in ZnO and the E$_1$(LO) band suggests the presence of oxygen vacancies and zinc interstitials or complex defects combining both [43]. The ratio of intensities of E$_{2H}$ and E$_1$(LO) therefore indicates that ZnO-Et has the lowest amount of oxygen vacancies.

3.2. Optical properties

The band gaps of the as-synthesized ZnO-nanoparticle samples and ZnO-nanorod samples were calculated via UV–vis absorption spectroscopy followed by Tauc plots presented in figures 7(a) and (b), respectively. The band gaps of the ZnO nanoparticles range from 3.11–3.28 eV, and for ZnO nanorod samples are $\sim$3.1–3.2 eV. All these values are within the range of the theoretical band gap of ZnO [44]. The absorption spectra of both, ZnO nanoparticle and nanorod samples revealed a sharp shoulder at 3.3 eV stretching down to 2 eV, shown in S5. However, shoulders related to defect level absorption in the visible region were absent.

The typical PL spectra of ZnO nanoparticles consisting of near band edge emission (NBE) and defect level emission (DLE) are presented in figure 7(c) without normalization, as the quantities of nanoparticle for each sample used for PL

analysis were identical ∼5 mg. In fact, an influence of the solvent medium on the intensities of the DLE is clearly observed. For example, sample ZnO-Et exhibits the highest DLE compared to sample ZnO-Et$_{aq}$ that emits the least intense NBE, owing to the absence of water in the former. The origin of the DLE is attributed to the combination of several point defects, such as V_O, V_{Zn}, O_i, Zn_i, and their complexes [45, 46]. Whereas, the NBE emission originates from the recombination of excitons due to band-to-band transitions [8]. Moreover, the ratio of NBE-to-DLE is indicative of the crystalline quality of the sample. In the case of the ZnO-Et$_{aq}$ sample, the NBE-to-DLE ratio is the highest, indicating the best crystalline quality. The high crystalline quality is attributed to the presence of water in the synthesis mixture that provides an oxidizing environment during ZnO nanoparticle growth, encouraging the precipitation of larger nanoparticles with lower quantities of surface defects. However, the NBE is slightly redshifted compared to the other samples, suggesting the presence of shallow donor states in the sample. Since, this sample also has the largest nanoparticles or the lowest surface-to-volume ratio, it therefore explains the negligible DLE that is surface-related.

On the other hand, samples synthesized with pure ethanol, methanol and isopropanol exhibited a lower NBE-to-DLE ratio, with the lowest for sample ZnO-Et. The increase in DLE for these samples is indicative of surface defects such as V_O^{++} i.e. surface-related oxygen vacancies at 2.2 eV [47]. Additionally, their very small particle size (∼5 nm) enhances the DLE. The 2.2 eV transition is associated with the capture of a surface-trapped holes by V_O^+ to form V_O^{++}. Eventually, an electron from the conduction band can recombine with V_O^{++} to subsequently emit at 2.2 eV. The singly ionized oxygen vacancy V_O^+ or volume oxygen vacancy emits at ∼2.5 eV. Both types of vacancies produce green photoluminescence in ZnO. In nanoparticles of size ∼5 nm, quantities Vo^+ are negligible compared to Vo^{++}.

Furthermore, the intensity of the green emission can be strongly influenced by chemisorbed species on the surface, especially for nanoparticles with very small sizes. Since PL measurements were performed in air, hydroxyl groups or oxygen molecules are adsorbed on the surface of the nanoparticles, creating a depletion region. The chemisorbed oxygen species induce an upward band bending in the as-synthesized ZnO nanoparticles, which allows V_O^{++} to convert into V_O^+ through the capture of an electron or oxygen radicals from the surface-depletion region [10, 48]. Therefore, the observed dominant green emission in ZnO-Met, ZnO-Et and ZnO-Iso samples is mainly surface related with differences in their relative intensities. The rather intense DLE of sample ZnO-Iso suggests that the unreacted precursors and isopropyl groups do not passivate the surface defects.

The PL spectra of ZnO nanorod samples consisting of NBE and DLE are shown in the figure 7(d). Here, the spectra were normalized in order to emphasize on the negligible defect level emission and secondly because the nanorod surface was not uniform for all the samples. Compared to the ZnO nanoparticle samples, the ZnO-nanorod samples show higher NBE-to-DLE ratio and therefore, harbor lower

intrinsic defects. However, for samples ZnO NR-Met and ZnO NR-Iso, there is a hint of DLE suggesting a higher amount of surface defects, despite their nanorod diameters being similar to ZnO NR-Et. The NBE of the ZnO nanorod samples are between 388–393 nm and correspond to the transitions from Zn shallow donor levels to the valence band. Apart from the NBE, two of the ZnO-nanorod samples also show DLE of low intensity, which is a combination of point defects including, V_O, V_{zn}, O_i, and Zn_i, similar to the ZnO nanoparticles. The growth solution for the ZnO nanorod samples was prepared using DI water as a solvent i.e. in oxygen-rich conditions that reduces the number of oxygen-related defects in the ZnO-nanorod samples. In particular, the major DLE components of the nanorod and nanoparticle samples, regardless of their relative intensities, are yellow-green (∼2.2 eV and ∼2.5 eV), orange–red (∼2.1 eV) and red (∼1.95 eV). The yellow–orange emission at ∼2.1 eV is due to the transitions from Zn_i to O_i. Whereas, the red emission at ∼1.95 eV is attributed to the transitions related to Zn_i, usually observed in oxygen-rich conditions [49].

3.3. Electrical and optoelectrical properties of ZnO nanorods

In figure 8(a), the *I–V* characteristics of the ZnO nanorod samples at room temperature are obtained in dark and under UV light in the range from −3 to +3 V. For all the ZnO nanorod samples, the *I–V* characteristics are ohmic with differences in the output currents. The overall output currents in decreasing order of magnitude were for ZnO NR-Met, ZnO NR-Et, ZnO NR-Iso, ZnO NR-Et$_{aq}$. Factors that affect the conductivity, include the presence of defects, as well as the uniformity of the nanorod layer. In the SEM images of figures 2(g)–(m), the ZnO NR-Met nanorod layer was the most continuous followed by ZnO NR-Et nanorod and ZnO NR-Iso. Finally, ZnO NR-Et$_{aq}$ was the least continuous and its surface revealed a large number of voids, which is the plausible explanation for the lowest output current, among all the nanorod samples. The *I–V* characteristics of ZnO-nanorod samples were also evaluated under UV light. The general tendency under UV radiation indicated a higher output current compared to dark conditions.

Figure 8(b) is the current versus time (*I–t*) curves of ZnO nanorod samples at a constant bias of 3 V, measured in dark. The conductivity of ZnO nanorods depends on the surface defects and the amount of oxygen adsorbed on the surface of ZnO nanorods, as oxygen plays an important role in the surface charge transport mechanism of ZnO nanorods [50, 51]. In fact, in dark conditions, an oxygen molecule is adsorbed on the surface of ZnO nanorods, resulting in an upward band bending and a depletion region of oxygen radicals is created at the nanorod surface, as illustrated in figures 8(c) and (d). With time, the adsorption of oxygen radicals increases, leading to trapping or storing of electrons at the depletion region, which in turn, results in the reduction of ZnO nanorod conductivity [52, 53]. The phenomenon of trapping is all the more pronounced when surface defects are present. In figure 8(b), all the ZnO nanorod samples exhibit a reduction in the conductivity as a result of charge trapping
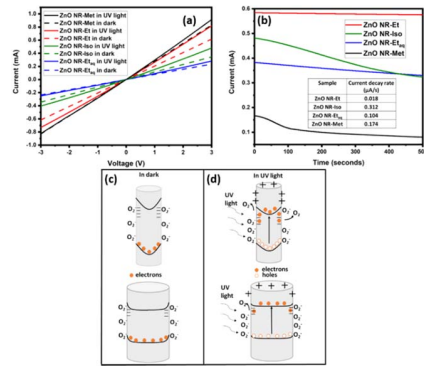
9

Figure 8. (a) *I–V* characteristics of ZnO nanorod samples taken in dark (dashed line) and UV light (solid line) from −3 to +3 V, (b) *I–t* characteristics of ZnO nanorod samples taken in dark at a constant bias of 3 V. The inset in (b) is calculations of current decay rate (μA/s). Schematic of the band bending and oxygen-ion adsorption–desorption mechanisms of smaller and larger nanorods in (c) dark and (d) UV irradiation.

over time. Both, ZnO NR-Met followed by sample ZnO NR-Iso show a 2-step decrease in current due to high charge trapping. The first step of current decrease is more abrupt and is attributed to the rapid filling of surface traps. Once the majority of the trap states are filled, a second slope appears, which corresponds to a more gradual filling of the remaining trap states that eventually should lead to a steady-state current. The defect states in these samples shown in the PL emission spectra of figure 7, consist of Zn_i or V_O, especially for samples ZnO NR-Met and ZnO NR-Iso that contribute to electron trapping and consequently, lower the conductivity over time in these samples. On the other hand, the decay rates of the current in sample ZnO-Et and ZnO-Et$_{aq}$ in the inset of figure 8(b), are much lower owing to a lower amount of surface defects. Besides, the nanorod diameter also plays an important role in terms of charge trapping. As illustrated in figure 8(c), a larger diameter nanorod will tend to have a smaller depletion region and consequently, a lower overall band banding. Additionally, a larger nanorod harbors lower number of surface defects due to the smaller surface-to-volume ratio. Therefore, the decrease in the current due to charge trapping is less dominant for ZnO NR-Et$_{aq}$ [54]. On the other hand, even though the diameter of ZnO-Et is comparable to ZnO-Iso and ZnO-Met, it displays the lowest current decay of 0.018 μA s^{-1}, which is mostly related to the negligible amount of surface defects leading to lower charge trapping.

Under UV light, Saxena *et al* demonstrated a higher photocurrent in vacuum than in air from ZnO microstructures. Similarly, their current decay time in dark was found to be higher in vacuum than in air [55]. Furthermore, Bao *et al* studied the photoconductivity of ZnO nanowires in vacuum

by radiating the ZnO nanowire with three different power sources of UV radiation for 5 h, until saturation photocurrent was reached. Subsequently, the sample was left in vacuum for another 12 h during which, the current maintained a steady state. Upon release of the vacuum, an immediate and abrupt decay of the current was observed [17]. In this study, several on–off cycles of UV radiation were examined in order to evaluate the photoresponse of each sample. The UV light was turned on 5 times at intervals of 10 s each, with possible errors of 2 s due to manual operation. For all the samples, the current obtained during the UV on-cycle shows an increase of 15%–25% for all cycles. In fact, under UV radiation, holes are generated in the valence band due to excitation and transfer of electrons to the conduction band, which in turn, reduce the overall band bending, along with the width of the depletion region as shown in figure 8(d). Nevertheless, due to the remnant upward band bending of ZnO, some holes are still accumulated on the surface. Simultaneously, some of the electrons are trapped at the surface of the nanorods, while others travel to the volume of the nanorod and contribute to the conductivity. The surface accumulated holes subsequently combine with the adsorbed oxygen radicals that then desorb from the ZnO nanoparticle surface in the form of oxygen molecules. Once again for larger nanorods, the oxygen-desorption mechanism is less dominant with regards to the conductivity. After each UV on-cycle, samples were maintained in dark for 50 s, during which an increase in the upward band bending and in turn, to a decrease in the current were observed. Ideally, the current should drop to its dark current value [56]; however, the dark current recovery depends on the rate at which photoexcited carriers recombine, which depends on the size of the depletion region, as illustrated in figures 8(c) and(d). The larger the depletion region, the slower the recombination rate, which results in a slow decay of current that persists even in dark. In general, the size of the depletion region is inversely proportional to the presence of surface defects and can be corroborated to PL results. PPC was observed during the UV off-cycles (50 s) for all samples, during which the current did not drop to its initial value. In fact, PPC is directly related to the surface defects and the oxygen environment around ZnO [57]. For sample ZnO NR-Et$_{aq}$, a fast decay compared to other samples was observed during UV off-cycles, which can be attributed to the lowest number of surface defects and relatively smaller depletion region. In addition, ZnO NR-Et, ZnO NR-Met and ZnO NR-Iso exhibit similar PPC behaviors, owing to the similarity in their diameters. Since the nanorod diameter can also affect the conductivity, hence, PPC is more pronounced in samples with smaller nanorod diameters harboring higher amount of surface defects or presenting more pronounced upward band bending. The *I–t* characteristics of ZnO NR-Et sample at a lower bias of 10 mV for various on–off cycles under UV radiation are provided in figure S6(a). At a low bias, a low current in the μA range was obtained compared to the high voltage bias of 3 V, where output currents were in mA ranges. Therefore, for this study, a 3 V bias was selected, in order to clearly highlight the differences in *I–t* characteristics. In addition, we measured *I–t* characteristics of sample
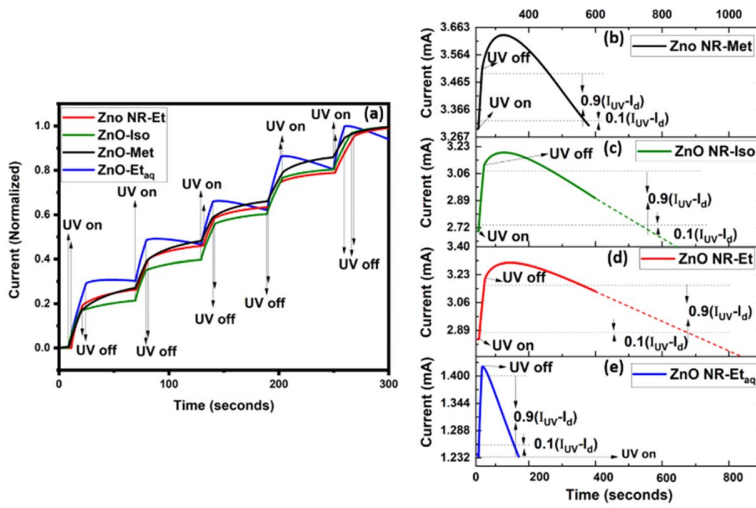
10

Figure 9. (a) *I–t* characteristics of ZnO nanorod samples under UV on-off cycles with total measurement for 300 s at a constant bias of 3 V. Single on-off cycle of samples (b) ZnO NR-Met, (c) ZnO NR-Iso, (d) ZnO NR-Et and (e) ZnO NR-Et$_{aq}$ at a constant bias of 3 V. The dashed line in figures (c) and (d) are the extrapolations of the decay to the X-intercept.

Table 3. List of parameters calculated from the *I–t* characteristics of UV on off cycle (figures 11(b)–(e)).

Sample	Sensitivity	Responsivity (mA W^{-1})	τ_{rise} (s)	I_{rise} rate (μA s^{-1})	τ_{decay} (s)	I_{decay} rate (μA s^{-1})	$\tau_{uv\text{-}light}$ (s)
ZnO NR-Met	1.067	116.8	8.4	20.5	107.5	1.6	10.9
ZnO NR-Iso	1.153	220.2	13.3	25.3	264.4	1.29	14.8
ZnO NR-Et	1.129	193.7	14.2	20.2	318.1	0.92	17.3
ZnO NR-Et$_{aq}$	1.145	95.5	7.9	18	77.8	1.84	11.6

ZnO NR-Etaq for a long on-cycle interval of ∼500 s to attain current saturation under UV radiation. The result is shown in supplementary figure S6(b). However, the current did not reach saturation in 500 s. Therefore, short intervals of ∼10–12 s were employed to study *I–t* characteristics under UV radiation for various on–off cycles, in this present study.

The properties of the nanorods for UV sensor applications were assessed using the responsivity, sensitivity and response time [58], as shown in figures 9(b)–(e). ZnO nanorod samples were irradiated with UV light at different on–off intervals ($\tau_{uv\text{-}light}$), as listed in table 3. After UV irradiation, the off cycle lasted for 350 s for all the samples. The *I–t* curves in figures 9(b)–(e) are plotted for one on–off cycle. Samples ZnO NR-Et$_{aq}$ and ZnO NR-Met reached their dark current within the off-cycle interval. However, for samples ZnO NR-Et and ZnO NR-Iso, the time required to reach the dark current value exceeded the off-cycle interval and was therefore estimated via extrapolation, shown by the dotted line in figures 9(c) and (d). The sensitivity was

determined using the equation: $S = \frac{I_{UV}}{I_{dark}}$, where I_{UV} is the current, when UV radiation is turned off, I_{dark} is the dark current just before switching on UV radiation. The sensitivities are similar for all the nanorod samples i.e. between ∼1.1 to 1.5, as listed in table 3. These values suggest that regardless of differences in I_{dark} and total UV-radiation time ($\tau_{uv\text{-}light}$), the increase of photocurrent with respect to dark current is approximately the same for all samples. The responsivity (μA/W) was calculated by using the equation, $R = \frac{I_{UV} - I_{dark}}{P_{in}A_{eff}}$, where P_{in} is the incident UV irradiation power of Hg UV lamp through the optical fiber and A_{eff} is the effective active area of the probe. The highest responsivity was calculated for sample ZnO NR-Iso, followed by samples ZnO NR-Et, ZnO NR-Met and lowest for sample ZnO NR-Et$_{aq}$ (table 3). The response time has two parameters i.e. the rise time (τ_{rise}), which is the amount of time required for the ZnO nanorod samples to reach 90% from 10% of the current under UV-radiation. On the other hand, τ_{decay} is the amount of time required for the current to decay from 90% to 10% once the

11

UV radiation is turned off. The τ_{rise} is directly dependent on the total UV radiation time i.e. $\tau_{\text{uv-light}}$, listed in table 3. On the other hand, τ_{decay} is an intrinsic property of the samples and depends on surface defects, oxygen adsorption and band bending of the sample. Furthermore, τ_{decay} is the parameter that provides information on the photoresponse or UV sensor applicability of the samples. Once the UV radiation is turned off, two phenomena are likely to occur. The first phenomenon is related to charge de-trapping, which causes a rapid increase in current before its decay after switching off the UV radiation. In samples ZnO NR-Met, ZnO NR-Iso and ZnO NR-Et, an increase in the current reaching a peak value before decay is observed, owing to charge de-trapping [52, 56]. The second phenomenon is related to PPC observed in all the samples due to which the τ_{decay} takes over 70 s to descend to dark current values [56]. Additionally, PPC without charge de-trapping is only observed in ZnO NR-Et$_{\text{aq}}$. Also, τ_{decay} was estimated by the extrapolation to $\sim$320 s for sample ZnO NR-Et and to $\sim$265 s for sample ZnO NR-Iso. The τ_{decay} was slowest for sample ZnO NR-Et, which suggests that persistent conductivity is the most dominant in this sample. The second fastest τ_{decay} ($\sim$110 s) was calculated for sample ZnO NR-Met and the fastest τ_{decay} of $\sim$80 s was calculated for sample ZnO NR-Et$_{\text{aq}}$. Since, sample ZnO NR-Et$_{\text{aq}}$ shows an immediate decay in current after turning off the UV radiation, it has potential as a UV detector with low heating effects owing to low charge trapping.

The sensitivity, responsivity and rise-decay time are affected by growth conditions, applied bias, power of the UV source and the presence of plasmonic nanoparticles. Several works on the UV responsivity and sensitivity of ZnO nanorods are available. The applied bias was as high as 5 V in certain studies [59–61]. For example, Sheikh *et al* have obtained a responsivity of 364.81 A W^{-1}, under 365 nm radiation with a flux of 1.8 μW cm^{-2} at 5 V bias [62]. The rise time and decay time were calculated as 17 s and 22 s, respectively. Since ammonia was used in the hydrothermal synthesis, N acceptor states could create additional defects that influence the rise and decay time. Plasmonic nanoparticles such as Al also tend to increase the sensitivity of the ZnO nanorod photodetector. For example, compared to bare ZnO nanorods, devices with plasmonic Al nanoparticles show increase in their responsivity from 53 to 267 mA W^{-1} and in their sensitivity from 9.5 to 47.8 under 325 nm UV light (5 mW cm^{-2}) at 3.0 V bias [63]. In addition, Liu *et al* demonstrated that photoresponse of ZnO nanorods can be enhanced by covering it with a polymer such as PMMA. Here, the PMMA itself does not contribute to the UV response as it is UV transparent and electrically insulating, but it helps to enhance the responsivity of ZnO nanorods, by passivating the surface states and hindering oxygen adsorption [64]. In those studies, either the applied bias or the incident flux was higher or the surface of the ZnO nanorods was also passivated. Nevertheless, electrical conductivity of ZnO nanorods depends also on its polarity and crystal orientation and is enhanced for highly directional nanorods that require well-textured seed layers for their growth [65].

4. Conclusion

In this work we have successfully grown ZnO nanoparticles and nanorod seed layers using four different solvents, i.e. methanol, ethanol, isopropanol and aqueous ethanol. The solvents played an important role on the surface defect generation, size and morphology of the nanoparticles and seed layer nucleation. In general, non-aqueous solvents produced spherically shaped nanoparticles of uniform size and allowed a better control of the reaction kinetics. Long chain alcohols tend to produce smaller, more uniform and monodispersed nanoparticles, with the drawback of leaving unreacted products in the final powders. Subsequently, these solvents were also used in the seed layer solutions for nanorod growth. Similar to nanoparticles, the nanorods with absolute alcohol seed layers possessed equivalent sizes, indicating that the seed layer nucleation played an important role in the nanorod diameters. Furthermore, the aqueous ethanol solvent produced larger nanorods, owing to the faster reaction kinetics of the seed layer, in turn, producing larger nucleation sites. Since, the growth of the nanorods was carried out in identical conditions after the seed layer deposition, the differences in the electrical properties can therefore be directly and uniquely linked to the solvent used in the seed layer solution. All the samples presented an ohmic behavior with changes in current output over time that can be directly related to the size of the nanorods, uniformity of the nanorod layer, band bending and surface defects. Under UV illumination, the *I–t* on–off cycles revealed their potential for UV sensor applications, especially for the ZnO Et$_{\text{aq}}$ sample that exhibited the fastest responses for UV on–off cycles. The other samples demonstrated PPC with slow current decay rates in off-cycles in ambient conditions. In fact, PPC is a defect- and ambient-related phenomenon, being sensitive to oxygen in the surrounding. Therefore, PPC can be useful in gas sensing, piezo and biosensing applications. Additionally, manipulating these nanorods under vacuum, would open applications in charge storage devices such as photocapacitors. In general, larger nanorods with fewer defects would serve as UV sensors while as, smaller nanorods demonstrate potential for photocapacitance. In the next step, a hybrid diode-structure will be prepared consisting of these ZnO nanorods and conducting polymers and other applications will be explored.

Data availability statement

The data in the work requires to be published in a PhD thesis. Once the thesis is publised it will be available on an open access repository. The data that support the findings of this study are available upon reasonable request from the authors.

180

ORCID iDs

Keshav Nagpal https://orcid.org/0000-0003-0040-9984
Erwan Rauwel https://orcid.org/0000-0001-8950-1415
Frederique Ducroquet https://orcid.org/0000-0001-8770-9650
Isabelle Gélard https://orcid.org/0000-0003-0102-7611
Protima Rauwel https://orcid.org/0000-0001-5393-2352

References

[1] Liu K, Sakurai M and Aono M 2010 ZnO-based ultraviolet photodetectors *Sensors* **10** 8604–34
[2] Chaudhary S, Umar A, Bhasin K K and Baskoutas S 2018 Chemical sensing applications of ZnO nanomaterials *Materials* **11** 287
[3] Wibowo A, Marsudi M A, Amal M I, Ananda M B, Stephanie R, Ardy H and Diguna L J 2020 ZnO nanostructured materials for emerging solar cell applications *RSC Adv.* **10** 42838–59
[4] Pearton S J and Ren F 2014 Advances in ZnO-based materials for light emitting diodes *Curr. Opin. Chem. Eng.* **3** 51–5
[5] Lin B, Fu Z and Jia Y 2001 Green luminescent center in undoped zinc oxide films deposited on silicon substrates *Appl. Phys. Lett.* **79** 943–5
[6] Park C H, Zhang S B and Wei S-H 2002 Origin of p-type doping difficulty in ZnO: the impurity perspective *Phys. Rev.* B **66** 073202
[7] Hu Z, Oskam G and Searson P C 2003 Influence of solvent on the growth of ZnO nanoparticles *J. Colloid Interface Sci.* **263** 454–60
[8] Nagpal K, Rapenne L, Wragg D S, Rauwel E and Rauwel P 2022 The role of CNT in surface defect passivation and UV emission intensification of ZnO nanoparticles *Nanomater. Nanotechnol.* **12** 1–10
[9] Oskam G and Soberanis Domínguez O E 2006 The effect of water on the nucleation kinetics of ZnO nanoparticles *ECS Trans.* **3** 17
[10] Nagpal K, Rauwel E, Estephan E, Soares M R and Rauwel P 2022 Significance of hydroxyl groups on the optical properties of ZnO nanoparticles combined with CNT and PEDOT:PSS *Nanomaterials* **12** 3546
[11] Jezequel D, Guenot J, Jouini N and Fievet F 1994 Preparation and morphological characterization of fine, spherical, monodisperse particles of ZnO *Mater. Sci. Forum* **152-153** 339–42
[12] Poul L, Ammar S, Jouini N, Fievet F and Villain F 2003 Synthesis of inorganic compounds (metal, oxide and hydroxide) in polyol medium: a versatile route related to the sol-gel process *J. Sol–Gel Sci. Technol.* **26** 261–5
[13] Rauwel E, Galeckas A, Rauwel P, Sunding M F and Fjellvåg H 2011 Precursor-dependent blue-green photoluminescence emission of ZnO nanoparticles *J. Phys. Chem. C* **115** 25227–33
[14] Ungula J and Dejene B F 2016 Effect of solvent medium on the structural, morphological and optical properties of ZnO nanoparticles synthesized by the sol–gel method *Physica B* **480** 26–30
[15] Foo K L, Kashif M, Hashim U and Liu W-W 2014 Effect of different solvents on the structural and optical properties of zinc oxide thin films for optoelectronic applications *Ceram. Int.* **40** 753–61
[16] Bayan S and Mohanta D 2012 ZnO nanorod-based UV photodetection and the role of persistent photoconductivity *Philos. Mag.* **92** 3909–19

[17] Bao J, Shalish I, Su Z, Gurwitz R, Capasso F, Wang X and Ren Z 2011 Photoinduced oxygen release and persistent photoconductivity in ZnO nanowires *Nanoscale Res. Lett.* **6** 404
[18] Altaf C T, Coskun O, Kumtepe A, Rostas A M, Iatsunskyi I, Coy E, Erdem E, Sankir M and Sankir N D 2022 Photo-supercapacitors based on nanoscaled ZnO *Sci. Rep.* **12** 11487
[19] Yadav H K, Sreenivas K and Gupta V 2010 Persistent photoconductivity due to trapping of induced charges in Sn/ZnO thin film based UV photodetector *Appl. Phys. Lett.* **96** 223507
[20] Anu Roshini R, Nagpal K and Senthamarai Kannan E 2019 Anomalous conductance induced by hydrogen on ZnO and catalyzed ZnO nanoflowers *Europhys. Lett.* **127** 57005
[21] Saidin N U, Choo T F and Kok K Y 2018 Hydrothermal growth of ZnO: a substrate-dependent study on nanostructures formation *IOP Conf. Ser.: Mater. Sci. Eng.* **298** 012016
[22] Baruah S, Thanachayanont C and Dutta J 2008 Growth of ZnO nanowires on nonwoven polyethylene fibers *Sci. Technol. Adv. Mater.* **9** 025009
[23] Park H K, Hong S P and Do Y R 2012 Vertical growth of ZnO nanorods prepared on an ITO-coated glass substrate by hydrothermal-electrochemical deposition *J. Electrochem. Soc.* **159** D355
[24] Song J and Lim S 2007 Effect of seed layer on the growth of ZnO nanorods *J. Phys. Chem. C* **111** 596–600
[25] Ong W L, Low Q X, Huang W, van Kan J A and Ho G W 2012 Patterned growth of vertically-aligned ZnO nanorods on a flexible transparent and conformable platform for feasible transparent and conformable electronics applications *J. Mater. Chem.* **22** 8518–24
[26] Wang C H, Wong A S W and Ho G W 2007 Facile solution route to vertically aligned, selective growth of ZnO nanostructure arrays *Langmuir* **23** 11960–3
[27] Hu Z, Escamilla Ramírez D J, Heredia Cervera B E, Oskam G and Searson P C 2005 Synthesis of ZnO nanoparticles in 2-propanol by reaction with water *J. Phys. Chem. B* **109** 11209–14
[28] Mao J, Gu Q and Gregory D H 2015 Revisiting the hydrogen storage behavior of the Na–O–H System *Materials* **8** 2191–203
[29] Stenger J, Kwan E, Eremin K, Speakman S, Dan K, Heather S, Huang S, Kennedy A, Richard N and Narayan K 2010 Lithol red salts: characterization and deterioration *E-Preservation Sci.* **7** 147–57 (https://researchgate.net/publication/49604014_LITHOL_RED_SALTS_CHARACTERIZATION_AND_DETERIORATION)
[30] Zhou Q, Wen J Z, Zhao P and Anderson W A 2017 Synthesis of vertically-aligned zinc oxide nanowires and their application as a photocatalyst *Nanomaterials* **7** 9
[31] Vieira N, Fernandes E, De Queiroz A, Guimarães F and Zucolotto V 2013 Indium tin oxide synthesized by a low cost route as SEGFET pH Sensor *Mater. Res.* **16** 1156–60
[32] Gerbreders V, Krasovska M, Sledevskis E, Gerbreders A, Mihailova I, Tamanis E and Ogurcovs A 2020 Hydrothermal synthesis of ZnO nanostructures with controllable morphology change *Cryst. Eng. Comm.* **22** 1346–58
[33] Murillo G, Leon-Salguero E, Martínez-Alanis P R, Esteve J, Alvarado-Rivera J and Güell F 2019 Role of aluminum and HMTA in the hydrothermal synthesis of two-dimensional n-doped ZnO nanosheets *Nano Energy* **60** 817–26
[34] Parize R, Garnier J, Chaix-Pluchery O, Verrier C, Appert E and Consonni V 2016 Effects of hexamethylenetetramine on the nucleation and radial growth of ZnO nanowires by chemical bath deposition *J. Phys. Chem. C* **120** 5242–50
[35] Chen X, Wang X and Fang D 2020 A review on C1s XPS-spectra for some kinds of carbon materials *Fullerenes, Nanotubes Carbon Nanostruct.* **28** 1048–58

13

[36] Sahai A and Goswami N 2014 Probing the dominance of interstitial oxygen defects in ZnO nanoparticles through structural and optical characterizations *Ceram. Int.* **40** 14569–78

[37] Zhao N, Li C and Guo X 2014 Long-life Na–O2 batteries with high energy efficiency enabled by electrochemically splitting NaO$_2$ at a low overpotential *Phys. Chem. Chem. Phys.* **16** 15646–52

[38] Kumar P, Mathpal M C, Inwati G K, Kumar S, Duvenhage M-M, Roos W D and Swart H C 2023 Study of defect-induced chemical modifications in spinel zinc-ferrites nanostructures by in-depth XPS investigation *Magnetochemistry* **9** 20

[39] Sharma A, Singh B P, Dhar S, Gondorf A and Spasova M 2012 Effect of surface groups on the luminescence property of ZnO nanoparticles synthesized by sol–gel route *Surf. Sci.* **606** L13–7

[40] Gao Q, Dai Y, Li C, Yang L, Li X and Cui C 2016 Correlation between oxygen vacancies and dopant concentration in Mn-doped ZnO nanoparticles synthesized by co-precipitation technique *J. Alloys Compd.* **684** 669–76

[41] Khachadorian S, Gillen R, Choi S, Ton-That C, Kliem A, Maultzsch J, Phillips M R and Hoffmann A 2015 Effects of annealing on optical and structural properties of zinc oxide nanocrystals *Physica. Status Solidi.*b **252** 2620–5

[42] Reddy C V, Babu B and Shim J 2018 Synthesis, optical properties and efficient photocatalytic activity of CdO/ZnO hybrid nanocomposite *J. Phys. Chem. Solids* **112** 20–8

[43] Souissi A, Amlouk M, Khemakhem H and Guermazi S 2016 Deep analysis of Raman spectra of ZnO:Mo and ZnO:In sprayed thin films along with LO and TA+LO bands investigation *Superlattices Microstruct.* **92** 294–302

[44] Davis K, Yarbrough R, Froeschle M, White J and Rathnayake H 2019 Band gap engineered zinc oxide nanostructures via a sol–gel synthesis of solvent driven shape-controlled crystal growth *RSC Adv.* **9** 14638–48

[45] Alvi N H, Ul Hasan K, Nur O and Willander M 2011 The origin of the red emission in n-ZnO nanotubes/p-GaN white light emitting diodes *Nanoscale Res. Lett.* **6** 130

[46] Kumar Jangir L, Kumari Y, Kumar A, Kumar M and Awasthi K 2017 Investigation of luminescence and structural properties of ZnO nanoparticles, synthesized with different precursors *Mater. Chem. Front.* **1** 1413–21

[47] Pramanik S, Mondal S, Mandal A C, Mukherjee S, Das S, Ghosh T, Nath R, Ghosh M and Kuiri P K 2020 Role of oxygen vacancies on the green photoluminescence of microwave-assisted grown ZnO nanorods *J. Alloys Compd.* **849** 156684

[48] Vanheusden K, Warren W L, Seager C H, Tallant D R, Voigt J A and Gnade B E 1996 Mechanisms behind green photoluminescence in ZnO phosphor powders *J. Appl. Phys.* **79** 7983–90

[49] Przezdziecka E, Guziewicz E, Jarosz D, Snigurenko D, Sulich A, Sybilski P, Jakiela R and Paszkowicz W 2020 Influence of oxygen-rich and zinc-rich conditions on donor and acceptor states and conductivity mechanism of ZnO films grown by ALD—experimental studies *J. Appl. Phys.* **127** 075104

[50] Ke J-J, Liu Z-J, Kang C-F, Lin S-J and He J-H 2011 Surface effect on resistive switching behaviors of ZnO *Appl. Phys. Lett.* **99** 192106

[51] Abdulrahman A F 2020 The effect of different substrate-inclined angles on the characteristic properties of ZnO nanorods for UV photodetectors applications *J. Mater. Sci., Mater. Electron.* **31** 14357–74

[52] Liao Z-M, Xu J, Zhang J-M and Yu D-P 2008 Photovoltaic effect and charge storage in single ZnO nanowires *Appl. Phys. Lett.* **93** 023111

[53] Harnack O, Pacholski C, Weller H, Yasuda A and Wessels J M 2003 Rectifying Behavior of Electrically Aligned ZnO Nanorods *Nano Lett.* **3** 1097–101

[54] Fang H and Hu W 2017 Photogating in low dimensional photodetectors *Adv. Sci.* **4** 1700323

[55] Saxena R S 2018 Study on photoconductivity in air and vacuum of ZnO prepared by different materials *Int. J. Res. in Appl. Sci. Eng. Technol.* **6** 2466–71

[56] Kushwaha A and Aslam M 2012 Defect induced high photocurrent in solution grown vertically aligned ZnO nanowire array films *J. Appl. Phys.* **112** 054316

[57] Hullavarad S, Hullavarad N, Look D and Claflin B 2009 Persistent Photoconductivity Studies in Nanostructured ZnO UV Sensors *Nanoscale Res. Lett.* **4** 1421

[58] Komatsu H, Kawamoto Y and Ikuno T 2022 Freestanding Translucent ZnO–Cellulose Nanocomposite Films for Ultraviolet Sensor Applications *Nanomaterials* **12** 940

[59] Ji L W, Peng S M, Su Y K, Young S J, Wu C Z and Cheng W B 2009 Ultraviolet photodetectors based on selectively grown ZnO nanorod arrays *Appl. Phys. Lett.* **94** 203106

[60] Pandey S, Shukla A and Tripathi A 2023 Highly sensitive and self powered ultraviolet photo detector based on ZnO nanorods coated with TiO2 *Sensors Actuators*, A **350** 114112

[61] Lin Y, Zou J, Wang W, Liu X, Gao J and Lu Z 2022 High-performance self-powered ultraviolet photodetector based on PEDOT:PSS/CuO/ZnO nanorod array sandwich structure *Appl. Surf. Sci.* **599** 153956

[62] Shaikh S K, Ganbavale V V, Mohite S V, Patil U M and Rajpure K Y 2018 ZnO nanorod based highly selective visible blind ultra-violet photodetector and highly sensitive NO2 gas sensor *Superlattices Microstruct.* **120** 170–86

[63] Shang S, Dong Y, Zhang W and Ren W 2022 Fabrication and performance of UV photodetector of ZnO nanorods decorated with al nanoparticles *Nanomaterials* **12** 3768

[64] Liu N, Fang G, Zeng W, Zhou H, Cheng F, Zheng Q, Yuan L, Zou X and Zhao X 2010 Direct growth of lateral ZnO nanorod UV photodetectors with schottky contact by a single-step hydrothermal reaction *ACS Appl. Mater. Interfaces* **2** 1973–9

[65] Cossuet T, Donatini F, Lord A M, Appert E, Pernot J and Consonni V 2018 Polarity-dependent high electrical conductivity of ZnO nanorods and its relation to hydrogen *J. Phys. Chem.* C **122** 22767–75

14

IV

K. Nagpal, E. Rauwel, F. Ducroquet, P. Rauwel "Assessment of the optical and electrical properties of light emitting diodes containing carbon-based nanostructures and plasmonic nanoparticles: a review", Beilstein J. Nanotechnol. 12, 1078–1092 (2021)

Assessment of the optical and electrical properties of light-emitting diodes containing carbon-based nanostructures and plasmonic nanoparticles: a review

Keshav Nagpal[‡1], Erwan Rauwel[‡1], Frédérique Ducroquet[2] and Protima Rauwel[*,‡1]

Abstract

Light-emitting diodes (LED) are widely employed in display applications and lighting systems. Further research on LED that incorporates carbon nanostructures and metal nanoparticles exhibiting surface plasmon resonance has demonstrated a significant improvement in device performance. These devices offer lower turn-on voltages, higher external quantum efficiencies, and luminance. De facto, plasmonic nanoparticles, such as Au and Ag have boosted the luminance of red, green, and blue emissions. When combined with carbon nanostructures they additionally offer new possibilities towards lightweight and flexible devices with better thermal management. This review surveys the diverse possibilities to combine various inorganic, organic, and carbon nanostructures along with plasmonic nanoparticles. Such combinations would allow an enhancement in the overall properties of LED.

Review
Introduction

Nanomaterials have engendered the miniaturization of devices, bringing about advances in a variety of fields, such as biomedicine, environmental technologies, optoelectronics, and photocatalysis [1,2]. In particular, light-emitting diodes (LED) have shown the most significant technological progress in display applications. They are incorporated into smart phones, TVs, traffic signals, and medical devices [3]. Similarly, lighting systems employing LED have longer life times (>50000 h), much lower

heating effects, ultrafast response times, and a wider choice of emission wavelengths compared to conventional lighting systems.

Inorganic LED consist of inorganic semiconductor materials in the active region, for example thin films of GaAs that emit in the red to near-infrared (>700 nm) region [4]. Ga-based LED belong to the III–V group of semiconductors and emit from the

UV to the red region of the visible spectrum via bandgap tuning (i.e., on alloying with In and Al [5-7]). Similarly, other active materials for quantum dot light-emitting diodes (QLED), such as the II–VI semiconductor family include ZnO, CdSe, CdS, CdTe, ZnSe, ZnS, ZnTe, and their core–shell structures with Zn-based compounds possessing higher bandgaps than Cd-based compounds [8-12]. The wide bandgap of Zn-based compounds has provided an opportunity to produce blue-emitting 'all ZnO'-based LED, following the successful fabrication of p-type ZnO [13].

Organic light-emitting diodes (OLED) possess several interesting properties and are therefore gaining popularity [14]. Their low-cost and facile fabrication routes, wider viewer angle, higher resolution, lower-power consumption, lightweight, higher contrast, and faster switching characteristics give them leverage over inorganic LED in display applications. Organic light-emitting diodes (OLED) consist of photoactive polymers, such as PPV and MEH-PPV that can be deposited as highly ordered crystalline thin films [15,16]. Despite several advantages, OLED have certain drawbacks, such as lower lifetime, high cost, early degradation, and a low overall performance including poor external quantum efficiencies (EQE) as compared to inorganic LED. A combination of LED and OLED or hybrid LED (HyLED) overcame some of these drawbacks. Nevertheless, HyLED presently may not be the most popular LED for the display market as they suffer from energy losses due to total internal reflection at the emitter/air interface.

Several methods have been proposed to tune the properties of LED. To that end, multiwall carbon nanotubes (MWNT) and single-wall carbon nanotubes (SWNT) have been applied to various layers in LED, such as the emissive layer (EML), the hole transport layers (HTL), the electron transport layers (ETL), the cathode, and the anode [17-21]. Enhancement in LED properties via surface plasmon resonance (SPR) of metal nanoparticles (MNP) such as Au and Ag have also been reported [22,23]. This manifests as an increment in the photoluminescence (PL), conductivity, and electroluminescence (EL) of the LED [24,25]. Other MNP with SPR properties include Al, Pt, Pd, and Cu [26-29]. In general, SPR not only increases the radiative recombination lifetime values, but also the quantum yield whereupon the luminous and internal quantum efficiencies of the device increase. However, SPR is very sensitive to the shape and size of MNP, which in turn directly influence the overall properties of LED.

This manuscript reviews the effect of carbon nanostructures, such as carbon nanodots, carbon nanotubes (CNT), and graphene (GR) towards producing cost-effective and efficient LED. A second strategy consisting of enhancing the optical and electrical properties of LED via SPR of MNP is also surveyed. The LED covered in this review include inorganic LED, OLED, inorganic/organic LED, and HyLED. The feasibility of incorporating GR and CNT in large-scale devices is also discussed. Even though plasmonic nanoparticles (NP) are a developing field, their applications are nonetheless promising. The effect of these nanostructures on the performance of LED when included in individual layers (i.e., anode, HTL, EML, ETL, and cathode) is analyzed. Subsequently, various characteristics of LED containing carbon nanostructures and plasmonic NP are discussed in terms of EQE, internal quantum efficiency, luminance, EL, and current–voltage (*I–V*) characteristics. A list of various abbreviations employed in this review is available in Table 1.

Table 1: List of abbreviations mentioned in this review.

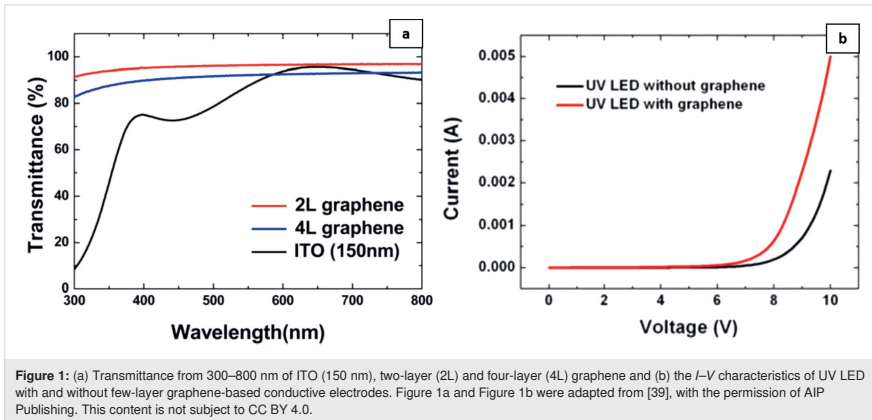| Abbreviation	Full name
CNT	carbon nanotubes
CQD	carbon quantum dots
EBL	electron blocking layer(s)
EIL	electron injection layer(s)
EML	emissive layer(s)
EL	electroluminescence
ETL	electron transport layer(s)
EQE	external quantum efficiency
FTO	fluorine-doped tin oxide(s)
HBL	hole blocking layer(s)
HIL	hole injection layer(s)
HOMO	highest occupied molecular level
HTL	hole transport layer(s)
HyLED	hybrid light-emitting diode(s)
IFOLED	inverted fluorescent OLED
IPOLED	inverted phosphorescent OLED
ITO	indium tin oxide(s)
LED	light-emitting diode(s)
LUMO	lowest unoccupied molecular level
MNP	metal nanoparticles
MWNT	multiwall carbon nanotubes
NP	nanoparticles
OLED	organic light-emitting diode(s)
PL	photoluminescence
QD	quantum dots
QLED	quantum dot light-emitting diode(s)
SACNT	super-aligned carbon nanotubes
SWNT	single-wall carbon nanotubes
TCO	transparent conducting oxide(s)

Enhancing the anode characteristics

For LED, the general strategy is to use a current-spreading layer (anode) with a high electrical conductivity and a high transparency ranging from the UV to the red region. Additionally, it

should also be cost-effective and producible on a large scale. For this purpose, transparent conducting oxides (TCO), such as thin films of In_2O_3, SnO_2, ZnO, and their mixtures have been extensively studied [30-34]. The most widely studied TCO is indium tin oxide (ITO), which possesses good physical properties, such as high optical transmittance (>80% in the visible region) and low sheet resistance (≈20 Ω/sq). Typically, ITO consists of 90% In_2O_3 and 10% SnO_2 by weight. Kim et al. have grown ITO on glass substrates with varying Sn concentrations [35]. Although ITO is a conventional favorite current-spreading layer, it nevertheless suffers from certain limitations, including high processing temperatures, cracking upon bending, and poor transparency in the blue and UV regions. In addition, ITO is expensive owing to the fact that it is deposited by high-vacuum thin-film deposition methods and the price of indium has escalated by almost 900% since the last decade. These disadvantages can be surmounted by the addition of a current-spreading layer composed of carbon-based nanomaterials, such as GR and CNT [36].

Carbon-based nanostructures play a dual role at the anode. Light-emitting diodes are self-heating, current-sensitive, and luminously intensive light sources. They are also highly dependent on ambient temperatures. The lifetime of LED, in particular OLED, is on an average reduced by 30–50% for each 10 °C rise in temperature. Further, self-heating in LED causes degradation of the active region, which further affects the efficiency and the operational lifetime of LED. Therefore, in order to obtain adequate performances from LED, proper thermal management of the device is required. In this regard, graphene at the anode tends to alleviate self-heating issues as it disperses the heat away from the active layer. This in turn also reduces

the thermal resistance between the device layers [37,38]. Furthermore, the transmittance of large-area few-layer graphene used as a current-spreading layer in InGaN-based UV LED is similar to the transmittance of ITO in the blue region (Figure 1a) [39]. Furthermore, the *I–V* results in Figure 1b show an increase of the maximum current value from 2.3 to 5 mA at 10 V, when graphene is present.

Guo et al. also reported an increase of about 40% in the EL intensity under a 5 mA current injection at room temperature in AlGaInP LED, after the deposition of graphene onto the anode or the GaP surface [40]. Roll-to-roll techniques and chemical vapor deposition, both industrially viable techniques, are capable of producing 30 inch wafers of graphene, thereby demonstrating the viable upscaling of its production [41]. Other carbon-based nanomaterials such as SWNT have also been employed as current-spreading layers. The optoelectronic properties of SWNT thin films make them ideal for transparent conducting flexible electrodes in LED. In Figure 2, Aguirre et al. pre-fabricated vertical sheets of SWNT and then transferred them onto a glass substrate [21]. The maximum brightness and efficiency achieved in these SWNT-based devices are 2800 cd/m^2 and 1.4 cd/A, respectively, at a turn-on voltage of 6.6 V. These values are however not as satisfactory as the ITO-based device: 6000 cd/m^2 and 1.9 cd/A at a turn-on voltage of 6.2 V. One reason for lower SWNT device performance is associated with its lower transmittance of 44% compared to 90% of ITO. A higher transmittance is nonetheless possible by optimizing the interface between HTL and SWNT via a parylene layer, which tends to increase the transparency of SWNT. Table 2 lists the polymers and their acronyms mentioned in this study.

Figure 1: (a) Transmittance from 300–800 nm of ITO (150 nm), two-layer (2L) and four-layer (4L) graphene and (b) the *I–V* characteristics of UV LED with and without few-layer graphene-based conductive electrodes. Figure 1a and Figure 1b were adapted from [39], with the permission of AIP Publishing. This content is not subject to CC BY 4.0.

Figure 2: Cross-sectional scanning electron microscopy (SEM) image of the layers of the OLED. The various layers in the device are clearly visible including the vertical SWNT sheet. Figure 2 was adapted from [21], with the permission of AIP Publishing. This content is not subject to CC BY 4.0.

Table 2: List of polymers and their acronyms mentioned in this review.

Acronyms	Full name
Alq$_3$	tris(8-hydroxyquinoline)aluminum
BCHA-PPV	poly[2,5-bis(cholestanoxy) phenylene vinylene]
CuPc	copper(II) phthalocyanine
DCM	4-(dicyanomethylene)-2-*tert*-butyl-6-[2-(1,1,7,7-tetramethyljulolidin-4-yl)vinyl]-4*H*-pyran
F8BT	poly(9,9-dioctylfluorene-*alt*-benzothiadiazole)
HAT-CN	1,4,5,8,9,11-hexaazatriphenylenehexacarbonitrile
MEH:PPV	poly[2-methoxy-5-(2'-ethylhexyloxy)-1,4-phenylene vinylene]
M3EH-PPV	poly[2,5-dimethoxy-1,4-phenylene-1,2-ethenylene-2-methoxy-5-(2-ethylhexyloxy)–(1,4-phenylene-1,2-ethenylene)]
MDMO-PPV	poly(3',7'-dimethyloctyloxy phenylene vinylene)
NPB	*N*,*N*'-di(1-naphthyl)-*N*,*N*'-diphenyl-(1,1'-biphenyl)-4,4'-diamine
NSD	*N*-(3-aminopropyl)propane-1,3-diamine
PBD	2-(4-biphenyl)-5-(4-*tert*-butylphenyl)-1,3,4-oxadiazole
PBD-PMMA	2-(4-biphenyl)-5-(4-*tert*-butylphenyl)-1,3,4-oxadiazole in poly(methyl methacrylate)
PEDOT:PSS	poly(3,4-ethylenedioxythiophene) polystyrene sulfonate
PET	polyethylene terephthalate
PFO	polydioctylfluorene
PmPV	poly[(*m*-phenylene vinylene)-*co*-(2,5-dioctoxy-*p*-phenylene vinylene)]
PMMA	poly(methyl methacrylate)
PPV	poly(*p*-phenylene vinylene)
PPE-PPV	poly(2,5-dialkoxy-1,4-phenylene ethynylene)
PVK	poly(9-vinylcarbazole)
spiro-OMeTAD	2,2',7,7'-tetrakis[*N*,*N*-di(4-methoxyphenyl)amino]-9,9'-spirobifluorene
TAD	1,2,4-triazoline-3,5-dione
TCTA	4,4',4-tris(carbazol-9-yl)triphenylamine
TmPyPB	1,3,5-tri(*m*-pyridin-3-ylphenyl)benzene
TPD	poly(*N*,*N*'-bis-4-butylphenyl-*N*,*N*'-bisphenyl)benzidine

The anode can be supplemented with various metal nanostructures for improved performance. Figure 3 presents optical images of GaN-based blue LED and UV LED with different current-spreading layers (ITO, Ni on graphene, and graphene) [42]. For a particular injection current value, the turn-on voltages for blue LED recorded on various anodes were 3.5 (ITO), 6.2 (graphene), and 4.8 V (Ni on graphene). However, for UV LED, the observed operating voltage reduced significantly from 13.2 (graphene) to 7.1 V (Ni on graphene). Even though the ITO anode remained superior, the Ni–graphene nanocomposite nevertheless displayed 83% of the EL intensity of ITO. Furthermore, a decrease in sheet resistance (from 500 to 30 Ω) when Ag nanowires are added to graphene increases the ability of graphene to function as a current-spreading layer [43].

1081

188

Figure 3: Optical images of light emission of (a) blue and (b) UV LED under different current-spreading layers (ITO, Ni on graphene, and graphene) at 1 and 20 mA current injections, respectively. Figure 3a and Figure 3b were adapted from [42], with the permission of AIP Publishing. This content is not subject to CC BY 4.0.
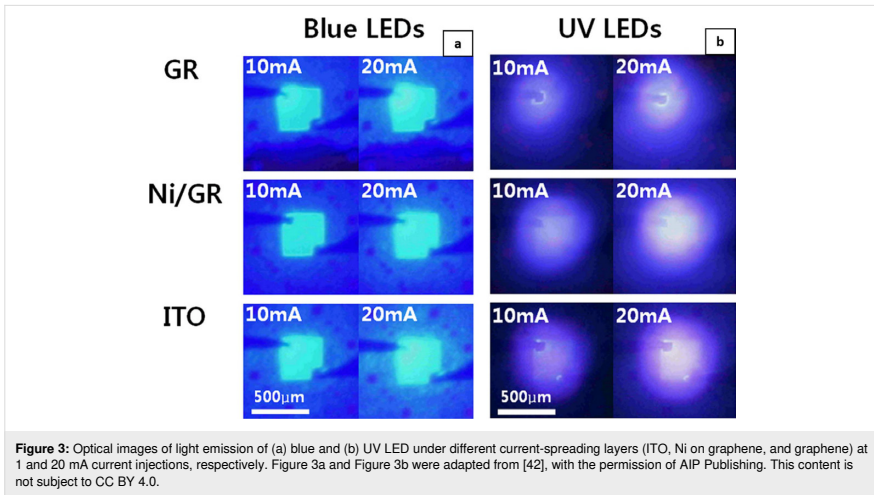
Equivalent to Ag, SPR of AuNP can also be applied to the anode in order to enhance the overall EL of the LED. Both of these MNP tend to increase the quantum efficiency of the LED. However, owing to the differences in the ranges of their SPR energies, different emission wavelengths are enhanced. In general, SPR of AgNP favors the quantum efficiency of the blue emission. On the other hand, Tanaka et al. reported that the SPR of AuNP positively influences the quantum efficiency of the red emission [44]. In addition, the shape of the MNP exhibiting SPR also plays a crucial role in the enhancement of the wavelength emanating from the LED. They studied the effect of Au nanorods (AuNR) and nanospheres (AuNS) in the device configuration of glass/ITO/AuNR and AuNS/CuPc/Alq$_3$ + DCM/Alq$_3$/LiF/Al red LED. The SPR absorption of Au nanorods and nanospheres were approx. 650 and 520 nm, respectively. Therefore, Au nanorods were able to enhance the red emission from the LED with an EQE of 6.8×10^{-4} at 10 V compared to the device with Au nanospheres (EQE = 2.4×10^{-4}).

In addition to the shape of AuNP, their size also influences the performance of LED. To that end, AuNP of diameters 2 and 5 nm were combined with CNT and deposited onto a p-GaN-based anode in a multiquantum-well LED [45]. The EL spectra of these devices at current injections of 100 mA have shown clear enhancements for both types of AuNP in Figure 4a and Figure 4b. Surface plasmon resonance absorbance tends to blueshift with decreasing sizes of the NP. Therefore, the 2 nm AuNP were able to enhance the blue emission from the LED. A similar effect was also observed with super-aligned carbon

nanotubes (SACNT) decorated with AuNP (2 nm) [46]. The hybrid material was employed as a current-spreading layer in AlGaInP LED. At a current injection of 2 mA, a decrease in the forward voltage from 2.18 (without SACNT) to 2.03 V (with Au-coated SACNT) was noted. A decrease in the forward voltage and an increase in the optical power (≈10%) also indicated a reduced sheet resistance. In addition, AlGaInP LED emanating red emissions in the range of 560–650 nm are boosted via SPR of AuNP by varying the AuNP size as explained above. Table 3 provides a list of various LED properties as a function of carbon-based nanomaterials and plasmonic NP incorporated into different layers.

Based on the data listed in Table 3, Figure 5 was plotted to compare the turn-on voltage and maximum luminance values of different OLED in order to evaluate the effectiveness of plasmonic nanoparticles and carbon-based nanostructures in the device architecture. Six types of OLED with AgNP, AuNP, GR, MWNT, SWNT, and GR + AuNP in the device structure were compared. In general, plasmonic nanoparticle-based OLED demonstrate lower turn-on voltages and higher luminance compared to the graphene or CNT-based ones. However, CNT and graphene tend to provide better thermal management and electrical properties; therefore, their integration into LED is of growing importance. Out of the three OLED-incorporating carbon-based nanostructures, OLED + GR possessed the lowest turn-on voltage; however, the luminance was rather low. Nevertheless, combing graphene with plasmonic nanoparticles (OLED + GR + Au) demonstrated a low turn-on voltage, equiv-
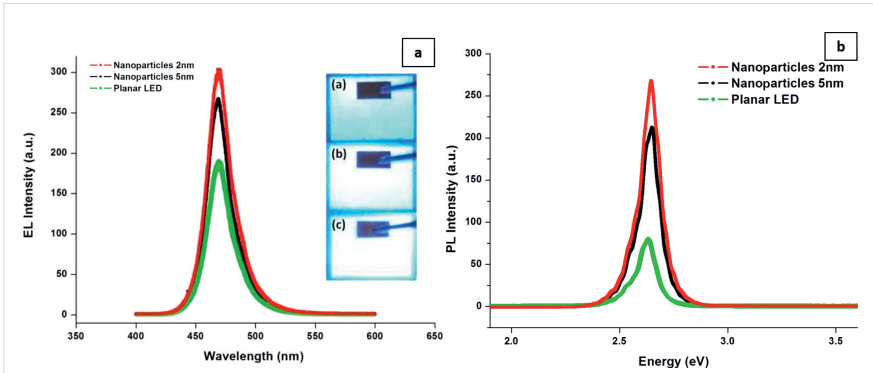
189

Figure 4: (a) EL spectra of LED having 2 and 5 nm Au–CNT system with an injection current of 100 mA measured at room temperature, using a planar LED as reference. The inset shows the optical images (a) without AuNP, (b) 5 nm Au–CNT system, and (c) 2 nm Au–CNT system. (b) Room temperature PL spectra of GaN LED with a 2 and 5 nm Au–CNT system and a planar LED as reference. Figure 4a and Figure 4b were adapted from [45] ("Enhanced optical output power of blue light-emitting diodes with quasi-aligned gold nanoparticles", © 2014 Y. Jin et al., distributed under the terms of the Creative Commons Attribution 2.0 International License, https://creativecommons.org/licenses/by/2.0/).

Table 3: EQE, turn-on voltage, and maximum luminance of various LED with carbon nanostructures, plasmonic, and metal oxide NP in the device layers.

| LED	Emissive layer	Graphene/CNT	Plasmonic NP/metal oxide NP	EQE (%)	Turn-on voltage (V)	Maximum luminance (cd/m^2)	Ref.
OLED	Alq$_3$	MWNT in HIL	—	—	8.3	6800	[18]
OLED	Alq$_3$	SWNT as the anode	—	—	6.6	2800	[21]
OLED	Alq$_3$ + DCM	—	Au in the anode	0.00068	—	—	[44]
OLED	Alq$_3$ + DCM	SWNT in HTL	—	0.05	—	—	[47]
OLED	Alq$_3$	—	Ag in HIL	—	5	782	[48]
OLED	Alq$_3$	—	Ag in HIL	2.08	5	4000	[49]
OLED	Alq$_3$	—	Au/Ag in the anode/HTL	—	3/5	9000/8665	[50]
OLED	Alq$_3$	graphene oxide as HIL	Au in HIL	0.77	3	3520	[51]
OLED	Ir(ppy)$_2$(acac)	—	Ag in ZnO EIL	21.2	3.5	—	[52]
OLED	SWNT	SWNT as EML	—	—	1.3	—	[53]
OLED	MEH-PPV	graphene in EML	—	—	6	480	[54]
OLED	MEH-PPV	—	TiO$_2$ in HIL	—	2.5	—	[55]
Inorganic LED	AlGaInP	graphene in anode	—	—	1.5	—	[40]
Inorganic LED	GaN	graphene as the anode	Ni in the anode	—	4.8/7.1	—	[42]
Inorganic LED	InGaN/AlGaN	graphene as the anode	Ag in the anode	—	4.48	—	[43]
Inorganic LED	GaN	—	Au in the anode	—	2.7	—	[45]
QLED	CdSe/ZnS	—	Ga doped ZnO as ETL	—	3	44000	[56]
QLED	MgZnO	—	Au in ZnO EIL	4.626	6	10206	[57]
QLED	Green QD	—	Yb and Ag in the cathode	9.8	2.2	—	[58]
HyLED	CdSe	—	Ag in the cathode	0.52	—	2000	[59]
HyLED	F8BT	—	ZnO as ETL	—	2	13100	[60]
HyLED	Imidazole	—	Ag-doped ZnO as EIL	15.2	1.75	10982	[61]
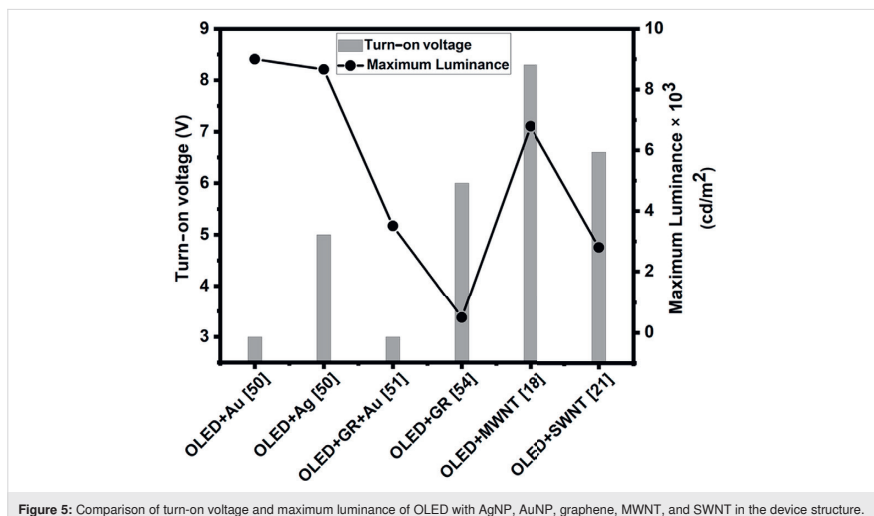
Figure 5: Comparison of turn-on voltage and maximum luminance of OLED with AgNP, AuNP, graphene, MWNT, and SWNT in the device structure.

alent to OLED + Au but a much lower luminance. Therefore, an ideal ratio between carbon-based nanostructures and plasmonic nanoparticles in OLED needs to be determined.

Enhancing hole mobility: hole injection and transport layers

The optimization of charge carrier injection also consists of reducing the driving voltage of the LED. For achieving this, holes should be readily injected from the high-work-function anode surface (e.g., ITO, SWNT), while the electrons should be injected from the low-work-function metal cathode surface. Therefore, HTL should possess excellent charge mobility and maintain morphological stability. Moreover, it should have an appropriate highest occupied molecular level (HOMO), ensuring a low energy barrier for hole injection from the anode into the EML. A suitable lowest unoccupied molecular level (LUMO) should be capable of blocking electron injection from the EML to the HTL. Thus, HTL play a very important role in OLED and HyLED.

With regards to carbon-based nanocomposites, Kim et al. have synthesized SWNT–PVK nanocomposites for HTL in OLED with the configuration ITO/PEDOT:PSS/SWNT–PVK nano-composite/DCM-doped Alq_3/Li:Al [47]. An efficient electron transport was also obtained from the Li:Al cathode (with work function of 2.9 eV) to the Alq_3 layer due to its higher LUMO level (3.2 eV) in comparison to the Li:Al work function. Therefore, this results in an efficient electron–hole recombination in

the DCM-based EML. Moreover, the EQE of the device with SWNT–PVK with 0.2 wt % CNT shows twice the enhancement as compared to the device without SWNT. In addition, MWNT also enhance hole-injection capabilities [62]. Certain concentrations of MWNT were studied in PET/ITO/MWNT–PEDOT:PSS (80 nm)/Alq_3/Al (40 nm) devices. At particular MWNT concentrations, higher current values (10 mA) and lower turn-on voltages (5 V) were noted. An optimal MWNT concentration of 0.6 wt % was deduced at which the EL intensity increased and the operating voltage decreased by a significant amount. However, a major concern regarding the reduction of the electron-blocking capability of PEDOT:PSS due to the addition of metallic MWNT needed further insight. Therefore, additional work by the same group [18] reported that the addition of MWNT in appropriate concentrations (0.4 wt %) improved the hole-injecting ability of PEDOT:PSS. Incorporation of 0.005 wt % of SWNT in PVK HTL resulted in 55% increment in hole mobility, which was initially 2.5×10^{-6} cm^2/V·s [63].

Other carbon-based nanostructures for HTL include graphene oxide. However, an optimum thickness of graphene oxide is required based on the device configuration. Shi et al. obtained similar results with an excellent luminance of 53000 cd/m^2, demonstrating its explicit applicability in flexible OLED [64]. Combinations of graphene oxide with polymers and metal oxides have also been evaluated. Lin et al. obtained an optimum concentration of 0.03 wt % of graphene in PEDOT:PSS [65]. A

1084

191

combination of MoS_2 and graphene sheets has also displayed good HIL tendencies due to the high surface coverage, work function, and low LUMO levels of graphene [66].

With regards to SPR of MNP, green emission enhancement in OLED has also been reported owing to the SPR of AgNP with an average size of 80 nm [48]. Silver nanoparticles were embedded in a PEDOT:PSS layer within the follwing device configuration: ITO (150 nm)/PEDOT:PSS (60 ± 10 nm)/AgNP/Alq_3 (100 nm)/LiF (1 nm)/Al (100 nm). The PL emission intensity at 535 nm from the device with AgNP increased by 30% compared to the device without AgNP. Choi et al. have used a scattering layer of AgNP in order to study the SPR effect, which increased the EQE by 24% in the flexible OLED [49].

Au and AgNP have also been embedded at the interface of the anode and the HTL in OLED [50]. Depending on the surface coverage of the plasmonic NP, an increment in the current density by a factor of two as compared to a device without plasmonic NP has been observed. The presence of Au and Ag reduces the work function of ITO due to the formation of dipoles at the interface and, therefore, reduces the hole injection barrier, which in turn creates a more efficient transfer to the HTL. In the device configuration of Figure 6a, a graphene oxide–Au nanocomposite HIL inserted between ITO and NPB was used to enhance the EL of Alq_3-based OLED [51]. The correlation between the wavelength absorbed (≈540 nm) by AuNP and the PL emission of the Alq_3 thin film (≈530 nm) implies a suitable plasmonic coupling with the NPB HTL (Figure 6b). In Figure 6c, the SPR coupling radius for a 20 nm AuNP was estimated to be ≈10 nm. This implies that the excitonic recombination occurs very close to the NPB and Alq_3 interface. The study reports that the devices with 10% graphene oxide–Au nanocomposites show approx. 45% improvement in

their maximum luminance, maximum current efficiency, and maximum EQE. Similar results were also obtained for AgNP in other studies [67].

Enhancing electron mobility: electron transport and injection layers

Similar to HTL and HIL, ETL and EIL play very crucial roles in optimizing charge carrier injection in OLED and HyLED. The latter follows an inverted OLED architecture (i.e., the EIL is in contact with the cathode followed by ETL). In order to enhance the OLED performance, ETL should have a high reduction potential and appropriate HOMO and LUMO values relative to the p-type emitter and HTL [68]. Other factors affecting their performance include a high electron mobility, an amorphous morphology, a high glass transition temperature, and the ability to be deposited as a uniform thin film. Some of the commonly used polymers and metal oxides for ETL are PBD, PBD-PMMA, BND, ZnO, SnO_2, and TiO_2 [69-71].

Improvements in the device performance have been reported, when using polymer–MWNT nanocomposite-based ETL. For example, Fournet et al. have investigated the role of MWNT by varying their concentration from 0–32% in PmPV [19]. They investigated a series of devices with configurations ITO/M3EH-PPV/Al (SL), ITO/PVK/M3EH-PPV/Al (DLH), ITO/M3EH-PPV/MWNT–PmPV/Al (DLE), and ITO/PVK(HTL)/M3EH-PPV(EML)/MWNT–PmPV (ETL)/Al (TL). The TL devices with 8 wt % of MWNT (Figure 7) present the best results in terms of luminance and EL emission. In addition, the electron conductivity of the device is increased by four orders of magnitude. Concerning graphene–polymer nanocomposites, Choudhary et al. have inserted MoS_2 and graphene oxide NP into a polyaniline ETL [72]. The conductivity of the nanocomposite was enhanced by 185% as compared to pure polyaniline.
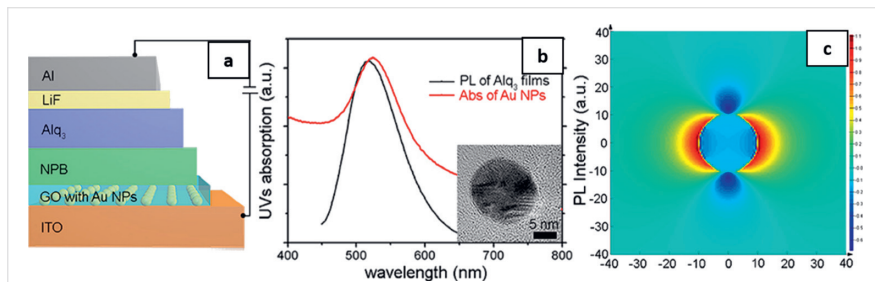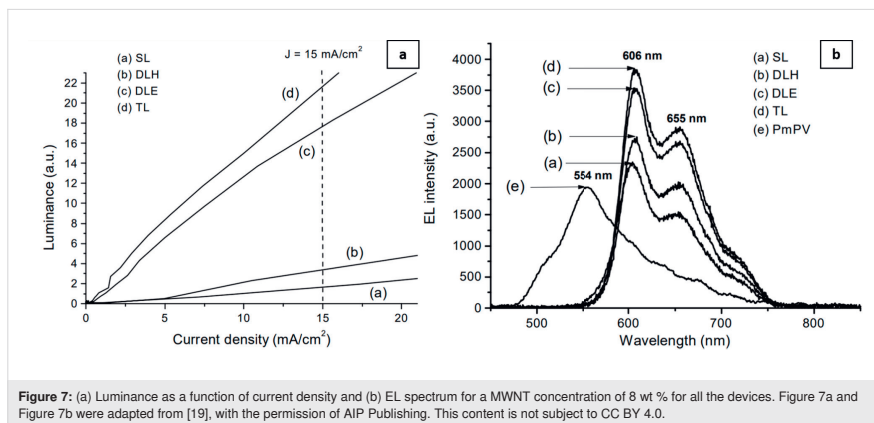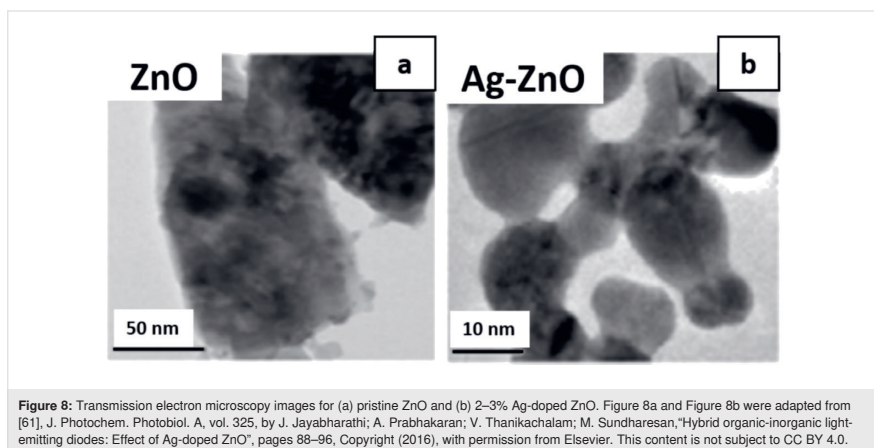

Figure 6: (a) OLED device structure with graphene oxide–AuNP inserted between ITO anode and NPB HTL. (b) The absorption spectrum of AuNP and PL emission spectrum of Alq_3 on ITO glass. The inset shows the TEM image of AuNP with a particle size of 20 nm. (c) The electromagnetic field distribution around AuNP with 20 nm diameter simulated by finite-difference time-domain modelling. Figure 6a–c was adapted from [51] (© 2018 J. Feng et al., distributed under the terms of the Creative Commons Attribution 4.0 International License, https://creativecommons.org/licenses/by/4.0/).

Figure 7: (a) Luminance as a function of current density and (b) EL spectrum for a MWNT concentration of 8 wt % for all the devices. Figure 7a and Figure 7b were adapted from [19], with the permission of AIP Publishing. This content is not subject to CC BY 4.0.

Further, the role of carbon quantum dots (CQD) in the ETL has also been examined in the device ITO/PEDOT:PSS/PFO/CQD/LiF/Al [73]. The turn-on voltage with CQD in the device configuration reduced from 8 to 6 V with enhancements in performance, efficiency, and lifetime compared to a pristine PFO device. In a work by Park et al., a remarkable enhancement in the electron mobility of ZnO ETL was reported on dispersing 0.08 wt % of n-doped CNT on its surface [74]. The effective electron mobility of the device without CNT was 1.5×10^{-6} cm^2/V·s. In contrast, the device with n-doped CNT showed an effective electron mobility of 7.0×10^{-6} cm^2/V·s, which corresponds to a five-fold improvement.

Incorporation of plasmonic NP in the ETL or EIL has further manifested a significant enhancement in the overall performance of LED. For example, Zhou et al. have used Ag-modified ZnO NP film as EIL in inverted fluorescent OLED (IFOLED) and inverted phosphorescent OLED (IPOLED) [52]. As a result, the IFOLED and IPOLED show very high current efficiencies of 8.4 and 95.3 cd/A and EQE of 4% and 21%, respectively, at a current density of 20 mA/cm^2. Similarly, the roles of Ag-doped ZnO and pristine ZnO as EIL in the imidazole organic EML-based HyLED were compared [61]. The transmission electron microscopy (TEM) images of Figure 8 illustrate that the pristine ZnO NP are larger ($\approx$50 nm) than

Figure 8: Transmission electron microscopy images for (a) pristine ZnO and (b) 2–3% Ag-doped ZnO. Figure 8a and Figure 8b were adapted from [61], J. Photochem. Photobiol. A, vol. 325, by J. Jayabharathi; A. Prabhakaran; V. Thanikachalam; M. Sundharesan, "Hybrid organic-inorganic light-emitting diodes: Effect of Ag-doped ZnO", pages 88–96, Copyright (2016), with permission from Elsevier. This content is not subject to CC BY 4.0.

1086

the Ag-doped ZnO (≈15 nm). In addition, the device with 2–3% Ag-doped ZnO EIL shows maximum luminance of 10982 cd/m^2, maximum current efficiency of 41.0 cd/A, and EQE of 15.2%. The addition of AgNP to PBD-based ETL enhances the green emission [75]. Kandulna et al. have addressed the effect of plasmonic NP on hybrid metal oxide–polymer nanocomposites [76]. They investigated Ag-doped ZnO (Ag:ZnO) and Ag:ZnO/PMMA nanocomposites for ETL applications in OLED. The pristine Ag:ZnO has an average particle size of ≈57 nm and the PMMA capping layer was ≈8 nm. Consequently, an increased rate of electron–hole recombination and an enhanced current density of ≈85% were obtained for optimized 10% Ag:ZnO/PMMA nanocomposite as compared to pristine Ag:ZnO.

Enhancing the emissive layer
The emissive layer is also known as the active luminescent region of an LED, where electron–hole recombination occurs. Light-emitting diodes and OLED are capable of emitting in the entire visible spectrum: GaAsP (red), GaN (green, blue/green), PPV (yellow/green), MEH-PPV and BCHA-PPV (yellow/orange), PPE-PPV (blue), and MDMO-PPV (red) [77-84]. Among these polymers, PPV appears to be the most popular light-emitting polymer. Burroughes et al. have reported on the first OLED using PPV that produces a yellow/green emission [80]. However, PPV has drawbacks, such as low-intensity PL emission and a high conversion temperature. Nevertheless, the derived versions of PPV, such as MEH-PPV, in which the emission shifts to orange from yellow/green in the unsubstituted PPV polymer, show improved properties.
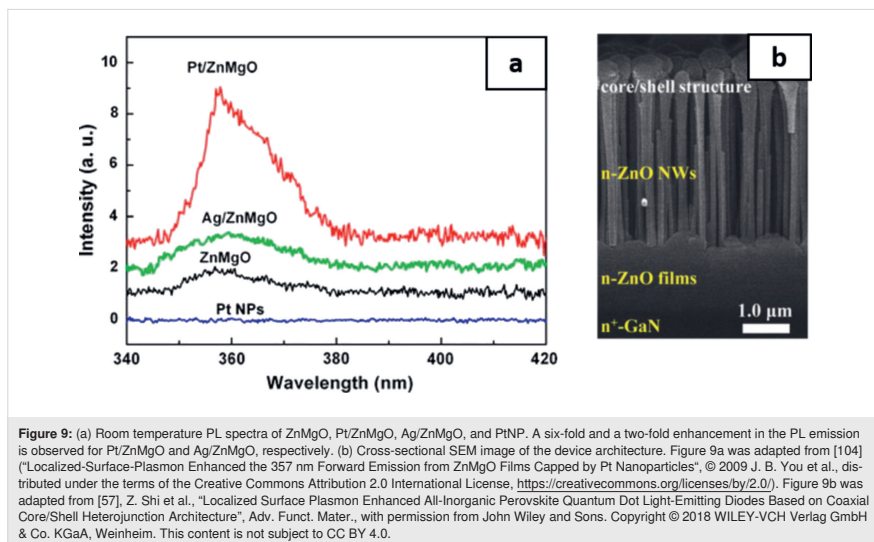
More recently, QD-based LED have shown an increase in the overall performance and longer lifetime values than OLED [85-89]. Furthermore, facile tuning of the emission wavelength by adjusting the particle size, their low fabrication cost, and saturated colors with a narrow bandwidth of EL (full width at half maximum ≈30 nm) have made the QLED attractive [90,91]. In effect, owing to the quantum confinement of CdSe QD, a decrease in particle size blueshifts the emission. Thus, their emission can be tuned to the entire visible spectrum by varying their sizes [92]. Generally, a QD-based EML is sandwiched between a polymer-based ETL and HTL.

Carbon-based nanomaterials such as SWNT have also been investigated as EML in OLED. Firstly, a SWNT p–n junction on a Si substrate has been investigated by Lee et al. [93]. Further, Mueller et al., with some modifications to the design of Lee et al., were able to produce a significantly narrower (≈35 meV) EL spectrum in the red region [17]. Wang et al. improved the device design of Mueller et al. by using a polymer layer of PMMA instead of split gates [53]. The device of Wang et al.

has several advantages: it is doping-free and cost-effective, it can be operated using a single bias, and it emanates a narrow EL spectrum of ≈30 meV. Similarly, white light LED can also consist of CQD at the EML along with metal oxides in the charge transport layers [94]. In addition, a maximum EQE of 0.083% has been obtained from CQD-based devices with configuration ITO/PEDOT:PSS (40 nm)/CQD (20 nm)/TPBI (40 nm)/LiF/Al [95]. These results clearly suggest that CQD are potential phosphors in the fabrication of white LED [96-100].

Prasad et al. have incorporated graphene nanosheets in MEH-PPV in order to evaluate the optimum quantity (0–0.1 wt %) for the luminance of the device [54]. They observed an approximate six-fold increase in the PL emission for 0.005 wt % of graphene nanosheets. The reason for the increased PL emission is attributed to the higher charge carrier mobility in graphene nanostructures, which balances out the charge carrier concentration in the EML.

InGaN-based LED have also benefited from the incorporation of AgNP in the EML. Consequently, a 14-fold PL enhancement and a seven-fold internal quantum efficiency have been reported [101]. A similar work reported an increase in the optical output power by 32% for an injection current of 100 mA [102]. By incorporating AgNP in F8BT, the current efficiency increased by a factor of 75, along with an approximate two-fold enhancement in the EL intensity [103]. You et al. have examined the PL emission from a ZnMgO alloy with a surface-capping of PtNP with thickness values ranging from 2 to 8 nm and with AgNP of 6 nm of thickness [104]. A six-fold and a two–fold enhancement in the PL emission has been observed by capping the ZnMgO alloy with Pt and AgNP, respectively. Figure 9a is the PL spectra of the ZnMgO, Pt/ZnMgO, Ag/ZnMgO and PtNP at room temperature showing a clear increase in the PL emission. Besides Ag nanorods and nanospheres, other plasmonic nanostructures, such as Ag nanocubes and nanostars tend to enhance LED properties owing to their sharp facets and edges [105,106]. Yu et al. have incorporated Ag nanocube core coated with SiO$_2$ shell in the EML of blue light-emitting diode [107]. A very high improvement in the current efficiency compared to the device without Ag nanocubes was noted. Shi et al. in a report, have introduced AuNP in the MgZnO QD layer with a device structure of p-NiO/CsPbBr$_3$/MgZnO/AuNP/n-ZnO film/n-GaN (Figure 9b) [57]. They further optimized the thickness of the MgZnO layer to 10 nm in order to control the distance between the CsPbBr$_3$ layer and AuNP. The EQE increased from 3 to 4.5% as the thickness of the MgZnO layer increased from 0 (no MgZnO layer) to 10 nm. The enhancement in the EQE and overall device performance has been associated with the spontaneous emission rate induced

Figure 9: (a) Room temperature PL spectra of ZnMgO, Pt/ZnMgO, Ag/ZnMgO, and PtNP. A six-fold and a two-fold enhancement in the PL emission is observed for Pt/ZnMgO and Ag/ZnMgO, respectively. (b) Cross-sectional SEM image of the device architecture. Figure 9a was adapted from [104] ("Localized-Surface-Plasmon Enhanced the 357 nm Forward Emission from ZnMgO Films Capped by Pt Nanoparticles", © 2009 J. B. You et al., distributed under the terms of the Creative Commons Attribution 2.0 International License, https://creativecommons.org/licenses/by/2.0/). Figure 9b was adapted from [57], Z. Shi et al., "Localized Surface Plasmon Enhanced All-Inorganic Perovskite Quantum Dot Light-Emitting Diodes Based on Coaxial Core/Shell Heterojunction Architecture", Adv. Funct. Mater., with permission from John Wiley and Sons. Copyright © 2018 WILEY-VCH Verlag GmbH & Co. KGaA, Weinheim. This content is not subject to CC BY 4.0.

by SPR coupling when an optimal distance of separation exists between the plasmonic and active layers.

New possibilities for cathode materials

The performance parameters of OLED, for example, turn-on voltage, operating voltage, current/power efficiency, and lifetime are strongly dependent on the physical parameters of the cathode material [108]. A cathode material should generally have a low work function as compared to the adjacent layer (generally ETL) in the device. The efficiency of electron transport depends on the energy difference between the Fermi level of the cathode material and the LUMO level of the adjacent material in which electrons have to be transported. Therefore, decreasing the energy barrier between the cathode and the adjacent layer can increase the electron injection efficiency and, hence, the device efficiency. Despite the high work function of Al (4.31 eV), it is among the most suitable cathode materials due to its high stability in ambient conditions. Alkali and alkali-rare earth metals have lower work function (2.8–3.7 eV) but are unstable in ambient conditions.

There are a few examples where plasmonic NP are used at the cathode to enhance the overall emission of the LED. Plasmonic AgNP have been inserted in Al (150 nm)/LiF (1 nm) cathode layer and a PL enhancement was observed [109]. In fact, the presence of AgNP tuned the carrier injection rate between cathode and Alq$_3$ EML. Carbon nanomaterials, such as

graphene and SWNT present interesting alternatives to overcome the drawbacks of metal and metal nanocomposite cathodes in OLED. Klain et al. have reported one possibility by doping graphene with n-type Ca [110]. The 1 nm Ca layer deposited by evaporation onto the surface of graphene reduced its work function by nearly 1 eV. Furthermore, the *I–V* characteristics of the device with Ca-doped graphene/Alq$_3$/Ag manifest a two-fold increase in current (at 2 V bias) as compared to only graphene. Similarly, Chang et al. have doped graphene with n-type CsF or Cs$_2$CO$_3$ on a SiO$_2$ substrate, thus reducing the work function of graphene from 4.4 to 3.2 eV, which was used to fabricate blue light-emitting OLED with maximum brightness of 1034 cd/m^2 [111]. On the other hand, very few works have been reported where SWNT are employed as cathodes in fully transparent OLED. Chien et al. have achieved highly efficient electron injection from SWNT-based films by modifying the surface of SWNT with a thin layer of Pd/Al/LiF while maintaining the transparency of the layer [112]. However, the device was ineffective as no emission was visible and the turn-on voltage was unusually low. The lack of emission was attributed to the charge unbalance in the EML due to high electron injection from the SWNT. Further efforts towards balancing electron–hole injection in the EML could also result in light emission from such devices. This could be brought about by optimizing the quantity of SWNT, functionalizing them, and combining them with other polymers. Nevertheless, this work demonstrates that SWNT can be used as cathode ma-

terials in LED, if improved. The successful implementation of such an electrode would open new possibilities to fabricate fully transparent OLED.

Conclusion

This article has provided an overview of the combination of various nanostructures that enhance the overall properties of various types of LED. In particular, CNT and MNP exhibiting SPR improve several characteristics of LED, such as lower turn-on voltages, higher EQE, and high luminance. The versatility of these nanomaterials lies in the fact that they can be accommodated into one or several layers of the LED. For example, carbon-based nanostructures can be added to the anode, hole injection, and transport layers as well as the EML. On the other hand, SWNT are still being tested as a viable cathode material. Depending upon the layer, these carbon-based nanostructures are able to enhance current spread, injection, and recombination lifetime values. Similarly, plasmonic NP, such as Au and Ag clearly enhance LED properties and can be integrated in all the layers of the device structure. Furthermore, incorporation of metal oxides, such as TiO_2, ZnO, SnO_2 in combination with Ag, Au, and PtNP has shown increment in the luminance and reduction in the operating voltages of the devices.

For several decades, inorganic LED based on III–V group semiconductors (i.e., GaAs, GaP, InGaAs, InGaP, GaN, InGaN, and AlGaInP) have been extensively studied and improved. More than 50% EQE for AlGaInP (red) and InGaN/GaN (blue/green) emitters has already been achieved with a future possibility of reaching up to 80%. Moreover, achievement in the device stability of up to 20000 h is remarkable for inorganic LED. However, these inorganic LED have poor color quality and they are fabricated with rare, costly, and non-flexible materials, which hinder their wide scale applications in wearables and display technologies. In addition, the self-heating of such structures is unavoidable. Carbon nanotubes and plasmonic NP exhibiting SPR have shown their superiority in enhancing the color quality of these inorganic LED by enhancing the PL, EL, current efficiency, and density. Moreover, graphene and SWNT incorporated into the anode have opened opportunities for thermal management in flexible inorganic LED.

Currently, OLED and QLED are dominating the display market. Light sources in OLED mainly consist of Alq_3 and derived version of PPV polymer, whereas QD based on Cd, Zn, Se, and S are mainly used for QLED. Both technologies have many advantages over traditional inorganic LED and liquid crystal displays in terms of low power consumption, wider view angle, higher resolution and cost-effectiveness. However, device degradation is common in both OLED and QLED due to charge accumulation in the layers. In the case of red QLED, HTL is rather stable and the device degradation rate is therefore low. On the other hand, in the blue QLED, their poor lifetime is caused by the quicker degradation of ETL. A similar degradation in OLED has also been observed but mainly in the HTL; the poor hole injection ability of polymers is also a cause for concern. From a commercial point of view, the present OLED displays are expensive as compared to QLED displays consisting of Cd-based QD. Graphene and CNT could be viable options in slowing or circumventing the degradation of HIL in OLED and QLED when combined with polymer nanocomposites.

In order to enhance the color purity of the OLED-based displays, SWNT combined with an emissive polymer tend to increase the luminance of the device and thereby achieve a higher color saturation. Nevertheless, SWNT display an emission spectrum with full width at half maximum of approximately 30 nm, which is very close to the color saturation of QLED displays ($\approx$25 nm). The blue/green emission from InGaN LED, ZnO NP, and OLED is enhanced through the SPR effect of AgNP, which in turn could counteract the high external luminance. Thus, the low brightness and short operation lifetime of blue QLED could be improved by using CNT–polymer or CNT–metal oxide nanocomposites as ETL and incorporating AgNP in this layer. Further strategies to counteract the outdoor luminance of 7000 cd/m^2 could also include a graphene oxide HIL, in which a luminance of 56000 cd/m^2 has been reported in such OLED. Doped ZnO in the ETL is also a suitable candidate for high-luminance blue OLED. Since the degradation of these nanocomposites is relatively slow as compared to pure CNT, they could therefore provide a workable pathway to enhance the lifetime of the blue QLED. Moreover, due to the localized SPR of AgNP the brightness of blue QLED can also be improved significantly. Enhancement of the red luminescence has been possible by the addition of AuNP. Enhancing the green luminescence has not been widely studied in OLED and QLED. However, AgNP has the potential to enhance the green emission through the engineering of its shape and size in order to modify their SPR properties.

OLED- and QLED-based displays are commercially available. Nonetheless, cost-effective and better quality displays are constantly being developed. The combination of various polymers with inorganic components or HyLED could very well fulfill the future needs of the display and lighting market. Even though HyLED is commercially available for lighting applications, further work still needs to be carried out in order to implement them in display technologies. Nevertheless, a combination of organic, inorganic, carbon nanostructures, and plasmonic NP could very well pave the way for future display technologies.

Funding

ORCID® iDs

Keshav Nagpal - https://orcid.org/0000-0003-0040-9984
Erwan Rauwel - https://orcid.org/0000-0001-8950-1415
Frédérique Ducroquet - https://orcid.org/0000-0001-8770-9650
Protima Rauwel - https://orcid.org/0000-0001-5393-2352

References

1. Salata, O. V. *J. Nanobiotechnol.* **2004,** *2,* 3. doi:10.1186/1477-3155-2-3
2. Kolahalam, L. A.; Kasi Viswanath, I. V.; Diwakar, B. S.; Govindh, B.; Reddy, V.; Murthy, Y. L. N. *Mater. Today* **2019,** *18,* 2182–2190. doi:10.1016/j.matpr.2019.07.371
3. Gayral, B. *C. R. Phys.* **2017,** *18,* 453–461. doi:10.1016/j.crhy.2017.09.001
4. Carr, W. N.; Pittman, G. E. *Appl. Phys. Lett.* **1963,** *3,* 173–175. doi:10.1063/1.1753837
5. Steranka, F. M. *Semicond. Semimetals* **1997,** *48,* 65–96. doi:10.1016/s0080-8784(08)62404-7
6. Kish, F. A.; Fletcher, R. M. *Semicond. Semimetals* **1997,** *48,* 149–226. doi:10.1016/s0080-8784(08)62406-0
7. Nakamura, S. *Proc. SPIE* **1997,** 3002. doi:10.1117/12.271048
8. Lin, Q.; Song, B.; Wang, H.; Zhang, F.; Chen, F.; Wang, L.; Li, L. S.; Guo, F.; Shen, H. *J. Mater. Chem. C* **2016,** *4,* 7223–7229. doi:10.1039/c6tc01531j
9. Sahbudin, U. K.; Wahid, M. H. A.; Poopalan, P.; Hambali, N. A. M. A.; Shahimin, M. M.; Ariffin, S. N.; Saidi, N. N. A.; Ramli, M. M. *MATEC Web Conf.* **2016,** *78,* 01114. doi:10.1051/matecconf/20167801114
10. Jang, E.-P.; Han, C.-Y.; Lim, S.-W.; Jo, J.-H.; Jo, D.-Y.; Lee, S.-H.; Yoon, S.-Y.; Yang, H. *ACS Appl. Mater. Interfaces* **2019,** *11,* 46062–46069. doi:10.1021/acsami.9b14763
11. Rahman, F. *Opt. Eng. (Bellingham, WA, U. S.)* **2019,** *58,* 010901. doi:10.1117/1.oe.58.1.010901
12. Neves, M. C.; Martins, M. A.; Soares-Santos, P. C. R.; Rauwel, P.; Ferreira, R. A. S.; Monteiro, T.; Carlos, L. D.; Trindade, T. *Nanotechnology* **2008,** *19,* 155601. doi:10.1088/0957-4484/19/15/155601
13. Tsukazaki, A.; Kubota, M.; Ohtomo, A.; Onuma, T.; Ohtani, K.; Ohno, H.; Chichibu, S. F.; Kawasaki, M. *Jpn. J. Appl. Phys., Part 2* **2005,** *44,* L643–L645. doi:10.1143/jjap.44.l643
14. Will, P.-A.; Reineke, S. Organic light-emitting diodes. In *Handbook of Organic Materials for Electronic and Photonic Devices (Second Edition);* Ostroverkhova, O., Ed.; Woodhead Publishing Series in Electronic and Optical Materials; Elsevier, 2019; pp 695–726. doi:10.1016/b978-0-08-102284-9.00021-8
15. He, Y.; Cheng, N.; Xu, X.; Fu, J.; Wang, J.-a. *Org. Electron.* **2019,** *64,* 247–251. doi:10.1016/j.orgel.2018.10.012
16. Ahn, J. H.; Wang, C.; Pearson, C.; Bryce, M. R.; Petty, M. C. *Appl. Phys. Lett.* **2004,** *85,* 1283–1285. doi:10.1063/1.1776621
17. Mueller, T.; Kinoshita, M.; Steiner, M.; Perebeinos, V.; Bol, A. A.; Farmer, D. B.; Avouris, P. *Nat. Nanotechnol.* **2010,** *5,* 27–31. doi:10.1038/nnano.2009.319
18. Wang, G.-F.; Tao, X.-M.; Wang, R.-X. *Compos. Sci. Technol.* **2008,** *68,* 2837–2841. doi:10.1016/j.compscitech.2007.11.004
19. Fournet, P.; Coleman, J. N.; Lahr, B.; Drury, A.; Blau, W. J.; O'Brien, D. F.; Hörhold, H.-H. *J. Appl. Phys.* **2001,** *90,* 969–975. doi:10.1063/1.1383023
20. Liu, G.; Johnson, S.; Kerr, J. B. *MRS Online Proc. Libr.* **2003,** *796,* 145–150. doi:10.1557/proc-796-v6.8
21. Aguirre, C. M.; Auvray, S.; Pigeon, S.; Izquierdo, R.; Desjardins, P.; Martel, R. *Appl. Phys. Lett.* **2006,** *88,* 183104. doi:10.1063/1.2199461
22. Jeong, S.-H.; Choi, H.; Kim, J. Y.; Lee, T.-W. *Part. Part. Syst. Charact.* **2015,** *32,* 164–175. doi:10.1002/ppsc.201400117
23. Liu, F.; Nunzi, J.-M. *Proc. SPIE* **2012,** *8424,* 84243E. doi:10.1117/12.927067
24. Lee, I.-H.; Jang, L.-W.; Polyakov, A. Y. *Nano Energy* **2015,** *13,* 140–173. doi:10.1016/j.nanoen.2015.01.050
25. Khadir, S.; Chakaroun, M.; Belkhir, A.; Fischer, A.; Lamrous, O.; Boudrioua, A. *Opt. Express* **2015,** *23,* 23647–23659. doi:10.1364/oe.23.023647
26. Diallo, A. T.; Chakaroun, M.; Khadir, S.; Hamdad, S.; Esparza-Villa, J. U.; Maître, A.; Boudrioua, A. *J. Nanophotonics* **2019,** *13,* 016004. doi:10.1117/1.jnp.13.016004
27. Hong, S.-H.; Cho, C.-Y.; Lee, S.-J.; Yim, S.-Y.; Lim, W.; Kim, S.-T.; Park, S.-J. *Opt. Express* **2013,** *21,* 3138–3144. doi:10.1364/oe.21.003138
28. Chen, H.-S.; Yang, P.; Khan, Z. H.; Wu, J. M.; Li, G.; Kamali, A. R. *J. Nanomater.* **2015,** *2015,* 371679. doi:10.3113/jsoa.2015.0036
29. Bhaumik, S.; Ghosh, B.; Pal, A. J. *Appl. Phys. Lett.* **2011,** *99,* 083106. doi:10.1063/1.3626455
30. Ameera, N.; Shuhaimi, A.; Surani, N.; Rusop, M.; Hakim, M.; Mamat, M. H.; Mansor, M.; Sobri, M.; Ganesh, V.; Yusuf, Y. *Ceram. Int.* **2015,** *41,* 913–920. doi:10.1016/j.ceramint.2014.09.009
31. Ling, B.; Sun, X. W.; Zhao, J. L.; Ke, C.; Tan, S. T.; Chen, R.; Sun, H. D.; Dong, Z. L. *J. Phys. Chem. C* **2010,** *114,* 18390–18395. doi:10.1021/jp106650p
32. Keller, J.; Stolt, L.; Edoff, M.; Törndahl, T. *Phys. Status Solidi A* **2016,** *213,* 1541–1552. doi:10.1002/pssa.201532883
33. Li, S.; Shi, Z.; Tang, Z.; Li, X. *Vacuum* **2017,** *145,* 262–267. doi:10.1016/j.vacuum.2017.09.011
34. Liu, H.; Avrutin, V.; Izyumskaya, N.; Özgür, Ü.; Morkoç, H. *Superlattices Microstruct.* **2010,** *48,* 458–484. doi:10.1016/j.spmi.2010.08.011
35. Kim, H.; Gilmore, C. M.; Piqué, A.; Horwitz, J. S.; Mattoussi, H.; Murata, H.; Kafafi, Z. H.; Chrisey, D. B. *J. Appl. Phys.* **1999,** *86,* 6451–6461. doi:10.1063/1.371708
36. Bonaccorso, F.; Sun, Z.; Hasan, T.; Ferrari, A. C. *Nat. Photonics* **2010,** *4,* 611–622. doi:10.1038/nphoton.2010.186
37. Han, N.; Viet Cuong, T.; Han, M.; Deul Ryu, B.; Chandramohan, S.; Bae Park, J.; Hye Kang, J.; Park, Y.-J.; Bok Ko, K.; Yun Kim, H.; Kyu Kim, H.; Hyoung Ryu, J.; Katharria, Y. S.; Choi, C.-J.; Hong, C.-H. *Nat. Commun.* **2013,** *4,* 1452. doi:10.1038/ncomms2448
38. Fu, Y.; Hansson, J.; Liu, Y.; Chen, S.; Zehri, A.; Samani, M. K.; Wang, N.; Ni, Y.; Zhang, Y.; Zhang, Z.-B.; Wang, Q.; Li, M.; Lu, H.; Sledzinska, M.; Torres, C. M. S.; Volz, S.; Balandin, A. A.; Xu, X.; Liu, J. *2D Mater.* **2019,** *7,* 012001. doi:10.1088/2053-1583/ab48d9
39. Kim, B.-J.; Lee, C.; Jung, Y.; Hyeon Baik, K.; Mastro, M. A.; Hite, J. K.; Eddy, C. R., Jr.; Kim, J. *Appl. Phys. Lett.* **2011,** *99,* 143101. doi:10.1063/1.3644496
40. Guo, X.; Feng, Y.; Liu, Q.; Hu, A.; He, X.; Hu, Z. *J. Appl. Phys.* **2018,** *123,* 175701. doi:10.1063/1.5018156

41. Bae, S.; Kim, H.; Lee, Y.; Xu, X.; Park, J.-S.; Zheng, Y.; Balakrishnan, J.; Lei, T.; Ri Kim, H.; Song, Y. I.; Kim, Y.-J.; Kim, K. S.; Özyilmaz, B.; Ahn, J.-H.; Hong, B. H.; Iijima, S. *Nat. Nanotechnol.* **2010,** *5,* 574–578. doi:10.1038/nnano.2010.132

42. Shim, J.-P.; Hoon Seo, T.; Min, J.-H.; Mo Kang, C.; Suh, E.-K.; Lee, D.-S. *Appl. Phys. Lett.* **2013,** *102,* 151115. doi:10.1063/1.4802800

43. Hoon Seo, T.; Kyoung Kim, B.; Shin, G.; Lee, C.; Jong Kim, M.; Kim, H.; Suh, E.-K. *Appl. Phys. Lett.* **2013,** *103,* 051105. doi:10.1063/1.4817256

44. Tanaka, T.; Totoki, Y.; Fujiki, A.; Zettsu, N.; Miyake, Y.; Akai-Kasaya, M.; Saito, A.; Ogawa, T.; Kuwahara, Y. *Appl. Phys. Express* **2011,** *4,* 032105. doi:10.1143/apex.4.032105

45. Jin, Y.; Li, Q.; Li, G.; Chen, M.; Liu, J.; Zou, Y.; Jiang, K.; Fan, S. *Nanoscale Res. Lett.* **2014,** *9,* 7. doi:10.1186/1556-276x-9-7

46. Guo, X.; Guo, C. W.; Jin, Y. H.; Chen, Y.; Li, Q. Q.; Fan, S. S. *Nanoscale Res. Lett.* **2014,** *9,* 171. doi:10.1186/1556-276x-9-171

47. Kim, J.-Y.; Kim, M.; Kim, H.; Joo, J.; Choi, J.-H. *Opt. Mater. (Amsterdam, Neth.)* **2003,** *21,* 147–151. doi:10.1016/s0925-3467(02)00127-1

48. Shin, J. B.; Baek, S.-W.; Lee, S. M.; Kim, M.; Lee, J.-Y.; Choi, K. C. *IEEE Photonics Technol. Lett.* **2016,** *28,* 371–374. doi:10.1109/lpt.2015.2496600

49. Choi, J.; Kim, S.; Park, C. H.; Kwack, J. H.; Park, C. H.; Hwang, H.; Im, H.-S.; Park, Y. W.; Ju, B.-K. *ACS Appl. Mater. Interfaces* **2018,** *10,* 32373–32379. doi:10.1021/acsami.8b07026

50. Jesuraj, P. J.; Jeganathan, K.; Navaneethan, M.; Hayakawa, Y. *Synth. Met.* **2016,** *211,* 155–160. doi:10.1016/j.synthmet.2015.11.024

51. Feng, J.; Sun, D.; Mei, S.; Shi, W.; Mei, F.; Zhou, Y.; Xu, J.; Jiang, Y.; Wu, L. *Front. Mater.* **2018,** *5,* 75. doi:10.3389/fmats.2018.00075

52. Zhou, L.; Xiang, H.-Y.; Zhu, Y.-F.; Ou, Q.-D.; Wang, Q.-K.; Du, J.; Hu, R.; Huang, X.-B.; Tang, J.-X. *ACS Appl. Mater. Interfaces* **2019,** *11,* 9251–9258. doi:10.1021/acsami.8b21355

53. Wang, S.; Zeng, Q.; Yang, L.; Zhang, Z.; Wang, Z.; Pei, T.; Ding, L.; Liang, X.; Gao, M.; Li, Y.; Peng, L.-M. *Nano Lett.* **2011,** *11,* 23–29. doi:10.1021/nl101513z

54. Prasad, N.; Singh, I.; Kumari, A.; Madhwal, D.; Madan, S.; Dixit, S. K.; Bhatnagar, P. K.; Mathur, P. C. *J. Lumin.* **2015,** *159,* 166–170. doi:10.1016/j.jlumin.2014.11.012

55. Nam Nguyen, P. H.; Nguyen, N. D. *Adv. Nat. Sci.: Nanosci. Nanotechnol.* **2013,** *4,* 025013. doi:10.1088/2043-6262/4/2/025013

56. Cao, S.; Zheng, J.; Zhao, J.; Yang, Z.; Li, C.; Guan, X.; Yang, W.; Shang, M.; Wu, T. *ACS Appl. Mater. Interfaces* **2017,** *9,* 15605–15614. doi:10.1021/acsami.7b03262

57. Shi, Z.; Li, Y.; Li, S.; Li, X.; Wu, D.; Xu, T.; Tian, Y.; Chen, Y.; Zhang, Y.; Zhang, B.; Shan, C.; Du, G. *Adv. Funct. Mater.* **2018,** *28,* 1707031. doi:10.1002/adfm.201707031

58. Lee, C.-Y.; Chen, Y.-M.; Deng, Y.-Z.; Kuo, Y.-P.; Chen, P.-Y.; Tsai, L.; Lin, M.-Y. *Nanomaterials* **2020,** *10,* 663. doi:10.3390/nano10040663

59. Coe, S.; Woo, W.-K.; Bawendi, M.; Bulović, V. *Nature* **2002,** *420,* 800–803. doi:10.1038/nature01217

60. Huang, C.-Y.; Lai, J.-H. *Org. Electron.* **2016,** *32,* 244–249. doi:10.1016/j.orgel.2016.02.031

61. Jayabharathi, J.; Prabhakaran, A.; Thanikachalam, V.; Sundharesan, M. *J. Photochem. Photobiol., A* **2016,** *325,* 88–96. doi:10.1016/j.jphotochem.2016.04.007

62. Wang, G.-F.; Tao, X.-M.; Chen, W.; Wang, R.-X.; Yang, A. *J. Lumin.* **2007,** *126,* 602–606. doi:10.1016/j.jlumin.2006.10.006

63. Yang, J.; Lee, J.; Lee, J.; Park, T.; Ahn, S. J.; Yi, W. *Diamond Relat. Mater.* **2017,** *73,* 154–160. doi:10.1016/j.diamond.2016.09.005

64. Shi, S.; Sadhu, V.; Moubah, R.; Schmerber, G.; Bao, Q.; Silva, S. R. P. *J. Mater. Chem. C* **2013,** *1,* 1708–1712. doi:10.1039/c3tc00707c

65. Lin, C.-H.; Chen, K.-T.; Ho, J.-R.; Cheng, J.-W. J.; Tsiang, R. C.-C. *J. Nanotechnol.* **2012,** *2012,* 942629. doi:10.1155/2012/942629

66. Park, M.; Nguyen, T. P.; Choi, K. S.; Park, J.; Ozturk, A.; Kim, S. Y. *Electron. Mater. Lett.* **2017,** *13,* 344–350. doi:10.1007/s13391-017-1612-3

67. Jung, M.; Mo Yoon, D.; Kim, M.; Kim, C.; Lee, T.; Hun Kim, J.; Lee, S.; Lim, S.-H.; Woo, D. *Appl. Phys. Lett.* **2014,** *105,* 013306. doi:10.1063/1.4890135

68. Jenekhe, S. A.; Zhang, X.; Chen, X. L.; Choong, V.-E.; Gao, Y.; Hsieh, B. R. *Chem. Mater.* **1997,** *9,* 409–412. doi:10.1021/cm960474q

69. Tardy, J.; Khalifa, M. B.; Vaufrey, D. *Mater. Sci. Eng., C* **2006,** *26,* 196–201. doi:10.1016/j.msec.2005.10.061

70. Park, M.; Song, J.; An, M.; Lim, J.; Lee, C.; Roh, J.; Lee, D. *RSC Adv.* **2020,** *10,* 8261–8265. doi:10.1039/d0ra00653j

71. Strukelj, M.; Miller, T. M.; Papadimitrakopoulos, F.; Son, S. *J. Am. Chem. Soc.* **1995,** *117,* 11976–11983. doi:10.1021/ja00153a018

72. Choudhary, R. B.; Mandal, G. *J. Mater. Sci.: Mater. Electron.* **2020,** *31,* 1302–1316. doi:10.1007/s10854-019-02643-9

73. Alam, M. B.; Yadav, K.; Shukla, D.; Srivastava, R.; Lahiri, J.; Parmar, A. *ChemistrySelect* **2019,** *4,* 7450–7454. doi:10.1002/slct.201901551

74. Park, J. S.; Lee, J. M.; Hwang, S. K.; Lee, S. H.; Lee, H.-J.; Lee, B. R.; Park, H. I.; Kim, J.-S.; Yoo, S.; Song, M. H.; Kim, S. O. *J. Mater. Chem.* **2012,** *22,* 12695–12700. doi:10.1039/c2jm30710c

75. He, X.; Wang, W.; Li, S.; Wang, Q.; Zheng, W.; Shi, Q.; Liu, Y. *Nanoscale Res. Lett.* **2015,** *10,* 468. doi:10.1186/s11671-015-1176-9

76. Kandulna, R.; Choudhary, R. B.; Maji, P. *J. Inorg. Organomet. Polym. Mater.* **2017,** *27,* 1760–1769. doi:10.1007/s10904-017-0639-0

77. Özdemir, O.; Mucur, S. P.; Tekin, E.; Boudiba, S.; Ulbricht, C.; Egbe, D. A. M.; Deneb Menda, U.; Kavak, P. A.; Kutlu, K. *Proc. SPIE* **2013,** *8829,* 8829B. doi:10.1117/12.2025395

78. Juhari, N.; Majid, W. H. A.; Ibrahim, Z. A. In *2006 IEEE International Conference on Semiconductor Electronics,* Kuala Lumpur, Malaysia, Oct 29–Dec 1, 2006; pp 112–115. doi:10.1109/smelec.2006.381030

79. Zhao, X.; Zhan, X. *Chem. Soc. Rev.* **2011,** *40,* 3728–3743. doi:10.1039/c0cs00194e

80. Burroughes, J. H.; Bradley, D. D. C.; Brown, A. R.; Marks, R. N.; Mackay, K.; Friend, R. H.; Burns, P. L.; Holmes, A. B. *Nature* **1990,** *347,* 539–541. doi:10.1038/347539a0

81. Han, D.-P.; Ishimoto, S.; Mano, R.; Lu, W.; Iwaya, M.; Takeuchi, T.; Kamiyama, S.; Akasaki, I. *Phys. Status Solidi A* **2020,** *217,* 1900713. doi:10.1002/pssa.201900713

82. Lee, M.-L.; Wang, S.-S.; Yeh, Y.-H.; Liao, P.-H.; Sheu, J.-K. *Sci. Rep.* **2019,** *9,* 3243. doi:10.1038/s41598-019-40095-7

83. Ozen, Y.; Sertel, T.; Cetin, S. S.; Ozcelik, S. *J. Electron. Mater.* **2018,** *47,* 7129–7133. doi:10.1007/s11664-018-6643-5

84. Salcedo-Reyes, J. C.; Vázquez, J.; Jiménez, L. C.; Méndez-Pinzón, H. *Proc. SPIE* **2017,** *10101,* 101010D. doi:10.1117/12.2253743

85. Coe-Sullivan, S.; Steckel, J. S.; Woo, W.-K.; Bawendi, M. G.; Bulović, V. *Adv. Funct. Mater.* **2005,** *15,* 1117–1124. doi:10.1002/adfm.200400468

198

86. Zhao, J.; Zhang, J.; Jiang, C.; Bohnenberger, J.; Basché, T.; Mews, A. *J. Appl. Phys.* **2004,** *96,* 3206–3210. doi:10.1063/1.1784611

87. Xu, J.; Wang, L.; Zhao, X.; Shi, Y.; Shi, Y.; Liu, T. *Nanomaterials* **2021,** *11,* 959. doi:10.3390/nano11040959

88. Su, Q.; Zhang, H.; Chen, S. *npj Flexible Electron.* **2021,** *5,* 8. doi:10.1038/s41528-021-00106-y

89. Shin, J. S.; Kim, T. Y.; Heo, S. B.; Hong, J.-A.; Park, Y.; Kang, S. J. *RSC Adv.* **2021,** *11,* 4168–4172. doi:10.1039/d0ra10422a

90. Bakueva, L.; Musikhin, S.; Hines, M. A.; Chang, T.-W. F.; Tzolov, M.; Scholes, G. D.; Sargent, E. H. *Appl. Phys. Lett.* **2003,** *82,* 2895–2897. doi:10.1063/1.1570940

91. Chaudhary, S.; Ozkan, M.; Chan, W. C. W. *Appl. Phys. Lett.* **2004,** *84,* 2925–2927. doi:10.1063/1.1699476

92. Choi, M. K.; Yang, J.; Hyeon, T.; Kim, D.-H. *npj Flexible Electron.* **2018,** *2,* 10. doi:10.1038/s41528-018-0023-3

93. Lee, J. U.; Gipp, P. P.; Heller, C. M. *Appl. Phys. Lett.* **2004,** *85,* 145–147. doi:10.1063/1.1769595

94. Paulo-Mirasol, S.; Martínez-Ferrero, E.; Palomares, E. *Nanoscale* **2019,** *11,* 11315–11321. doi:10.1039/c9nr02268f

95. Wang, F.; Chen, Y.-h.; Liu, C.-y.; Ma, D.-g. *Chem. Commun.* **2011,** *47,* 3502–3504. doi:10.1039/c0cc05391k

96. Guo, X.; Wang, C.-F.; Yu, Z.-Y.; Chen, L.; Chen, S. *Chem. Commun.* **2012,** *48,* 2692–2694. doi:10.1039/c2cc17769b

97. Li, X.; Liu, Y.; Song, X.; Wang, H.; Gu, H.; Zeng, H. *Angew. Chem., Int. Ed.* **2015,** *54,* 1759–1764. doi:10.1002/anie.201406836

98. Cui, B.; Feng, X.-t.; Zhang, F.; Wang, Y.-l.; Liu, X.-g.; Yang, Y.-z.; Jia, H.-s. *New Carbon Mater.* **2017,** *32,* 385–401. doi:10.1016/s1872-5805(17)60130-6

99. Ghosh, D.; Sarkar, K.; Devi, P.; Kim, K.-H.; Kumar, P. *Renewable Sustainable Energy Rev.* **2021,** *135,* 110391. doi:10.1016/j.rser.2020.110391

100. Masha, S.; Oluwafemi, O. S. *Mater. Lett.* **2021,** *283,* 128790. doi:10.1016/j.matlet.2020.128790

101. Okamoto, K.; Niki, I.; Shvartser, A.; Narukawa, Y.; Mukai, T.; Scherer, A. *Nat. Mater.* **2004,** *3,* 601–605. doi:10.1038/nmat1198

102. Kwon, M.-K.; Kim, J.-Y.; Kim, B.-H.; Park, I.-K.; Cho, C.-Y.; Byeon, C. C.; Park, S.-J. *Adv. Mater. (Weinheim, Ger.)* **2008,** *20,* 1253–1257. doi:10.1002/adma.200701130

103. Chen, S.-H.; Huang, C.-L.; Yu, C.-F.; Wu, G.-F.; Kuan, Y.-C.; Cheng, B.-H.; Li, Y.-R. *Opt. Lett.* **2017,** *42,* 3411–3414. doi:10.1364/ol.42.003411

104. You, J. B.; Zhang, X. W.; Dong, J. J.; Song, X. M.; Yin, Z. G.; Chen, N. F.; Yan, H. *Nanoscale Res. Lett.* **2009,** *4,* 1121. doi:10.1007/s11671-009-9366-y

105. Deng, L.; Yang, J.; Zhan, N.; Yu, T.; Yu, H.; Chen, S. *Opt. Lett.* **2019,** *44,* 983–986. doi:10.1364/ol.44.000983

106. Munkhbat, B.; Pöhl, H.; Denk, P.; Klar, T. A.; Scharber, M. C.; Hrelescu, C. *Adv. Opt. Mater.* **2016,** *4,* 772–781. doi:10.1002/adom.201500702

107. Yu, T.; Deng, L.; Xia, P.; Lu, Y.; Zhan, N.; Chen, S. *Org. Electron.* **2019,** *75,* 105388. doi:10.1016/j.orgel.2019.105388

108. Veinot, J. G. C.; Marks, T. J. *Acc. Chem. Res.* **2005,** *38,* 632–643. doi:10.1021/ar030210r

109. Yang, K. Y.; Choi, K. C.; Ahn, C. W. *Appl. Phys. Lett.* **2009,** *94,* 173301. doi:10.1063/1.3125249

110. Klain, C.; Linde, S.; Shikler, R.; Sarusi, G. *Carbon* **2020,** *157,* 255–261. doi:10.1016/j.carbon.2019.10.028

111. Chang, J.-H.; Lin, W.-H.; Wang, P.-C.; Taur, J.-I.; Ku, T.-A.; Chen, W.-T.; Yan, S.-J.; Wu, C.-I. *Sci. Rep.* **2015,** *5,* 9693. doi:10.1038/srep09693

112. Chien, Y.-M.; Shih, I.; Izquierdo, R. *ECS Trans.* **2019,** *35* (25), 69–74. doi:10.1149/1.3655513

V

K. Nagpal, M. S. Rosario, K. Praakle, E. Rauwel, P. Rauwel, "Investigation of the optical and antibacterial properties of biosynthesized ZnO nanoparticles using Thuja tincture" Journal of Physics: Conference Series 2315, 012016 (2022)

Investigation of the optical and antibacterial properties of biosynthesized ZnO nanoparticles using Thuja tincture

To cite this article: K. Nagpal *et al* 2022 *J. Phys.: Conf. Ser.* **2315** 012016

View the article online for updates and enhancements.

Investigation of the optical and antibacterial properties of biosynthesized ZnO nanoparticles using Thuja tincture

K. Nagpal[1], M. S. Rosario[2], K. Praakle[3], E. Rauwel[1], P. Rauwel[1*]

[1]Institute of Technology, Estonian University of Life Sciences, Kreutzwaldi 56/1, Tartu (Estonia)
[2]CICECO, University of Aveiro, 3810-193Aveiro, Portugal
[3]Institute of Veterinary Medicine & Animal Sciences, Estonian University of Life Sciences, Kreutzwaldi 62, 51006 Tartu, Estonia

Email: protima.rauwel@emu.ee

Abstract: The present study deals with the green synthesis of ZnO nanoparticles using Thuja tincture as a solvent and two different Zn precursors. The crystallinity of the as-synthesized ZnO nanoparticles was investigated by XRD. The biomolecules bonded to the surfaces of the nanoparticles were assessed by Fourier transform infrared spectroscopy. The band gap and defects in these nanoparticles were investigated by UV-Vis and photoluminescence spectroscopies, respectively. The antibacterial properties of these nanoparticles were also investigated against *Escherichia coli*.

1. Introduction

In recent years, there has been a surge of interest in nanoparticle-based semiconductors due to their novel properties, which have applications in optoelectronics, piezoelectric devices, solar cells, light emitting diodes, catalysts, cosmetic additives and antimicrobial agents. Among the various nanoparticles, ZnO is a versatile semiconductor exhibiting interesting chemical, thermal and optical properties. Its most important properties are a wide band gap of 3.36 eV and a high exciton binding energy of 60 meV at room temperature. In addition, ZnO nanoparticles display significant optical transparency and luminescence in the ultraviolet-visible (UV-Vis) region [1]. Recently, several biological methods using microorganisms, enzymes and plant extracts have been investigated for the biosynthesis of ZnO nanoparticles. These methods are gaining popularity as they are often one-step, eco-friendly, safe and cost-effective synthesis routes. In addition, these methods offer a possible alternative to chemical and physical methods that usually produce toxic by-products. Among the various biological methods, the use of plant extracts offers important advantages; for example, nanoparticles synthesized using plant extracts are useful for agriculture, food industry, antimicrobial testing, medicine and biology [2]. Various plant extracts of Aloe barbadensis miller, Poncirus trifoliate plant dried fruits, Cassia fistula, Trifolium pratense and Ocimum basilicum have been used for green or eco-friendly synthesis of ZnO nanoparticles [3-5].

   In this report, we have investigated the synthesis of ZnO nanoparticles using absolute Thuja occidentalis tincture and two different zinc (Zn) salts, i.e. Zn acetate dihydrate ($Zn(CH_3CO_2)_2.2H_2O$) and Zn acetate

anhydrous ($Zn(CH_3CO_2)_2$) as precursors. These nanoparticles were structurally and optically characterized in order to elucidate the effect of the precursor on their properties. The antibacterial assessment of the as-synthesized ZnO nanoparticles against *Escherichia coli (E. coli)* was also carried out.

2. Experimental

2.1 Preparation of the Thuja tincture:

To prepare a solution of Thuja tincture, 2 g of grounded Thuja plant leaves were dissolved in 50 ml of absolute ethanol. The solution was mixed manually and covered with an aluminum foil and stored in a dark place. After 24 h, the solution was manually shaken and stored in the same place for another 24 h. The solution was thereafter filtered to remove the plant residues and the impurities.

2.2 Synthesis of ZnO nanoparticles:

All the chemicals used for the synthesis of ZnO nanoparticles were of analytical reagent grade. In order to prepare a 0.05 M solution, 219.5 mg and 183.5 mg of $Zn(CH_3CO_2)_2.2H_2O$ (99.9%, Aldrich) (sample Z-D) and $Zn(CH_3CO_2)_2$ (99.9%, Aldrich) (sample Z-A), respectively were dissolved in 20 ml of Thuja solution in a beaker placed in a water bath. The solution was maintained at 60°C under continuous magnetic stirring until the Zn precursor was dissolved. Further, 0.1 M NaOH (99.9%, Aldrich) in 20 ml of absolute ethanol was prepared and was added drop wise to 0.05 M precursor solutions to obtain mixtures of 1:2 molar ratio. Thereafter, the mixtures were maintained at 60°C for 2 h and cooled to ambient temperature; light-green ZnO precipitates settled at the bottom of the reaction vessel. The resulting solutions containing ZnO nanoparticles were then centrifuged at 4500 rpm for 6 min and dried for 24 h in air at 60°C to obtain very fine ZnO nanopowders.

2.3 Antibacterial activity by agar disc method:

Agar disc method was adopted for the evaluation of the antibacterial activity. Bacterial lawn was prepared using MacConkey agar culture in a petri dish and colonies of Gram-negative *Escherichia coli* (*E. coli*) bacteria were grown in an oven at 37°C for 24 h. Seven points were marked on the top of the petri dish that served as references for dropping ZnO nanoparticles. Then, 6 mg of Z-A and Z-D were dissolved in 7.5 ml of distilled water (DI). Subsequently, 2 µl of these solutions were then dropped onto each of the seven sites on the petri dishes using a micropipette. The petri dishes were placed in an oven at 37°C for 24 h. After that, each spot containing ZnO nanoparticles was irradiated with UV light of wavelength 365 nm. The petri dishes were subsequently placed in an oven at 37°C for 24 h. The growth of bacteria was compared after the incubation period.

2.4 Characterization

XRD patterns were collected in Bragg-Brentano geometry using a Bruker D8 Discover diffractometer (Bruker AXS, Germany) with CuKα1 radiation (λ = 0.15406 nm) selected by a Ge (1 1 1) monochromator and LynxEye detector. FTIR spectrometer (Nicolet is10 Thermo Scientific, Germany) was cooled with liquid nitrogen and spectra were acquired in the range of 540-4000 cm^{-1}. The optical absorbance of ZnO and ZnO-CNT nanohybrids were determined using a NANOCOLOR UV-VIS II spectrometer (MACHEREY-NAGEL, Germany) in 200-900 nm region. The bandgap of ZnO nanoparticles was subsequently calculated with Tauc plots. PL was investigated at 300 K at an excitation wavelength of 365 nm of a LSM-365A LED (Ocean insight, USA) with an output power of 10 mW. The emission was collected by FLAME UV-Vis spectrometer (Ocean optics, USA) with a spectral resolution of 1.34 nm.

2

3. Results and discussions:

Table 1 shows the list of ZnO samples studied in this work. Sample Z-A corresponds to molar ratio 1:2 of $(Zn(CH_3CO_2)_2:NaOH)$ and sample Z-D corresponds to molar ratio 1:2 of $(Zn(CH_3CO_2)_2.2H_2O:NaOH)$. For UV light-assisted antibacterial study of ZnO nanoparticles, the petri dishes were abbreviated as Z-A-UV and Z-D-UV.

Table 1. List of ZnO samples studies in this work

Sample Name	Precursor	Precursor amount (g)	NaOH amount (g)	Molar ratio
Z-A	Zn acetate anhydrous	0.1835	0.0799	1:2
Z-D	Zn acetate dihydrate	0.2195	0.0799	1:2

3.1 Structural properties

XRD patterns of the ZnO samples are shown in Figure 1. The peaks (100), (002), (101), (102), and (110) correspond to the ZnO hexagonal wurtzite structure (a = 3.25 Å and c = 5.20 Å) of ZnO (JCPDS, Card Number 36-1451). Secondary phases are absent, confirming the phase purity of the as-synthesized ZnO nanoparticles. In addition, the intensity of the (002) diffraction peak is significantly lower than that of the (100) and (101) diffraction peaks. This probably indicates that there is no preferential growth of the ZnO nanoparticles along the c-axis. The Scherrer equation applied to (100), (002) and (101) reflections provided nearly the same particle sizes for both samples, suggesting spherically shaped particles. The average particle sizes of samples Z-A and Z-D using all 3 reflections were calculated to be ~4.5 nm and ~4.8 nm, respectively.
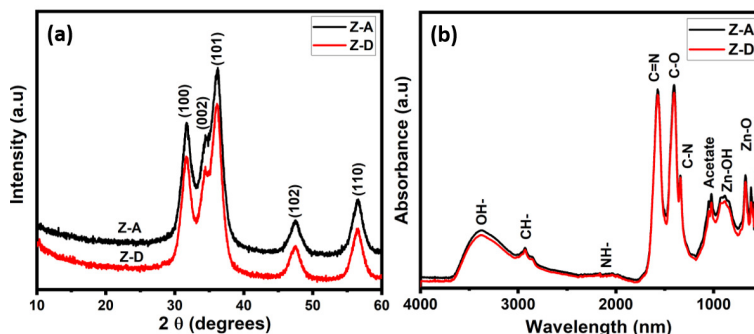

Figure 1. (a) XRD patterns and (b) FTIR spectra of ZnO samples Z-A and Z-D.

Figure 1b illustrates the FTIR spectra that provide information on the nature of the bonds formed during the synthesis of samples Z-A and Z-D. The band located between 700-500 cm^{-1} corresponds to the Zn-O stretching bond, confirming the formation of ZnO. The vibrational band of ZnO is located at similar positions in both ZnO samples, indicating indistinguishable morphology of the samples. The broad band near 3300 cm^{-1} corresponds to the OH- stretching, originating from NaOH, Zn precursors and absolute ethanol used during the preparation of the ZnO samples. In addition, the OH- functional groups bonded to Zn i.e. the Zn-OH bonds are located between 1000-800 cm^{-1}. The bands between 3000-2800 cm^{-1} correspond to the CH- stretching of the alkane groups. The small intense peak around 2400 cm^{-1} can be attributed to the NH- functional groups [6]. The peak located at 1612 cm^{-1} could be attributed to the C=O stretching in the

carboxyl or C=N bending in the amide group [7]. The peaks located between 1350-1050 cm^{-1} correspond to alcohol, phenolic groups, carboxylate (COO^-) functional groups and C-N stretching vibrations of aromatic amines of biomolecules [8].

3.2 Band gap
The band gaps of ZnO samples were calculated through UV-Vis absorption spectroscopy followed by Tauc plots presented in figure 2. The absorption properties of samples Z-A and Z-D are similar. In addition, the band gap values of samples Z-A and Z-D were calculated to be 3.34 eV and 3.31 eV, respectively.
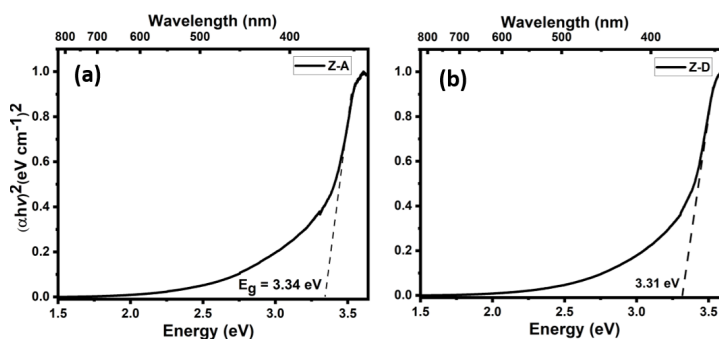

Figure 2. Tauc plots of samples (a) Z-A and (b) Z-D.

3.3 Photoluminescence
The emission properties of samples Z-A and Z-D were examined through room temperature PL measurements. The 365 nm (3.4 eV) excitation source was used to incite band-to-band transitions in samples Z-A and Z-D with bandgaps of 3.34 and 3.31 eV, respectively. The PL spectra in figure 3 manifest typical PL emission characteristics of ZnO nanoparticles, consisting of the UV emission or the NBE and the visible emission or the DLE [9]. The PL emission spectra provide the most significant emission peaks, as green emission at 2.2 eV, orange emission at ~2.1 eV, red emission at ~1.95 eV. It can be observed that the DLE of both samples Z-A and Z-D are dominated by green emission originating from surface oxygen vacancies (V_O^{++}) at ~2.2 eV, owing to the small size of the nanoparticles. The yellow-orange emission ~2.1 eV is attributed to the transitions from Zn_i to O_i, which are the other most significant components in the PL emission spectra. The red emission at ~1.95 eV originating from V_{zn} is the least significant emission. Moreover, it is also noticeable that the NBE of sample Z-D is more intense than that of sample Z-A.
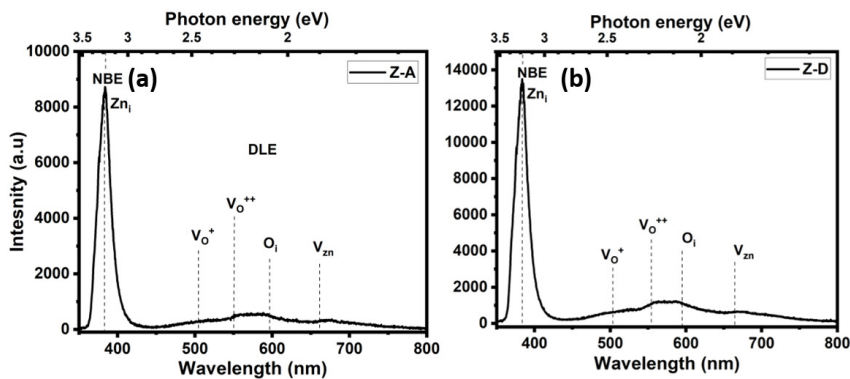
4

Figure 3. PL emission spectra of samples (a) Z-A and (b) Z-D, showing various defect states in their structure.

3.4 Antibacterial properties

The mechanisms of antibacterial activity of ZnO nanoparticles are usually attributed to reactive oxygen species (ROS) production, Zn^{+2} soluble ions, surface charge, membrane potential charge, and particle size and shape. One possible mechanism explaining the inhibition of bacterial growth by the addition of ZnO nanoparticles is governed by ROS caused by splitting of water molecules by photo-generated electron-hole pairs under room light [10]. This mechanism strongly depends on the shape and size of the nanoparticles. In our case, the nanoparticles are spherical and have a very small particle size (average size < 5 nm), as estimated from the XRD study. Therefore, they have a high surface-to-volume ratio and should in principle produce a large amount of ROS, which is favorable for inhibiting *E. coli* [11, 12]. Therefore, in order to increase the amount of ROS, we illuminated the bacterial dishes with UV light, which should liberate hydroxyl, oxygen and peroxide groups. However, we found that samples Z-A and Z-D did not significantly inhibit the growth of colonies at the seven marked spots under room and UV light illuminations (Figure 4a - 4d). Even Z-D that displayed a more intense NBE did not demonstrate a higher antibacterial activity than Z-A. The low antibacterial inhibition suggests that the amount of ZnO nanoparticles used for the study may not be sufficient. Other factors, such as the quantity of Thuja dried plant (2g) in the tincture along with the short soaking time of two days could be responsible for the negligible antimicrobial activity. Additionally, they may be covered with some biomolecules that prevent the formation of ROS as explained in the following paragraph.

As an example, antimicrobial study against *E. coli* of ZnO nanoparticles synthesized with absolute ethanol (without Thuja extract) was compared in Figure 4e and 4f. UV light was not applied to the petri dishes. Under room light activation, clear inhibition zones are visible on the petri dishes. The quantities of ZnO used for inhibition synthesized with and without Thuja extract were identical. This clearly suggests that the biomolecules of Thuja hinder the creation of ROS that ZnO is capable of producing even under room light conditions.
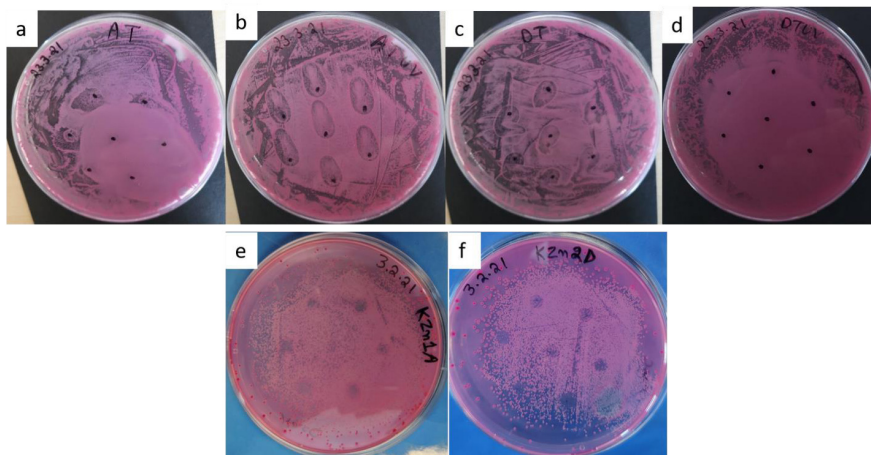
5

Figure 4. Antibacterial activity of samples a) Z-A, b) Z-A-UV, c) Z-D, d) Z-D-UV, e) Z-A without Thuja and, f) Z-D without Thuja.

4. Conclusion

We synthesized ZnO nanoparticles by using absolute Thuja tincture as a solvent instead of absolute ethanol and two different Zn precursors. The XRD patterns show that our method produces ZnO nanoparticles with an average size of less than 5 nm. The PL spectra show high intensity of NBE and low intensity of DLE for both samples Z-A and Z-D. This could be attributed to the fact that the surface of the ZnO nanoparticles is covered with organic molecules from the tincture prepared with Thuja plant, which suppresses the surface defects. When the antibacterial properties were investigated, the as-synthesized ZnO nanoparticles showed insufficient inhibition. Even under UV illumination, no significant enhancement was observed. Several factors could contribute to the low bacterial inhibition. However, the major factor affecting the lack of inhibition to *E. coli* was the presence of biomolecules of Thuja covering the surface of ZnO and hindering the production of ROS. This was proven by synthesizing ZnO without Thuja extract and obtaining successful *E. coli* inhibition. The biomolecule free surfaces of ZnO were capable of producing ROS even in room light conditions. Finally, no synergistic effect with the Thuja tincture was observed, which suggests that zinc nitrate precursors could be more suitable for green synthesis using plant extract and will be the subject of further investigations.

6

References

[1]   Zhao J-H, Liu C-J and Lv Z-H 2016 *Optik* **127** 1421-3 https://doi.org/10.1016/j.ijleo.2015.11.018

[2]   Xu J, Huang Y, Zhu S, Abbes N, Jing X and Zhang L 2021 *J. Eng. Fibers Fabr.* **16**
      https://doi.org/10.1177%2F15589250211046242

[3]   Nagajyothi P C, Minh An T N, Sreekanth T V M, Lee J-i, Joo Lee D and Lee K D 2013 *Mater. Lett.*
      108 160-3 https://doi.org/10.1016/j.matlet.2013.06.095

[4]   Rajiv P, Rajeshwari S and Venckatesh R 2013 *Spectrochim Acta A Mol Biomol Spectrosc* **112** 384-7
      https://doi.org/10.1016/j.saa.2013.04.072

[5]   Küünal S, Rauwel P and Rauwel E 2018 *Emerging Applications of Nanoparticles and Architecture
      Nanostructures,* ed A Barhoum and A S H Makhlouf: (Elsevier)
      https://doi.org/10.1016/B978-0-323-51254-1.00014-2

[6]   Alamdari S, Sasani Ghamsari M, Lee C, Han W, Park H-H, Tafreshi M J, Afarideh H and Ara M H
      M 2020 *Appl. Sci.* **10** 3620 https://doi.org/10.3390/app10103620

[7]   M. Awwad A, Albiss B and L. Ahmad A 2014 *Adv. Mater. Lett* **5** 520-4
      https://doi.org/10.5185/amlett.2014.5575

[8]   Huang J, Li Q, Sun D, Lu Y, Su Y, Yang X, Wang H, Wang Y, Shao W, He N, Hong J and Chen C
      2007 *Nanotechnology* **18** 105104 https://doi.org/10.1088/0957-4484/18/10/105104

[9]   Rauwel E, Galeckas A, Rauwel P, Sunding M F and Fjellvåg H 2011 *J. Phys. Chem. C* **115** 25227-33
      https://doi.org/10.1021/jp208487v

[10] Raghupathi K R, Koodali R T and Manna A C 2011 *Langmuir* **27** 4020-8
      https://doi.org/10.1021/la104825u

[11] Dutta R K, Nenavathu B P, Gangishetty M K and Reddy A V R 2012 *Surf. B* **94** 143-50
      https://doi.org/10.1016/j.colsurfb.2012.01.046

[12] Applerot G, Lipovsky A, Dror R, Perkas N, Nitzan Y, Lubart R and Gedanken A 2009 *Adv. Funct.
      Mater.* **19** 842-52 https://doi.org/10.1002/adfm.200801081

7

VI

K. Nagpal, E. Rauwel, F. Ducroquet, I. Gelard, P. Rauwel, "Fabrication and evaluation of figures of merit of ZnO-polymer based hybrid UV photodiodes" APL Materials 12(6), (2024)

Fabrication and evaluation of figures of merit of ZnO polymer-based hybrid UV photodiodes

Keshav Nagpal ; Erwan Rauwel ; Frédérique Ducroquet; Isabelle Gélard ; Protima Rauwel

Check for updates

View Online

Export Citation

07 June 2024 06:51:50

Fabrication and evaluation of figures of merit of ZnO polymer-based hybrid UV photodiodes

View Online   Export Citation   CrossMark

Keshav Nagpal,[1] Erwan Rauwel,[2] Frédérique Ducroquet,[3] Isabelle Gélard,[4] and Protima Rauwel[1,a]

AFFILIATIONS

[1] Institute of Forestry and Engineering, Estonian University of Life Sciences, Kreutzwaldi 56/1, Tartu, Estonia
[2] Institute of Veterinary Medicine and Animal Science, Estonian University of Life Sciences, Kreutzwaldi 62, Tartu, Estonia
[3] Université Grenoble Alpes, IMEP, F-38016 Grenoble, France
[4] Université Grenoble Alpes, LMGP, F-38016 Grenoble, France

[a] Author to whom correspondence should be addressed: protima.rauwel@emu.ee

ABSTRACT

This work reports on the fabrication of ZnO polymer-based hybrid ultraviolet (UV) photodiodes with a configuration of ITO/ZnO-nanorod/F8BT/PEDOT:PSS/Ag. The diode was fabricated by spin-coating p-type F8BT and PEDOT:PSS polymers on hydrothermally grown n-type ZnO nanorods. The growth of ZnO nanorods was carried out by varying seed layer alcohols, viz., methanol, ethanol, isopropanol, and aqueous ethanol (70% alcohol). These solvents influenced the nanorod diameter, surface coverage, and surface defects. Herein, we demonstrate that the uniformity and defects in ZnO nanorods govern the electrical properties, photoresponse, and figures of merit of the photodiodes. In particular, the photodiodes are evaluated on their rectification ratio, ideality factor (η), responsivity (R), external quantum efficiency (EQE), and response time (T_{decay}). The photodiode fabricated with ZnO nanorods grown on the methanol seeding layer has demonstrated the best performance, owing to the uniform surface coverage of the nanorods. It also presented the highest rectification ratio of ~640, a T_{decay} of 108 s, a η of 2, an EQE of ~2760%, and an R of ~8.14 A/W at −2 V.

I. INTRODUCTION

Ultraviolet (UV) light detection is required for several military, civilian, and scientific applications such as missile warning, flame detection, environmental monitoring, image sensing, and satellite communication.[1,2] Inorganic wide bandgap semiconductors, including SiC, TiO$_2$, GaN, AlGaN, diamond, and ZnO, are widely used for UV photodetection.[3,4] Among them, the intrinsic n-type ZnO is the most popular because of its wide direct bandgap of 3.3 eV, high excitation binding energy of 60 meV, low toxicity and cost of production, high chemical stability, and remarkable electrical and optical properties.[5–8] When ZnO nanostructures are excited with UV light, oxygen molecules desorb from the surface, leaving behind free electrons that contribute to the generation of photocurrent in ZnO nanostructures.[9,10] Due to these surface reactions, charge trapping at various defect states occurs. Therefore, after the removal of UV irradiation, the phenomenon of persistent photoconductivity (PPC) in ZnO nanostructures becomes prominent.[10–12]

In our previous study, four ZnO nanorod samples prepared with different seeding alcohols were excited with 365 nm UV light. A low responsivity of 0.1–0.2 A/W with a high recovery time of 75–300 s was obtained from such samples, owing to PPC.[13] Singh *et al.* also reported a low responsivity of 0.022 A/W at 365 nm UV excitation for a Ni/Al:ZnO/Ni metal–semiconductor–metal UV sensor.[14] Therefore, even though ZnO nanostructure-based devices show high photoconductivity on UV exposure, they, nevertheless, suffer from low photoresponsivity and high recovery times due to PPC, limiting their applicability in UV photodetectors.

A p–n heterojunction between n-type and p-type semiconductors enhances the photoresponse and photocurrent in photodiodes.[15,16] Under a reverse bias, a built-in potential at the interface of the p–n heterojunction allows the directional movement of photogenerated electrons and holes, leading to an increase in the photocurrent in the photodiodes. In that regard, p–n heterojunctions with n-type ZnO nanorods have been constructed using several inorganic CuO, NiO, p-Si, and p-GaN, as well as

214

organic p-type semiconductors such as poly(3, 4 ethylenedioxythiophene):polystyrenesulfonate (PEDOT:PSS).[17–20] Among them, the organic PEDOT:PSS is highly beneficial because of its high electrical conductivity of up to 10^3 S/cm, work function of 5.0–5.2 eV, and high photo- and electrical stability under ambient conditions.[17,21] In addition, PEDOT:PSS can be easily coated on both rigid and flexible substrates using cost-effective coating techniques such as spin-coating and spray-coating. However, PEDOT:PSS-ZnO hybrid p–n junctions suffer from large band offsets at the interface, which results in energy loss due to the recombination of photogenerated carriers and, in turn, a reduction of the photocurrent.[18] Therefore, the band alignments need to be adjusted by introducing a third material between PEDOT:PSS and ZnO that bridges the potential at the interface of the layers. Subsequently, it reduces the recombination of photogenerated carriers, which enhances the photocurrent.[18]

In this study, a p-type poly(9,9-dioctylfluorene-alt-benzothiadiazole) (F8BT) polymer layer was introduced in between n-type ZnO nanorods and p-type PEDOT:PSS polymer. In fact, F8BT has its highest occupied molecular orbital (HOMO) level at −3.3 eV and lowest unoccupied molecular orbital (LUMO) level at −5.9 eV, close to the PEDOT:PSS HOMO level of −3.5 eV and LUMO level of −5.2 eV. Therefore, due to their closely aligned HOMO and LUMO levels, the F8BT layer improved the band alignment by reducing the band offset between ZnO nanorods and PEDOT:PSS, allowing a more efficient charge transfer and lower energy losses.

II. RESULTS AND DISCUSSION

In our previous work, we highlighted the influence of seeding alcohols, i.e., methanol, ethanol, isopropanol, and aqueous ethanol (70% ethanol, 30% water), on the nanorod diameter, uniformity, and surface defects.[13] In that work, photoluminescence spectroscopy revealed a higher number of surface defects in ZnO nanorods grown on methanol and isopropanol seed layers than those grown on

ethanol and aqueous ethanol seed layers. In addition, scanning electron microscopy (SEM) images of these ZnO nanorods revealed that the most uniform surface coverage of the nanorod growth was for the methanol, followed by ethanol, isopropanol, and aqueous ethanol seed layers.[13]

In order to fabricate photodiodes in this study, similar ZnO nanorods were grown on a 100 nm thick indium tin oxide (ITO) substrate with a 20 × 15 mm^2 area and 20 Ω/square resistance. A step-by-step description of the photodiode fabrication process is shown in the supplementary material, Fig. S.1. For the nanorod growth, first seed layers prepared with the four alcohols were drop cast, as shown in Fig. S.1(b). Subsequently, the ZnO nanorods were grown by hydrothermal growth, as shown in Fig. S.1(c), as described elsewhere.[13] Then, a solution of 20 mg F8BT (Sigma-Aldrich, 698 687) in 2 ml of toluene (Honeywell) was prepared, and 20 μl of the F8BT solution was spin-coated over the ZnO nanorods at a speed of 2000 rpm for 30 s, as shown in Fig. S.1(d). The ZnO–F8BT layers were annealed at 110 °C for 10 min. Then, 20 μl of the as-purchased PEDOT:PSS (OSSILA, F HC Solar) was spin-coated at a speed of 3000 rpm for 50 s [Fig. S.1(e)], and the substrate was again annealed at 110 °C for 10 min. For the electrical measurements, Ag (Chemtronics) front and back contacts were deposited on the top of the PEDOT:PSS layer and on ITO, as shown in Fig. S.1(f). Therefore, four photodiodes with a configuration of ITO/ZnO nanorods/F8BT/PEDOT:PSS/Ag were prepared, where the only differences were in the ZnO-nanorod seed layer alcohol solvents. The four photodiodes are abbreviated as device-M, device-E, device-I, and device-E$_{aq}$, where M stands for methanol, E for ethanol, I for isopropanol, and E$_{aq}$ for aqueous ethanol, respectively. In addition, SEM on the photodiodes was carried out on an FEI QUANTA 250 environmental SEM FEG operating at 15 kV with a resolution of 0.5 nm. Two source measurement units (Agilent 4156) with a step size of 20 mV and maximum compliance of 100 mA were used for the electrical measurements. Their photoresponse evaluation was carried out using a 125 W Hg lamp with an output wavelength of 365 nm, an optical fiber diameter of 4 mm, and an irradiance power
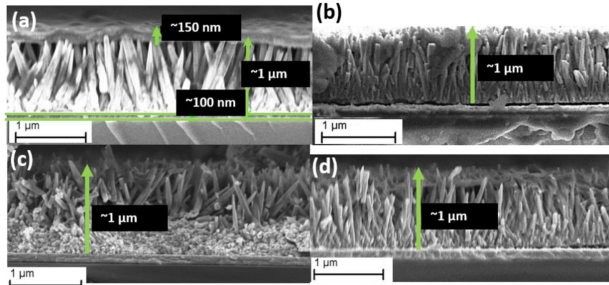

FIG. 1. Cross-sectional SEM image view of (a) device-M, (b) device-E, (c) device-I, and (d) device-E$_{aq}$.

of ~15 mW/cm². In order to obtain optimized polymer thickness and control the reproducibility of the photodiodes, several other devices were fabricated and tested by measuring their I–V in the dark. The results are provided in Figs. S.2 and S.3. Figure S.2 indicates that the optimal quantities of F8BT and PEDOT:PSS for device fabrication are 20 μl for both polymers. Figure S.3 suggests that there could be a ±10 mA difference in the output current among the two sets of devices. These arise from parameters such as the surface area of the top Ag contact as Ag contacts were deposited by hand using a thin wire, and the position of the Ag contacts. Nevertheless, the four sets of devices show similar I–V characteristics or good reproducibility.

Figure 1 is the cross-sectional view of the SEM images of the four photodiodes with different layer thicknesses labeled in Fig. 1(a) of device-M. The ZnO-nanorod layer is ~1 μm thick, and the nanorod diameter is ~100 nm. The nanorods of device-M, device-E, and device-E$_{aq}$ show clear vertical growth on the ITO substrate, as observed in Figs. 1(a), 1(b), and 1(d), respectively, whereas nanorods of device-I present random orientations along with some vertical growth, as observed in Fig. 1(c). In addition, a combined F8BT-PEDOT:PSS-polymer layer of thickness of ~150 nm is visible for device-M in Fig. 1(a). However, for other photodiodes, the polymer layers detached from the surface during SEM sample preparation and, therefore, were not visible. The bottom layer of ~100 nm observed in SEM images is the ITO layer, coated on a glass substrate.

Figures 2(a) and 2(b) are the I–V and semi-log (I)–V characteristics of the photodiodes in the dark and under UV irradiations from −3 to +3 V. The dark I–V curves represented by dashed lines exhibit a diode-like rectifying behavior for the photodiodes,[22] with the highest rectification ratio $I_{reverse}/I_{forward}$ of 640 for device-M, followed by 80 for device-I, 70 for device-E, and the lowest rectification of 44 for device-E$_{aq}$, calculated at ±2 V. Here, $I_{reverse}$ is the current at reverse bias, and $I_{forward}$ is the current at forward bias. In addition, for every photodiode, the reverse current in dark tends to increase with an increase in the reverse bias voltage, attributable to the generation–recombination centers at the p–n heterojunction

interface between the ZnO nanorod surface and F8BT.[23] These centers also play a role in the ideality factor (η) of the diodes, calculated using Cheung's method;[24] η of ~1.8, ~2.0, ~2.4, and ~3.2 was calculated for device-I, device-M, device-E, and device-E$_{aq}$, respectively. In addition, η of ~2.0 and ~1.8 of device-M and device-I, respectively, indicate that the main current generation mechanisms in these two photodiodes are via diffusion and recombination.[25] On the other hand, a high ideality factor of $\eta > 2$ indicates extended defects or local non-linear shunts, due to which the electron–hole recombination current flows inhomogeneously.[26] Our previous study shows that the nanorods prepared using aqueous ethanol have the most non-uniform surface with several voids;[13] therefore, the extended defects and local non-linear shunts are most plausible in device-E$_{aq}$, leading to a high η of ~3.2.

The solid lines in Figs. 2(a) and 2(b) represent the I–V and semi-log (I)–V characteristics under UV irradiations, showing an increase in the overall output current compared to the dark current. The depletion region formed at the p–n interface between n-type ZnO nanorods and p-type F8BT/PEDOT:PSS polymers induces a built-in electric field that provides a driving force for the separation of photogenerated electron–hole pairs. Therefore, an enhancement in the overall output current under UV irradiation compared to dark conditions occurs.[18] In Fig. 2(b), device-M and device-I demonstrate an increase in three orders of magnitude in the output current, owing to the higher number of surface defects in their bare nanorods, whereas, due to the lower amount of surface defects in the bare nanorods of device-E and device-E$_{aq}$, these two photodiodes exhibit only one order of magnitude enhancement in the output current under UV irradiations. Since all the other parameters of photodiode fabrication are identical, i.e., nanorod growth solution and thickness of the polymer layers, the differences in the output current can be directly correlated with the surface defects in the bare nanorods arising from the seeding layer alcohol solvent.

Figure 2(c) is the energy band diagram of photodiodes with the configuration ITO/ZnO nanorods/F8BT/PEDOT:PSS/Ag. The figure shows that the F8BT intermediate layer between ZnO and
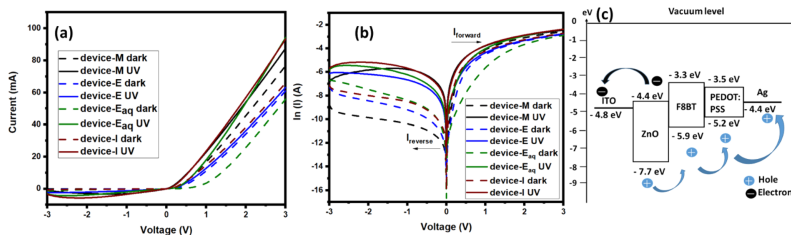

FIG. 2. (a) I–V and (b) semi-log (I)–V characteristics of device-M, device-E, device-I, and device-E$_{aq}$, and (c) band energy diagram of the photodiodes, drawn to scale, illustrating directional charge transfer between the different layers.

216

PEDOT:PSS creates a bridging potential that reduces the band offsets between ZnO and F8BT, promoting an efficient charge transfer between the layers. In addition, the n- and p-type semiconductor materials of the photodiodes exhibit band bending because of differences in their valance-conduction and HOMO–LUMO energy levels.[18] In fact, electrons, being the majority carriers of n-type ZnO nanorods, migrate to PEDOT:PSS due to the upward band bending exhibited by ZnO, leaving behind holes at the surface of ZnO. On the other hand, PEDOT:PSS accepts these electrons on its surface, as it exhibits downward band bending. The collection of positive and negative charges at the interface results in a depletion region with a built-in electric field directed from ZnO towards PEDOT:PSS, generating rectifying I–V characteristics of the photodiodes. In addition, there is a potential barrier of ~1.8 eV between the ZnO-nanorod valence band and the F8BT HOMO level. Under UV irradiation, such a potential difference supports the directional transfer of photogenerated holes from the ZnO nanorod valence band to the F8BT HOMO level, which can be further transferred to the PEDOT:PSS HOMO level. Therefore, the charge transfer mechanism explains the high photocurrent under UV irradiation compared to dark conditions for the photodiodes.

Figure 3 provides the I–t characteristics and photoresponse of the photodiodes at four different reverse biases of −0.1, −0.5, −1, and −2 V. These I–t measurements were performed under a series of UV on−off cycles; the UV-on cycles were fixed to 10 s and the UV-off cycles to 140 s, with a plausible error of 1 s due to manual operation. In particular, the magnitude of the photocurrent increases with an increase in the reverse voltage, owing to the increase in the width of the depletion region.[18,27] However, the stability of the photoresponse evaluated in the UV-on and UV-off cycles is different at different biases for the photodiodes. The most stable photoresponse

is demonstrated by device-E and the second most by device-E_aq at three reverse biases of −0.5, −1, and −2 V. At the reverse bias of −2 V, both device-E and device-E_aq exhibit similar maximum photocurrents of ~4.2 mA, as shown in Figs. 2(b) and 2(d). However, the photocurrent is higher for device-E_aq at other voltages, owing to slight differences in their surface defects. This suggests that the reverse bias of −2 V deactivates the defect states. Similarly, device-M and device-I show similar maximum photocurrents of ~24.5 mA at −2 V in Figs. 3(a) and 3(c), while as for other biases, device-M presents a relatively higher maximum photocurrent than device-I. However, for reverse biases of −0.1, −0.5, and −1 V, there is an increase in the onset current at every UV-on cycle for device-I, as observed in Figs. 3(o), 3(k), and 3(g), respectively, suggesting that the trapped charges contribute to the photocurrent, along with excitons. The voltages of −0.1, −0.5, and −1 V are, therefore, not sufficient to compensate for the defect states in device-I. A similar behavior is also shown by device-M at −0.5 V in Fig. 3(i). In fact, due to the high number of surface defects in the bare nanorods of device-M and device-I, the probability of charge trapping in ZnO nanorods, leading to instabilities in their photoresponse, is rather high. In addition, there are differences in the nanorod layer morphology or the random orientation of nanorods for device-I in Fig. 1(c) compared to other devices, in which all the ZnO nanorods are vertically oriented. This reduces the surface and the quality of contact of the nanorods with the polymer overlayer, creating instabilities in the output current at lower voltages in device-I. On the other hand, at a reverse bias of −0.1 V, device-M and device-E_aq show a drop in their photocurrents during subsequent UV-on/off cycles, as shown in Figs. 3(m) and 3(p), respectively. The current decrease is, therefore, attributed to the trapping of photogenerated carriers in the ZnO-nanorod defect states.
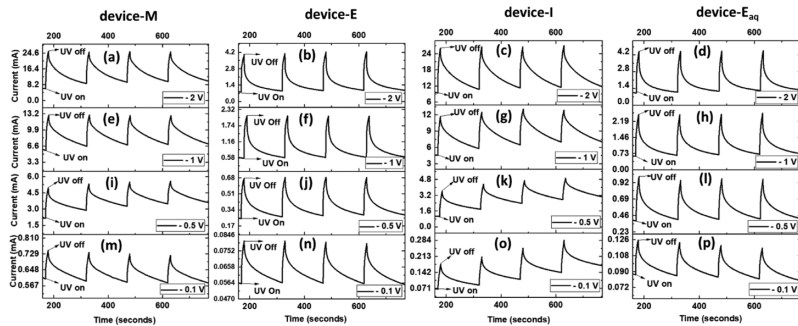

FIG. 3. Photoresponse under several UV on–off cycles of device-M, device-E, device-I, and device-E_aq at reverse biases of −0.1, −0.5, −1, and −2 V.

TABLE I. List of figures of merit, including S, R (A/W), T_{rise} (s), T_{decay} (s), and EQE (%) of device-M, device-E, device-I, and device-E$_{aq}$. The experimental error associated with I originating from the instrument is ± 20 pA.

	Bias (V)	S	R (A/W)	T_{rise} (s)	T_{decay} (s)	EQE (%)
Device-M	−0.1	1.24	0.08	7.7	97.1	25.2
	−0.5	1.6	1.19	7.3	125.4	379.8
	−1	1.9	3.15	6.6	111.8	1071.8
	−2	2.5	8.14	6.6	108.3	2764.4
Device-E	−0.1	1.4	0.01	7.6	90.2	4.2
	−0.5	2.4	2.1	6.8	84.2	71.5
	−1	3.5	0.79	6.2	70.6	268
	−2	4.4	1.74	6.4	62.6	590
Device-I	−0.1	2	0.08	7.5	225.1	25.8
	−0.5	1.8	1.15	7.5	147.7	391.5
	−1	1.83	3.11	7.2	109.8	1054.8
	−2	2.3	8.16	7.6	108.5	2773.2
Device-E$_{aq}$	−0.1	1.4	0.02	7.6	81	6.3
	−0.5	2.3	0.29	6.7	89.9	99.4
	−1	3.6	1	7.0	80.7	335.1
	−2	3.7	1.78	7.0	69.4	603.2

The figures of merit of the photodiodes were evaluated in terms of their sensitivity (S), responsivity (R), and external quantum efficiency (EQE),[28,29] which are defined as

$$S = \frac{I_{UV}}{I_{dark}}, \tag{1}$$

$$R = \frac{I_{UV} - I_{dark}}{P_{in} A_{eff}}, \tag{2}$$

$$EQE = R\frac{hc}{q\lambda}. \tag{3}$$

Here, I_{UV} is the current when UV illumination is switched off, I_{dark} is the dark current, P_{in} is the incident power of the UV radiations, A_{eff} is the effective area of the optical fiber of the UV lamp source, h is the Planck's constant, c is the speed of light, q is the elementary charge, and λ is the wavelength of the UV illumination. In addition, the figures of merit of the photodiodes were also evaluated in terms of response times T_{rise} and T_{decay}, where T_{rise} is the time taken to raise the current from 10% to 90% under the UV irradiations, while T_{decay} is the time taken for the current to drop from 90% to 10% when the UV irradiation is turned off.[28] Table I lists the figures of merit for the photodiodes, where S, R, and EQE of the photodiodes tend to increase with an increase in reverse bias.

Figure 4 compares the R and EQE of these photodiodes in terms of the reverse bias voltage. The figure reveals that device-M and device-I demonstrate similar performances and EQE at the same reverse bias. In fact, they both have an EQE of ~2760% at a reverse bias of −2 V. Similarly, device-E and device-E$_{aq}$ show similar performances, with similar EQE of ~600% at the same reverse bias of −2 V. However, compared to the EQE of device-E and device-E$_{aq}$, the EQE of device-M and device-I are much higher. The higher EQE
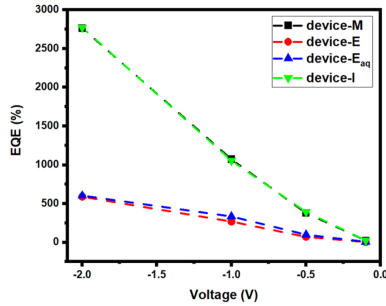

FIG. 4. Comparison of EQE in terms of the reverse bias voltages of four photodiodes: device-M, device-E, device-I, and device-E$_{aq}$.

of device-M and device-I are attributed to the higher surface defects in their bare nanorods. In fact, these defects are active centers for charge generation. A higher number of charge carriers leading to both recombination and diffusion currents produce a lower ideality factor of ~2 and ~1.8, respectively, as compared to device-E and device-E$_{aq}$. Ideality factors of <2 imply more efficient diode operation.

However, the response times, i.e., T_{rise} and T_{decay} of device-E and device-E$_{aq}$, tend to be quicker than that of device-M and device-I, listed in Table I. In fact, T_{rise} is directly dependent on the total UV irradiation time. On the other hand, T_{decay} is the intrinsic property of the device and depends on various parameters, such as generation–recombination centers at the p–n interface, the probability of recombination of excitons, charge trapping in the defects of bare ZnO nanorods, and the width of the depletion region.[13,30] In addition, the higher the applied voltage, the quicker the T_{decay}. Therefore, device-E and device-E$_{aq}$ display a better T_{decay} of ~60 s, compared to the longer T_{decay} of ~108 s for device-I and device-M at −2.0 V. For other voltages as well, the T_{decay} of device-E and device-E$_{aq}$ is quicker than that of device-M and device-I. Therefore, in terms of T_{decay}, device-E and device-E$_{aq}$ are more efficient than that of device-M and device-I. However, when selecting the best photodiode, several different parameters need to be considered. In that regard, device-M appears to have better ZnO-nanorod surface coverage, the highest rectification ratio, relatively stable on/off-cycles, a η of 2, as well as good S, R, and EQE. Therefore, in this study, device-M appears to be the most suitable candidate for photodiode applications.

III. CONCLUSION

We have successfully fabricated ZnO nanorods and polymer-based hybrid UV photodiodes with a device configuration of ITO/ZnO nanorod/F8BT/PEDOT:PSS/Ag. In general, the photodiodes with ZnO-nanorods grown with methanol and isopropanol

seeding layers possess the same *EQE*, which is also the highest among the photodiodes in this study. In addition, lower reverse biases are insufficient for the proper working of photodiodes, and better performances are obtained at −2 V, demonstrating the highest stability during UV on–off cycles. Furthermore, photodiodes fabricated with ZnO nanorods harboring higher amounts of surface defects, i.e., ZnO nanorods in the methanol and isopropanol seed layers, exhibited a higher *EQE* of ~2760% but also produced a longer T_{decay} at −2 V. This suggests that higher amounts of surface defects in nanorods support one figure of merit at the detriment of the other. Furthermore, the best performing photodiode in this study was selected by comparing several of their figures of merit. In that regard, the photodiode with the methanol seed layer was considered the best performing photodiode, as it possesses the highest rectification ratio of ~640, a η of 2, the most uniform ZnO-nanorod coverage, a high *EQE* of ~2760%, a *R* of ~8.14 A/W, and a good T_{decay} of ~108 s at −2 V. To the best of our knowledge, this work is the first to demonstrate the effect of the seed-layer solvents on the functionalities of the ZnO nanorod-polymer based UV photodiodes. Therefore, this study provides a novel methodology to fabricate UV photodiodes, consolidated by a detailed analysis of the influence of these defects harbored by the ZnO nanorods on the figures of merit of the UV photodiodes.

SUPPLEMENTARY MATERIAL

A step-by-step procedure for the fabrication of photodiodes is provided in Fig. S.1 of the supplementary material. Figures S.2(a) and S.2(b) are the dark I–V and semi-log(I)–V characteristics of three ethanol nanorod based devices that were prepared by varying F8BT amounts, showing 20 μl F8BT and 20 μl PEDOT:PSS used in this work are the optimum amounts for these devices. Figures S.3(a) and S.3(b) are the dark I–V and semi-log(I)–V characteristics of two sets of four photodiodes. In this study, we used the best of two sets of devices in terms of dark I–V characteristics to further evaluate their I–t characteristics.

ACKNOWLEDGMENTS

AUTHOR DECLARATIONS

Conflict of Interest

The authors have no conflicts to disclose.

Author Contributions

K.N. performed all the experiments and wrote the paper. F.D. performed and confirmed experiments. I.G. contributed to the experimental analysis. E.R. participated in the experiments, discussion, and writing. P.R. conceptualized the study, and K.N. performed experiments, supervised, provided funding, and wrote and reviewed the work.

Keshav Nagpal: Conceptualization (equal); Data curation (lead); Formal analysis (lead); Investigation (lead); Visualization (equal); Writing – original draft (lead). **Erwan Rauwel**: Funding acquisition (lead); Methodology (supporting); Project administration (lead); Resources (lead); Supervision (supporting); Validation (supporting); Writing – review & editing (supporting). **Frederique Ducroquet**: Formal analysis (equal); Funding acquisition (lead); Investigation (supporting); Validation (supporting). **Isabelle Gélard**: Data curation (supporting); Formal analysis (equal); Investigation (equal). **Protima Rauwel**: Conceptualization (equal); Funding acquisition (equal); Investigation (equal); Methodology (equal); Project administration (equal); Resources (equal); Supervision (equal); Validation (equal); Writing – review & editing (equal).

DATA AVAILABILITY

The data that support the findings of this study are available from the corresponding author upon reasonable request.

REFERENCES

[1]Q. Cai, H. You, H. Guo, J. Wang, B. Liu, Z. Xie, D. Chen, H. Lu, Y. Zheng, and R. Zhang, Light: Sci. Appl. **10**(1), 94 (2021).
[2]H. Liang, Z. Han, and Z. Mei, Phys. Status Solidi A **218**(1), 2000339 (2021).
[3]K. Liu, M. Sakurai, and M. Aono, Sensors **10**(9), 8604–8634 (2010).
[4]W. Fang, Q. Li, J. Li, Y. Li, Q. Zhang, R. Chen, M. Wang, F. Yun, and T. Wang, Crystals **13**(6), 915 (2023).
[5]K. Nagpal, L. Rapenne, D. S. Wragg, E. Rauwel, and P. Rauwel, Nanomater. Nanotechnol. **12**, 1–10 (2022).
[6]K. Nagpal, E. Rauwel, E. Estephan, M. R. Soares, and P. Rauwel, Nanomaterials **12**(19), 3546 (2022).
[7]E. Rauwel, A. Galeckas, P. Rauwel, M. F. Sunding, and H. Fjellvåg, J. Phys. Chem. C **115**(51), 25227–25233 (2011).
[8]R. Khokhra, B. Bharti, H.-N. Lee, and R. Kumar, Sci. Rep. **7**(1), 15032 (2017).
[9]A. Castro, S. Calderon, and L. Marques, Materials **16**(3), 1275 (2023).
[10]J. Bao, I. Shalish, Z. Su, R. Gurwitz, F. Capasso, X. Wang, and Z. Ren, Nanoscale Res. Lett. **6**(1), 404 (2011).
[11]S. Hullavarad, N. Hullavarad, D. Look, and B. Claflin, Nanoscale Res. Lett. **4**(12), 1421 (2009).
[12]R. Anu Roshini, K. Nagpal, and E. Senthamarai Kannan, Europhys. Lett. **127**(5), 57005 (2019).
[13]K. Nagpal, E. Rauwel, F. Ducroquet, I. Gélard, and P. Rauwel, Nanotechnology **34**(48), 485602 (2023).
[14]S. Singh and S.-H. Park, Optik **145**, 576–581 (2017).
[15]I.-S. Jeong, J. H. Kim, and S. Im, Appl. Phys. Lett. **83**(14), 2946–2948 (2003).
[16]Y. Chen, L. Su, M. Jiang, and X. Fang, Mater. Sci. Technol. **105**, 259–265 (2022).
[17]A. Kadir, R. Jamal, T. Abdiryim, X. Liu, H. Zhang, N. Serkjan, D. Zou, and Y. j. Liu, Nanoscale Res. Lett. **17**(1), 67 (2022).
[18]Y. Lin, J. Zou, W. Wang, X. Liu, J. Gao, and Z. Lu, Appl. Surf. Sci. **599**, 153956 (2022).
[19]N. A. M. Asib, F. S. Husairi, K. A. Eswar, A. N. Afaah, M. H. Mamat, M. Rusop, and Z. Khusaimi, Sens. Actuators, A **302**, 111827 (2020).
[20]H. Zhou, P. Gui, L. Yang, C. Ye, M. Xue, J. Mei, Z. Song, and H. Wang, New J. Chem. **41**(12), 4901–4907 (2017).
[21]Y. He, S. Gong, R. Hattori, and J. Kanicki, Appl. Phys. Lett. **74**(16), 2265–2267 (1999).

[22] N. Hernandez-Como, G. Rivas-Montes, F. J. Hernandez-Cuevas, I. Mejia, J. E. Molinar-Solis, and M. Aleman, Mater. Sci. Semicond. Process. **37**, 14–18 (2015).

[23] J. D. Hwang and K. S. Lee, Electrochem. Soc. **155**(4), H259 (2008).

[24] S. K. Cheung and N. W. Cheung, Appl. Phys. Lett. **49**(2), 85–87 (1986).

[25] G. W. Lee, J.-I. Shim, and D.-S. Shin, Appl. Phys. Lett. **109**(3), 031104 (2016).

[26] O. Breitenstein, P. Altermatt, K. Ramspeck, and A. Schenk, "The origin of ideality factors n > 2 of shunts and surfaces in the dark I-V curves of Si solar cells," in Proceedings of the 21st European Photovoltaic Solar Energy Conference and Exhibition, Dresden, Germany, 4-8 October 2006 (WIP-Renewable Energies, 2006).

[27] A. Henning, V. K. Sangwan, H. Bergeron, I. Balla, Z. Sun, M. C. Hersam, and L. J. Lauhon, ACS Appl. Mater. Interfaces **10**(19), 16760–16767 (2018).

[28] H. Komatsu, Y. Kawamoto, and T. Ikuno, Nanomaterials **12**(6), 940 (2022).

[29] S. S. Mousavi, B. Sajad, and M. H. Majlesara, Mater. Des. **162**, 249–255 (2019).

[30] Z.-M. Liao, J. Xu, J.-M. Zhang, and D.-P. Yu, Appl. Phys. Lett. **93**(2), 023111 (2008).

07 June 2024 06:51:50

220

CURRICULUM VITAE

Contact information

Name: Keshav Nagpal
Date of birth: 01.06.1995
Citizenship: Indian
Email: keshav.nagpal@student.emu.ee

Education

2020-2024   PhD studies in nanoscience at Estonian University of Life Sciences
2013-2018   BS-MS degree with MS in Physics from Indian Institute of Sciences Education and Research, India

Work experience

2020-2024   Junior research fellow at Estonian University of Life Sciences
2022-2023   Internship at IMEP-LaHC, MINATEC, France for electrical measurements
2022   Internship at University of Montpellier, France for Raman spectroscopy measurements
2018-2019   Research project assistant under SERB program at Birla Institute of Technology and Science India
2016   Summer internship at Birla Institute of Technology and Science India

Research Projects

2022-2023   "Cu3N-CNT nanomaterials for photocatalysis and electrophotocatalysis", **PhD student participant,** NFFA EU Horizon (V220149MIEQ)
2020-2023   "Recyclable nanocomposites for water remediation and heavy metal ion extraction from polluted water", **PhD student participant,** baseline fund (P200030TIBT)
2020-2021   "Structural and optical characterization of HfO2-CNT based hybrid nanostructures for photocatalysis and photovoltaics", **PhD student participant,** NFFA EU Horizon (V210108TIEQ)
2020-2021   "Polymer nanocomposites applied to anti-viral additives and antiviral coatings for surfaces

protection", **PhD student participant,** Target grants aimed at solving the problems caused by the SARS-CoV-2 virus (COVSG)

2015-2023   "Emerging orders in quantum and nanomaterial" (TK134), **PhD student participant**, Estonian Centre of Excellence (F180175TIBT)

Teaching experience

2023-2024   "Electrical and photo response properties of ZnO nanorods for photodiode applications" **Master's thesis** supervision of Taavi Murel. Supervisors: **Keshav Nagpal** and Protima Rauwel.

2022-2023   "Photoelectric effect of ZnO nanorods" **Master's thesis** supervision of Henno Kaeval. Supervisors: **Keshav Nagpal**, Protima Rauwel and Erwan Rauwel

2022-2023   "Transmittance properties of ZnO nanorods for solar cell applications" **Bachelor's thesis** supervision of Sten Kelus. Supervisors: **Keshav Nagpal**, and Protima Rauwel.

2022   Assisted Prof. Erwan Rauwel in the laborarory work for the course Nanotechnology (3 ECTS, TE 1050)

2021-2022   "Determining the absorption wavelengths of solar cell nanomaterials – case of ZnO nanoparticles" **Bachelor's thesis** of Henno Kaeval. Supervisors: Protima Rauwel, Erwan Rauwel and **Keshav Nagpal**

Publications

2024   **K. Nagpal**, E. Rauwel, F. Ducroquet, I. Gelard, P. Rauwel, "Fabrication and evaluation of figures of merit of ZnO-polymer based hybrid UV photodiodes" APL materials, AIP publishing (2024) **1.1 ETIS classified** (Article under publication)

2023   **K. Nagpal**, E. Rauwel, F. Ducroquet, I. Gelard and P. Rauwel, "Relevance of alcoholic solvents in the growth of ZnO nanoparticles and ZnO hierarchical nanorod structures on their optical and opto-electrical

properties" , Nanotechnology **34**, 485602 (2023), **1.1 ETIS classified**

Hendrix, E. Rauwel, **K. Nagpal**, R. Haddad, E. Estephan, C. Boissière, P. Rauwel, "Revealing the Dependency of Dye Adsorption and Photocatalytic Activity of ZnO Nanoparticles on Their Morphology and Defect States" , Nanomaterials 13(13), 1998 (2023), **1.1 ETIS classified**

2022   **K. Nagpal**, E. Rauwel, E. Estephan, M. R. Soares, P. Rauwel, "Significance of Hydroxyl Groups on the Optical Properties of ZnO Nanoparticles Combined with CNT and PEDOT:PSS" Nanomaterials **12**, 3546 (2022), **1.1 ETIS classified**

K. Nagpal, L. Rapenne, D. S. Wragg, E. Rauwel, P. Rauwel, "The role of CNT in surface defect passivation and UV emission intensification of ZnO nanoparticles" Nanomaterials and Nanotechnology, 12, 1–10 (2022), **1.1 ETIS classified**

K. Nagpal, M. S. Rosario, K. Praakle, E. Rauwel, P. Rauwel, "Investigation of the optical and antibacterial properties of biosynthesized ZnO nanoparticles using Thuja tincture" Journal of Physics: Conference Series 2315, 012016 (2022), **3.1 ETIS classified**

2021   **K. Nagpal**, E. Rauwel, F. Ducroquet and Protima Rauwel "Assessment of the optical and electrical properties of light emitting diodes containing carbon-based nanostructures and plasmonic nanoparticles: a review", Beilstein J. Nanotechnol. **12**, 1078–1092 (2021), **1.1 ETIS classified**

ELULOOKIRJELDUS

Kontaktinfo

Nimi: Keshav Nagpal
Sünniaeg: 01.06.1995
Kodakondsus: India
E-post: keshav.nagpal@student.emu.ee

Haridus

2020-2024   nanoteaduste doktoriõpe Eesti Maaülikoolis
2013-2018   BS-MS kraad koos MS-ga füüsikas India Teaduste
                   Haridus- ja Teadusinstituudist, India

Töökogemus

2020-2024   Eesti Maaülikooli nooremteadur
2022-2023   Praktika IMEP-LaHC-s, MINATECis, Prantsusmaal
                   elektrimõõtmiste alal
2022-2022   Praktika Montpellieri ülikoolis, Prantsusmaal Raman
                   spektroskoopia mõõtmiste alal
2018–2019   India Birla Tehnoloogia- ja Teadusinstituudi SERB
                   programmi uurimisprojekti assistent
2016-2016   Suvepraktika, Birla Tehnoloogia- ja Teadusinstituudis,
                   India

Uurimisprojektid

2022-2023   "Cu3N-CNT nanomaterjalid fotokatalüüsiks ja
                   elektrofotokatalüüsiks", doktorant, NFFA EU
                   Horizon (V220149MIEQ)
2020-2023   "Taaskasutatavad nanokomposiidid vee puhastamiseks
                   ja raskmetallide ioonide eraldamiseks saastunud
                   veest", doktorant, baasfond (P200030TIBT)
2020-2021   "HfO2-CNT-põhiste hübriidnanostruktuuride
                   struktuurne ja optiline iseloomustus fotokatalüüsi ja
                   fotogalvaanika jaoks", doktorant, NFFA EU Horizon
                   (V210108TIEQ)
2020-2021   "Polümeeride nanokomposiidid, mida kasutatakse
                   pindade kaitseks viirusevastastes lisandites ja
                   viirusevastastes katetes", doktorant, SARS-CoV-2

viiruse (COVSG) põhjustatud probleemide lahendamisele suunatud sihttoetused

2015-2023 "Emerging orders in quantum and nanomaterial" (TK134), doktorant, Eesti tippkeskus (F180175TIBT)

Õpetamise kogemus

2023-2024 "ZnO nanovarraste elektri- ja fotoreaktsiooni omadused fotodioodirakendustes" Taavi Mureli magistritöö juhendamine, juhendajad Keshav Nagpal ja Protima Rauwel

2022-2023 "ZnO nanovarraste fotoelektriline efekt" Henno Kaevali magistritöö juhendamine, juhendajad Keshav Nagpal, Protima Rauwel ja Erwan Rauwel

2022-2023 "ZnO nanovarraste läbilaskvusomadused päikesepatareide rakendustes" Sten Keluse bakalaureusetöö juhendamine, juhendajad Keshav Nagpal ja Protima Rauwel

2022- 2022 Abistanud prof Erwan Rauweli kursuse Nanotehnoloogia (3 EAP, TE 1050) laboritöödel

2021-2022 "Päikesepatarei nanomaterjalide neeldumislainepikkuste määramine – ZnO nanoosakeste juhtum" Henno Kaevali bakalaureusetöö, juhendajad Protima Rauwel, Erwan Rauwel ja Keshav Nagpal

Publikatsioonid

2024 **K. Nagpal**, E. Rauwel, F. Ducroquet, I. Gelard, P. Rauwel, "Fabrication and evaluation of figures of merit of ZnO-polymer based hybrid UV photodiodes" APL materials, AIP publishing (2024) **1.1 ETIS classified** (Article under publication)

2023 **K. Nagpal**, E. Rauwel, F. Ducroquet, I. Gelard and P. Rauwel, "Relevance of alcoholic solvents in the growth of ZnO nanoparticles and ZnO hierarchical nanorod structures on their optical and opto-electrical

properties" , Nanotechnology **34**, 485602 (2023), **1.1 ETIS classified**

Hendrix, E. Rauwel, **K. Nagpal**, R. Haddad, E. Estephan, C. Boissière, P. Rauwel, "Revealing the Dependency of Dye Adsorption and Photocatalytic Activity of ZnO Nanoparticles on Their Morphology and Defect States" , Nanomaterials 13(13), 1998 (2023), **1.1 ETIS classified**

2022   **K. Nagpal**, E. Rauwel, E. Estephan, M. R. Soares, P. Rauwel, "Significance of Hydroxyl Groups on the Optical Properties of ZnO Nanoparticles Combined with CNT and PEDOT:PSS" Nanomaterials *12*, 3546 (2022), **1.1 ETIS classified**

K. Nagpal, L. Rapenne, D. S. Wragg, E. Rauwel, P. Rauwel, "The role of CNT in surface defect passivation and UV emission intensification of ZnO nanoparticles" Nanomaterials and Nanotechnology, 12, 1–10 (2022), **1.1 ETIS classified**

K. Nagpal, M. S. Rosario, K. Praakle, E. Rauwel, P. Rauwel, "Investigation of the optical and antibacterial properties of biosynthesized ZnO nanoparticles using Thuja tincture" Journal of Physics: Conference Series 2315, 012016 (2022), **3.1 ETIS classified**

2021   **K. Nagpal**, E. Rauwel, F. Ducroquet and Protima Rauwel "Assessment of the optical and electrical properties of light emitting diodes containing carbon-based nanostructures and plasmonic nanoparticles: a review", Beilstein J. Nanotechnol. **12**, 1078–1092 (2021), **1.1 ETIS classified**

VIIS VIIMAST KAITSMIST

MAGNUS LAURINGSON
LÕHE-NEERUEOSLIKU (*T. BRYOSALMONAE*) LEVIKUMUSTRID,
PEREMEESLIIKIDE SISENE JA VAHELINE
ESINEMIS- JA HAIGUSDÜNAAMIKA LÕHILASTEL
DISTRIBUTION PATTERNS, INTER- AND INTRA-HOST DYNAMICS OF AN
EMERGING SALMONID PARASITE *T. BRYOSALMONAE* ACROSS TEMPORAL AND
SPATIAL SCALES
Professor Anti Vasemägi, vanemlektor Priit Päkk
30. mai 2024

UPENDRA BHELE
SUURE MADALA JÄRVE TOIDUAHELATE MODELLEERIMINE PIKAAJALISTE
SEIREANDMETE PÕHJAL
MODELLING OF LARGE SHALLOW LAKE FOOD WEB BASED ON LONG TERM
MONITORING DATA
Vanemteadur Fabien André Daniel Cremona
30. mai 2024

TANA WUYUN
EOSTAIMEDE LEHTEDE STRUKTUUR, FÜSIOLOOGIA JA HORMOONVASTUSED
LEAF STRUCTURE-FUNCTION RELATIONSHIPS AND RESPONSES TO PLANT
HORMONES IN NON-SEED PLANTS
Professor Ülo Niinemets
4. juuni 2024

MARGARETA NOVIAN CAHYANTI
JÄTKUSUUTLIKUD ENERGIAKANDJAD TAASTUVENERGIASÜSTEEMIDELE:
TORREFITSEERITUD LIGNOTSELLULOOSSE BIOMASSI POTENTSIAALI
UURIMINE
SUSTAINABLE ENERGY CARRIERS FOR RENEWABLE ENERGY SYSTEMS:
EXPLORING THE POTENTIAL OF TORREFIED LIGNOCELLULOSIC BIOMASS
Professor Timo Kikas
11. juuni 2024

PRIIT BERNOTAS
ANGERJA (*ANGUILLA ANGUILLA*) LOODUSLIKE JA ASUSTATUD
POPULATSIOONIDE ARVUKUSE HINNANG EESTI VEEKOGUDES
THE ESTIMATION OF STOCKED AND NATURAL EUROPEAN EEL (*ANGUILLA
ANGUILLA*) POPULATIONS IN ESTONIAN WATERS
Professor Markus Vetemaa, professor Peeter Nõges
19. juuni 2024